Dynamics of interacting graphene membranes

Dolleman, Robin Joey

DOI
10.4233/uuid:118b4d3e-2d06-4ce7-b5a8-bcc934f0468a

Publication date
2018

Document Version
Final published version

Citation (APA)
Dolleman, R. J. (2018). *Dynamics of interacting graphene membranes*. [Dissertation (TU Delft), Delft University of Technology]. https://doi.org/10.4233/uuid:118b4d3e-2d06-4ce7-b5a8-bcc934f0468a

DYNAMICS OF INTERACTING GRAPHENE MEMBRANES

DYNAMICS OF INTERACTING GRAPHENE MEMBRANES

Proefschrift

ter verkrijging van de graad van doctor
aan de Technische Universiteit Delft,
op gezag van de Rector Magnificus prof. dr. ir. T. H. J. J. van der Hagen
voorzitter van het College voor Promoties,
in het openbaar te verdedigen op
dinsdag 20 november 2018 om 15:00 uur

door

Robin Joey DOLLEMAN

Werktuigkundig ingenieur,
Technische Universiteit Delft, Nederland,
geboren te Gouda, Nederland.

Dit proefschrift is goedgekeurd door de promotoren.

Samenstelling promotiecommissie bestaat uit:

Rector Magnificus,	voorzitter
Prof. dr. P. G. Steeneken,	Technische Universiteit Delft, promotor
Prof. dr. ir. H. S. J. van der Zant,	Technische Universiteit Delft, promotor
Onafhankelijke leden:	
Prof. dr. J. E. Sader,	University of Melbourne
Prof. dr. M. Schleberger	Universität Duisburg-Essen
Prof. dr. G. A. Steele,	Delft University of Technology
Prof. dr. ir. P. M. Sarro,	Delft University of Technology
Dr. R. van Rijn,	Applied Nanolayers B.V.

Dit werk maakt deel uit van het onderzoeksprogramma Integrated Graphene Pressure Sensors met projectnummer 13307 dat (mede)gefinancierd is door de Nederlandse Organisatie voor Wetenschappelijk Onderzoek (NWO).

Keywords: graphene, two-dimensional materials, molybdenum disulfide, nanomechanics, pressure sensors, gas sensors, NEMS, nonlinear dynamics, Fabry-Perot interferometer, thermal characterization, parametric resonance, stochastic switching, squeeze-film effect, selective permeation, osmosis

Printed by: Gildeprint, Enschede

Front & Back: Artist impression of a wrinkled graphene osmotic pressure sensor (chapter 12).

Casimir PhD Series, Delft-Leiden 2018-39

ISBN 978-90-8593-369-4

An electronic version of this dissertation is available at
http://repository.tudelft.nl/.

The science of today
is the technology of tomorrow.

Edward Teller

Contents

SUMMARY

Micro and nanomechanical sensors are indispensable in modern consumer electronics, automotive and medical industries. Gas pressure sensors are currently the most widespread membrane-based micromechanical sensors. By reducing their size, their unit costs and energy consumption drops, making them more attractive for integration in new applications. Reducing the size requires the membrane to be as thin as possible, but also very strong. Graphene is the perfect material for such a membrane since it is only one atom thick but also the strongest material ever measured. This dissertation investigates the dynamics of suspended graphene membranes for sensing applications. These sensing applications are not restricted to pressure sensors alone, but the dynamics of graphene can also be used as a sensor for other physical properties. Thus, the topic of this thesis goes into the broader subject of the dynamics of interacting graphene membranes.

Part I of this work describes the research methods used throughout the dissertation, starting with the fabrication of samples and the experimental setup in chapter 3. The resonators used in this study are graphene membranes suspended over a cavity in a thin silicon dioxide layer. These samples are fabricated by mechanical exfoliation and transferred using a viscoelastic polymer, or we use single-layer graphene grown by chemical vapor deposition. Two classes of samples are used: either the graphene fully covers the circular cavity (closed drum) or there is a venting channel to the environment (open drum). Fabry-Perot interferometry is used to detect the motion of the graphene membrane, by measuring the position dependence of the laser light reflected from the sample. This position-dependence is nonlinear, which is used to develop a novel method to calibrate the sensitivity of the instrument to the amplitude of the resonance in chapter 4, requiring only that the wavelength of the laser light is known. A blue laser is used to modulate the temperature of the suspended graphene, actuating the motion due to thermal expansion. The mechanisms that play a role in this actuation scheme are a recurring theme throughout the dissertation.

The dynamics of 2D material resonators interacting with heat is discussed in part II. We examine the mechanical response of both single-layer graphene (chapter 5) and single-layer molybdenum disulfide (chapter 6) membranes to a high frequency intensity modulation of the blue laser. We observe the effects of the diffusion of heat in the mechanical response, from which we can derive the thermal time constant of the system. In the case of graphene, existing models fail to explain the value of the thermal time constant and its diameter-dependence. A linear diameter-dependence is found, while a quadratic dependence is expected. We propose that a combination of boundary effects and the mesoscopic scale of phonon transport lies at the root of this observation. In the case of MoS_2, we find that the thermal time constants are consistent with the classical theory of diffusive heat transport, allowing us to make the first estimate of the specific heat of a 2D material.

Part III studies the nonlinear dynamics of graphene membranes. The temperature modulation causes rapid variations of tension in the resonator, resulting in parametric resonance. Since the restoring force for every mode is determined by the tension in the membrane, each mode can be parametrically excited resulting in a record number of 14 mechanical modes brought into parametric resonance in a single mechanical element as shown in chapter 7. We also show that unconventional dynamic phenomena govern the linewidth of the mechanical response. The nonlinear resonance is also sensitive to random fluctuations, causing the resonator to show stochastic switching between the low- and high amplitude attractors (chapter 8). We achieve 100 times faster switching rates, while the effective temperature of the random fluctuations is ten times lower than the state-of-the-art in MEMS. This opens the door for detecting small signals in the audible domain in a way that mimics nature.

Having performed all the experiments in high vacuum environments up to this point, the graphene membranes are now introduced to a fluid environment in part IV. We first show the squeeze-film pressure sensors, which are operated by compressing gas in a thin cavity underneath the membrane that raises its stiffness, which is detected through the resonance frequency. First, a proof-of-principle is shown on a multi-layer graphene sample of 31 layer thickness in chapter 9, followed by a more extensive study on single-layer devices in chapter 10. We show that inertia in the gas flow plays an important role at high pressures and high frequencies by measuring the gas dependence of the squeeze-film effect. Also, we show an actuation scheme that exploits the squeeze-film effect, by fast temperature modulation of the gas due to the blue laser which causes the gas to expand, which can be detected by an increase in the actuation force as a function of pressure. After this, we show that graphene membranes that separate two gases can be deflected by osmotic gas pressure in chapter 11. This time-dependent osmotic pressure occurs when the two gases have different permeation rates, which can be used in future gas sensors. The final chapter 12 of this part studies graphene membranes in water. Using liquid-cell atomic force microscopy, we show that selectively permeable graphene membranes can be deflected by osmotic pressure induced by a concentration gradient of sucrose.

Part V provides an outlook and valorization. The outlook (chapter 13) shows the results of several projects that build on the research presented in the preceding parts. We extensively discuss two methods to measure the mass of graphene, which we typically find to be much higher than expected. Considerable steps towards CMOS integration were taken, we show squeeze-film pressure sensors and Pirani type pressure sensors that were fabricated in CMOS compatible processes. A method is shown that measures leakage through the graphene membranes at very fast timescales, building on the detection of thermal time constants. We end the outlook by investigating the motion of graphene membranes that are actuated by two incommensurable frequencies. The valorization chapter 14 shows the possible practical applications that can emerge from this work. The dissertation ends with the conclusions in chapter 15.

SAMENVATTING

Micro- en nanomechanische sensoren (MEMS-sensoren) zijn onmisbaar voor toepassingen in moderne consumentenelektronica-, automobiel- en medische industrieën. Gasdruksensoren zijn de meest voorkomende MEMS-sensoren die gebruik maken van een membraan. Door deze sensoren kleiner te maken, worden ze goedkoper en verbruiken ze minder energie, waardoor ze makkelijker in nieuwe toepassingen passen. Om druksensoren kleiner te maken is het nodig om het membraan dunner te maken, maar daarvoor moet het materiaal sterk genoeg zijn. Grafeen is daarvoor het perfecte materiaal, want het is maar 1 atoomlaag dik, maar tegelijk het sterkste materiaal dat ooit is gemeten. Dit proefschrift onderzoekt de beweging van vrijhangende grafeen membranen voor toepassing in sensoren. Deze sensor-toepassing is niet beperkt tot gasdruksensoren, de dynamiek van grafeen kan ook gebruikt worden om andere fysische eigenschappen te onderzoeken. Dit proefschrift neemt dus een bredere belangstelling in de beweging van grafeen membranen die een interactie ondergaan.

Deel I van dit werk beschrijft de methoden die verder in het proefschrift steeds opnieuw gebruikt worden, beginnend met de vervaardiging van proefstukken en de experimentele opstelling in hoofdstuk 3. De mechanische resonatoren die gebruikt worden in dit onderzoek zijn grafeen membranen, die vrij hangen boven een gaatje in een dunne laag siliciumdioxide. Deze proefstukken worden gemaakt door mechanische exfoliatie en een overdracht met een viscoelastisch polymeer, of we gebruiken enkellaags grafeen dat is vervaardigd met een chemische opdamptechniek. We gebruiken twee soorten proefstukken: of het grafeen bedekt het cirkelvormige gat volledig (een gesloten drum), of het gat heeft een ontluchtingskanaal naar de buitenwereld (een open drum). Fabry-Perot interferometrie wordt gebruikt om de beweging van het membraan te bepalen, door de positieafhankelijkheid van het weerkaatste licht vanaf het proefstuk te meten. Deze afhankelijkheid is niet-lineair, waar we gebruik van kunnen maken om de gevoeligheid van het instrument voor de uitwijking van het membraan te kalibreren in hoofdstuk 4, daarvoor is het alleen nodig om de golflengte van de laser te weten. Een blauwe laser word gebruikt om de beweging aan te drijven, door op hoge frequentie het membraan op te warmen zal deze gaan bewegen door thermische expansie. Er zijn verschillende mechanismen die een rol spelen in dit aandrijfschema die steeds terug zullen komen in dit proefschrift.

De beweging van tweedimensionale materialen die een interactie vertonen met warmte wordt besproken in deel II. We onderzoeken de mechanische respons op de hoogfrequente intensiteitsmodulatie van de blauwe laser van enkellaags grafeen (in hoofdstuk 5) en enkellaags molybdeendisulfide (in hoofdstuk 6). We observeren de effecten van warmtediffusie in de mechanische beweging, waaruit we de karakteristieke thermische tijdconstante van het systeem kunnen afleiden. In het geval van grafeen, kunnen we de waarde van deze tijdsconstante en zijn diameterafhankelijkheid niet verklaren met bestaande modellen. We observeren een lineaire diameterafhankelijkheid, terwijl men

een kwadratische afhankelijkheid zou verwachten. We stellen voor dat een combinatie van effecten aan de rand en de mesoscopische schaal van het transport van fononen deze observatie kan verklaren. In het geval van molybdeendisulfide kunnen we de gemeten thermische tijdsconstanten goed verklaren met klassieke modellen voor diffusief warmtetransport, dit stelt ons in staat om voor het eerst een schatting te maken van de specifieke warmte van een tweedimensionaal materiaal.

Deel III bestudeert de niet-lineaire dynamica van grafeen membranen. De temperatuurmodulatie van de blauwe laser veroorzaakt snelle variaties in de spanning van het materiaal, wat leidt tot het parametrische resonantie-effect. Doordat de herstelkracht van iedere trillingsvorm van het membraan word bepaald door de spanning in het membraan, kan iedere trillingsvorm parametrisch aangedreven worden. Dit leidt tot een recordaantal van 14 trillingsvormen die parametrische resonantie vertonen in een enkel mechanisch element, zoals aangetoond in hoofdstuk 7. Hier laten we ook zien dat ongebruikelijke fenomenen ten grondslag liggen aan de piekbreedte van de mechanische resonantie. De niet-lineaire resonantie is ook gevoelig voor willekeurige fluctuaties, waardoor de resonator stochastisch wisselt tussen de hoog- en laag amplitude attractor (hoofdstuk 8). Deze wisselingen zijn 100 maal sneller dan in de meest geavanceerde MEMS-technologie, terwijl de effectieve temperatuur van de fluctuaties een factor 10 lager is. Dit maakt grafeen aantrekkelijk om zeer zwakke signalen te meten in het hoorbare domein, op een manier die de natuur nabootst.

Tot dusver zijn alle experimenten in een hoogvacuüm omgeving uitgevoerd, maar in deel IV word het membraan blootgesteld aan gassen en vloeistoffen. We laten eerst de gasdruksensor gebaseerd op het squeeze-film (samengedrukte gasfilm) effect zien, welke werkt door gas onder het membraan samen te drukken. Dit vergroot de stijfheid van het systeem, wat wordt gemeten met behulp van de resonantiefrequentie. Eerst laten we de principiële bruikbaarheid van deze sensoren zien op 31-laags grafeen in hoofdstuk 9, gevolgd door een meer uitgebreid onderzoek op enkellaags grafeen in hoofdstuk 10. We laten zien dat massatraagheid in de gasstroom een grote rol speelt bij hoge drukken en hoge trillingsfrequenties door het squeeze-film effect met verschillende gassen te meten. Ook laten we een nieuw aandrijfschema zien dat gebruik maakt van het squeeze-film effect: door het gas in de dunne film heel snel op te warmen zal dit gaan uitzetten, wat wordt gemeten als een onverwachte toename van de aandrijfkracht bij hoge gasdruk. Hierna laten we in hoofdstuk 11 zien dat grafeen membranen die twee verschillende gassen scheiden worden doorgebogen door osmotische gasdruk. Deze tijdsafhankelijke druk onstaat als de twee gassen verschillende permeatiesnelheden hebben en kan gebruikt worden in toekomstige gassensoren. Het laatste hoofdstuk (12) in dit deel bestudeert grafeen membranen in water. Door gebruik te maken van atomaire-krachtmicroscopie in een vloeistofcel, laten we zien dat selectief permeabele grafeen membranen worden doorgebogen door osmotische druk, die wordt opgewekt door een verschil in concentratie van oploste sucrose in het water.

Deel V geeft een vooruitzicht in hoofdstuk 13 en valorisatie in hoofdstuk 14. Het vooruitzicht laat resultaten van projecten zien die verder bouwen op het onderzoek in de voorgaande hoofdstukken. We bespreken uitgebreid twee verschillende methodes om de massa van grafeen te meten, welke vaak veel hoger dan verwacht is. Er zijn ook vergaande stappen naar CMOS-integratie van de sensoren genomen, we laten deze zien

voor de squeeze-film en de Pirani druksensor. Een methode om lekkage door grafeen op zeer snelle tijdschalen te meten word besproken. En we eindigen de vooruitblik door te kijken naar de dynamica van grafeen membranen die door twee signalen word aangedreven. Het valorisatie hoofdstuk 14 bespreekt de praktische toepassingen die uit dit proefschrift kunnen voortkomen. Het proefschrift sluit af met de conclusies in hoofdstuk 15.

1

INTRODUCTION

Micromechanical sensors have become widespread in numerous applications, due to continuous effort to reduce their size, power consumption, and unit costs. An example of a micromechanical sensor is the gas pressure sensor, recently introduced on a large scale in mobile phones. To continue the trend of downscaling their size, the membranes of the pressure sensors have to become thinner. This thesis explores the ultimate limit of membrane-based pressure sensors by employing graphene, the strongest material ever measured but only one atom thick. Sensing implies that the graphene membrane interacts with a physical entity, here we study how these physical entities affect the mechanical motion of the membranes. The work focuses mainly on the effects of heat and fluid dynamics on the mechanics of suspended graphene. In this chapter we introduce these interactions and relevant studies performed to date. Also, we show the pressure sensor concepts proposed at the start of the project Integrated Graphene Pressure Sensors, which resulted in this thesis.

1

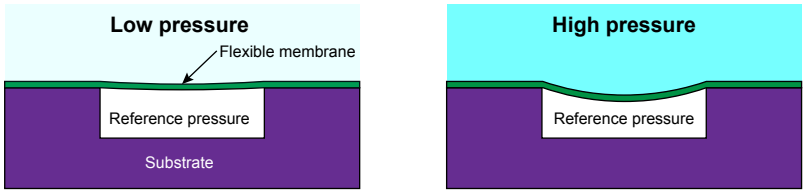

Figure 1.1: Cross section of a classical MEMS pressure sensor. The deflection of the flexible membrane is a measure of the pressure in the environment.

In recent decades micro-electromechanical systems (MEMS) have become indispensable in the automotive, aerospace, medical and consumer electronics industry. This development is due to the continuous effort to scale down MEMS to smaller dimensions. Reducing the size also leads to lower unit cost and less power consumption, making them more attractive for integration into electronic devices. Consequently, most modern mobile handsets contain multiple micro-mechanical sensors such as accelerometers, gyroscopes, and gas pressure sensors to increase their functionality. Modern cars use multiple MEMS sensors such as the accelerometer of the airbag and pressure sensors to monitor tire pressure. Today it is difficult to envision a world without micro-mechanical sensors, demonstrating the truly disrupting and revolutionary character of the sensor industry.

Pressure sensors are the most widespread membrane-based MEMS, mainly due to their recent introduction into smartphones. Current state-of-the-art sensors can count the number of stairs the user has climbed by the change in ambient air pressure. These sensors operate by employing a flexible membrane over a hermetically sealed cavity that contains a well-known reference pressure (Fig. 1.1). One can determine the ambient pressure in the environment from the membrane's deflection. Compared to other MEMS, pressure sensors remain relatively large (in the order of ~100 μm), while the increase in production volume introduces a strong drive to reduce the area of pressure sensors. However, a smaller area requires a thinner membrane to retain the sensitivity of the sensor.

In this respect, atomically thin membranes can provide ultimate performance in pressure sensitivity while reducing the sensor's size. These membranes will have to withstand large pressure loads, therefore they require high strength. Recently, researchers have discovered a group of such strong and atomically thin materials, known as two-dimensional materials. Graphene is the most studied and strongest of these materials and will be the focus of this thesis.

1.1. GRAPHENE

Graphene is a single layer of carbon atoms arranged in a flat hexagonal structure (Fig. 1.2). The first isolation and measurement of its unusual electrical properties were first performed in 2004 [1–4]. Andre Geim and Konstantin Novoselov received the 2010 Nobel Prize in Physics for these groundbreaking experiments. The perfect hexagonal lattice results in remarkable electronic properties, for example, it enables electrons to travel

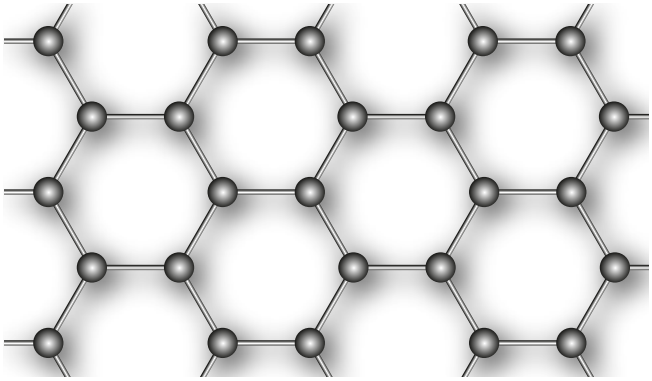

Figure 1.2: The hexagonal lattice of graphene viewed from above.

long distances without disturbance. More remarkable is that the electrons behave like they have no mass, moving at a constant velocity of one million meters per second [3, 5]. These electronic properties make graphene interesting for a new generation of transistors, potentially smaller, faster, and less power-consuming compared to silicon counterparts. Since graphene is 98% transparent [6], while able to conduct electricity, applications such as transparent touchscreens [7], light panels and solar cells [8] are also of interest.

This thesis will not go into the remarkable electronic properties of graphene, but the remarkable mechanical properties of this perfect hexagonal lattice. It is possible to freely suspend this material since it forms wrinkles that stabilizes the structure [9]. Lee et al. measured the breaking strength of suspended graphene and found this is 20 times stronger than steel: to date graphene is the strongest material ever measured [10]. The high density of the lattice makes these membranes graphene impermeable to the smallest gas atom: helium [11]. Graphene is thus strong, thin, able to conduct electricity and impermeable: these properties make it a perfect candidate as a membrane in gas pressure sensors. With its high surface-to-mass ratio, graphene is also an attractive material for other applications such as mass [12] and electrochemical gas sensors [13–15].

The remarkable mechanical properties of the graphene lattice result in unique phenomena in heat transport through this material. Several groups have attempted to measure the thermal conductivity of graphene and, while the results can vary, researchers are in agreement that the thermal conductivity is much higher than that of copper [16–29]. The lattice vibrations (phonons) can travel undisturbed for long distances, giving rise to thermal conductivities that depends on the geometry of the device [23]. By exploiting the unique properties of the lattice vibrations, researchers have implemented more exotic devices such as thermal rectifiers [30]. The lattice waves or phonons in graphene come in three polarizations: the in-plane longitudinal and transverse phonons; and the out-of-plane flexural phonons. Flexural phonons travel slowly through the graphene since the atomically flat structure has little bending rigidity. The in-plane phonons, however, travel fast through the rigid hexagonal structure, around 100 times faster than the flexural phonons. Some researchers suggest that most of the heat is carried by flexural, rather

than the in-plane phonons, which is unusual considering their low group velocity [31].

1.2. GRAPHENE PRESSURE SENSORS

Several researchers have studied the potential application of graphene as a pressure sensor, revealing the hurdles that need to be overcome for industrial application. Bunch *et al.* [11] were the first to demonstrate the potential application of graphene as a pressure sensor. Using a suspended graphene membrane, they sealed a cavity and found that upon changing the pressure in the environment, the resonance frequency of the suspended membrane changed. The leakage rates were independent of the thickness of the graphene flakes, leading to the conclusion that graphene is impermeable. The actual path of leakage remains a subject of debate. The initial hypothesis states that diffusion through the silicon dioxide substrate is to blame [11], but later research points towards the interface between the graphene and the oxide [32]. To date, no research has demonstrated a hermetically sealed cavity using graphene at the timescale of years, whether is achievable remains an open question.

Five years later, Smith *et al.* [33, 34] demonstrated a piezoresistive pressure sensor. It operated by suspending graphene over a sealed cavity and measuring the change in electrical resistance as the membrane deflects under a pressure difference. This sensor demonstrated the highest sensitivity per unit area of any piezoresistive sensor. However, the presence of oxygen in the atmosphere and leakage affected the sensor's performance.

Koenig *et al.* [35] demonstrated graphene's feasibility as a molecular sieve, being able to separate gas molecules based on their size. Since graphene is atomically thin and is still able to support large pressure loads, it has the potential to demonstrate high permeation fluxes through the membrane while retaining high selectivity [36, 37]. The same holds in the case for water: extensive research looks into water purification and desalination using graphene [38–41]. Considerable challenges remain for the application of graphene as a purification membrane, such as the requirement of large areas with intact graphene [42].

This thesis investigates the potential application of graphene as pressure or gas sensors, building on the existing research. Since the hermetic sealing of graphene is a considerable challenge, we focus on pressure sensors that do not require a sealed cavity. The selective nature of the leakage through the graphene membrane is however interesting for gas sensing applications. Such a sensor opens a pathway towards detecting gases that are inert, by measuring the size of the particles instead. Also, the selective properties in water are interesting to build microscale sensors since on this scale it is less challenging to control the number and the size of the pores.

1.3. INTEGRATED GRAPHENE PRESSURE SENSORS

This thesis is part of the project Integrated Graphene Pressure Sensors (IGPS), funded by an HTSM (High Tech Systems and Materials) proposal from the Netherlands Organisation for Scientific Research (NWO-TTW). The project aims to demonstrate CMOS integrated graphene pressure sensors. Different pressure sensors were proposed at the start of the project, based on the existing research. Figure 1.3 shows the proposed concepts and the implementations demonstrated at this time.

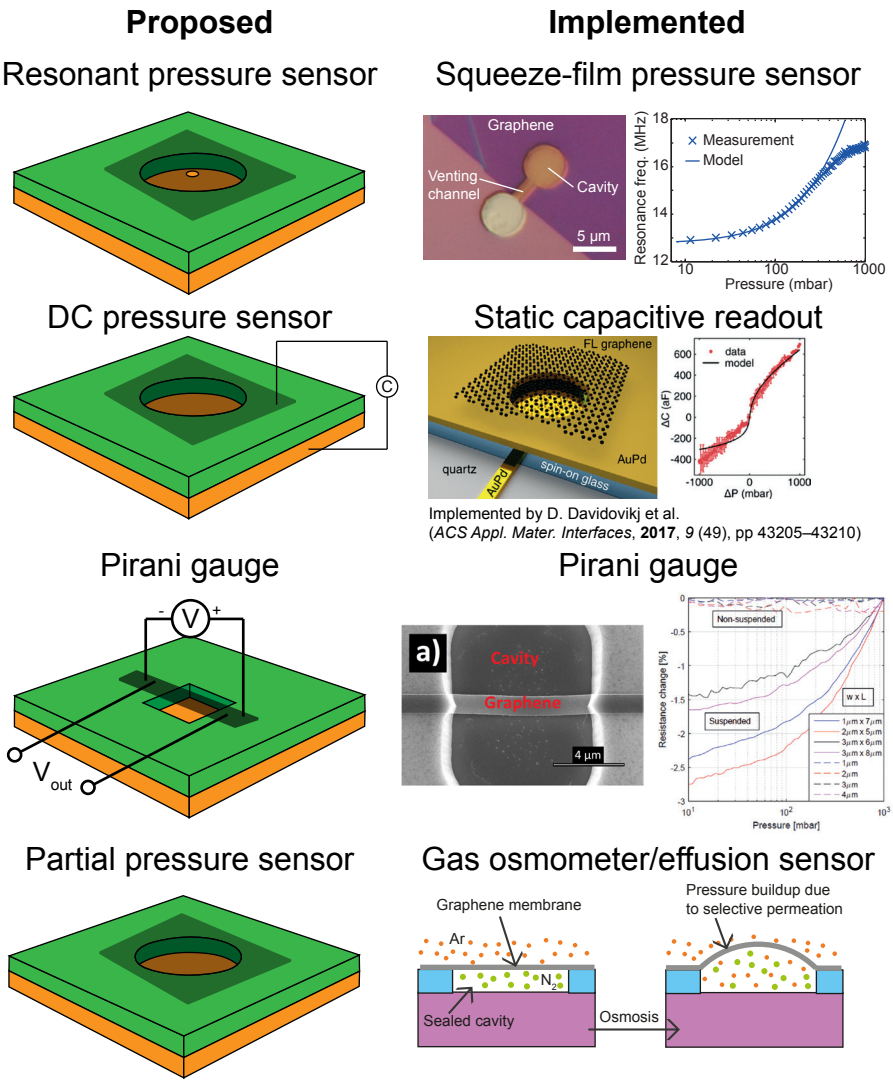

Figure 1.3: Overview of proposed sensor concepts.

- The *resonant pressure sensor* measures the pressure-dependent resonance frequency of a graphene membrane. Nanopores make sure that gases enter slowly into the cavity, but at the high resonance frequency, the membrane will compress the gas. Compression leads to an increase in stiffness, detected from the resonance frequency shift of the resonator. During the project, the design changed to exploit the squeeze-film effect, which only requires a membrane suspended close to the substrate and can be open to the sides, removing the need for nanopores. High-frequency vibration is enough to trap the gas in its position by viscous forces, so

it will be compressed [43]. This concept is the *squeeze-film pressure sensor* and it overcomes the hurdle of hermetically sealing a cavity since it is open through a venting channel. Graphene is a perfect material to build this sensor since it has a high surface-to-mass ratio and will therefore, respond very sensitively to gas compression. The sensor is first introduced in chapter 9 and the properties of the squeeze-film gas flow are more extensively studied in chapter 10. In collaboration with the Else Kooi Laboratory at TU Delft, considerable steps have been taken to fabricate these sensors on wafer-scale using a CMOS-compatible transferless process developed by Sten Vollebregt et al. [44]. The outlook (chapter 13) shows results on the mechanical characterization of these sensors.

- The static pressure sensor measures the static deflection of the graphene membrane subjected to a pressure difference. This is the classical sensor concept in Fig. 1.1 that requires the cavity to be hermetically sealed. Different readout mechanisms can be used to measure the deflection of the drum, such as piezoresistive [33] or capacitive [45] readout of the position. Hermetic sealing with graphene is a considerable challenge that has seen some improvement in recent years [32, 40]. In this thesis, we do not try to resolve this problem, but rather shift the focus towards the development of pressure sensors without hermetically sealed cavities, or exploit the properties of leakage at the nanoscale to construct gas sensors. Davidovikj et al. have demonstrated static capacitive readout of a single layer graphene drum, demonstrating the feasibility of these sensors once the hermetic sealing problem is resolved [45]. This type of readout can be useful in practical applications of the osmotic pressure sensors discussed in chapter 11 and chapter 12.

- The Pirani gauge exploits the pressure-dependence of the thermal conductance of gas through a nanogap. Collaboration with the Else Kooi Laboratory at TU Delft has resulted in considerable progress to fabricate these sensors in a scalable manner. Similar to the squeeze-film pressure sensor it requires the membrane to be suspended close to the substrate. The graphene membrane is then heated by passing an electrical current and since the cooling rate is pressure-dependent, the temperature is as well. Since the electrical resistance of the graphene is temperature dependent, readout of the resistance can be used to measure the pressure. The sensor has been demonstrated to work using graphene and it was also shown by Joost Romijn et al. that CMOS integration of these sensors is feasible [46]. Experimental characterization of the pressure and gas dependence of these sensors is shown in the outlook (chapter 13).

- The partial pressure sensor uses (sub-)nanometer pores in the suspended graphene membrane that allows some gases to pass through while the membrane remains impermeable to other gases. The pressure difference is then a measure of the partial pressure of the gases for which the sensor is impermeable. During the course of the project, it was found that the ideal sieving of gases is not feasible. Nevertheless, the partial pressures of the gas can be determined as long as the permeation rate of each gas is different. If such a device is brought out of thermodynamic equilibrium, the time-dependent osmotic gas pressures that occur during the relaxation towards equilibrium contain information on the composition of the gas. These

devices are named *gas osmometers* and its physical principle is demonstrated in chapter 11.

- A graphene-based microphone was proposed at the start of the project. However, the considerable design challenges regarding the fast sampling times required while also obtaining a significant reduction of the size made this concept too ambitious at this point. The microphone was therefore abandoned in the course of the project.

In the course of the project, a new sensing concept was developed, namely the osmotic pressure sensor operating in liquids. This sensor uses a graphene membrane that is selectively permeable and seals a cavity filled with water. When the osmotic pressure in the surroundings is changed, it will deflect the membrane until the hydrostatic pressure this membrane exerts is equal to the osmotic pressure difference. The physical principle of this concept is demonstrated in chapter 12.

1.4. CONTENTS OF THE THESIS

This thesis studies the dynamics of graphene membranes which shows an interaction with another physical phenomenon. Understanding these interactions allows us to study the sensing capabilities of graphene. These sensing capabilities are partly aimed to develop practical industrial applications, but can also be used to sense fundamental physical phenomena or properties of the material. The broad range of interactions and phenomena that these moving membranes can show, resulted in a wide range of topics that will be discussed in this thesis.

The remainder of this work is structured as follows. First, chapter 2 explains some of the basic principles of dynamics that form the basis of this thesis. After this, the dissertation is divided into 5 parts: (I) Fabrication and methods, (II) Dynamics of 2D materials interacting with heat, (III) Nonlinear dynamics of graphene membranes, (IV) Dynamics of graphene membranes interacting with fluids and (V) Outlook and valorization.

PART I: FABRICATION AND METHODS

First, the fabrication and measurement of suspended graphene resonators are discussed in chapter 3. These resonators were made by mechanical exfoliation of graphite and dry transfer or by using single layer graphene via a wet transfer process. This chapter also discusses the experimental setup used throughout this thesis to actuate and detect the motion of these membranes. The detection of graphene's motion is discussed in detail in the first experimental chapter 4, which examines the interaction between graphene's motion and light. This results in a new method to calibrate the amplitude of 2D material resonators in a Fabry-Perot interferometer.

PART II: DYNAMICS OF 2D MATERIALS INTERACTING WITH HEAT

First, the mechanical motion of graphene in response to a very fast heat source is studied in chapter 5. The unprecedented timescale of this experiment reveals the important role that the boundary plays in heat transport through suspended graphene. It is interesting to compare these results to a material with a much lower thermal conductivity, therefore

the experiment was also performed on single-layer molybdenum disulfide in chapter 6. These experiments provide the first estimates of the specific heat of 2D materials.

PART III: NONLINEAR DYNAMICS OF GRAPHENE MEMBRANES

At faster timescales, the fast temperature modulation enables the stiffness of the resonator to be modulated by thermal expansion. This results in a phenomenon known as parametric resonance, which is studied in chapter 7. What is unique about these graphene resonators is that this can happen in all the vibrational modes, enabling us to show a record number of parametric resonances in a single mechanical element. The next chapter 8 treats a phenomenon known as stochastic switching, which occurs due to the fluctuations caused by the finite temperature in the environments. Such effects are readily observed in these resonators and can be used in new sensing schemes that mimic nature.

PART IV: DYNAMICS OF GRAPHENE MEMBRANES INTERACTING WITH FLUIDS

Having studied the dynamics of graphene membranes in high vacuum, the system is now introduced to fluid environments. We propose several sensing schemes that exploit the unique properties of suspended graphene membranes. The squeeze-film pressure sensor in chapter 9 exploits the ultrahigh surface-to-mass ratio of graphene to detect gas pressure with very high responsivity. The following chapter 10 treats the properties of the gas flow in more detail. Next, the gas osmometer is introduced that uses selective permeation to sense gases in the environment (chapter 11). Finally, we study the deflection of graphene membranes by osmotic pressure in a liquid environment in chapter 12.

PART V: OUTLOOK AND VALORIZATION

Chapter 13 provides an outlook on further research that builds on the work in this thesis. We discuss measurement techniques to characterize the mass of graphene, the Pirani pressure sensor, gas sensors based on effusion, wafer scale fabrication of squeeze-film pressure sensors and quasiperiodic attractors in nonlinear graphene resonators. In chapter 14 we discuss how the research in this work can be used in practical applications. The dissertation ends with the conclusions in chapter 15.

2

THEORY

This chapter serves as an introduction to some of the general models and concepts that form the basis of this work. Most of the theory shown here is well-established and is the basis for much of the data analysis in this dissertation. The harmonic oscillator and the circular membrane resonator are first treated in detail. After this, we discuss what happens when the resonance becomes nonlinear at large amplitudes. We also examine some special cases of the actuation force that can actuate the membrane.

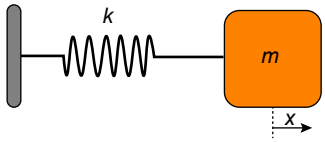

Figure 2.1: The classical harmonic oscillator.

2.1. HARMONIC OSCILLATOR

THE classical harmonic oscillator is a model system used in many different branches of physics. Figure 2.1 shows a schematic drawing of the simple harmonic oscillator. In this system, we consider a mass m attached to a fixed wall with a spring of stiffness k. The mass is constrained to move only in the direction of x, which is the single coordinate used to describe the motion of the system. The spring exerts a restoring force F on the mass:

$$F = -kx \tag{2.1}$$

which strives to keep the mass in position $x = 0$. Now we use Newton's second law:

$$m\ddot{x} = -kx, \tag{2.2}$$

where $\ddot{x}$ is the second order time derivate of x, which is the acceleration of m. A general solution for $x = A\cos\omega t + B\sin\omega t$, substituting:

$$-m\omega^2(A\cos\omega t + B\sin\omega t) = -k(A\cos\omega t + B\sin\omega t), \tag{2.3}$$

yielding the simple expression:

$$\omega^2 = \frac{k}{m} \tag{2.4}$$

where ω is radial frequency. We find that by solving the equation of motion, the system seems to have a "special" frequency, $\omega_0 = \sqrt{k/m}$. This is the resonance frequency of the system: the system has a natural preference to vibrate at this particular frequency. This principle is highly important in many applications, without this property clocks would not be able to keep time and musical instruments would not exist. The graphene membranes in this work also show resonance and in many instances in this work (chapters 9, 10 and 11) we use the change in resonance frequency to track changes in the stiffness of the system.

2.2. DAMPED HARMONIC OSCILLATOR

The simple harmonic oscillator is often not a realistic case: once the system is in motion it will keep vibrating forever. In reality, we will have to account for the fact that in each cycle some energy is dissipated, which damps out the motion. The most simple model that is often applied to this situation is viscous dissipation, which assumes a force proportional to the velocity $\dot{x}$ of the system:

$$F = -c\dot{x}. \tag{2.5}$$

Now we write the equation of motion as:

$$m\ddot{x} = -c\dot{x} - kx, \tag{2.6}$$

which is more convenient to write in terms of the resonance frequency ω_0 and the dimensionless quality factor $Q = \frac{\omega_0 m}{c}$:

$$\ddot{x} + \frac{\omega_0}{Q}\dot{x} + \omega_0^2 x = 0. \tag{2.7}$$

To induce motion in the system, requires some external excitation force. Here, we consider the periodic actuation force $F = Ae^{i\omega t}$, resulting in the equation:

$$\ddot{x} + \frac{\omega_0}{Q}\dot{x} + \omega_0^2 x = \frac{A}{m}e^{i\omega t}. \tag{2.8}$$

We substitute $x = ze^{i\omega t}$, this gives the expression:

$$-\omega^2 ze^{i\omega t} + i\frac{\omega_0\omega}{Q}ze^{i\omega t} + \omega_0^2 ze^{i\omega t} = \frac{A}{m}e^{i\omega t} \tag{2.9}$$

this yields the amplitude z of the resonator as a complex number:

$$z = \frac{A/m}{\omega_0^2 - \omega^2 + i\omega_0\omega/Q}. \tag{2.10}$$

Which can be expressed as the magnitude and phase:

$$|z| = \frac{A/m}{\sqrt{\left(\omega_0^2 - \omega^2\right)^2 + \left(\frac{\omega_0\omega}{Q}\right)^2}}, \tag{2.11}$$

$$\angle z = -\arctan\left(\frac{\omega_0\omega}{Q\left(\omega_0^2 - \omega^2\right)}\right). \tag{2.12}$$

If we experimentally measure the resonance frequency and quality factor in this work, we measure the resonator by sweeping the frequency of the actuation force, while keeping the amplitude of the force constant. We can then fit eq. (2.11) to the experimentally obtained response and extract the resonance frequency and quality factor. At the resonance frequency, the amplitude peaks and its value is given by:

$$|z|_{\omega=\omega_0} = \frac{AQ}{\omega_0^2 m}, \tag{2.13}$$

which can be useful if one wants to track changes in the amplitude of the force A.

2.3. MODAL ANALYSIS

In this work, we almost exclusively study the dynamics of graphene resonators with a circular shape, also called drum resonators. At first sight, it seems that a drum resonator is not the same as a simple harmonic oscillator: it is a continuous body that can in principle move in many different manners. Yet, even this continuous system has resonance frequencies and we can simplify its dynamic behavior using its special properties at resonance.

Here we consider the case of a circular drum resonator. We assume that the membrane is very thin and we can neglect bending rigidity, instead the restoring force of the membrane is given by its pre-tension n_0. This tension is already present in the membrane even when it is in a fully flat configuration and for simplicity, we assume that this tension is uniformly distributed over the membrane. This results in the following equation of free motion for the deflection w of the membrane in cylindrical coordinates:

$$\frac{\partial^2 w}{\partial r^2} + \frac{1}{r^2}\frac{\partial^2 w}{\partial \theta^2} + \frac{1}{r}\frac{\partial w}{\partial r} = \frac{\rho h}{n_0}\frac{\partial^2 w}{\partial t^2}, \tag{2.14}$$

where r is the radial coordinate from the center of the drum and θ the angular coordinate. Note that the deflection is dependent on both these coordinates. To find a solution, we use separation of variables:

$$w(r,\theta,t) = R(r)T(\theta)\tau(t), \tag{2.15}$$

now we assume an harmonic vibration for the time dependent component τ:

$$w(r,\theta,t) = R(r)T(\theta)\sin\omega t. \tag{2.16}$$

Using the seperation constant $\lambda^2 = \frac{\omega^2\rho h}{n_0}$ we write the equation of motion as:

$$\left(R'' + \frac{1}{r}R' + \lambda^2 R\right)T + \frac{1}{r^2}R(r)T'' = 0 \tag{2.17}$$

which can again be seperated into two ordinary differential equations using the constant m^2:

$$T'' + m^2 T = 0 \tag{2.18}$$

$$R'' + \frac{1}{r}R' + \left(\lambda^2 - \frac{m^2}{r^2}\right)R = 0. \tag{2.19}$$

Equation (2.18) is an harmonic equation with general solution:

$$T(\theta) = C_{1,m}\sin m\theta + C_{2,m}\cos m\theta \tag{2.20}$$

where $m = 0,1,2,\ldots$. Equation (2.19) is a Bessel-type equation which has the general solution:

$$R(r) = J_m(\lambda r), \tag{2.21}$$

which at the radius a of the drum yields:

$$J_m(\lambda a) = 0 \tag{2.22}$$

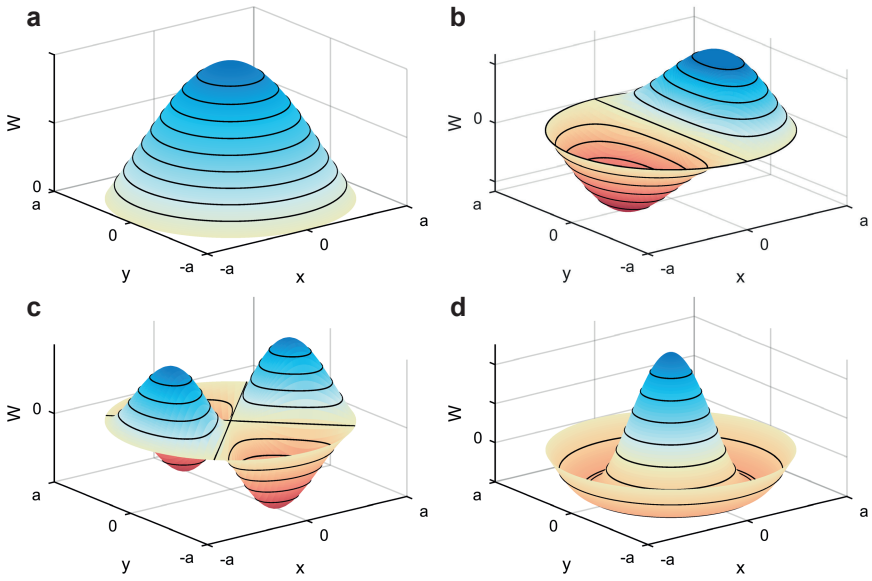

Figure 2.2: Four mode shapes of the circular membrane with the lowest frequency. **a** First (or fundamental) mode W_{01} corresponding to $\gamma_{01} = 2.405$. **b** Mode W_{11} corresponding to $\gamma_{11} = 3.832$. **c** Mode W_{21} corresponding to $\gamma_{21} = 5.135$. **d** Mode W_{02} corresponding to $\gamma_{02} = 5.520$.

Taking $\gamma_{mn} = \lambda a$ for convenience, we find an infinite number of roots for this equation, the lowest value is $\gamma_{01} = 2.405$. If we substitute this back into the definition of the seperation constant, we find:

$$\omega_{mn} = \frac{\gamma_{mn}}{a}\sqrt{\frac{n_0}{\rho h}} \tag{2.23}$$

which are the resonance frequencies of the membrane. The consequence of the membrane being a continuum system is that it now has an infinite number of resonance frequencies at which the system can vibrate. The solutions of W are now given by:

$$W^{(1)}_{mn}(r,\theta) = R(r)T(\theta) = J_m(\gamma_{mn} r/a)\cos m\theta \tag{2.24}$$

$$W^{(2)}_{mn}(r,\theta) = J_m(\gamma_{mn} r/a)\sin m\theta. \tag{2.25}$$

Note that each resonance frequency ω_{mn} corresponds to a certain special shape of the membrane, either $W^{(1)}_{mn}$ or $W^{(2)}_{mn}$. These shapes are called the mode shapes of the resonator, the four mode shapes with the lowest frequency are shown in Fig. 2.2. $W^{(1)}_{mn}$ and $W^{(2)}_{mn}$ are always 90 degrees apart and are called degenerate modes, since they have the same frequency. The fact that the resonance occurs at a certain well-defined shape is very useful, since it means that once the deflection is known in any point of the membrane [1], the deflection in any other part of the membrane is also well known. This property allows us to take a single resonance of the membrane and describe it with a single

[1] Except at the nodes where $W_{mn} = 0$.

degree of freedom x, which is also known as the generalized coordinate. This reduces the equation of motion to:

$$\ddot{x} + \frac{\omega_{mn}}{Q_{mn}}\dot{x} + \omega_{mn}^2 x = 0. \tag{2.26}$$

Thus, we are able to describe each mode of resonance as a damped harmonic oscillator with a certain resonance frequency and quality factor. Sometimes it is more convient to write:

$$m_{\text{eff}}\ddot{x} + \frac{m_{\text{eff}}\omega_{mn}}{Q_{mn}}\dot{x} + k_{\text{eff}}x = 0, \tag{2.27}$$

where m_{eff} is the modal (or effective) mass of the resonance and k_{eff} the modal (or effective) stiffness. Note, that m_{eff} and k_{eff} do relate to the actual mass and stiffness of the resonator, but their values also depends on the mode shape and the definition of the generalized coordinate x.

2.4. NONLINEAR RESONANCE

The damped harmonic oscillator usually describes the motion of the graphene resonator well at small amplitudes. However, at large amplitudes the equation of motion becomes nonlinear. This situation can still be described by investigating the resonance modes of the membrane and projecting them to a single generalized coordinate x. The most appropriate equation of motion for a graphene membrane is the Duffing-van der Pol equation [47]:

$$m_{\text{eff}}\ddot{x} + \frac{\omega_0}{Q}\dot{x} + \eta x^2\dot{x} + kx + k_3x^3 = F\cos\omega t, \tag{2.28}$$

where μ is the damping coefficient, ν the nonlinear damping coefficient, β the resonance frequency, k_3 the cubic stiffness and F is the force. In the case of the graphene membrane, the cubic stiffness k_3 arises from the additional tension and geometry of the system, which was shown by Davidovikj *et al.* to be [48]:

$$k_3 = \frac{\pi}{1.27 - 0.97\nu - 0.27\nu^2}\frac{Eh}{a^2}, \tag{2.29}$$

where Eh is the 2D Youngs modulus and ν Poisson's ratio. The nonlinear term $\eta x^2\dot{x}$ is known as the van der Pol-term. Several works [49–53], including this dissertation (chapter 7), have found that this term is necessary to describe the motion of graphene resonators. However, the exact origin of nonlinear (or linear) dissipation in graphene remains an open question.

The presence of nonlinear terms in the equation of motion highly impact the properties of the resonance. Figure 2.3 compares a damped linear resonance (eq. (2.11)) to a nonlinear resonance described by eq. (2.28). In the linear case, we find the amplitude is maximum at the resonance frequency. The width of the peak depends on the quality factor of the resonance. In the nonlinear case, the resonance frequency becomes amplitude-dependent. In a certain frequency range, three solutions can be found of which two are stable. The point where a stable solution meets an unstable solution is called a saddle-node bifurcation. In an experiment, if one sweeps the frequency from low to high one would follow the high amplitude branch until the second saddle-node bifurcation is reached. Then the amplitude jumps down to the other stable branch. If

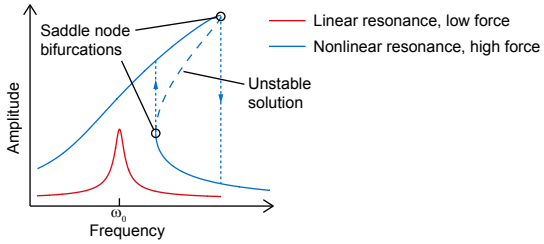

Figure 2.3: Comparison between a linear and nonlinear resonance peak.

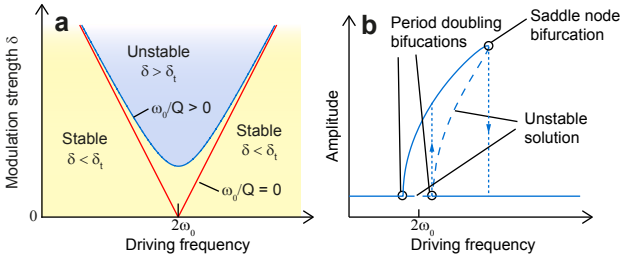

Figure 2.4: **a** Instability diagram for the parametric oscillator. **b** Amplitude as a function of driving frequency in the case of parametric resonance.

the frequency is swept backward, one would follow the lower amplitude branch until the first saddle-node bifurcation is reached. The amplitude then jumps up to the high amplitude branch. Nonlinear resonance peaks thus possess a characteristic hysteresis if they are strongly driven, we also see this behavior in chapters 7 and 8. The case shown here involves a spring hardening nonlinearity, where $k_3 > 0$. If $k_3 < 0$, the system shows a spring softening nonlinearity, which makes the resonance bend toward lower instead of higher frequencies.

2.5. PARAMETRIC RESONANCE

Another important type of resonance is parametric resonance. Parametric resonance does not involve a direct external excitation force, but a modulation of one of the parameters of the resonator such as stiffness or mass. A unique property of this type of resonance is that the modulation does not have to occur at the resonance frequency of the system to induce resonance. If the system is parametrically driven at $2\omega_0/n$, where n is a positive integer, parametric resonance can occur. For parametric resonance to occur, the drive has to exceed a certain driving level to overcome the linear dissipation force in the resonator. Figure 2.4**b** shows a typical parametric response described by the equation of motion:

$$m_{\text{eff}}\ddot{x} + \frac{\omega_0}{Q}\dot{x} + \eta x^2\dot{x} + (k + \delta\cos\omega t)x + k_3x^3 = 0. \tag{2.30}$$

Above the threshold of the modulation δ, the zero amplitude solution becomes unstable and the resonance occurs. This unstable zero amplitude branch meets the stable

amplitude branch at the period doubling bifurcations, which derives its name because the mechanical response is at half the frequency of the drive. Figure 2.4**a** plots the period doubling bifurcations as function of δ, showing where the instability occurs. The threshold of the instability depends on the dissipation, a resonator with high quality factor shows parametric resonance at lower driving levels. Note that the instability diagram in Fig. 2.4**a** only depends on the linear terms in eq. 2.30, because the instability is reached from a flat configuration of the membrane. The mechanical response in Fig. 2.4**b** bends towards higher frequencies due to the spring hardening nonlinearity and one saddle-node bifurcation is found. This saddle-node bifurcation depends strongly on the nonlinear dissipation and only little on the linear dissipation [47]. Note that there are now two unstable branches in the amplitude, one is the unstable solution between the period doubling bifurcation, the other between the saddle-node and the second period doubling bifurcation is due to the Duffing nonlinearity. Sweeping the frequency forward and backward results in hysteresis, similar to the case of the nonlinear resonance.

2.6. FREQUENCY-DEPENDENT FORCING

Ideally, the harmonic oscillator is driven by a force that has a constant amplitude as a function of frequency. However, at very high frequencies diffusive effects can cause this force to become frequency dependent. One specific case that is extensively studied in this work is opto-thermal actuation, where the force becomes frequency dependent due to the thermal diffusivity of the system. In general, the graphene membrane will show a delayed response in its deflection with a certain time delay τ. This time-delay can be described by a function $h(t-t')$ that leads to the following formulation for the force:

$$F(t) = \int_0^t \left(\frac{\partial F_{\mathrm{ph}}}{\partial t'} \right) h(t-t') \mathrm{d}t'. \tag{2.31}$$

where F_{ph} is a photo-induced force (which can be photo-thermal, radiation pressure or radiometric pressure) that is exerted on the compliant graphene membrane. This force can be inserted into the equation of motion for the mechanical resonator:

$$m\ddot{x} + \frac{m\omega_0}{Q_{mn}}\dot{x} + m\omega_0^2 x = \int_0^t \left(\frac{\partial F_{\mathrm{ph}}}{\partial t'} \right) h(t-t') \mathrm{d}t', \tag{2.32}$$

m is the modal mass. Using the properties of Laplace transforms for convolutions and assuming F_{ph} is an harmonic function: $F_{\mathrm{ph}} = \varepsilon \cos \omega t$, we can now write eq. 2.32 in the frequency domain:

$$-\omega^2 m x_\omega + i\omega m \zeta x_\omega + K x_\omega = i\omega \varepsilon h_\omega \tag{2.33}$$

Note that if we examine the system far below its resonance frequency and assume damping is small, we can approximate the equation of motion and immediately find the amplitude x:

$$x_\omega = i\omega \frac{\varepsilon}{k} h_\omega. \tag{2.34}$$

Thus, it is possible to directly find the delay function h_ω from a measurement of the complex amplitude below the resonance frequency. Usually we simplify the analysis by

taking a single relaxation time approximation for $h(t)$:

$$h(t) = 1 - e^{-t/\tau}, \tag{2.35}$$

which has the Laplace transform:

$$h_\omega = \frac{1}{i\omega(1 + i\omega\tau)}. \tag{2.36}$$

This gives for the low frequency complex amplitude of the system:

$$\mathscr{R}(x_\omega) = \frac{\varepsilon}{k(1+\omega^2\tau^2)}, \tag{2.37}$$

$$\mathscr{I}(x_\omega) = -\frac{\varepsilon\omega\tau}{k(1+\omega^2\tau^2)}. \tag{2.38}$$

In chapter 5 and chapter 6 we use this equation to find the thermal time constant τ, where the delayed force arises from the diffusion of heat. We will also show a case in chapter 10 where gas pressure actuates the membrane, and the same theory can be applied to find the pressure relaxation time, or leak time, of the cavity. A more complex situation where h_ω is determined by both a thermal time constant and a pressure relaxation time is shown in the outlook (chapter 13).

2.7. THERMAL MOTION

Any mechanical resonator at a finite temperature experiences thermal motion due to the fluctuations in the environment. This fluctuating force F_{th} can be added into the equation of motion of the harmonic oscillator:

$$\ddot{x} + \frac{\omega_0}{Q}\dot{x} + \omega_0^2 x = \frac{F_{\text{th}}}{m_{\text{eff}}}. \tag{2.39}$$

We know from eq. (2.11) that the solution to the equation of motion is:

$$\langle|x|\rangle = \frac{F_\omega}{m_{\text{eff}}} \frac{1}{\sqrt{\left(\omega_0^2 - \omega^2\right)^2 + \left(\frac{\omega_0\omega}{Q}\right)^2}}, \tag{2.40}$$

where $\langle|x|\rangle$ is now the Fourier transform of the time averaged amplitude and F_ω is also the Fourier transform of the time averaged force. It is more convenient however to express the resonator's amplitude as its one-sided power spectral density S_{xx}:

$$S_{xx} = \frac{S_{FF}}{m_{\text{eff}}^2\left[(\omega^2 - \omega_0^2)^2 + (\omega\omega_0/Q)^2\right]} \tag{2.41}$$

where S_{FF} is the PSD of the thermal force, using the equipartition theorem [54] this can be expressed as:

$$S_{FF} = \frac{4k_B T\omega_n m_{\text{eff}}}{Q}. \tag{2.42}$$

which results in the expression:

$$S_{xx} = \frac{4k_B T\omega_n}{m_{\text{eff}}\left[(\omega^2 - \omega_0^2)^2 + (\omega\omega_0/Q)^2\right]}. \tag{2.43}$$

Measurements of the PSD are used in micromechanical resonators to calibrate the amplitude, which works provided that the temperature and effective mass of the resonance are well known. This method is known as thermomechanical calibration. We use an adapted version of this method to find the mass or temperature of the resonator with a well-known amplitude in chapter 8 and in the outlook in chapter 13.

Part I: Methods

3

FABRICATION AND MEASUREMENT OF SUSPENDED GRAPHENE RESONATORS

This chapter describes the fabrication procedures used in this thesis to make graphene resonators and shows the setup that actuates and reads out the motion of the membranes. It shows the technique to make cavities in the chips over which graphene will be suspended. Then it proceeds into the fabrication techniques to make graphene suspended over cavities with a venting channel to the environment. Finally, the interferometer setup for actuating and readout of the motion of the resonators is presented.

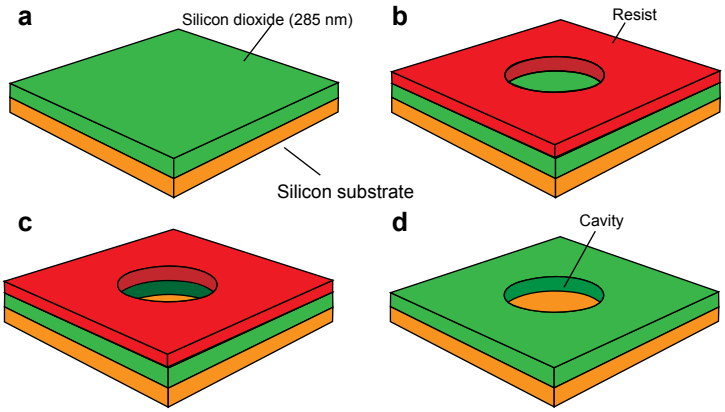

Figure 3.1: Fabrication of substrates with cavities. **a** Silicon substrate with a 285 nm layer of thermally grown silicon dioxide. **b** A layer of electron beam resist is spin-coated, exposed and developed. **c** Reactive ion etching into the silicon dioxide layer creates the cavity. **d** The resist is stripped and the cavity is finished.

3.1. FABRICATION

FABRICATION of graphene resonators starts with the substrate, which contains cavities over which the graphene is suspended. These substrates consist of a silicon chip with a layer of approximately 285 nm thermally grown silicon dioxide (Fig. 3.1**a**). This provides a thin optical layer that enhances the visibility of thin flakes of graphene on top of the substrate [55]. In order to create cavities in the silicon dioxide layer, the chips are spin-coated with a resist which is patterned using electron beam (e-beam) lithography (Fig. 3.1**b**). After development of the resist, the silicon dioxide layer is etched using reactive ion etching (Fig. 3.1**c**). This dry etching process results in cavities with high aspect ratios and well-defined dimensions after removal of the resist (Fig. 3.1**d**).

E-beam lithography allows the shape and size of the cavity to be easily varied, hence in this work, two types of cavities were employed. The first is a simple circular cavity which is completely sealed once the graphene is transferred on top, as shown in Fig. 3.1. The second type of cavities are dumbbell shaped: they consist of two circular cavities connected with a channel as shown in Figs. 3.2 and 3.3. The idea behind these cavities is to cover one side of the dumbbell with a suspended graphene membrane, while the other side remains open to the environment. In this manner, the channel that connects the dumbbell forms a venting channel which ensures that the gas pressure in the cavity is always equal to the pressure in its environment.

3.1.1. MECHANICAL EXFOLIATION AND DETERMINISTIC TRANSFER

Exfoliation of graphene crystals is a powerful and simple tool to create atomically thin membranes for research purposes. Using blue Nitto tape, thin pieces of graphite are exfoliated from a natural graphite crystal. This is transferred on a viscoelastic, optically transparent PDMS stamp [56]. Using optical microscopy, the flakes are examined for thickness and size, until a suitable flake of single-layer or few-layer graphene is found.

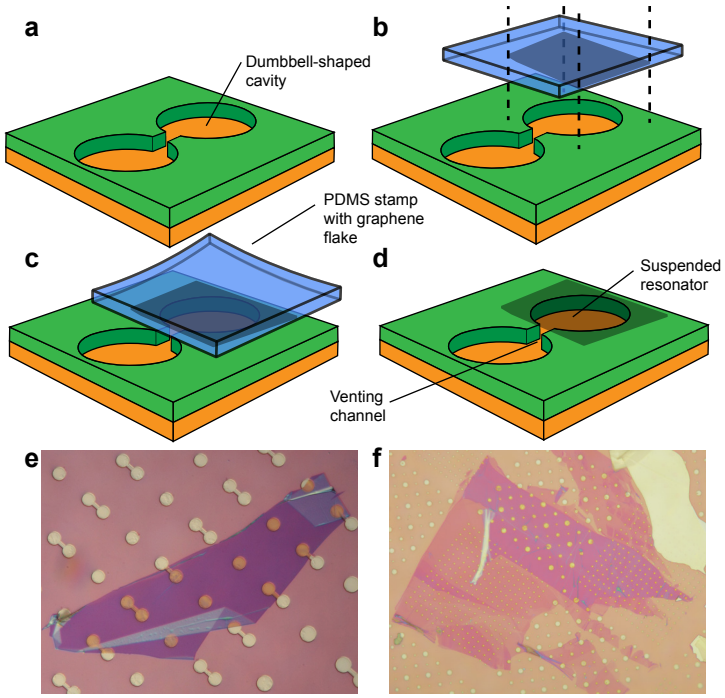

Figure 3.2: Fabrication of resonators with a venting channel from exfoliated graphene. **a** Cavities are etched into the silicon dioxide layer using the process in Fig 3.1. **b** Graphene is exfoliated on a dry stamp and positioned above the substrate. **c** The stamp is brought in contact with the substrate and slowly released. **d** After peeling off the PDMS the flake is transferred to the substrate. The positioning allows us to cover only half of the dumbbell, creating a resonator with a venting channel. **e** Optical microscope image of a graphene flake used in chapter 9, which has suspended resonators with a venting channel but also closed drums. **f** Optical image of a graphene flake over a large number of closed cavities, used in chapter 11.

The stamp is then flipped upside down and mounted on an XYZ stage above the target chip containing the cavities (Fig. 3.2**b**). An optical microscope is used to align the flake at the correct position, for example, to cover one side of a dumbbell cavity. Once the correct position is found, the stamp is brought into contact with the substrate and then slowly released (Fig. 3.2**c**). Due to the viscoelastic properties of the stamp, the slow release will cause the flake to adhere to the substrate, rather than the PDMS stamp. After the release of the stamp, the graphene flake forms a suspended resonator over the cavity (Fig. 3.2**d**). Figure 3.2**e** shows a flake transferred over dumbbell-shaped cavities such that a venting channel is formed, along with a few circular closed drums, this sample was used in chapter 9. Figure 3.2**f** shows another sample containing many closed resonators which was used in chapter 11.

3.1.2. SINGLE-LAYER GRAPHENE RESONATORS

Single-layer graphene resonators are difficult to exfoliate and transfer using the deterministic transfer method, due to their delicate nature. Mechanical exfoliation can also

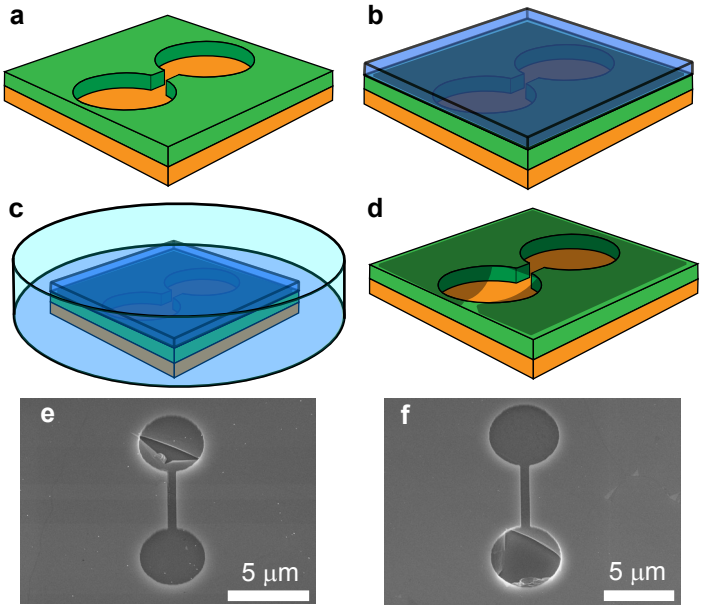

Figure 3.3: Fabrication of single-layer graphene resonators. **a** Substrate with cavities fabricated using the method in Fig 3.1. **b** A large sheet of single-layer CVD graphene is transferred on top of the sample using a protective polymer. **c** The polymer is dissolved and subsequently dried using critical point drying. **d** Resonator with one side of the dumbbell broken, creating a resonator with a venting channel on the other side. **e** Scanning electron microscope (SEM) image of a successfully fabricated resonator. The top side of the dumbbell is broken while the bottom is intact and suspended. **f** Another example of a successfully fabricated resonator, where the bottom part is broken while the top part is intact.

only create a few suspended resonators at a time, meaning that costly time is required to fabricate these resonators. In order to solve these problems, graphene grown by chemical vapor deposition was used to fabricate devices. Transfer of a large sheet of graphene to create suspended structures is not straightforward since it is desired to transfer over dumbbell shaped cavities and create a venting channel.

This requirement resulted in the transfer process shown in fig. 3.3. A large sheet of single-layer graphene is transferred on top of the substrate with the help of a protective polymer (Fig. 3.3**b**). This polymer is dissolved and subsequently the sample is dried by critical point drying (CPD) using liquid carbon dioxide, to prevent that this suspended graphene resonator collapses and adheres to the substrate (Fig. 3.3**c**). The idea behind this process is that the dumbbell-shaped cavities are fully covered with graphene, however, the fluid forces in this process will break the weakest part of the dumbbell. After CPD, on the other side of the dumbbell, there will be a suspended graphene resonator (Fig. 3.3**d**). This process worked with reasonable yield for drum diameters between 2 to 7 μm. Figures 3.3**e** and **f** shows scanning electron microscope images of two resonators where this process successfully yielded a suspended drum on one side of the dumbbell while the other side is broken.

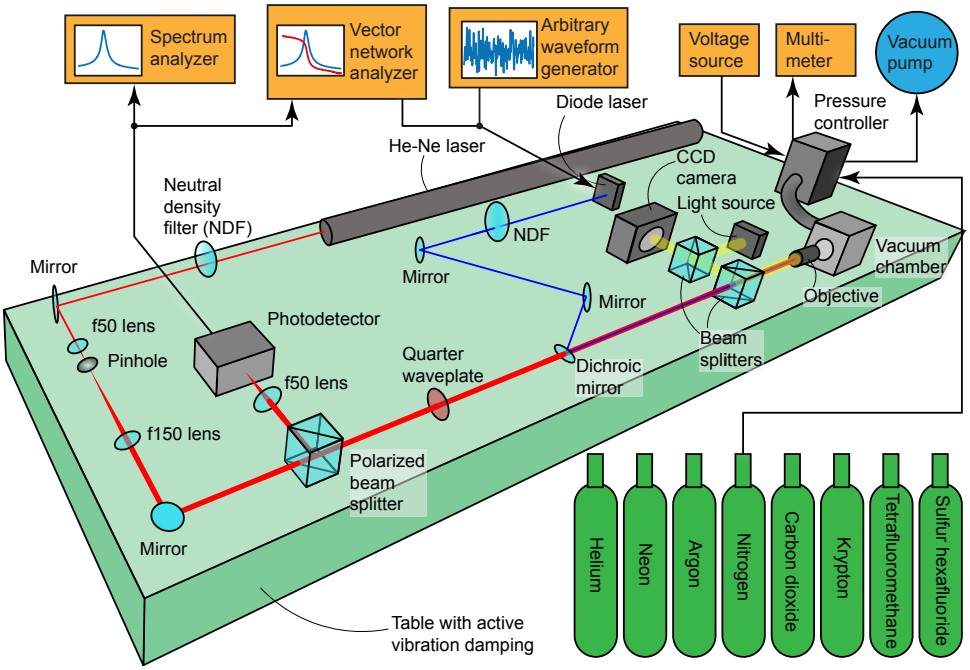

Figure 3.4: Illustration showing the most important components of the experimental setup.

3.2. EXPERIMENTAL SETUP

With the fabrication of suspended graphene samples complete, we need an experimental setup to measure and actuate their motion. An illustration of the experimental setup is shown in Fig. 3.4. A red helium neon laser is used for the readout of the motion. This is performed using Fabry-Perot interferometry, in which the substrate acts as a back mirror and the suspended graphene sheet as a moving mirror. The resulting optical cavity has a very low finesse due to the low optical reflectivity of graphene, nevertheless the reflected intensity is a clear function of the membranes position and can be used to measure the membrane's deflection. The readout of the membrane's motion is nonlinear which can be exploited to calibrate the amplitude of the resonator as shown in chapter 4.

Next, a means of actuating the membrane is required. To this end, a blue diode laser is brought into the optical path. This diode laser is modulated at high frequencies by applying an alternating current. The blue laser light provides a periodically changing heat flux to the membrane, which will be actuated due to the thermal expansion. Several clues on how this exactly results in mechanical motion were found in chapters 5, 6, 7 and 10. The membrane's motion can be detected using different machines. Mostly a vector network analyzer (VNA) is employed, which measures the transmission from the diode laser modulation to the signal detected by the photodiode. This transmission measurement gives the amplitude and phase of the signal as function of frequency. The VNA has the ability to perform frequency conversion measurements, allowing us to drive the resonator at a certain frequency and detect the motion at a different frequency,

this is mainly used in chapters 4 and 7. Frequency conversions measurements have the drawback that they do not detect the phase of the signal. The Brownian motion of the thermally driven resonator can also be measured by directly connecting a spectrum analyzer at the output port of the photodetector. Besides the VNA and lock-in amplifier, a waveform generator can be employed for the actuation signal, which was used as a generator of random fluctuations to raise the effective temperature of the resonator in chapter 8.

To perform measurements as function of gas pressure in the chamber, we use a dual-valve PID pressure controller. This controller is rigidly connected to the vacuum chamber and a voltage setpoint is used as a reference. The controller is connected to a vacuum pump and to a gas supply. Different gases are available to use in the experiment, non flammable gases are chosen because of safety reasons and to prevent damage to the samples. If experiments are performed in high vacuum, the pressure controller is no longer used and the chamber is directly connected to a turbomolecular vacuum pump.

4

AMPLITUDE CALIBRATION BY NONLINEAR OPTICAL TRANSDUCTION

Contactless characterization of mechanical resonances using Fabry-Perot interferometry is a powerful tool to study the mechanical and dynamical properties of atomically thin membranes. However, amplitude calibration is often not performed, or only possible by making assumptions on the device parameters such as its mass or the temperature. In this work, we demonstrate a calibration technique that directly measures the oscillation amplitude by detecting higher harmonics that arise from nonlinearities in the optical transduction. Employing this technique, we calibrate the resonance amplitude of two-dimensional nanomechanical resonators, without requiring knowledge of their mechanical properties, actuation force, geometric distances or the laser intensity.

Parts of this chapter have been published in Applied Physics Letters **111** (25), 253104 (2017) [57].

THERE is an enormous interest to study the dynamics of 2D material resonators because of their sensitivity to the surrounding environment, paving the way towards gas (chapter 11) [35, 58] and pressure sensors (chapters 9, 10 and 13) [11, 59]. Additionally, the intricate thermal (chapters 5, 6) [60, 61], optical [62] and mechanical properties [63] (chapter 7) of these materials are of interest as well. The analysis of the linear frequency response of suspended 2D membranes usually provides information on their pre-tension n_0 through the resonance frequency f_0 and on their energy dissipation rate through the quality factor Q. Besides f_0 and Q, it is often desirable to calibrate the amplitude of the resonant motion. This enables force sensing and also allows for determination of the mass, Young's modulus [63] and the thermal properties [60]. However, current calibration techniques assume that the temperature or the mass are well known, which is difficult to justify for 2D material membranes.

Readout of the dynamic displacement of 2D resonators is usually performed by the following two methods: (i) transconductance measurements [12, 64–66], where motion is detected via a gate-induced conductance modulation or (ii) laser interferometry [49, 64, 67–70], where a Fabry-Perot cavity is formed between the resonator and a fixed mirror so that the motion of the resonator modulates the intensity of the reflected light. Thermomechanical calibration of the amplitude relies on the equipartition theorem [54] (chapter 2). This method is widely used for calibrating cantilevers for atomic force microscopy [54] and has recently been applied to few-layer graphene resonators [63, 67]. When applied to single-layer 2D materials, however, thermomechanical calibration has the drawback that one has to assume that both the temperature and modal mass are known. The mass can be significantly affected by impurities and polymer contamination [12] (chapter 13), therefore resulting in considerable errors in the calibration of the motion amplitude of the membrane.

At high amplitudes, the assumption of a linear transduction coefficient breaks down, since the output signal is no longer proportional to the displacement. In Fabry-Perot interferometry, this happens because the intensity of the reflected light is a periodic function of the membrane's position. This nonlinear relation between membrane position and the intensity of the reflected light is well-known [55, 71–76] and manifests itself in the frequency domain by higher harmonic generation at integer multiples of the driving frequency f.

Here, we use heterodyne detection to measure these higher harmonics and derive mathematical expressions that relate their intensity ratios to the motion amplitude. We show that using only three harmonics we can deduce both the resonant amplitude and the position of the resonator, i.e. the cavity depth. This procedure provides an alternative for the thermomechanical amplitude calibration method, but is instead independent of the mass and temperature of the resonator and only requires the wavelength of the light to be known.

4.1. MATHEMATICAL DERIVATIONS

We now use optical theory to show how these higher harmonics can be used to determine the motion amplitude and average position. Figure 4.1**a** shows a cross-section of the graphene device suspended over the cavity. The reflected intensity $I(x)$ of the red laser light (red solid curve in Fig. 4.1**b**) is a periodic function of the membrane position,

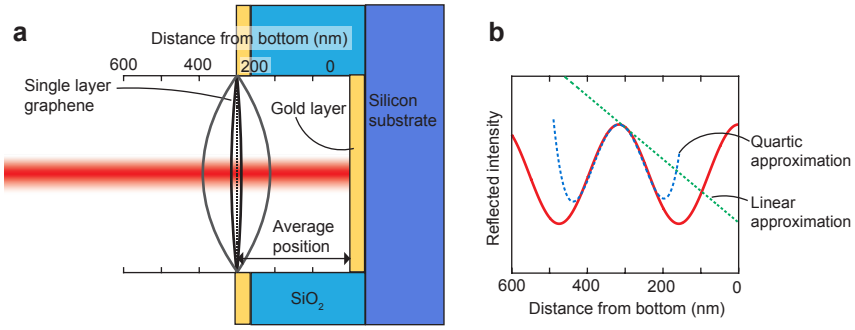

Figure 4.1: **a** Cross section of the suspended graphene device. **b** The reflected intensity detected by the photodetector (solid red line) as a function of membrane distance from the cavity (eq. 4.2), which deviates from the linear approximation when the amplitude becomes large compared to the wavelength.

therefore it can be described by a Fourier series:

$$I(x) = \frac{A_0}{2} + \sum_{n=1}^{N} A_n \sin\left(\frac{4\pi n(g+x)}{\lambda} + \phi_n\right), \tag{4.1}$$

where A_n are constants, g is the average distance between the membrane and the bottom of the cavity, x the membrane's deflection and λ the wavelength of the light used for the readout. If the membrane is thin enough and the reflectivity of the back mirror is sufficiently high, the reflected intensity I as a function of distance from the cavity bottom can be approximated by a single term in the series:

$$I(t) = A + B\cos\left(4\pi\frac{g+x(t)}{\lambda}\right), \tag{4.2}$$

where A and B are constants. For small amplitudes a linear approximation can be used for eq. 4.2, however for large amplitudes this approximation breaks down and a Taylor expansion with more orders is necessary to accurately describe the amplitude (Fig. 4.1**b**). Performing the series expansion up to $m = 4$ gives for the intensity $I(x)$:

$$\begin{aligned} I(x) = A + B\cos(\gamma g) - B\gamma\sin(\gamma g)x \\ -B\gamma^2\cos(\gamma g)\frac{x^2}{2} + B\gamma^3\sin(\gamma g)\frac{x^3}{6} + B\gamma^4\cos(\gamma g)\frac{x^4}{24} + O(5), \end{aligned} \tag{4.3}$$

where $\gamma = 4\pi/\lambda$. Using this Taylor series expansion, for a sinusoidal motion of the graphene membrane $x(t) = \delta\sin(\omega t)$ the detected optical modulation amplitudes can be expressed

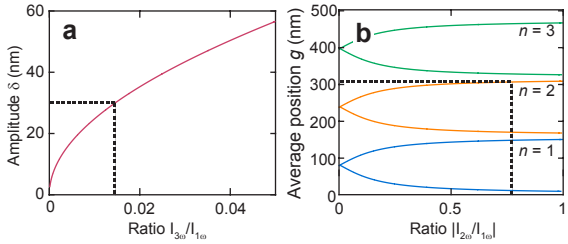

Figure 4.2: Explanation of the calibration procedure. **a** The amplitude δ of the membrane versus the ratio $I_{3\omega}/I_{1\omega}$. From the measurement of this ratio the amplitude can be directly determined from Eq. 4.8. **b** Average position g versus the ratio $I_{2\omega}/I_{1\omega}$ from Eq. 4.10, with a known amplitude of δ. From the measured ratio, the gap size can be determined. However a rough initial guess of this gap size is required to choose the correct value of n in Eq. 4.10.

4

by the series $I(t) = \sum_m I_{m\omega} \sin m\omega t$ where $m = 1, 2, 3...$:

$$I_{1\omega} = -B\gamma\delta \sin(\gamma g) + \frac{1}{8} B\delta^3\gamma^3 \sin(\gamma g), \tag{4.4}$$

$$I_{2\omega} = \frac{1}{4} B\delta^2\gamma^2 \cos(\gamma g) - \frac{1}{48} B\gamma^4\delta^4 \cos(\gamma g), \tag{4.5}$$

$$I_{3\omega} = -\frac{1}{24} B\delta^3\gamma^3 \sin(\gamma g), \tag{4.6}$$

$$I_{4\omega} = \frac{1}{192} B\gamma^4\delta^4 \cos(\gamma g). \tag{4.7}$$

Note, that $I_{1\omega}$ contains a term linearly proportional to δ, but also a term proportional to δ^3, which causes deviations from linear response in the conventional homodyne Fabry-Perot readout. Using the ratio between the harmonics $I_{3\omega}/I_{1\omega}$ an expression is obtained that is independent of A and B:

$$\delta = \frac{2\sqrt{6 I_{3\omega}/I_{1\omega}}}{\sqrt{\gamma^2 - 3 I_{3\omega}/I_{1\omega}\gamma^2}}. \tag{4.8}$$

With this equation the amplitude δ can be determined directly from the measured ratio $I_{3\omega}/I_{1\omega}$ and the wavelength of the light λ, since $\gamma = 4\pi/\lambda$, as is shown in Fig. 4.2**a**. Alternatively, the amplitude δ can also be obtained from the ratio $I_{4\omega}/I_{2\omega}$, which can be more accurate when $\sin(\gamma g)$ is small:

$$\delta^* = \frac{4\sqrt{3 I_{4\omega}/I_{2\omega}}}{\sqrt{4\gamma^2 I_{4\omega}/I_{2\omega} + \gamma^2}}. \tag{4.9}$$

Once the amplitude δ is determined from eq. 4.8, the ratio $I_{2\omega}/I_{1\omega}$ can now be used to obtain the average position g:

$$g = \frac{1}{\gamma}\left(\pi n + \arctan\left(\frac{12\delta\gamma - \delta^3\gamma^3}{(6\delta^2\gamma^2 - 48) I_{2\omega}/I_{1\omega}}\right)\right) \quad \text{where } n = 0, 1, 2, 3... \tag{4.10}$$

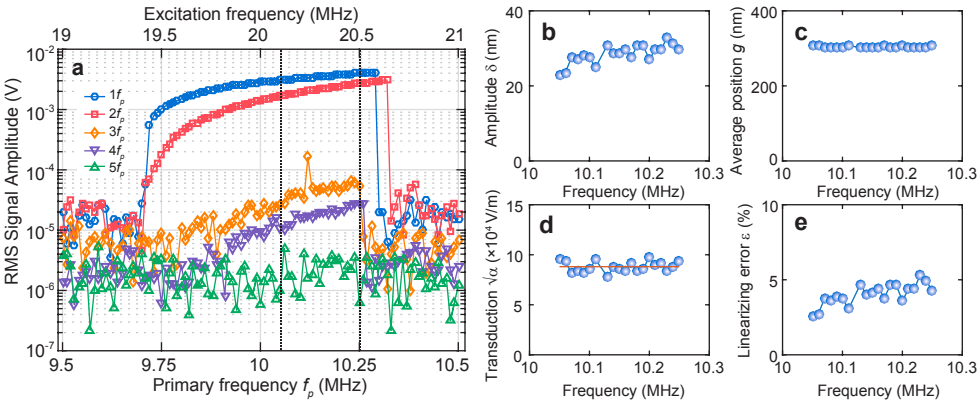

Figure 4.3: **a** Detection of 5 harmonics of the parametrically driven fundamental mode for a 5 μm circular drum. The fifth harmonic has a magnitude smaller than the noise floor; the lower harmonics are readily detected. Dashed lines indicate the window in which the analysis was performed. **b** Amplitude extracted from the data using eq. 4.8. **c** Average position extracted from the data using eq. 4.10. **d** Transduction coefficient $\sqrt{\alpha}$, the change in root mean square voltage per meter of the amplitude of motion. **e** Estimated error in the response by assuming that the transduction is linear.

The procedure to obtain g from this equation is shown in Fig. 4.2**b**. Note, that the value of g needs to be roughly known from the fabrication process, with an accuracy better than $\lambda/4$, to determine the value of n in eq. 4.10. Since the fabricated depth of the cavities is 300 nm, $n = 2$ gives the correct average position in our case (Fig. 4.2**b**). Other ratios between even and odd harmonics, such as $I_{3\omega}/I_{2\omega}$, yield similar expressions for g:

$$g_{32} = \frac{1}{\gamma}\left(\pi n + \arctan\left(\frac{(12-\delta^2\gamma^2)\,I_{3\omega}/I_{2\omega}}{-2\delta\gamma}\right)\right), \tag{4.11}$$

$$g_{41} = \frac{1}{\gamma}\left(\pi n + \arctan\left(\frac{\delta^3\gamma^3}{(24\delta^2\gamma^2-192)\,I_{4\omega}/I_{1\omega}}\right)\right), \tag{4.12}$$

$$g_{43} = \frac{1}{\gamma}\left(\pi n + \arctan\left(-\frac{\delta\gamma}{8\,I_{4\omega}/I_{3\omega}}\right)\right). \tag{4.13}$$

4.2. RESULTS

We now experimentally demonstrate the method for a 5-micron diameter, single-layer graphene drum (the fabrication is shown in chapter 3). Using the Fabry-Perot interferometer from chapter 3, we detect the harmonics due to nonlinear transduction. The intensity modulated laser heats the drum, this causes a tension modulation in the membrane by thermal expansion. Since the spring constant of the membrane is proportional to the tension, this modulation results in a parametric excitation of the drum resonances if the modulation frequency is twice the resonance frequency. Parametric driving was chosen because it resulted in larger amplitudes than direct driving, which increased the accuracy of the calibration method. Further investigations into parametric resonance can be found in chapter 7. Parametric excitation was achieved by setting the frequency f_{ext} of the excitation port of the VNA to twice the primary frequency f_p: $f_{\text{ext}} = 2f_p$. By

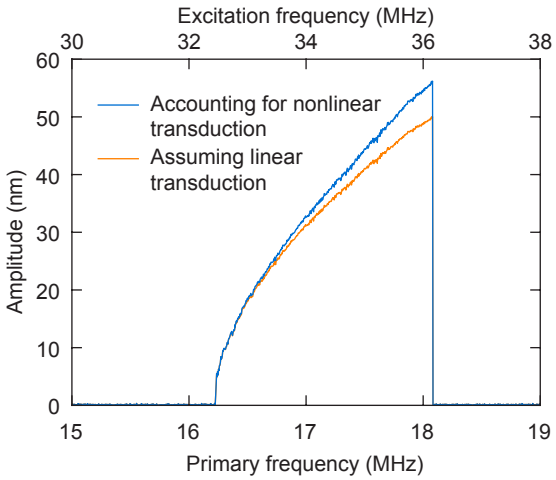

Figure 4.4: Measured amplitude assuming nonlinear transduction and the corrected signal taking nonlinear transduction into account.

scanning f_p across the mechanical fundamental resonance frequency f_0, the drum is brought into parametric resonance. To detect the first, second, third, fourth and fifth harmonic the frequency of the analyzer port was set to $f_a = f_p$, $2f_p$, $3f_p$, $4f_p$ and $5f_p$ respectively. The resulting signal amplitudes are shown in Fig. 4.3**a**. In the frequency window indicated by dashed vertical lines in Fig. 4.3**a**, four harmonics are clearly above the noise level and the calibration procedure can be applied. The data-points are averaged within this frequency window to reduce the error due to measurement noise.

First, we determine the amplitude of oscillation δ for all the frequencies in the window using eq. 4.8 (Fig. 4.3**b**). A remarkably large amplitude is detected, close to 100 times the thickness of the graphene membrane (0.335 nm), which increases with frequency as expected. Now that the amplitude is known, Eq. 4.10 is used to find the equilibrium position shown in Fig. 4.3**c**. An average position of $g = 304.9$ nm is calculated with a standard error (SDE) of 0.16 nm. The transduction coefficient $\sqrt{\alpha}$ is deduced from the relation $I_{1\omega} \approx \sqrt{\alpha}\delta$, by taking the detected root mean square voltage $I_{1\omega}$ at the VNA and dividing it by the amplitude δ from Fig. 4.3**b**. The resulting $\sqrt{\alpha} \approx -B\gamma\sin(\gamma g)$ within the frequency window is shown in Fig. 4.3**d**. We find $\sqrt{\alpha} = (8.8 \pm 0.1) \times 10^4$V/m. As expected, the average position g and the transduction coefficient $\sqrt{\alpha}$ are independent of excitation frequency or membrane amplitude.

4.3. CORRECTING THE ERROR DUE TO NONLINEAR TRANSDUCTION

The calibration method can also be used to correct for the effects of nonlinear transduction, improving the high-amplitude accuracy of the interferometer. As discussed above, the expression for $I_{1\omega}$ (eq. 4.4) contains a term proportional to δ^3, which can be used to

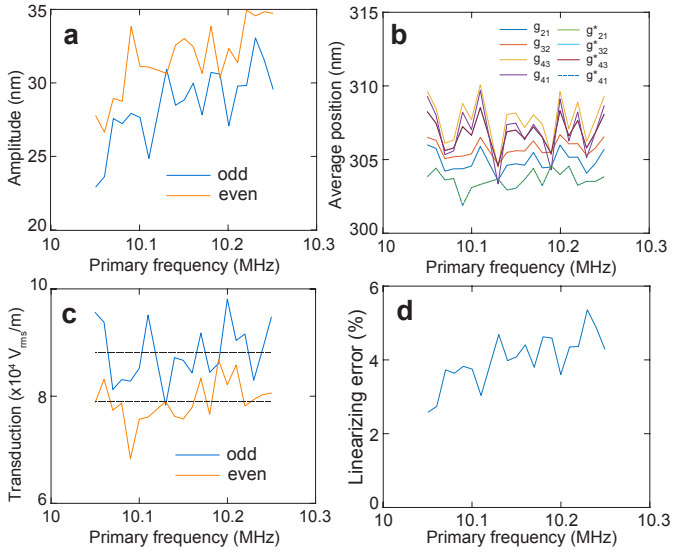

Figure 4.5: Result of the extended analysis. **a** amplitude obtained by using the ratio $I_{3\omega}/I_{1\omega}$, denoted by δ and the ratio $I_{4\omega}/I_{2\omega}$, denoted by δ^*. A slightly higher amplitude is found for δ^*, this is either due to the simplifying assumption behind eq. 4.2, or a small contribution due to mechanical nonlinearities. **b** Average position using eight different expressions, the notation g^* is used to indicate that δ^* was used in to find the position. **c** Transduction coefficient $\sqrt{\alpha}$, derived from both δ and δ^*.

estimate the relative error ϵ due to nonlinear transduction, from eq. 4.4:

$$\frac{I_{1\omega}}{\sqrt{\alpha}} = \delta\left(1 - \frac{1}{8}\delta^2\gamma^2\right) \equiv \delta(1-\epsilon), \tag{4.14}$$

where $\epsilon = \frac{1}{8}\delta^2\gamma^2$ [63]. For small ϵ, the amplitude δ can now be derived from the uncorrected amplitude $I_{1\omega}/\sqrt{\alpha}$:

$$\delta = \left(1 + \frac{1}{8}\left(\frac{I_{1\omega}}{\sqrt{\alpha}}\right)^2\gamma^2\right)\frac{I_{1\omega}}{\sqrt{\alpha}}, \tag{4.15}$$

with a known value of $\sqrt{\alpha}$ from the calibration, δ can be found from the measurement of $I_{1\omega}$. Since $\sqrt{\alpha}$ is constant this correction also works outside the frequency window where the calibration is performed. To illustrate the error in the graphene membrane amplitude, we apply this correction to a different drum in Fig. 4.4, which exhibits large motion amplitudes. In this case, the maximum amplitude gets underestimated by more than 10%. This correction is thus important to take into account when measuring the motion of resonators with large amplitudes.

4.3.1. EXTENDED ANALYSIS

Figure 4.5 shows the results of the extended analysis. Using $\frac{I_{4\omega}}{I_{2\omega}}$ we find a slightly higher amplitude (Fig. 4.5**a**). As shown section 4.4 this can be largely contributed to the error made by taking only the first term in the Fourier series in eq. 4.2. The differences in the detected average postion all fall within 2% of each other. The resulting transduction

coefficient found by using $\frac{I_{4\omega}}{I_{2\omega}}$, is about 10% lower then the coefficient found by using $\frac{I_{3\omega}}{I_{1\omega}}$ (Fig. 4.5**c**).

From the extended analysis, we find that the systemic error due to the simplification of the transduction coefficient $\sqrt{\alpha}$ is lower than 10%. This is considerably smaller than existing techniques that require the mass to be known since the mass can show deviations as high as 600% [12] in literature. The results presented in the outlook chapter of this dissertation (chapter 13), suggests even larger uncertainty in the mass.

4.4. NUMERICAL ROUTINE FOR MORE ACCURATE OPTICAL MODELS

The presented method is applicable not only for thin 2D material resonators but also for other nanomechanical systems in Fabry-Perot cavities, such as nanowires [77], provided that they are thin enough for eq. 4.2 to remain valid. The method could also be extended to thicker membranes, however since eq. 4.2 does not hold anymore in that case, the mathematics becomes rather complex and requires numerical routines. In this section, we demonstrate a numerical routine that can be used to calibrate any resonator in a Fabry-Perot interferometer, as long as its optical properties are well known and the motion can be considered harmonic. This numerical method no longer required to use the simple expression in eq. 4.2, but works with any arbitrary position-dependent intensity $I(x)$.

4.4.1. OPTIMIZATION ROUTINE

Suppose we have a resonator with a well-known position dependence of the reflected laser light intensity $I(x)$. Assuming the membrane shows harmonic motion, a time dependent reflected intensity can be numerically evaluated for one period of the oscillation. The harmonic components that arise due to nonlinear optical transduction can then immediately be evaluated by expressing $I(t)$ as a Fourier series:

$$I_N(t) = \sum_{n=-N}^{N} c_n e^{i\omega n t}, \tag{4.16}$$

where N is an integer number for each harmonic and c_n the Fourier coefficient. The Fourier coefficient can directly be determined from one period of $I(t)$:

$$c_n = \frac{\omega}{2\pi} \int_0^{2\pi/\omega} I(t) e^{-i\omega n t} \mathrm{d}t. \tag{4.17}$$

These coefficients depend on the value of δ and g, if these are equal to the experimental value the following relation should hold: $c_n \propto I_{n\omega}$, where $I_{n\omega}$ is the experimentally measured intensity. This allows us to build an optimization routine for δ and g that match the experimentally observed ratio's between the harmonics to the numerically evaluated Fourier coefficients. This routine attempts to find the optimal values of δ and g to minimize the objective function $f(\delta, g)$:

$$f(\delta, g) = \frac{|I_{1\omega}|}{|I_{3\omega}|}\left(\frac{|c_3|}{|c_1|} - \frac{|I_{3\omega}|}{|I_{1\omega}|}\right)^2 + \frac{|I_{1\omega}|}{|I_{2\omega}|}\left(\frac{|c_2|}{|c_1|} - \frac{|I_{2\omega}|}{|I_{1\omega}|}\right)^2, \tag{4.18}$$

subject to constraints on g to prevent the effect of local minima that arise due to the periodicity of $I(x)$.

4.4.2. BENCHMARK

Without expressing I as a single term in the Fourier series, the relative reflected intensity of the laser light as function of position of the membrane is given by:

$$I = \left| \frac{r_1 e^{i(\Phi_1+\Phi_2)} + r_2 e^{-i(\Phi_1-\Phi_2)} + r_3 e^{-i(\Phi_1+\Phi_2)} + r_1 r_2 r_3 e^{i(\Phi_1-\Phi_2)}}{e^{i(\Phi_1+\Phi_2)} + r_1 r_2 e^{-i(\Phi_1-\Phi_2)} + r_1 r_3 e^{-i(\Phi_1+\Phi_2)} + r_2 r_3 e^{i(\Phi_1-\Phi_2)}} \right|^2, \tag{4.19}$$

where:

$$r_1 = \frac{n_0 - n_1}{n_0 + n_1}, \tag{4.20}$$

$$r_2 = \frac{n_1 - n_0}{n_1 + n_0}, \tag{4.21}$$

$$r_3 = \frac{n_0 - n_3}{n_0 + n_3}, \tag{4.22}$$

$$\Phi_1 = \frac{2\pi n_1 d_1}{\lambda}, \tag{4.23}$$

$$\Phi_2 = \frac{2\pi n_0 d_2}{\lambda} = \frac{2\pi n_0 (g + \delta \sin(\omega t))}{\lambda}, \tag{4.24}$$

here n_0 is the refractive index of vacuum, n_1 the refective index of the resonator, n_3 the refractive index of the back reflector, d_1 the resonator thickness and d_2 the distance between the resonator and the membrane. It can be shown that for for very thin membranes where $\Phi_1 \ll \Phi_2$, eq. 4.19 reduces to the cosine function (eq. 4.2). Equation 4.19 is substituted in eq. 4.17 and numerically evaluated for $n = 1,2,3$ for different values of g and δ. A thrust-region alogrithm is used to evaluate eq. 4.18 for different values of δ and g until the ratio of Fourier coefficients match the experimentally measured intensity ratios.

Figure 4.6 shows the results from the numerical routine compared to the analytical result from the simplified optical model in eq. 4.2. We test both the objective function in eq. 4.18, which we call the *odd* objective function and we test:

$$f(\delta, g) = \frac{|I_{2\omega}|}{|I_{4\omega}|} \left(\frac{|c_4|}{|c_2|} - \frac{|I_{4\omega}|}{|I_{2\omega}|} \right)^2 + \frac{|I_{1\omega}|}{|I_{2\omega}|} \left(\frac{|c_2|}{|c_1|} - \frac{|I_{2\omega}|}{|I_{1\omega}|} \right)^2, \tag{4.25}$$

which we call the *even* objective function. Both objective functions show local minima are present close to the global minima in the parameter space of δ, g. The local minima are shown in Figs. 4.6**a** - **c** and the global minima are shown in Figs. 4.6**d**-**f**. The deviations from the simplified model are expected to grow as higher order harmonics are employed and we indeed find that the even harmonics in the global minimum results in a larger disparity with the numerical routine. The numerical routine corrects for this error and places the amplitude closer to the one found by taking the odd ratio. Both minima of the objective functions are close to each other, which is a consequency of the lack of phase information in the measurement. To resolve this problem, the experimental setup could be adapted to yield phase information. Another approach can make use

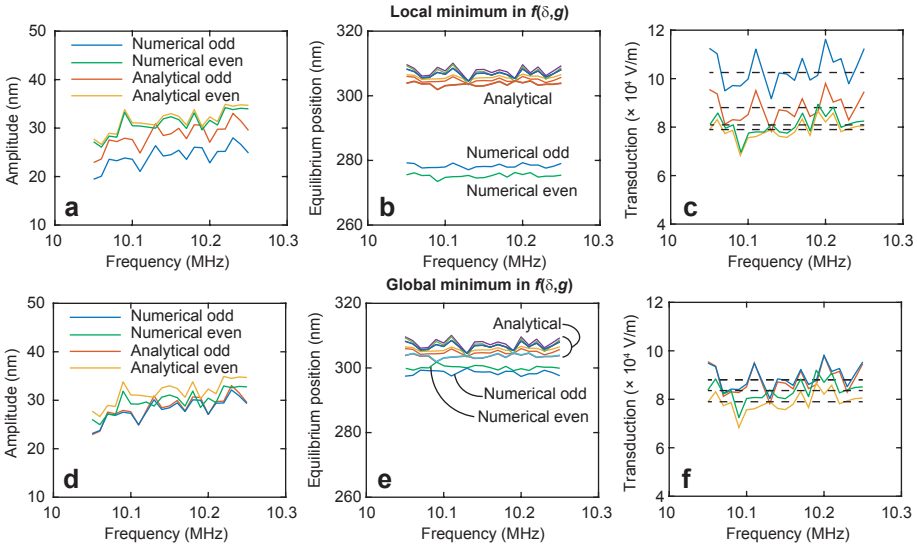

Figure 4.6: Comparison between the numerical routine and the simplified analytical solution. **a** Amplitude as function of frequency, showing the results from the numerical routine compared to the analytical approximation. **b** Average position as function of the frequency. **c** Transduction coefficient as function of frequency,

of the fact that the incorrect minima of eqs. 4.18 and 4.25 yield different δ, g, but the correct minima closely match. The objective function:

$$f(\delta,g) = \frac{|I_{1\omega}|}{|I_{3\omega}|}\left(\frac{|c_3|}{|c_1|} - \frac{|I_{3\omega}|}{|I_{1\omega}|}\right)^2 + \frac{|I_{2\omega}|}{|I_{4\omega}|}\left(\frac{|c_4|}{|c_2|} - \frac{|I_{4\omega}|}{|I_{2\omega}|}\right)^2 + \frac{|I_{1\omega}|}{|I_{2\omega}|}\left(\frac{|c_2|}{|c_1|} - \frac{|I_{2\omega}|}{|I_{1\omega}|}\right)^2, \tag{4.26}$$

should perform better in that respect, provided that a proper algorithm for a global minimum search is used.

4.5. DISCUSSION

Another source of error that should be considered is due to the finite spot size of the laser. The amplitude measured by this technique should be regarded as an average over the spot size. In our case, the spot size of the laser is estimated to be 1 μm. Assuming that the laser is aligned in the center of the drum and that the system is vibrating with the fundamental mode shape, we estimate the error due to the finite spot size to be 2% compared to the maximum deflection. While this is small for the 5 μm drum diameter used here, this error can grow significantly for smaller drums. For example, a 2-micron diameter drum would result in an error of 12%.

It is interesting to point out that the transition from high to low amplitude in Fig. 4.3**a** does not occur at exactly the same frequency. This is attributed to the effects of fluctuations on the nonlinear response of the membrane, discussed in detail in chapter 8. Due to these fluctuations, there is always a finite chance that the resonator will jump down from the high amplitude solution before reaching its saddle-node bifurcation. Since the

harmonics $I_{3\omega}$ and $I_{4\omega}$ were detected with a lower bandwidth to reduce the noise, the probability of such a premature jump to occur is higher. This has no effect on the results of the analysis since the amplitude follows the same backbone in each measurement. The effect is easily accounted for by choosing an appropriate frequency window for the analysis.

4.6. CONCLUSION

We demonstrate a technique that directly determines the amplitude and average position of suspended single-layer graphene resonators in a Fabry-Perot interferometer. This technique takes advantage of the nonlinear transduction of the membrane motion by detecting the higher harmonics that arise due to optical nonlinearities. The technique can be used to calibrate the motion without any assumptions or knowledge of the mass, the mechanical properties, the actuation force and the intensity of the laser power. Only knowledge of the wavelength of the light is required, thus providing a powerful means towards fully contactless characterization of the mechanical properties of atomically thin membranes.

PART II: DYNAMICS OF 2D MATERIAL MEMBRANES INTERACTING WITH HEAT

5

TRANSIENT THERMAL CHARACTERIZATION OF SUSPENDED GRAPHENE

The thermal response of graphene is expected to be extremely fast due to its low heat capacity and high thermal conductivity. In this work, the thermal response of suspended single-layer graphene membranes is investigated by characterization of their mechanical motion in response to a high-frequency modulated laser. A characteristic delay time τ between the optical intensity and mechanical motion is observed, which is attributed to the time required to raise the temperature of the membrane. We find, however, that the measured time constants are significantly larger than the predicted ones based on values of the specific heat and thermal conductivity. The measurements provide a noninvasive way to characterize thermal properties of suspended atomically thin membranes, providing information that can be hard to obtain by other means. In order to explain the discrepancy between measured and modeled τ, we propose two models. The first model takes a thermal boundary resistance at the edge of the graphene drum into account, which explains the thermal time constant for a boundary conductance of 30 ± 20 *MW/(m^2·K). The second model takes into account the scattering at the boundary and suggests that the measured τ can be solely attributed to the flexural phonons.*

Parts of this chapter have been published in Physical Review B **96**, 165421 (2017) [60] and an article in preparation [78].

THE high surface-to-mass ratio of graphene should make the cooling of this material extremely sensitive to the environment, which can be exploited in the Pirani pressure sensor concept proposed in chapter 1. To predict the feasibility of such sensors requires an understanding of the thermal transport through the material, which has recently attracted major attention due to its unusual properties [79, 80]. Extremely high thermal conductivities have been demonstrated up to 5000 W/(m·K), well exceeding the thermal conductivity of graphite [16, 17]. These measurements were performed by Raman spectroscopy, that uses the temperature dependence of the phonon frequency [81]. By measuring the thermal resistance R, which is the local temperature increase ΔT per unit of heat flux ΔQ, one can employ analytical models of the heat transport to extract the thermal conductivity of graphene k. This method allowed the demonstration that the thermal conductivity decreases when the number of graphene layers is increased from 2 to 4 [82]. The method has been subsequently improved, for example by better calibration of absorbed laser power [18] or removing parallel conduction paths through the air [19]. Also, the amplitude ratio between Stokes and anti-Stokes signals has been exploited [22] as an alternative to the shift in phonon frequency. As an alternative to Raman measurements, electrical heaters [23], pump-probe methods [83, 84], scanning thermal microscopy [85] and temperature sensors [86] have been used to study heat transport in graphene, demonstrating length dependence of the thermal conductivity [23] and a reduced thermal conductivity when graphene is supported on silicon dioxide rather than freely suspended [86]. Different groups have demonstrated a large variety in thermal conductivity of pristine graphene between 2000 to 5000 W/(m·K) experimentally [16–29] and between 100 to 8000 W/(m·K) theoretically [28], making the thermal conductance of graphene a debated subject.

Besides these steady-state studies of the thermal properties of graphene, it is of interest to study its time-dependent thermal properties. The thermal response time of graphene is expected to be one of the fastest known, due to its low heat capacitance and high thermal conductivity. To obtain this response time, one needs to measure small temperature fluctuations in suspended graphene at frequencies in the MHz range. However, since the suspended integration of temperature sensors poses problems and optical techniques for temperature measurement in suspended graphene, like Raman spectroscopy, do not offer the temperature resolution and frequency bandwidth, direct high-frequency temperature measurement in suspended graphene is difficult.

In this work, it is therefore proposed to use the thermomechanical response of suspended graphene to characterize its thermal properties at MHz frequencies. This method was previously used by Metzger *et al.* [87] to determine the thermal time constant τ of silicon cantilevers. Similarly, it is found that the mechanical motion of suspended graphene is delayed by a characteristic thermal time constant τ with respect to the intensity-modulation of the laser that opto-thermally actuates the membrane. This is attributed to the time necessary for heat to diffuse through the system. The optomechanics thus provides a tool for studying the dynamic thermal properties of 2D materials. Interestingly, it is found that the measured values of τ are much higher than those expected based on literature values for the thermal conductivity k, specific heat c_p and density ρ of graphene. Models and measurements of drums of different diameters and on different substrates are analyzed in order to account for the large value of τ. Two models are proposed that

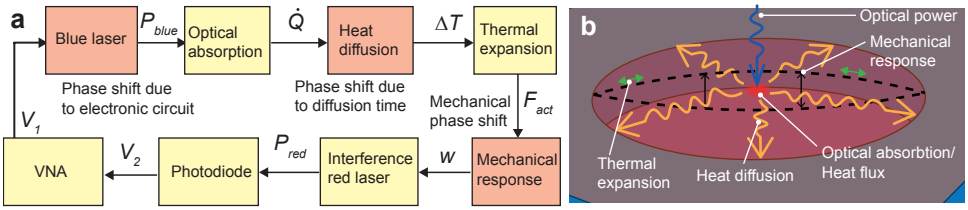

Figure 5.1: Measurement method to determine the characteristic thermal time of suspended graphene resonators. **a** Block diagram showing how the deflection signal is transduced using opto-thermal actuation. **b** Illustration showing how the optical power is transduced into mechanical motion of the drum.

can explain this effect. The first model assumes a large thermal boundary resistance at the edge of the drum. The second model evaluates the boundary scattering due to sidewall adhesion and proposes that the measured τ can be solely attributed to the flexural phonons, while the much faster thermal time of in-plane phonons is obscured in the mechanical resonances.

5.1. OPTOMECHANICAL DELAY

Here we identify the potential source of the time delay between the modulation of the blue laser and the mechanical response in the measurement setup. The block diagram in Fig. 5.1**a** identifies the elements and processes that play a role in actuation and detection of the membrane's motion and Fig. 5.1**b** provides a schematic illustration of these processes in the suspended drum. The modulated intensity of the blue laser is absorbed in the graphene, generating a virtually instantaneous heating power since photoexcited carriers in graphene lose their energy to phonons on timescales of a few picoseconds [88]. The generated heat will increase the temperature of the membrane and flow toward the substrate, resulting in a time-dependent temperature increase of the membrane, where the temperature is delayed with respect to the heating power. The temperature increase causes thermal expansion forces that deflect the membrane. At frequencies far below the resonance frequency, the motion will be in-phase with the thermal expansion force, especially since the quality factor of the resonator is typically higher than 100 resulting in a narrow bandwidth of the resonance. The intensity modulation of the red laser due to the interference effect that is used to detect the motion can be regarded as instantaneous and will not cause a delay. The measurements are corrected for other delays, related to delays in the instruments (VNA, photodiode) and light path delays, using a calibration procedure discussed in the Appendix A2.

It is thus concluded that in the frequency range below the mechanical resonance, the delay between optical actuation and deflection in Fig. 5.1 is nearly completely due to the delay between heating power and temperature. A thermal system with a single time constant τ, driven by an ac heating power $P_{ac}e^{i\omega t}$ can be described by the heat equation:

$$\frac{\mathrm{d}\Delta T}{\mathrm{d}t} + \frac{1}{\tau}\Delta T = \frac{P_{ac}}{C}e^{i\omega t}, \tag{5.1}$$

where ΔT is the temperature difference with respect to the steady-state temperature, C

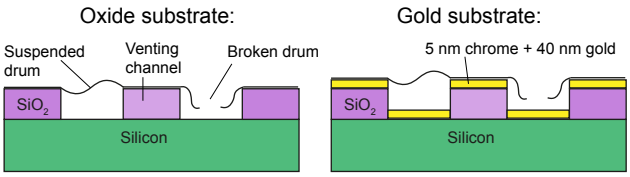

Figure 5.2: Cross section of a dumbbell on the two types of substrates used in this chapter. One is labeled the oxide substrate which is fabricated as shown in chapter 3, the other sample has 5 nm of chrome and 40 nm of gold evaporated on top (before graphene transfer) and is labeled the gold substrate.

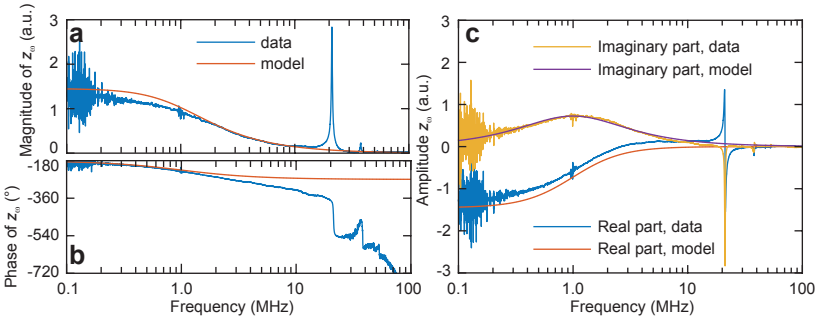

Figure 5.3: Typical measured frequency response function. **a** Magnitude and **b** phase of the VNA signal after calibration, showing a decrease in magnitude and a phase shift well before the resonance frequency at 22 MHz. **c** Real and imaginary parts of the signal, with a fit from eq. 5.2 to the imaginary part. The expected real part from this model is also shown in this plot.

is the thermal capacitance and $\tau = RC$ is the thermal RC product. At frequencies significantly below the mechanical resonance frequency, the thermal expansion induced amplitude $z = \alpha\Delta T$ is proportional to temperature by an effective thermal expansion coefficient α. Solution of the heat equation gives:

$$z_\omega e^{i\omega t} = \alpha R P_{ac} \frac{e^{i\omega t}}{i\omega\tau + 1}. \tag{5.2}$$

Which is the form of the frequency-dependent force equation derived in chapter 2. This equation will be used to fit the experimental data, with the parameters $B = \alpha R P_{ac}$ and τ.

5.2. RESULTS

The measurements are performed on suspended single-layer graphene membranes with a venting channel, the fabrication is shown in chapter 3. We use two types of substrates as shown in Fig. 5.2, one is labeled the oxide substrate and the other is labeled the gold substrate. The large difference in thermal properties allows one to determine the influence of the substrate on the measurements. An example of the measured magnitude and phase of the deflection for a resonator with a diameter of 5 μm on a cavity in silicon dioxide is shown in Figs. 5.3**a** and **b** respectively. In the 0.1 to 10 MHz range, the response is frequency dependent with a decrease in magnitude as the frequency increases. Also, a phase delay is observed that increases as a function of frequency. Note, that the mea-

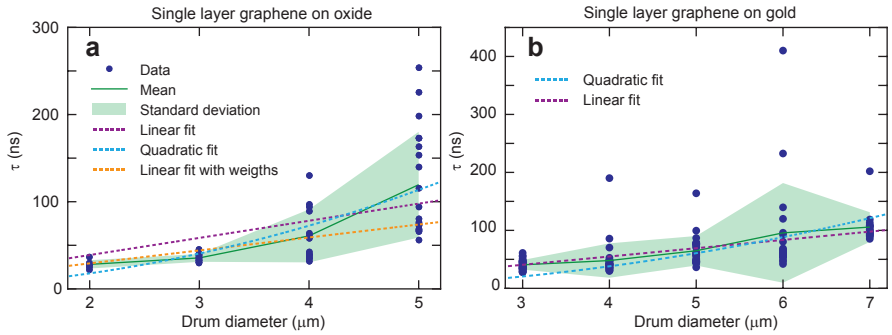

Figure 5.4: Measured characteristic times compared for different diameters. Dashed lines are fits to the data in order to examine the scaling behavior of τ. **a** τ for single layer graphene suspended on a silicon dioxide substrate, showing that both τ and the spread in τ increase with diameter. **b** τ for single layer graphene drums suspended on a gold coated substrate.

5

sured phase at low frequencies is not 0, but 180 degrees. This is attributed to the small offset in the deflection that the graphene membrane has, in some membranes this was reversed in sign (indicated by 0 degrees phase at low frequencies), one example is shown in chapter 10. Figure 5.3**c** shows a measurement result which is split into a real and an imaginary part. The imaginary part of the amplitude z_ω can be fit by eq. 5.2, resulting in a value of characteristic delay time of $\tau = 159$ ns, with a clearly observable maximum at radial frequency $\omega = 1/\tau$. The real part of eq. 5.2, with the same B and τ, is shown in Fig. 5.3**c** showing a small offset with respect to the data which is analyzed further in section 5.6. The same effect causes the difference between the model and the magnitude and phase of the amplitude response (see Fig. 5.3**a**, **b**).

We repeat the measurements on drums of different diameters on two different substrates. One substrate is the silicon dioxide fabricated as shown in chapter 3, the second substrate is identical to the first, but with an additional 5 nm chrome and 40 nm gold layer on top. Values of τ as a function of diameter for both the silicon dioxide and the gold coated substrate are plotted in Figs. 5.4**a**, **b**, respectively. Each point in the graph indicates a different drum resonator. A trend is observed where τ increases as a function of diameter. Furthermore, it is observed in Fig. 5.4 that there is a large variation in the value of τ for drums with the same radius. Repeated measurements of τ on the same device yields an estimated error of 8% and the scatter observed here is therefore due to device-to-device variations. Possible causes of the scatter will be discussed further below.

5.3. MODELS FOR THE THERMAL TIME CONSTANT

The measured time constants in this work are significantly larger than expected based on the intrinsic properties of graphene. For example, Barton et al. [62] use an expression that estimates the time constant based on the thermal properties of graphene:

$$\tau = \frac{a^2 \rho c_p}{2k}, \tag{5.3}$$

where a is the membrane radius, ρ the density of graphene, c_p specific heat and k the thermal conductivity. Using approximate values $c_p = 600$ J/(kg·K) (calculated in the Appendix A4), $k = 2500$ W/(m·K) and $\rho = 2300$ kg/m^3 we obtain $\tau = 0.3$ ns for a 2 micron drum and $\tau = 2$ ns for a 5 micron drum. The observed values of τ range between 25 to 250 ns, which is one to two orders of magnitude larger than those predicted by eq. 5.3. Even if the most extreme values for c_p and k are used, eq. 5.3 gives a lower τ than measured. The theoretical limit for c_p is given by the Petit-Dulong law ($c_p = 2100$ J/kg/K), and the lowest experimental literature value for k is 600 W/(m·K) [22]. Indeed a fit with a quadratic dependence on the radius to the values of τ in Fig. 5.4 gives $k = 36$ W/(m·K) for graphene on silicon dioxide and $k = 66$ W/(m·K) on gold. It thus appears that eq. 5.3 cannot account for the experimental τ.

We first consider the possibility that the thermal conduction is limited by the substrate that supports the graphene resonator. In order to investigate this, we compare the results obtained on gold-coated and uncoated substrates. It is found that the τ on the different substrates are similar (Figs. 5.4**a**-**b**), despite the much higher thermal conductivity of the gold-coated substrate. We investigate the substrate effects further using finite element simulations (see Appendix A3) of the system. These simulations predict no diameter dependence of the value of τ in the uncoated sample, while the gold-coated sample should be in agreement with eq. 5.3. From this disparity between the experiments, it is thus concluded that substrate effects are not responsible for the observed values of τ.

It is well known that a thermal resistance can be present at the interface between two solids [89–94]. This effect is called interfacial thermal (or Kapitza) resistance and is caused by differences in the phonon velocities, which leads to scattering that limits the phonon transport across the interface. Several works have predicted interfacial resistances in graphene using molecular dynamics simulations [95, 96]. Between suspended and supported graphene a value of the boundary conductance of 2×10^{10} W/(K·m^2) was reported [96]. Also, grain boundaries in graphene have been shown to cause an interfacial thermal resistance [97]. Below we argue that an interfacial thermal resistance between supported and suspended graphene could account for the unexpectedly long thermal delay times we measured.

5.4. THERMAL INTERFACE RESISTANCE MODEL

The boundary resistance will cause the formation of a temperature discontinuity at the interface between suspended and supported graphene that can be modeled by Fourier's law [90]:

$$Q_B = \frac{T_{\text{sus}} - T_{\text{sup}}}{R_B} \equiv G_B(T_{\text{sus}} - T_{\text{sup}}), \tag{5.4}$$

where Q_B is the boundary heat flux, T_{sus} the temperature in the suspended part of the graphene and T_{sup} temperature of the supported part. R_B is the thermal boundary resistance and G_B is the thermal boundary conductance. In order to estimate G_B we use a thermal RC model, where the thermal time τ is given by de product of the heat capacity of suspended graphene C and the thermal resistance R. It is assumed that R is dominated by the interfacial thermal resistance R_B, such that τ becomes independent of k of

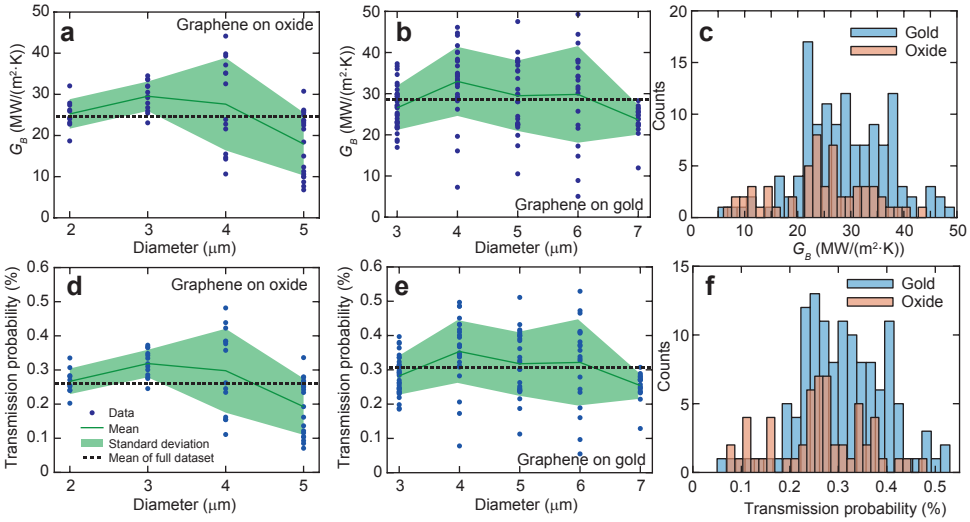

Figure 5.5: Properties of the thermal boundary extracted from the measurements. **a** Thermal boundary conductance G_B extracted using eq. 5.7 as function of diameter for the oxide sample and **b** for the sample covered with gold. **c** Histogram comparing all measured conductances showing the similar distributions between both the oxide and gold dataset. **d** Transmission probability from the supported to the suspended part of graphene for the oxide and **e** for the gold sample. **f** Histogram showing all obtained transmission probabilities.

graphene:

$$C = c_p \rho h_g \pi a^2, \tag{5.5}$$

$$R = (G_B h_g 2\pi a)^{-1}, \tag{5.6}$$

where h_g is the thickness of single layer graphene. Combining both expressions yields for the thermal time τ:

$$\tau = \frac{\rho c_p a}{2G_B}. \tag{5.7}$$

This model thus predicts a linear dependence between τ and a, which is clearly different from eq. 5.3. A linear fit to the data yields good agreement for graphene on gold (Fig. 5.4**b**). In the case of graphene on silicon dioxide (Fig. 5.4**a**), a weighted linear fit to the lower values of τ produces better results, due to the large scatter in the 4 and 5 micron diameter drums. The slopes of the weighted fit on silicon dioxide and the fit on gold yields nearly identical slopes within 5% of each other. Furthermore, the linear fits all fall within the error determined by the spread in τ, while the quadratic fit predicts too low values of τ for small diameters. From the slope of the linear fits, we estimate that the boundary conductance lies near $G_B = 24$ MW/(m^2·K).

To obtain a more accurate values of G_B, we use eq. 5.7 and derive the thermal boundary conductance ($G_B = \rho c_p a/2\tau$) from the measurements of τ for each individual device as shown in Figs. 5.5**a**-**c**. This shows that the value of the thermal boundary conductance lies around 30 MW/(m^2·K). For the purpose of extracting G_B the derived value $c_p = 600$ J/(kg·K) is used and a density $\rho = 2300$ kg/m^3. Equation 5.7 has been verified using fi-

nite element simulations that include a thermal boundary conductance, confirming the validity of neglecting the heat conductance k (see Appendix A3).

In order to relate the derived value of G_B to the phonon transmission probability across the interface, the following expression is derived using the derivations in the Appendix A4:

$$\tau = \frac{\rho c_p a}{2G_B} = \frac{a}{2} \frac{\frac{1}{c_{1l}^2} + \frac{1}{c_{1t}^2} + \frac{\pi\hbar^2}{3\zeta(3)A_{uc}k_B^2T^2}}{\frac{\bar{w}_{1l}}{c_{1l}} + \frac{\bar{w}_{1t}}{c_{1t}} + \frac{\pi\hbar^2\bar{w}_{1z}c_{1z}}{\zeta(3)A_{uc}k_B^2T^2}} \tag{5.8}$$

Here c_{1j} is the velocity of the j-th phonon mode, $j = z$ for the flexural (ZA), $j = l$ for longitudinal (LA) and $j = t$ for the transverse (TA) mode. The number 1 corresponds to the suspended material. $\bar{w}_{1j}$ is the integrated transmission probability (the sum over each possible angle of incidence) of phonons over the interface, k_B is Boltzmann constant, T is temperature, $\hbar$ the reduced Planck's constant and A_{uc} is the area of the unit cell of graphene.

By using eq. 5.8, an average phonon transmission probability $\bar{w}$ is plotted in Figs. 5.5**d**-**f** corresponding to the boundary conductances in Figs. 5.5**a**-**c**. The average phonon transmission probability is found to be $\bar{w} = 0.3 \pm 0.2$ %. Potential mechanisms that limit $\bar{w}$ are discussed below.

5.4.1. DISCUSSION ON THERMAL INTERFACE RESISTANCE

It is worth discussing whether the model proposed in eq. 5.8 can account for the considerable scatter in the value of τ observed in the measurements in Fig. 5.4. Equation 5.8 shows that potential causes are differences in the phonon velocity c_{1j} or in the transmission probability w_{1j}. Temperature variations only affect the flexural phonons and are therefore expected to give a too small contribution to account for the observed scatter. Device to device variations in the transmission probability w_{1j} due to boundary roughness [98] and kinks [99] in the graphene due to sidewall adhesion [11] might play a role. The thermal conductance over kinks can be modeled and will be discussed further below. In addition to geometrical mechanisms that can cause phonon velocity variations between devices, like wrinkling [29], contamination [100] and the presence of grain boundaries [101] are potentially of influence. Since these mechanisms might also affect the tension in the membranes, the correlation between τ and the resonance frequency is studied (see Appendix A1), however, no significant correlation is found. It is thus not possible to identify the microscopic mechanism that causes the scatter in τ directly from these measurements.

The tendency of the scatter in τ to increase with diameter is in accordance with eq. 5.8, since τ is linearly proportional to the radius a. A notable exception to this trend is the 7-micron drums, which show significantly lower spread. Possibly this is due to a selective mechanism, due to which large wrinkled drums are eliminated by collapsing on the cavity bottom [76]. In order to reduce the scatter in τ, further work on fabrication methods (e.g. transfer, growth) is needed to improve the uniformity of suspended CVD graphene drums. Once the scatter is reduced, variations in device geometry can be used to further investigate the scaling laws that govern thermal time constants in graphene.

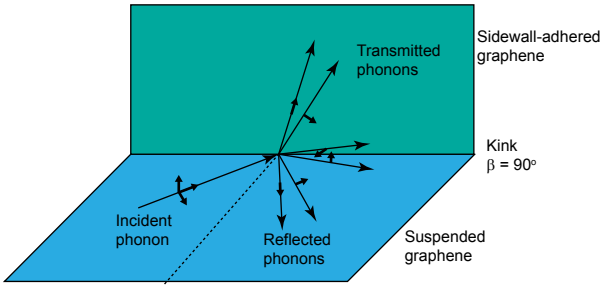

Figure 5.6: Phonon scattering on a kink in graphene.

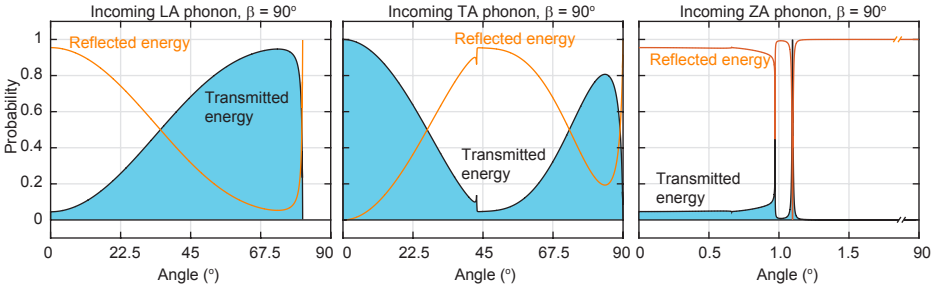

Figure 5.7: Transmission probability $w_{1j}(\theta)$ as function of incident angle for all three phonon modes.

This can also shed light on the role of interfacial thermal resistance and its relation to microscopic thermal mechanisms.

5.5. GEOMETRIC PHONON MISMATCH MODEL

In this section, we discuss a possible mechanism that might account for the experimental observations in this work. We examine the effect of sidewall adhesion on phonon transport in graphene. For this purpose, a mechanical model was developed that evaluates the phonon scattering on a sharp kink and calculates the transmission probabilities which can be substituted in eq. 5.8. We assume that due to the sidewall adhesion, a sharp kink is formed with an angle β of 90 degrees. Figure 5.6 shows all the possible modes in which an incident phonon can scatter: reflection as LA, TA or ZA phonon or transmission as LA, TA and ZA phonons. To find the transmission probability for each phonon mode requires solving of 6 equations simultaneously: 3 for the continuity of deflection and 3 for the continuity of stress as shown in the Appendix A5.

Figure 5.7 shows the angular dependent transmission probability $w_{1j}(\theta_0)$ for all the three phonon modes, assuming an initial tension of 0.03 N/m and Lame parameters $\lambda = 15.55$ J/m^2 and $\mu = 103.89$ J/m^2 [102]. We assume for simplicity that both the suspended and supported graphene have the same elastic parameters and tension, thus only observing the effects of the kink. LA phonons are mostly affected at small incident angles because they can only transmit into ZA phonons which are significantly mismatched in velocity. At larger incident angles, efficient transmission into TA phonons

becomes possible, raising the transmission probability. Incident TA phonons can fully transmit at shallow incident angles, indeed from the continuity of deflection the kink should not see any effect at $\theta_0 = 0$. Near $\theta_0 = 40°$ we observe a sharp feature, which corresponds to the critical angle where TA phonons can no longer be transmitted into LA phonons. The incoming ZA phonon shows a remarkably low transmission, due to the large velocity differences between in-plane and out-of-plane phonons ($c_{1l} = 17.0$ km/s, $c_{1t} = 11.6$ km/s and $c_{1z} = 0.2$ km/s for the elastic parameters used in this section). From continuity of deflection, flexural phonons can only transmit into in-plane phonons. The low velocity of the flexural phonons compared to the in-plane phonons causes total internal reflection at very small incident angles close to $\theta_0 = 1°$. Evaluating the integrated transmission probability (assuming the incoming phonon distribution is uniform) yields $\bar{w}_{1l} = 54.56\%$, $\bar{w}_{1t} = 48.15\%$ and $\bar{w}_{1z} = 0.073\%$.

We can use these transmission probabilities to find the thermal boundary conductance at the edge of the drum, which is derived in the Appendix A4:

$$G_B = \frac{3\zeta(3)k_B^3 T^2}{\pi\hbar^2 h_g}\left(\frac{\bar{w}_{1l}}{c_{1l}} + \frac{\bar{w}_{1t}}{c_{1t}} + \frac{\pi\hbar^2 \bar{w}_{1z} c_{1z}}{k_B^2 T^2 \zeta(3) A_{uc}}\right). \tag{5.9}$$

We find $G_B = 5.3$ GW/(m$^2\cdot$ K), which is orders of magnitude higher than what was found in the experiments. Mainly the large contribution from the LA and TA phonons to the heat transport makes it impossible for the continuum model to explain our results.

5.5.1. PHONON ENERGY EXHANGE

An explanation for the experimental results might be found if we do not consider the graphene membrane as a thermal material with a single specific heat and conductivity. Several works suggest the interaction between the in-plane phonons and out-of-plane phonons is very low and the mean free paths of the phonons are very long [31, 103–106], even at room temperature. Considering the very different phonon velocities in graphene and the large differences in the boundary transmission probability found for each phonon mode above, one will have to consider that each phonon mode gains energy at completely different timescales. In this subsection, we thus assume that the LA, TA, and ZA phonons are different thermal baths on the suspended graphene drum, which can each exchange energy through boundary scattering or with the heat sink to the environment.

The energy per unit volume is denoted by U_j for each mode j. For each phonon mode, the rate of change of energy on the suspended graphene drum is equal to the sum of the fluxes of heat leaving the membrane:

$$V\frac{\mathrm{d}U_j}{\mathrm{d}t} = \sum_j Q_{ij\to qr}. \tag{5.10}$$

Where V is the total volume of the suspended drum and $Q_{ij\to qr}$ the heat flux of mode j on domain i to mode r on domain q. We assume that for all phonon modes, the flux of heat is limited by scattering at the boundary, thus ignoring the effects of anharmonic scattering on the suspended graphene membrane. At the boundary, phonons can reflect which either keeps the energy in the same mode or to one of the other modes. Another possibility is that the phonon transmits to the environment, which is the supported

graphene, but phonons also come from the environment onto the suspended graphene. Taking all these effects into account, we write the heat flux for each process as:

$$Q_{ij\to qr} = U_{ij} c_{ij} \bar{w}_{ij\to qr} \tag{5.11}$$

For the phonons coming from the environment (heat sink), it is more convenient to express the heat flux in terms of the environmental temperature T_{env}. We sum the contribution for each phonon mode on the suspended graphene j (see Appendix A4):

$$Q_{2\to 1j} = \frac{2}{a}\frac{\zeta(3)k_B^3 T_{\text{env}}^3}{\pi\hbar^2 h_g} \times \left(\frac{\bar{w}_{2l\to 1j}}{c_{2l}} + \frac{\bar{w}_{2t\to 1j}}{c_{2t}} + \frac{\pi\hbar^2 \bar{w}_{2z\to 1j} c_{1z}}{k_B^2 T_{\text{env}} \zeta(3) A_{uc}} \right) \tag{5.12}$$

Now we can sum all the contributions and write 3 equations for U_j using eq. 5.10:

$$\frac{\mathrm{d}\mathbf{U}}{\mathrm{d}t} = \mathbf{R}\cdot\mathbf{U} + \mathbf{T}\cdot\mathbf{U} + \mathbf{S} + \mathbf{q} \tag{5.13}$$

where $\mathbf{U}$ is a vector containing all the energies on the suspended drum:

$$\mathbf{U} = \begin{pmatrix} U_{1l} \\ U_{1t} \\ U_{1z} \end{pmatrix}, \tag{5.14}$$

and $\mathbf{R}$ is the boundary reflection matrix:

$$\mathbf{R} = -\frac{2}{a}\begin{pmatrix} \bar{w}_{1l\to 1t} c_{1l} + \bar{w}_{1l\to 1z} c_{1l} & -\bar{w}_{1t\to 1l} c_{1t} & -\bar{w}_{1z\to 1l} c_{1z} \\ -\bar{w}_{1l\to 1t} c_{1l} & \bar{w}_{1t\to 1l} c_{1t} + \bar{w}_{1t\to 1z} c_{1t} & -\bar{w}_{1z\to 1t} c_{1z} \\ -\bar{w}_{1l\to 1z} c_{1l} & -\bar{w}_{1t\to 1z} c_{1t} & \bar{w}_{1z\to 1l} c_{1z} + \bar{w}_{1z\to 1t} c_{1z} \end{pmatrix}, \tag{5.15}$$

$\mathbf{T}$ is the boundary transmission matrix:

$$\mathbf{T} = -\frac{2}{a}\begin{pmatrix} \bar{w}_{1l\to 2l2t2z} c_{1l} & 0 & 0 \\ 0 & \bar{w}_{1t\to 2l2t2z} c_{1t} & 0 \\ 0 & 0 & \bar{w}_{1z\to 2l2t2z} c_{1z} \end{pmatrix}, \tag{5.16}$$

$\mathbf{S}$ is the heat sink:

$$\mathbf{S} = \frac{2}{a}\frac{\zeta(3)k_B^3 T_{\text{env}}^3}{\pi\hbar^2 h_g}\begin{pmatrix} \frac{\bar{w}_{2l\to 1l}}{c_{2l}} + \frac{\bar{w}_{2t\to 1l}}{c_{2t}} + \frac{\pi\hbar^2 \bar{w}_{2z\to 1l} c_{1z}}{k_B^2 T_{\text{env}} \zeta(3) A_{uc}} \\ \frac{\bar{w}_{2l\to 1t}}{c_{2l}} + \frac{\bar{w}_{2t\to 1t}}{c_{2t}} + \frac{\pi\hbar^2 \bar{w}_{2z\to 1t} c_{1z}}{k_B^2 T_{\text{env}} \zeta(3) A_{uc}} \\ \frac{\bar{w}_{2l\to 1z}}{c_{2l}} + \frac{\bar{w}_{2t\to 1z}}{c_{2t}} + \frac{\pi\hbar^2 \bar{w}_{2z\to 1z} c_{1z}}{k_B^2 T_{\text{env}} \zeta(3) A_{uc}} \end{pmatrix}, \tag{5.17}$$

and $\mathbf{q}$ is the heat flux on the membrane:

$$\mathbf{q} = \begin{pmatrix} q_{1l} \\ q_{1t} \\ q_{1z} \end{pmatrix} \tag{5.18}$$

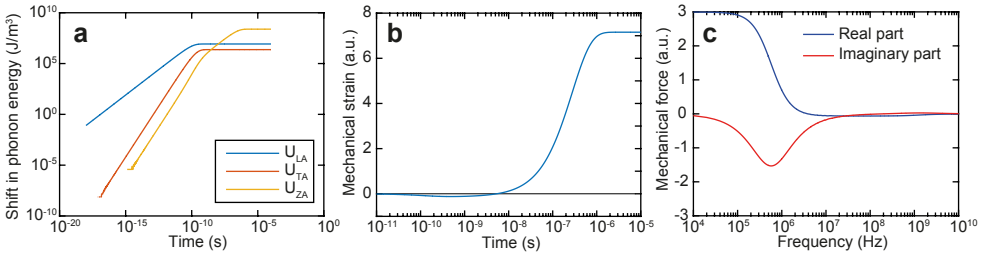

Figure 5.8: **a** Change in phonon energies **U** as function of time in response to a step in $q_{1l} = 1 \times 10^{11}$ W/m^3 at $t = 0$. **b** Mechanical strain as function of time in response to a step in q_{1l}. **c** Mechanical force as function of frequency for a forcing function $q_{1l} = Ae^{i\omega t}$.

We can calculate all the transmission probabilities using the model in Appendix A5, assuming $\beta = 90$ degrees. With known transmission probabilities and phonons velocities, 5.13 is first solved with $\mathbf{q} = 0$ and $T_{\text{eff}} = 293.15$K to find the initial conditions for **U**. Since the primary source of the heat flux from the laser is the generation of longitudinal phonons due to Normal electron-phonon scattering at a time scale less than 1 ps [107–109], we assume a heat flux of $q_{1l} = 1 \times 10^{11}$ W/m^3 at $t \geq 0$, $q_{1l} = 0$ at $t < 0$ and $q_{1t} = q_{1z} = 0$ at all times. Figure 5.8**a** shows the change in phonon energies as function of time. Note, that the flexural phonons have a two orders of magnitude longer thermalization time.

Next, we use the following expression to estimate the time-dependent strain in the membrane [103]:

$$\frac{\mathrm{d}\epsilon}{\mathrm{d}T} = -\frac{1}{4V_0 B}\left(\frac{\mathrm{d}U_l}{\mathrm{d}T}\gamma_l + \frac{\mathrm{d}U_t}{\mathrm{d}T}\gamma_t + \frac{\mathrm{d}U_z}{\mathrm{d}T}\gamma_z\right). \tag{5.19}$$

Since we are only interested in the time-dependence of the strain, we approximate the mechanical response as:

$$\Delta\epsilon \propto -\Delta U_l\gamma_l - \Delta U_t\gamma_t - \Delta U_z\gamma_z \tag{5.20}$$

we take the Grunheisen parameters $\gamma_l \approx 1.4$, $\gamma_t \approx 0.6$ and $\gamma_z \approx -3$. Figure 5.8**b** shows the time-dependent strain due to the step in the heat flux. Note that first, the strain is negative (compressive strain) and later becomes positive (tensile strain). The positive strain is in agreement with the negative thermal expansion coefficient of graphene and is due to the large negative Grunheisen parameter of the ZA phonons.

To compare this model to the experiment, we calculate the delay function h_w from the impulse response. This is calculated by differentiating the step response in Fig. 5.8**b** and calculating the Fourier transform. Figure 5.8**c** shows the real and imaginary part of the mechanical strain, which is proportional to the actuation force of a mechanical resonator. The frequency dependence closely resembles the experimentally obtained amplitude in experiments on single-layer graphene. Note, that the model predicts that the thermal expansion coefficient becomes positive at high frequencies. This is because at these high frequencies flexural phonons don't have time to thermalize and no longer play a role in expanding the lattice, the in-plane phonons with a positive Grunheisen parameter thus dominate the thermal expansion.

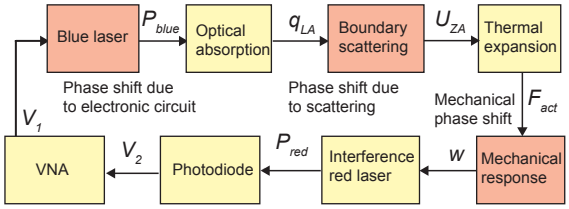

Figure 5.9: Dominant processes that lead to the measured mechanical response below the resonance frequency according to the geometric phonon mismatch model.

5.5.2. DISCUSSION ON GEOMETRIC PHONON MISMATCH

The geometric phonon mismatch model thus proposes that the measurements of the thermal time constant in this chapter can be attributed to the flexural phonons, which thermalize at a much slower rate due to boundary effects. We thus propose that the diagram in Fig. 5.1 has to be adapted. Figure 5.9 shows the dominant processes that lead to the thermomechanical response at the frequencies below the resonance frequency according to the geometric phonon mismatch model. The blue laser absorption leads to (virtually instantaneous) generation of LA phonons. Scattering at the boundary leads to a much slower generation of ZA phonons, which cause a large mechanical response. At higher frequencies the diagram in Fig. 5.9 becomes more complex, as the in-plane phonons start to dominate the response and lead to a positive thermal expansion coefficient. The transient heat flow of these in-plane phonons occurs at such fast time scales that it is obscured in these experiments since it is much faster than one period of the resonance. More advanced modeling is necessary to determine whether this scenario is realistic, the anharmonic scattering of phonons opens additional pathways for the phonon baths to exchange energy [20, 31] and these could affect the timescales of the phonon energy exchange. Singh *et al.* have shown that the conversion of LA/LO phonon into ZA phonons is also a bottleneck in the thermal system [108]. Thus, another explanation might be that the measured τ is due to this conversion process, more sophisticated modeling is necessary whether this scenario is consistent with the diameter dependence of τ in this work. From the experimental side, pump-probe measurements or time-resolved Raman spectroscopy could help to gain more insight into whether the thermal expansion is time-dependent. Especially a transition from negative to positive strain would be a strong indication that the flexural phonons exchange energy at much longer timescales than the in-plane phonons.

5.6. DISCUSSION

Besides the models proposed here, other scenarios also deserve further investigation. Polymer contamination is a serious candidate for the higher values of τ found in this work, in chapter 13 we find that the mass of the resonance is likely much higher than expected. Polymers typically have a specific heat c_p with is twice as high as graphene, but half the density and they have a very low thermal conductivity. The thermal conductivity of graphene itself is also reduced due to higher phonon scattering rates. The specific heat and thermal conductivity of the polymer can be added to the equation for

the transient heat transport. AFM characterization of the graphene shown in Appendix A6 finds a thickness of around 1.2 nm, this would increase the heat capacity by a factor of around 3.5 if it can be attributed to polymer contamination. From eq. 5.3, using a k = 600 W/(m·K) and ρc_p 3.5 times the theoretical value we find τ = 25 ns for a 5 micron diameter drum. This is closer to the experimental values, but it cannot account for the diameter dependence measured in this work. For example, a 2-micron diameter drum would have a 4 ns time constant, the experimentally observed τ is more than 5 times higher. This estimation and the observed diameter dependence makes polymer contamination an unlikely explanation for the experimental observations.

Other researchers have not pointed towards a thermal conductance that is limited by boundary effects. The geometric phonon mismatch model can account for this fact since it predicts that only the flexural phonons are significantly affected by the boundary. However, to exclude that something in our graphene or substrate is affecting the conductance measurement we performed a Raman spectroscopy measurement in Appendix A6. We found a G-peak shift as function of 488 nm wavelength incident laser power of -0.63 cm^{-1}/mW for a 2 micron diameter drum, Balandin *et al.* measured -1.29 cm^{-1}/mW on a 3 micron long bridge with the same oxide substrate thickness and trench depth [16]. Considering the fact that our sample is smaller, a somewhat smaller shift in phonon frequency is expected. We can thus conclude that our system is, in principle, representative of the other suspended graphene membranes published in the literature. We did not attempt to convert the measured phonon frequencies to temperature and extract the thermal conductivity for several reasons. First, the Raman measurement was performed in air, while the thermomechanical method was performed in a high vacuum making any measured conductance not representative of the thermal properties of graphene [19]. Second, calibration of the absorbed laser power and measuring the spot size is rather cumbersome [18], while knowing the spot size exactly is important to extract the conductance of the system. Third, we currently cannot identify which of the models in this work should be applied in order to relate Raman measurements (which is a spot measurement) to the optomechanical measurement of τ (which is sensitive to thermal expansion in the entire drum).

5.6.1. OFFSET IN THE REAL PART OF THE RESPONSE

We now discuss the offset that is observed in the real part in Fig. 5.3**c**. When the imaginary part is fitted using eq. 5.2, a difference remains between the real part that is measured and the one predicted by this fit, which is observed in all of the 201 resonators studied in this chapter. Previously this was attributed to optical crosstalk of the blue laser, which should always be in phase, resulting in a positive difference between the model and measurement as shown in Fig.5.3**c**. However, if the phase of the motion at low frequencies is reversed, the offset also changes in sign as shown in Fig. 5.10**a**. Examining the response of all the drums in this study, there is no exception to this observation as shown in Fig. 5.10**b**. Optical cross-talk is excluded as a possible cause of this effect, since this should always be in phase with the modulation and thus result in a positive difference between the measured and modeled real part.

The offset thus originates from the motion of the membrane, which implies that a

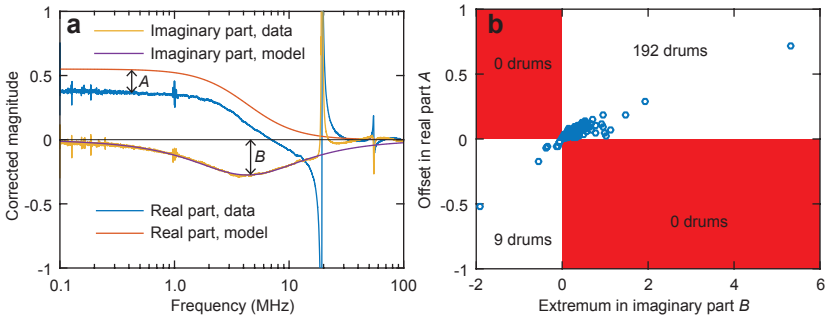

Figure 5.10: Offset of the real part of the response. **a** Real and imaginary part of the amplitude of a resonator with a diameter of 4 μm. **b** Comparison between the extremum in the imaginary part and the offset in the real part, defined as the average difference in amplitude between model and measurement in the frequency range where the imaginary part was fitted.

second force is present that actuates the membrane. Adding this second force to eq. 5.2:

$$z_\omega e^{i\omega t} = C_1 \frac{e^{i\omega t}}{i\omega\tau_1 + 1} + C_2 \frac{e^{i\omega t}}{i\omega\tau_2 + 1}, \tag{5.21}$$

where C_1 and C_2 are constants and τ_1, τ_2 are thermal time constants. To explain the offset observed in this work, $\tau_2 \ll \tau_1$ and C_1 has the opposite sign of C_2, which results in a more-or-less constant offset in the real part at low frequencies. The second force opposes the one that causes the slow time constant τ_1, which is the one observed in this work.

The observation of this second force is in accordance with the model proposed in section 5.5.1. Flexural phonons result in negative thermal expansion from their negative Grunheisen parameter but heat up slowly due to boundary effects. The in-plane phonons heat up much faster, as they have a very low thermal resistance and result in a positive thermal expansion from their positive Grunheisen parameter. Using eq. 5.20 these effects are in superposition, both occurring at the same time and thus resulting in the two distinct forces as proposed in eq. 5.21. The observation of these two distinct forces makes the boundary resistance model proposed in section 5.4 unlikely, as only one force with a single time constant should be observed.

5.7. CONCLUSION

To summarize, a dynamic optomechanical method to measure transient heat transport in suspended graphene is demonstrated. The method does not require electrical contacts, which allows high-throughput characterization of arrays of devices. The method is used to characterize the thermal time τ of many graphene membranes. It is found that τ is a function of diameter and its value is much larger than expected based on existing models. Measurements on gold-coated and uncoated silicon dioxide samples show similar results, showing that τ cannot be attributed to the substrate. A potential cause for the large values of τ is the presence of an interfacial thermal resistance between the suspended and supported graphene. From the measurements we determine that a

thermal boundary conductance with values of 30 ± 20 MW/(m^2·K) can account for the measurements, corresponding to a low phonon transmission probability on the order of 0.3%. A model is proposed that no longer assumes a single value of the specific heat of graphene: the in-plane phonons and out-of-plane phonons should be regarded as separate heat baths due to the low phonon scattering rate. The kink due to sidewall adhesion at the edge of the graphene drum then poses a large thermal resistance for the flexural phonons and their relaxation time is possibly the one observed in the experiments.

APPENDIX

A1: CORRELATION BETWEEN THE RESONANCE FREQUENCY AND τ

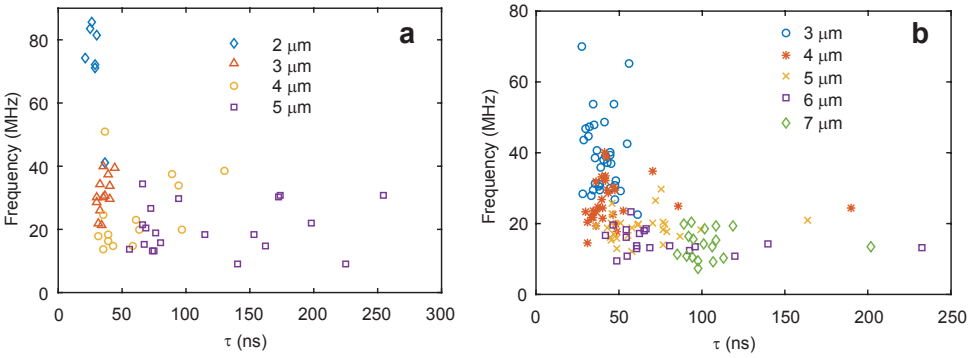

Figure 5.11: **a** Scatter plot between resonance frequency and τ for the uncoated sample. **b** Gold-coated sample (one data point with $\tau = 410$ ns, 6 micron diameter and $f = 13.6$ MHz not shown here).

Figure 5.11 shows scatter plots between the resonance frequency and characteristic thermal time τ extracted from the measurements. Since both the resonance frequency and characteristic thermal time are correlated to diameter, correlations between the two variables should only be determined for the same diameter. We found low correlations close to zero with outliers at -0.24 for the 6-micron diameter drums on gold and 0.14 for the 5-micron diameter drums on gold. The low correlations and the low agreement between different diameters suggest that transient thermal transport is not strongly related to the strain present in the graphene resonators.

A2: CALIBRATION PROCEDURE

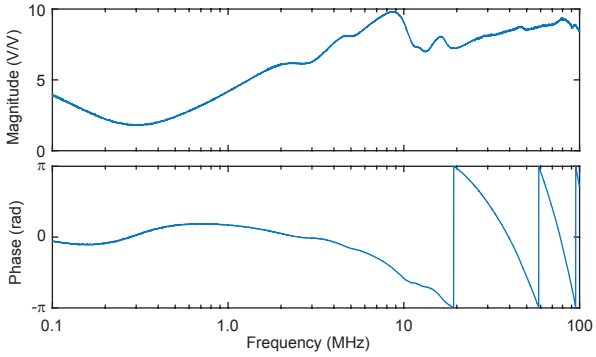

Figure 5.12: Magnitude and phase of the photo-diode signal obtained when the blue laser is directly aimed at the photo-diode.

In order to correct the intrinsic phase shifts in our measurement setup, we directly point the blue laser to the photodiode to obtain an calibration curve for our system (Fig.

5.12). This can be corrected by deconvolution of the measured response with this calibration curve, which is done by expressing the blue laser modulation parameters as a frequency-dependent phasor ε_ω. Since the calibration was taken at discrete frequencies, a cubic interpolation was used to make sure the frequencies match the ones from the measurement that needs to be corrected. Now one can deconvolve the measured frequency response function f_ω using:

$$|f_{\omega,\text{corr}}| = \frac{|f_\omega|}{|\varepsilon_\omega|}, \tag{5.22}$$

$$\angle f_{\omega,\text{corr}} = \angle f_\omega - \angle \varepsilon_\omega, \tag{5.23}$$

where $f_{\omega,\text{corr}}$ is the corrected frequency response function of our measurement.

A3: FINITE ELEMENT SIMULATIONS OF GRAPHENE ON A SILICON DIOXIDE SUBSTRATE

In order to examine the impact of the silicon dioxide substrate on the heat transport, we use COMSOL Multiphysics to model the graphene on top of the cavity and estimate the delay function $h(t)$. A simulation result of $h(t)/P_{\text{laser}}$, where P_{laser} is the incident laser power (assuming 2.3% absorption of optical power), can be seen in Fig. 5.13. This simulation predicts that the heat transport is more complex than expected. A very fast increase in temperature is observed with a time constant that is in the order of 0.5 ns. This is followed by a much slower exponential increase in temperature, which can be fitted with a single exponential to obtain a time constant of 32.6 ns. The fast time constant should not be observed in our measurement, since the cut-off frequency $2\pi\omega_{c,\text{fast}} = 1/\tau_{\text{fast}} \approx 320$ MHz is much larger than the bandwidth in our measurements. The slow time constant can be observed in our measurement since the cut-off is in a measurable frequency range and lower than the resonance frequency. This could be the thermal relaxation time found in the measurements.

Figure 5.14 shows $h(t)$ for different material parameters. From Fig. 5.14**a** we conclude that changes in the thermal conductivity or specific heat of the graphene membrane affect the fast time constant τ_{fast}, the slow time constant τ_{slow} remains unchanged. We conclude that the observed time constant τ in our measurements does not depend on the properties of graphene itself. For the thermal contact resistance between the graphene and silicon dioxide interface shown in Fig. 5.14**b**, we draw the same conclusion.

Figure 5.14**c** shows a different situation; if the thermal properties of the silicon dioxide layer are changed, the fast time constant remains unchanged. However, the slow time constant changes a lot, from 32 ns to 66 ns if the thermal conductivity is changed from 1.4 W/m/K to 0.7 W/m/K. Therefore, we conclude that the slow time constant in the simulation depends only on the properties of the substrate. Due to the poor thermal properties of this layer, it takes much longer to reach thermal equilibrium than expected if only the graphene itself is considered. Figure 5.14**d** shows the diameter dependence on $h(t)$, again the slow time constant is hardly affected, therefore this model does not account for the diameter dependence in our measurement. Since the slow time constant modeled here only depends on the properties of the substrate, it should significantly

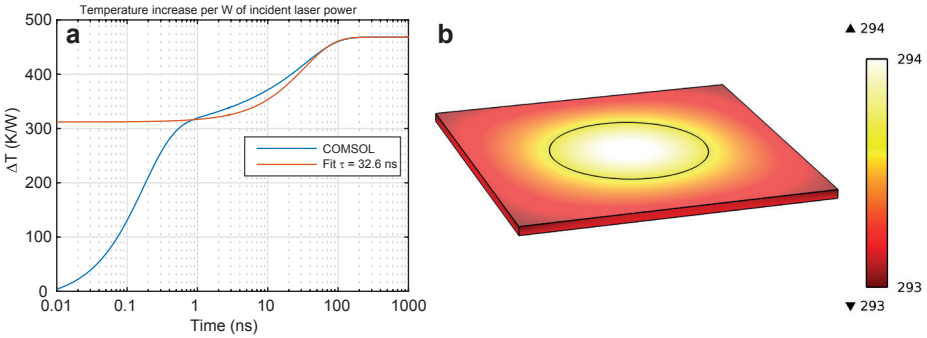

Figure 5.13: **a** Average temperature of the graphene membrane as function of time obtained by COMSOL, simulating a graphene membrane (ρ = 2100 kg/m^3, C = 700 J/kg/K, k = 2500 W/m/K and thickness 0.335 nm) on top of silicon dioxide (ρ = 2200 kg/m^3, C = 730 J/kg/K, k = 1.4 W/m/K and thickness 300 nm) with a thermal conductance $h_T = 8.33 \times 10^7$ W/m^2/K between the graphene and the oxide. **b** Simulated oxide layer and drum with diameter in thermal equilibrium and 1 mW of laser power. The simulation suggests significant temperature increase outside the drum.

change value when the silicon dioxide is replaced with gold. Since the values simulated here are not diameter dependent, this model shows that the experimental observations cannot be explained by the thermal properties of the substrate.

Figure 5.15 shows a simulation with identical parameters as in Fig. 5.13 with the addition of a limited thermal boundary conductance G_B = 40 MW/(m$^2\cdot$ K). The interfacial thermal resistance dominates the heat transport in this situation as illustrated by the uniform temperature in the drum. The materials outside the drum do not raise in temperature significantly. This validates the simple model in the main part of this work, where only the boundary conductance is considered.

A4: INTERFACIAL THERMAL RESISTANCE IN 2D MATERIALS

The interfacial thermal resistance R_B can be determined by using the heat flux:

$$R_B = \frac{A\Delta T}{Q}, \tag{5.24}$$

where A is the cross-sectional area of the boundary, ΔT the temperature difference and Q the heat flux. The first step in determining the interfacial resistance is thus to determine the heat flux that crosses the interface. The heat flux that crosses from interface 1 to interface 2 can be expressed by [92, 113]:

$$Q_{1\to 2} = U v \bar{w}, \tag{5.25}$$

where U is the total energy per unit volume of the heat carriers, v the velocity at which they propagate and $\bar{w}$ the probability that the heat carriers transmit over the interface. In the calculation of thermal interfacial resistance, the difficulty lies in calculating the transmission probability $\bar{w}$, while the calculation of energy and propagation velocity is quite straightforward.

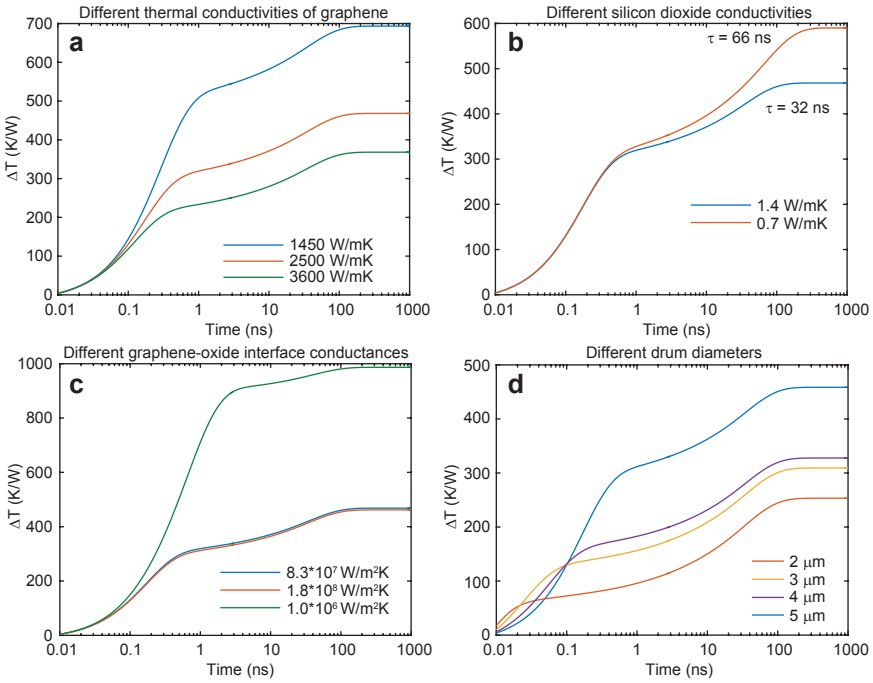

Figure 5.14: **a** $h(t)$ for different thermal conductivities of graphene. It can be seen that τ_{fast} shows some variation, but the slow thermal time constant does not change significantly. The fits of τ_{slow} are between 31.9 ns and 32.7 ns. **b** $h(t)$ for different thermal conductivities of the silicon dioxide layer. τ_{slow} is highly affected by this value: changing the value from 1.4 W/m/K to 0.7 W/m/K doubles τ_{slow} to 66 ns. **c** $h(t)$ for different thermal contact resistances. First two values are within ranges typically observed in literature [110]. τ_{slow} is again hardly affected, with values between 31.6 ns and 31.9 ns. The last value is an extreme example that is much lower than found in the literature. [18, 110–112] **d** $h(t)$ for different drum diameters, here only the fast time constant shows large variations, but the slow time constant is not significantly affected.

Our approach is thus, to calculate the energy and velocity and use that to estimate the value of $\bar{w}$ from the measurement. In order to do this, it is assumed that the heat in graphene is carried by phonons and that all the heat is carrier by three acoustic phonon polarizations, the longitudinal (LA), transverse (TA) and flexural (ZA). The LA and TA branch are far below the Debye temperature of 2100 K due to their large velocities, but the ZA branch will be fully thermalized since its Debye temperature is at 50 K [114]. The contribution to the heat flux of each polarization can be added to obtain:

$$Q_{1\to 2} = \sum_j U_j v_j \bar{w}_j, \tag{5.26}$$

and the total heat flux becomes:

$$Q_{1\to 2} - Q_{2\to 1} = \sum_j U_{1j} v_{1j} \bar{w}_{1j} - \sum_j U_{2j} v_{2j} \bar{w}_{2j}, \tag{5.27}$$

the index ij now describes the material ($i = 1$ for suspended, $i = 2$ for supported graphene) and phonon mode j.

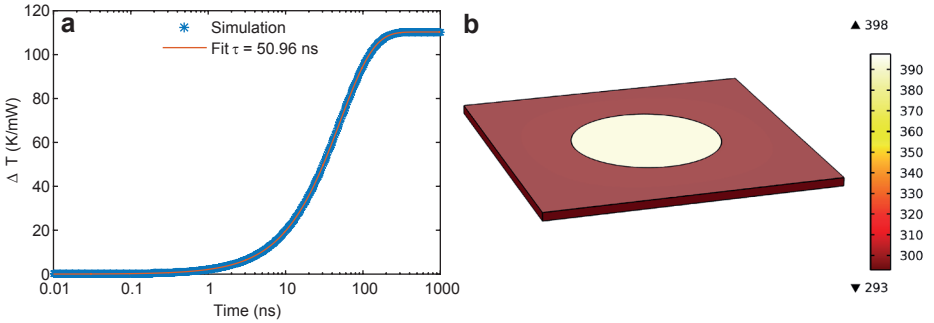

Figure 5.15: Simulation with a boundary conductance G_B = 40 MW/(m^2· K) between suspended and supported graphene. **a** $h(t)$ showing a single exponential function. **b** Temperature profile of the drums, showing that the temperature is uniform and the materials outside the drum do not change temperature significantly.

To calculate the energy U_{ij}, we start from the Bose-Einstein distribution to find the average phonon number $\langle n(\omega)\rangle$ at a fixed frequency ω:

$$\langle n(\omega)\rangle = \frac{1}{e^{\hbar\omega/k_BT}-1}, \tag{5.28}$$

where $\hbar$ is the reduced Plack's constant, k_B the Boltzmann constant and T temperature. The energy carried by each phonon is $\hbar\omega$, therefore we can write the average energy $\langle E(\omega)\rangle$ that phonons have at this frequency:

$$\langle E(\omega)\rangle = \hbar\omega\langle n\rangle = \frac{\hbar\omega}{e^{\hbar\omega/k_BT}-1}. \tag{5.29}$$

The number of states (density of states $D(\omega)$) that is accessible to the system between the frequencies ω and $\omega + d\omega$ is defined by:

$$dN_{ij} = D_{ij}(\omega)d\omega \tag{5.30}$$

and this makes the total energy V_{ij} in the system:

$$V_{ij} = \int_0^\infty d\omega D_{ij}(\omega)\langle E(\omega)\rangle = \int_0^\infty d\omega D_{ij}(\omega)\frac{\hbar\omega}{e^{\hbar\omega/k_BT}-1}. \tag{5.31}$$

Next, one has to know for the density of states, how many modes are available in the momentum space. In a 2-dimensional crystal, if we know the size of the system A, the uncertainty in momentum is $(2\pi\hbar)^2/A$ and the number of modes available to the system becomes:

$$N = A\int\frac{d^2p}{(2\pi\hbar)^2} = A\int\frac{d^2k}{(2\pi)^2}, \tag{5.32}$$

where one can integrate over circles with circumference $2\pi k$ to obtain:

$$N = A\int\frac{kdk}{2\pi}. \tag{5.33}$$

Using $\mathrm{d}N = D(\omega)\mathrm{d}\omega$ we obtain for the total energy in the system:

$$\mathrm{d}V_{ij}(\omega)\mathrm{d}\omega = A\frac{k\mathrm{d}k}{2\pi}\frac{\hbar\omega}{\mathrm{e}^{\hbar\omega/k_BT}-1}, \tag{5.34}$$

which is divided by the total volume of the system to obtain for U_{ij}:

$$\mathrm{d}U_{ij}(\omega)\mathrm{d}\omega = \frac{k\mathrm{d}k}{2\pi h_g}\frac{\hbar\omega}{\mathrm{e}^{\hbar\omega/k_BT}-1}, \tag{5.35}$$

to perform the integration, it is necessary to use the dispersion relation that relates the frequency to the wavenumber. Since the flexural phonons have different properties than the transverse and longitudinal phonon, these will have to be analyzed separately in the sections below.

5

LONGITUDINAL AND TRANVERSE MODES

For the longitudinal and transverse acoustic phonons, we can write the linear dispersion relationship:

$$\omega = c_{ij}k, \tag{5.36}$$

where c_{ij} is the propagation velocity of the phonons, since $v = \frac{\mathrm{d}\omega}{\mathrm{d}k} = c_{ij}$. Substitution into eq. 5.35 gives:

$$\mathrm{d}U_{ij}(\omega)\mathrm{d}\omega = \frac{\hbar\omega^2\mathrm{d}\omega}{2\pi c_{ij}^2 h_g}\frac{1}{\mathrm{e}^{\hbar\omega/k_BT}-1}, \tag{5.37}$$

Using this, we can write for the heat flux over an interface of area A from material 1 to material 2:

$$Q_{1\to2,j} = AU_{1j}v_{1j}\bar{w}_{1j} = \int_0^{\omega_D}\frac{A\bar{w}_{1j}\hbar\omega^2\mathrm{d}\omega}{2\pi c_{1j}h_g}\frac{1}{\mathrm{e}^{\hbar\omega/k_BT}-1}. \tag{5.38}$$

To solve the frequency integral, we assume $k_BT \ll \hbar\omega_D$ and using a coordinate transform $x = \hbar\omega/k_BT$:

$$Q_{1\to2,j} = \int_0^{\infty}\frac{A\bar{w}_{1j}k_B^3T_1^3}{2\pi\hbar^2c_{1j}h_g}\frac{x^2\mathrm{d}x}{\mathrm{e}^x-1} \tag{5.39}$$

We assume that the transmission probability frequency-independent. This results in:

$$Q_{1\to2,j} = \frac{A\zeta(3)\bar{w}_{1j}k_B^3T_1^3}{\pi\hbar^2c_{1j}h_g} \tag{5.40}$$

and for the heat flux from material 2 to material 1:

$$Q_{2\to1,j} = AU_{2j}v_{2j}\bar{w}_{2j} = \frac{A\zeta(3)\bar{w}_{2j}k_B^3T_2^3}{\pi\hbar^2c_{2j}h_g}. \tag{5.41}$$

FLEXURAL MODE

When strain is present in a 2D lattice, the dispersion of the flexural phonons can be written as [115]:

$$\omega^2 = s_{iz}^2 k^4 + c_{iz}^2 k^2 \tag{5.42}$$

which has 4 solutions for k, however implying the conditions $s_{iz} > 0$, $c_{iz} > 0$, $k > 0$ and enforcing that k must be a real number, we only have one solution:

$$k = \frac{1}{\sqrt{2}} \sqrt{\frac{\sqrt{c_{iz}^4 + 4 s_{iz}^2 \omega^2}}{s_{iz}^2} - \frac{c_{iz}^2}{s_{iz}^2}}, \tag{5.43}$$

this can be substituted in eq. 5.35 to obtain:

$$\mathrm{d}U_{iz}(\omega)\mathrm{d}\omega = \frac{\hbar \omega^2 \mathrm{d}\omega}{2\pi h_g \sqrt{c_{iz}^4 + 4 s_{iz}^2 \omega^2}} \frac{1}{\mathrm{e}^{\hbar\omega/k_B T} - 1} \tag{5.44}$$

Note, that this equation converges either to the expression for linear dispersion if $c_{iz}^4 \gg 4 s_{iz} \omega^2$ or to the expression for quadratic dispersion if $c_{iz}^4 \ll 4 s_{iz}^2 \omega^2$. The propagation velocity becomes:

$$v = \frac{\mathrm{d}\omega}{\mathrm{d}k} = \frac{\mathrm{d}\sqrt{s_{iz}^2 k^4 + c_{iz}^2 k^2}}{\mathrm{d}k} = \frac{c_{iz}^2 k + 2 s_{iz}^2 k^3}{\sqrt{c_{iz}^2 k^2 + s_{iz}^2 k^4}} = \frac{c_{iz}^2 + 2 s_{iz}^2 k^2}{\sqrt{c_{iz}^2 + s_{iz}^2 k^2}} \tag{5.45}$$

substituting eq. 5.43 gives:

$$v_{iz} = \frac{\sqrt{2}\sqrt{c_{iz}^4 + 4 s_{iz}^2 \omega^2}}{\sqrt{c_{iz}^2 + \sqrt{c_{iz}^4 + 4 s_{iz}^2 \omega^2}}}, \tag{5.46}$$

which in the limit case of purely quadratic dispersion $c_{iz} = 0$ becomes $v_{iz} = 2\sqrt{\omega s_{iz}}$ and in the case of linear dispersion $s_{iz} = 0$ becomes $v_{iz} = c_{iz}$.

EFFECT OF STRAIN ON FLEXURAL PHONONS

The analysis can be simplified by assuming either high or low strains, which should follow from our experiments. It can be seen, that the condition:

$$\frac{2 k_B T s_{iz}}{\hbar} \gg c^2 \tag{5.47}$$

allows us to use descibe the heat transport of the ZA branch by a quadratic dispersion without strain, while the condition:

$$\frac{2 k_B T s_{iz}}{\hbar} \ll c^2 \tag{5.48}$$

allows one to use a linear dispersion for the ZA branch. From the resonance frequencies in our experiments, we can estimate the strain present in the drum resonators:

$$\epsilon = \frac{\rho h \omega^2 a^2}{Eh 2.4048^2}, \tag{5.49}$$

assuming $\rho h = 7.7 \times 10^{-7}$ kg/m^2 and $Eh = 340$ N/m, we find the lowest observed strain $\epsilon_{\text{low}} = 1.026 \times 10^{-5}$ and the highest observed strain $\epsilon_{\text{high}} = 1.71 \times 10^{-4}$. Expressions for coefficients s_{iz} and c_{iz} are given by Lifshitz [115]:

$$s_{iz} = \sqrt{\frac{\kappa}{\rho}} \tag{5.50}$$

where κ is the bending rigidity, which is $\kappa = 1 \times 10^{-19}$ J for single-layer graphene, and:

$$c_{iz} = \sqrt{2u\frac{\lambda+\mu}{\rho}} \tag{5.51}$$

where u is the dilatation and λ, μ are the Lame parameters. Now we can calculate the coefficients for the lowest strain:

$$\frac{4k_B^2 T^2 s_{iz}^2}{\hbar^2} = 2.6828 \times 10^5, \tag{5.52}$$

$$c_{iz}^4 = 1.3683 \times 10^8 \tag{5.53}$$

from which we conclude that for each drum measured in this work the condition in eq. 5.48 holds. Due to the low velocities the Debye temperature of the flexural phonons is much lower than the in-plane phonons. Therefore, we have to write the heat flux as:

$$Q_{1\to 2,z} = \int_0^{\omega_D} \frac{A\bar{w}_{1z}\hbar\omega^2 \mathrm{d}\omega}{2\pi c_{1z} h_g} \frac{1}{\mathrm{e}^{\hbar\omega/k_B T} - 1} = \int_0^{\theta/T} \frac{A\bar{w}_{1z} k_B^3 T^3 \mathrm{d}x}{2\pi c_{1z}\hbar^2 h_g} \frac{x^2}{\mathrm{e}^x - 1}, \tag{5.54}$$

where θ is the Debye temperature, since we are above the Debye temperature $e^x \approx 1 + x$:

$$Q_{1\to 2,z} = \int_0^{\theta/T} \frac{A\bar{w}_{1z} k_B^3 T^3 x \mathrm{d}x}{2\pi c_{1z}\hbar^2 h_g} = \frac{A\bar{w}_{1z} k_B^3 T}{4\pi c_{1z}\hbar^2 h_g}\theta^2, \tag{5.55}$$

the total number of states in the system is:

$$N = A_g \int_0^{\omega_D} \frac{\omega \mathrm{d}\omega}{2\pi c_{1z}^2} = A_g \frac{\omega_D^2}{4\pi c_{1z}^2} \tag{5.56}$$

the Debye temperature becomes:

$$\theta = \frac{\hbar\omega_D}{k_B} = \frac{\hbar}{k_B}\sqrt{\frac{4\pi c^2 N}{\pi a^2}}, \tag{5.57}$$

here $N/\pi a^2$ is the number of states per unit square, which is limited by the area of the unit cell $A_{uc} = 5 \times 10^{-20}$ m^2. The heat flux from the ZA mode now becomes:

$$Q_{1\to 2} = \frac{A\bar{w}_{1z} k_B T c_{1z}}{h_g A_{uc}} \tag{5.58}$$

and the total heat flux now becomes:

$$\begin{aligned} Q_{tot} &= \frac{\zeta(3) A k_B^3 T_1^3}{\pi\hbar^2 h_g}\left(\frac{\bar{w}_{1l}}{c_{1l}} + \frac{\bar{w}_{1t}}{c_{1t}}\right) + \frac{A\bar{w}_{1z} k_B T_1 c_{1z}}{h_g A_{uc}} \\ &\quad - \frac{\zeta(3) A k_B^3 T_2^3}{\pi\hbar^2 h_g}\left(\frac{\bar{w}_{2l}}{c_{2l}} + \frac{\bar{w}_{2t}}{c_{2t}}\right) - \frac{A\bar{w}_{2z} k_B T_2 c_{2z}}{h_g A_{uc}} \\ &= \frac{\zeta(3) A k_B^3 T_1^3}{\pi\hbar^2 h_g}\left(\frac{\bar{w}_{1l}}{c_{1l}} + \frac{\bar{w}_{1t}}{c_{1t}} + \frac{\pi\hbar^2 \bar{w}_{1z} c_{1z}}{k_B^2 T_1^2 \zeta(3) A_{uc}}\right) \\ &\quad - \frac{\zeta(3) A k_B^3 T_2^3}{\pi\hbar^2 h_g}\left(\frac{\bar{w}_{2l}}{c_{2l}} + \frac{\bar{w}_{2t}}{c_{2t}} + \frac{\pi\hbar^2 \bar{w}_{2z} c_{2z}}{k_B^2 T_2^2 \zeta(3) A_{uc}}\right) \end{aligned} \tag{5.59}$$

The condition $Q_{tot} = 0$ has to apply if $T_1 = T_2$, this implies that:

$$\frac{\bar{w}_{1l}}{c_{1l}} + \frac{\bar{w}_{1t}}{c_{1t}} + \frac{\pi\hbar^2 \bar{w}_{1z} c_{1z}}{k_B^2 T^2 \zeta(3) A_{uc}} = \frac{\bar{w}_{2l}}{c_{2l}} + \frac{\bar{w}_{2t}}{c_{2t}} + \frac{\pi\hbar^2 \bar{w}_{2z} c_{2z}}{k_B^2 T^2 \zeta(3) A_{uc}} \tag{5.60}$$

which makes the heat flux:

$$Q_{tot} = \frac{\zeta(3) A k_B^3 (T_1^3 - T_2^3)}{\pi\hbar^2 h_g}\left(\frac{\bar{w}_{1l}}{c_{1l}} + \frac{\bar{w}_{1t}}{c_{1t}} + \frac{\pi\hbar^2 \bar{w}_{1z} c_{1z}}{k_B^2 T_1^2 \zeta(3) A_{uc}}\right) \tag{5.61}$$

This can be linearized for small temperature differences ΔT to obtain:

$$Q_{tot} = \frac{3\zeta(3) A k_B^3 T^2 \Delta T}{\pi\hbar^2 h_g}\left(\frac{\bar{w}_{1l}}{c_{1l}} + \frac{\bar{w}_{1t}}{c_{1t}} + \frac{\pi\hbar^2 \bar{w}_{1z} c_{1z}}{k_B^2 T^2 \zeta(3) A_{uc}}\right) \tag{5.62}$$

and the boundary resistance is directly obtained from eq. 5.24:

$$R_B = \frac{\pi\hbar^2 h_g}{3\zeta(3) k_B^3 T^2}\left(\frac{\bar{w}_{1l}}{c_{1l}} + \frac{\bar{w}_{1t}}{c_{1t}} + \frac{\pi\hbar^2 \bar{w}_{1z} c_{1z}}{k_B^2 T^2 \zeta(3) A_{uc}}\right)^{-1} \tag{5.63}$$

SPECIFIC HEAT

We can also calculate the specific heat c_p by starting from equation 5.37:

$$\mathrm{d}U_{ij}(\omega)\mathrm{d}\omega = \frac{\hbar\omega^2 \mathrm{d}\omega}{2\pi c_{ij}^2 h_g} \frac{1}{\mathrm{e}^{\hbar\omega/k_B T} - 1}, \tag{5.64}$$

$$U_{1j} = \int_0^{\omega_D} \frac{\hbar\omega^2 \mathrm{d}\omega}{2\pi c_{ij}^2 h_g} \frac{1}{\mathrm{e}^{\hbar\omega/k_B T} - 1} = \int_0^{\infty} \frac{x^2 k_B^3 T^3 \mathrm{d}x}{2\pi c_{ij}^2 \hbar^2 h_g} \frac{1}{\mathrm{e}^{x} - 1} = \frac{\zeta(3) k_B^3 T^3}{\pi c_{ij}^2 \hbar^2 h_g}, \tag{5.65}$$

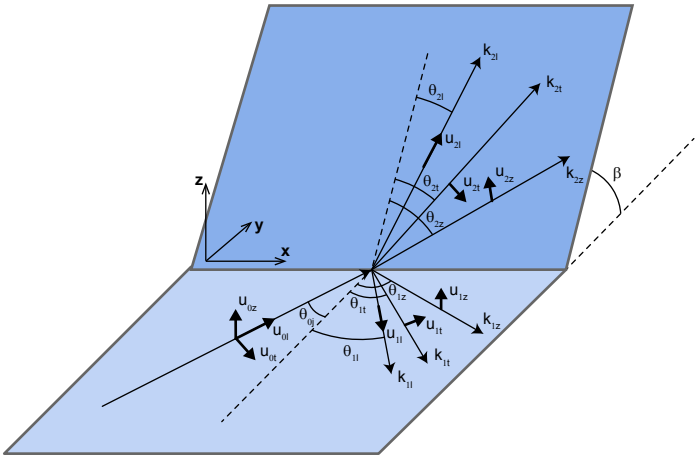

Figure 5.16: Phonon incident on the kinked boundary and the six possibilites for reflection or transmission.

which is valid for the LA and TA branches. For the ZA phonons we have to take the high temperature limit:

$$U_{1z} = \int_0^{\theta/T} \frac{x^2 k_B^3 T^3 \mathrm{d}x}{2\pi c_{ij}^2 \hbar^2 h_g} \frac{1}{\mathrm{e}^x - 1}, \tag{5.66}$$

using $\mathrm{e}^x \approx 1 + x$:

$$U_{1z} = \int_0^{\theta/T} \frac{x k_B^3 T^3 \mathrm{d}x}{2\pi c_{ij}^2 \hbar^2 h_g} = \frac{k_B^3 T}{4\pi c_{1z}^2 \hbar^2 h_g} \theta^2, \tag{5.67}$$

now by substituting:

$$\theta_{1z} = \frac{\hbar}{k_B} \sqrt{\frac{4\pi c_{1z}^2}{A_{uc}}}, \tag{5.68}$$

the energy density becomes:

$$U_{1z} = \frac{k_B T}{h_g A_{uc}} \tag{5.69}$$

$$U_1 = \sum_j U_{1j} = \frac{\zeta(3) k_B^3 T^3}{\pi \hbar^2 h_g} \left(\frac{1}{c_{1l}^2} + \frac{1}{c_{1t}^2} \right) + \frac{k_B T}{h_g A_{uc}}, \tag{5.70}$$

Now we find:

$$\rho c_p = \frac{\mathrm{d}U}{\mathrm{d}T} = \frac{3\zeta(3) k_B^3 T^2}{\pi \hbar^2 h_g} \left(\frac{1}{c_{1l}^2} + \frac{1}{c_{1t}^2} \right) + \frac{k_B}{h_g A_{uc}}, \tag{5.71}$$

$$c_p = \frac{3\zeta(3) k_B^3 T^2}{\pi \rho \hbar^2 h_g} \left(\frac{1}{c_{1l}^2} + \frac{1}{c_{1t}^2} + \frac{\pi \hbar^2}{3\zeta(3) A_{uc} k_B^2 T^2} \right) \tag{5.72}$$

A5: GEOMETRIC PHONON MISMATCH

Here we discuss the model to calculate the transmission coefficients w_{ij} over an interface in graphene formed by a geometrical deformation. Figure 5.16 shows the basic parameters of the model. We assume the graphene membrane has a kink with an angle β and a phonon with deflection u_{0i} is incident on the interface with an angle θ_0. If the phonon group velocity c_{ij} is known, we can find the angles of reflection and refraction with respect to the normal using Snell's law:

$$\sin\theta_{ij} = \frac{c_{ij}}{c_{0j}} \sin\theta_{0j} \tag{5.73}$$

CONTINUITY RELATIONS

We first enforce continuity of deflection in each direction on the interface, this yields:

- In **x** direction:

$$u_{0l}\sin\theta_{0l} + u_{0t}\cos\theta_{0t} + u_{1l}\sin\theta_{1l} + u_{1t}\cos\theta_{1t} - u_{2l}\sin\theta_{2l} - u_{2t}\cos\theta_{2t} = 0 \tag{5.74}$$

- In **y** direction:

$$\begin{aligned} &u_{0l}\cos\theta_{0l} - u_{0t}\sin\theta_{0t} - u_{1l}\cos\theta_{1l} + u_{1t}\sin\theta_{1t} \\ &-u_{2l}\cos\theta_{2l}\cos\beta + u_{2t}\sin\theta_{2t}\cos\beta + u_{2z}\sin\beta = 0 \end{aligned} \tag{5.75}$$

- In **z** direction:

$$u_{0z} + u_{1z} - u_{2l}\cos\theta_{2l}\sin\beta + u_{2t}\sin\theta_{2t}\sin\beta - u_{2z}\cos\beta = 0 \tag{5.76}$$

CONTINUITY OF STRESS

Continuity of stress implies that the sum of all stresses is equal on both sides of the interface: $\Sigma n_1 = \Sigma n_2$. For the flexural phonons, we assume that the disturbances in the tension are small and the out-of-plane deflections w only rotate the stress component out-of-plane. For the in-plane phonons, we only take into account the disturbance in the tension δn and ignore constant pre-tension n, since the velocity of these phonons are not altered by the tension, but governed by their Lame parameters μ_i and λ_i. The continuity of stress equations at the kinked boundary are:

- In **x** direction:

$$\Sigma\delta n_{1,xy} = \Sigma\delta n_{2,x'y'} \tag{5.77}$$

- In **y** direction:

$$\Sigma\delta n_{1,yy} = \bar{n}_{2,y'y'}\frac{\mathrm{d}w}{\mathrm{d}y'}\sin\beta + \Sigma\delta n_{2,y'y'}\cos\beta + \bar{n}_{2,x'y'}\frac{\mathrm{d}w}{\mathrm{d}x'}\sin\beta \tag{5.78}$$

- In **z** direction:

$$\bar{n}_{1,yy}\frac{\mathrm{d}w}{\mathrm{d}y} + \bar{n}_{1,xy}\frac{\mathrm{d}w}{\mathrm{d}x} = \Sigma\delta n_{2,y'y'}\sin\beta + \bar{n}_{2,y'y'}\frac{\mathrm{d}w}{\mathrm{d}y'}\cos\beta + \bar{n}_{2x'y'}\frac{\mathrm{d}w}{\mathrm{d}x'}\cos\beta \tag{5.79}$$

Writing down the stress components of each individual wave as function of their deflection, following the same procedure as Kolsky [116], we obtain 3 equations for the continuity of stress:

- In **x** direction:

$$2\mu_1 \frac{u_{0l}\omega \sin\theta_{0l}\cos\theta_{0l}}{c_{0l}} + \mu_1 \frac{u_{0t}\omega\cos 2\theta_{0t}}{c_{0t}} - 2\mu_1 \frac{u_{1l}\omega\cos\theta_{1l}\sin\theta_{1l}}{c_{1l}} - \mu_1 \frac{u_{1t}\omega\cos 2\theta_{1t}}{c_{1t}} - 2\mu_2 \frac{u_{2l}\omega\sin\theta_{2l}\cos\theta_{2l}}{c_{2l}} - \mu_2 \frac{u_{2t}\omega\cos 2\theta_{2t}}{c_{2t}} = 0 \tag{5.80}$$

- In **y** direction:

$$\begin{aligned} 2\mu_1 \frac{u_{0l}\omega\cos^2\theta_{0l}}{c_{0l}} + \lambda_1 \frac{u_{0l}\omega}{c_{0l}} - 2\mu_1 \frac{u_{0t}\omega\cos\theta_{0t}\sin\theta_{0t}}{c_{0t}} \\ +2\mu_1 \frac{u_{1l}\omega\cos^2\theta_{0l}}{c_{1l}} + \lambda_1 \frac{u_{1l}\omega}{c_{1l}} - 2\mu_1 \frac{u_{1t}\omega\cos\theta_{1t}\sin\theta_{1t}}{c_{1t}} \\ +\bar{n}_{2,y'y'} u_{2z} \frac{\omega\cos\theta_{2z}}{c_{2z}} \sin\beta - 2\mu_2 \frac{u_{2l}\omega\cos^2\theta_{2l}}{c_{2l}} \cos\beta - \lambda_2 \frac{u_{2l}\omega}{c_{2l}} \cos\beta \\ +2\mu_2 \frac{u_{2t}\omega\cos\theta_{2t}\sin\theta_{2t}}{c_{2t}} \cos\beta = 0 \end{aligned} \tag{5.81}$$

- In **z** direction:

$$\begin{aligned} u_{0z}\bar{n}_{1,yy} \frac{\omega\cos\theta_{0z}}{c_{0z}} - u_{1z}\bar{n}_{1,yy} \frac{\omega\cos\theta_{1z}}{c_{1z}} - 2\mu_2 \sin\beta \frac{u_{2l}\omega\cos^2\theta_{2l}}{c_{2l}} \\ -\lambda_2 \sin\beta \frac{u_{2l}\omega}{c_{2l}} + 2\mu_2 \sin\beta \frac{u_{2t}\omega\cos\theta_{2t}\sin\theta_{2t}}{c_{2t}} - u_{2z}\bar{n}_{2,y'y'} \frac{\omega\cos\theta_{2z}}{c_{2z}} \cos\beta = 0 \end{aligned} \tag{5.82}$$

Note that we have ignored the shear stress components in these equations for simplicity. We can solve the 6 equations for continuity of deflection and stress simultaneously for each incident mode, assuming $u_0 j = 1$. From these amplitudes of the transmitted and reflected waves, we can calculate the energy flux of each wave S_{ij} leaving the boundary:

$$\frac{S_{ij}}{S_{0j}} = \frac{c_{ij}|u_{ij}|^2 \mathrm{Re}(\cos\theta_{ij})}{c_{ij}\cos\theta_{0j}} \tag{5.83}$$

the transmission probability w_{1j} for each incoming mode j can now be evaluated as:

$$w_{1j} = \frac{S_{2l}}{S_{0j}} + \frac{S_{2t}}{S_{0j}} + \frac{S_{2l}}{S_{0j}}. \tag{5.84}$$

With the transmission coefficients known, we can evaluate the thermal boundary resistance in Eq. 5.63.

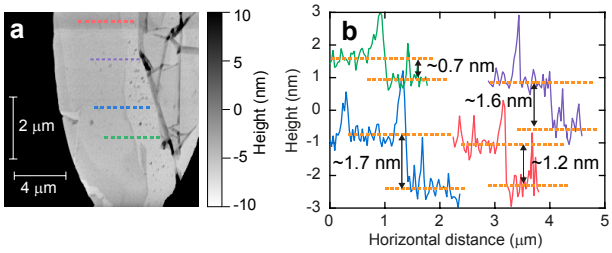

Figure 5.17: **a** Tapping mode AFM scan of a very large collapsed drum on the bottom of the cavity. **b** Step heights of the single layer graphene, the average thickness is 1.3 nm.

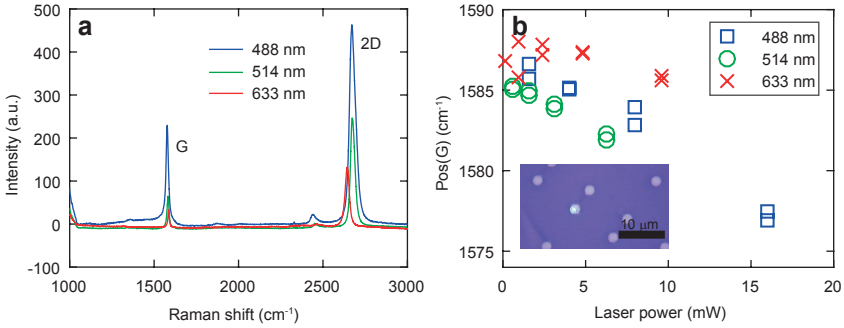

Figure 5.18: **a** Raman spectrum of graphene taken at the highest incident power of each available wavelength. **b** Position of the G peak as a function of incident laser power. The inset shows an optical image of the laser spot on top of the 2-micron diameter drum.

A6: GRAPHENE CHARACTERIZATION

Figure 5.17**a** shows a tapping mode atomic force microscopy scan of the graphene collapsed on the bottom of a large cavity. Several lines were taken along the flake to measure its thickness, as shown in Fig. 5.17**b**. These result in an average thickness of 1.3 nm. We further characterize the graphene using Raman spectroscopy as shown in Fig. 5.18. We use three different wavelengths which show spectra consistent with single layer graphene. Figure 5.18**a** shows the spectra at the highest available laser power. We find a very low intensity of the D-peak at all wavelengths. The G-peak shift as function of 488 nm wavelength incident laser power was found to be -0.63 cm^{-1}/mW, consistent with other experimental observations (Fig. 5.18**b**).

6

TRANSIENT THERMAL CHARACTERIZATION OF SUSPENDED MONOLAYER MoS_2

We measure the thermal time constants of suspended single layer molybdenum disulfide drums by their thermomechanical response to a high-frequency modulated laser. From this measurement the thermal diffusivity of single layer MoS_2 is found to be 1.14×10^{-5} m^2/s on average. Using a model for the thermal time constants and a model assuming continuum heat transport, we extract thermal conductivities at room temperature between 10 to 40 W/(m·K). Significant device-to-device variation in the thermal diffusivity is observed. Based on statistical analysis we conclude that these variations in thermal diffusivity are caused by microscopic defects that have a large impact on phonon scattering but do not affect the resonance frequency and damping of the membrane's lowest eigenmode. By combining the experimental thermal diffusivity with literature values of the thermal conductivity, a method is presented to determine the specific heat of suspended 2D materials, which is estimated to be 255 ± 104 J/(kg·K) for single layer MoS_2.

Parts of this chapter are published as a preprint on Arxiv (arXiv:1806.10769) [61].

THE distinct electronic [117–119] and mechanical [68, 120] properties of atomically thin molybdenum disulfide opens up possibilities for novel nanoscale electronic [121] and opto-electronic [122–124] devices. The large and tunable Seebeck coefficient of single-layer MoS_2 makes this material interesting for on-chip thermopower generation and thermal waste energy harvesting [125]. Since the power efficiency of these devices depends on the thermal conductivity, it is of interest to study the transport of heat in single-layer MoS_2. Several theoretical works have found values of the thermal conductivity k of single layer MoS_2 ranging between $k = 1.35$ up to 83 W/(m·K) [126–130]. By exploiting the temperature-dependent phonon frequency shifts in Raman spectroscopy [131], several experimental works have measured the thermal conductivity of single-layer MoS_2. Experimental values of $k = 34.5$ and 84 W/(m·K) of exfoliated single layer MoS_2 have been reported [132, 133], while single-layer MoS_2 grown by chemical vapor deposition was found to show a significantly lower thermal conductivity of 13.3 W/(m·K) [134].

Here, we thermally characterize suspended single-layer MoS_2 drum resonators by measuring their thermal time constants. This was achieved by measuring the frequency-dependent vibration amplitude in response to sinusoidally varying heat flux delivered by a modulated diode laser, similar to the characterization of single-layer graphene in chapter 5 [60]. Since these are frequency-based measurements, the result is to first order independent of the absorbed laser power, which greatly facilitates calibration compared to Raman spectroscopy based methods. With respect to prior studies of thermal transport in single-layer MoS_2 [132–134] the current work determines the thermal conductivity of this 2D material using a different method, which helps to resolve the large controversy between the previously obtained values of this parameter. In addition, the study obtains the transient thermal time constant of the material, which is closely related to the phonon dynamics and thermalization, but can also provide information on thermomechanical dissipation mechanisms in 2D materials [135]. Furthermore, the method allows one to study relations between the mechanical and thermal properties of the material. From measurements of the thermal time constant τ, we find the thermal diffusivity of MoS_2 to be on average 1.05×10^{-5} m^2/s for 5 μm diameter drums and 1.29×10^{-5} m^2/s for 8 μm drums. Assuming a specific heat value of 373 J/(kg·K), this corresponds to $k = 19.8$ W/(m·K) and $k = 24.7$ W/(m·K).

6.1. EXPERIMENTAL SETUP

We use a substrate with many circular cavities to perform the experiment, similar to the ones used for the graphene devices in chapter 3. The fabrication starts with a silicon chip with 285 nm of silicon dioxide. Circular cavities of approximately 300 nm deep and with a diameter of 8 and 5 microns are etched in the oxide layer. Many single layer MoS_2 flakes grown by chemical vapor deposition are transferred over the substrate by a dry transfer method using PMMA as a transfer polymer [136–138] to create suspended drum resonators. After transfer, the sample was annealed in vacuum with argon gas at a temperature of 340 °C for 6 hours to reduce polymer contamination. An optical image of several devices is shown in Fig. 6.1**b**. The Raman and photoluminescence (PL) spectra of the suspended MoS_2 flakes are shown in Figs. 6.1**c** and **d**, data was taken on suspended drums to prevent the effects of substrate doping [124, 139, 140]. These

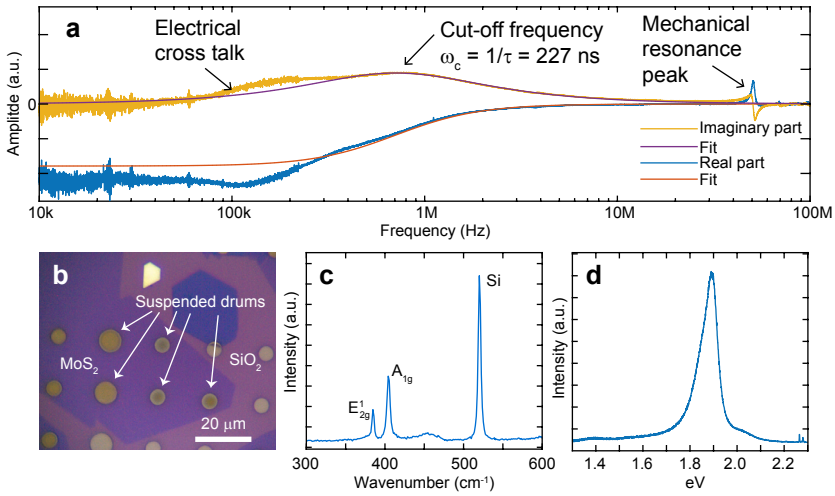

Figure 6.1: **a** Typical experimental result of the real (in-phase) and imaginary (out-of-phase part) of the amplitude of the mechanical response of the drum. The imaginary part of the amplitude was fitted to Eq. 5.2 to find the thermal time constant. At lower frequencies, a feature due to electrical crosstalk becomes visible due to the low optical gain during the experiment (see Appendix A2). At higher frequencies, the fundamental resonance is clearly visible. **b** Optical image of the device showing a single-layer MoS_2 sheet on top of the substrate and several suspended drums. **c** Raman spectrum of the suspended MoS_2. **d** Photoluminescence spectrum of the suspended MoS_2. The A^0 peak position is found at 1.89 eV.

6

measurements ensure that the MoS_2 flakes are single-layer, since no indirect transition is observed in the PL spectrum (Fig. 6.1**d**) [140]. In the Raman spectra (Fig. 6.1**c**) the E^1_{2g} peak is found at 384.9 cm^{-1} and the A_{1g} peak at 404.5 cm^{-1}, also in accordance with single-layer MoS_2 [141]. Furthermore, the positions of both the E^1_{2g} Raman peak and PL A^0 (1.89 eV) suggests that no large strains (> 1%) are induced by the transfer [138]. More details on the CVD growth and transfer can be found in ref. [137]. The samples are kept in an atmosphere with a maximum pressure of 1×10^{-6} mbar for two weeks before and during the experiment to ensure all gas has escaped from the cavity.

The setup to actuate the motion of the membranes and read out their motion is shown in chapter 3. During the measurement of the parasitic phase shifts a blue laser power of 2.35 mW with a sinusoidal AC-power modulation of 1 mW was used, but during experimental characterization, a neutral density filter reduced the optical power (measured before the objective) of the blue laser to 0.10 mW to prevent damage to the sample. The red laser power to probe the mechanical motion was set at 0.17 mW. A beam expander with a pinhole after the red laser ensures a Gaussian beam with an estimated waist diameter of 671 nm for the red laser spot in the focal point of the objective. The blue laser diode is coupled to a single-mode fiber, also resulting in a Gaussian beam with a waist diameter of 569 nm. Both lasers were aligned to the center of the drums during the experiments.

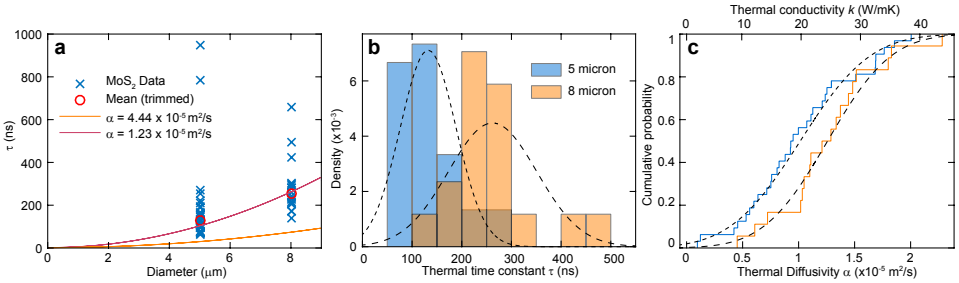

Figure 6.2: **a** Thermal time constants as function of diameter. Predictions using eq. 6.6 are plotted with several values of k obtained from literature: $k = 23.3$ W/(m· K) corresponding to $\alpha = 1.23 \times 10^{-5}$ m^2/s, [127] and 84 W/(m·K) to $\alpha = 4.44 \times 10^{-5}$ m^2/s. [133] **b** Density plot of the thermal time constant for both diameter, drums with extremely large values of τ and low resonance frequency were excluded. **c** CDF (cumulative density function) of the thermal conductivity k estimated from the values of τ using $c_p = 373.5$ J/(kg·K) and $\rho = 5060$ kg/m^3.

6.2. DATA ANALYSIS

Figure 6.1**a** shows the real and imaginary part of the experimentally obtained frequency response from a MoS_2 drum with a diameter of 8 μm. It follows from eq. 5.2 (chapter 5) that the imaginary part of the response function has a maximum amplitude at $\omega\tau = 1$. This maximum is indeed observed at a cut-off frequency of $\omega_c = 2\pi \times 800$ kHz in Fig. 6.1**d**, which is far below the membrane's lowest resonance frequency such that the relation $z_\omega = A\Delta T$ is valid. By fitting the imaginary part using eq. 5.2 the thermal time constant of the membrane is determined to be $\tau = 1/\omega_c = 227$ ns. The resonance peaks were analyzed by fitting a harmonic oscillator model to the data (chapter 2), from which the resonance frequency and quality factor are found. Although both the real and imaginary part of the response function fit well to eq. 5.2, deviations around 300 kHz are observed which are attributed to electrical cross-talk, most likely due to capacitive coupling to the optical table containing the experimental setup. Because the laser powers are low in these experiments to prevent damage to the drums, the total optical signal on the photodiode is very low, making the system very susceptible to parasitic crosstalk. In the Appendix A2, we show additional experiments on single-layer graphene that shows that at higher laser powers the feature disappears. The low-frequency data was excluded for the fit in order to prevent cross-talk from affecting the value of τ.

6.3. RESULTS

Frequency response fits as shown in Fig. 6.1**a** are obtained on a total of 32 single layer MoS_2 drums with a 5 micron diameter and 18 drums with a 8 μm diameter. Figure 6.2**a** shows the experimentally obtained values from all the drums as function of drum size and Fig. 6.2**b** shows a density plot for both diameters. Significant spread in the value of τ is found, even for drums of the same diameter. To exclude large effects of outliers, we only analyzed 80% of the samples with value τ closest to the mean and find $\bar{\tau} = 126$ ns for the 5 micron diameter drums and $\bar{\tau} = 253$ ns for the 8 micron drums.

Aubin derived an expression for the thermal time constant for a uniformly heated circular drum [142, 143]:

$$\tau = \frac{a^2 \rho c_p}{\mu^2 k}, \tag{6.1}$$

where a is the drum radius, ρ the density, c_p the specific heat at constant pressure and k the thermal conductivity of the material. For a uniformly heated drum, $\mu = 2.4048$ is the first root of the Bessel function $J_0(x)$ (chapter 2). However, in the experiments the membrane is heated by a focused laser spot in the center of the drum. We therefore use a numerical COMSOL model that adapts the value of μ by taking a point heat source in the center of the membrane (see Appendix A1). The measurement of the temperature is taken as the average temperature over the surface over the drum, since we expect the mechanical response to depend on the temperature field in the entire drum. From the simulations it was found that $\mu^2 = 5.0$ is an accurate representation of the experiments. This should predict the value of k with an error less than 10% as long as $15 < k < 100$ W/(m·K) and assuming that $c_p = 373.5$ J/(kg·K) (See Appendix A1). Using Eq. 6.6 we can estimate the thermal diffusivity of MoS_2 $\alpha = k/\rho c_p$:

$$\alpha = \frac{a^2}{5\tau}. \tag{6.2}$$

This expression was used to estimate the thermal diffusivity for each drum as shown in Fig. 6.2**c**. We find the diffusivity is slightly diameter-dependent with an average diffusivity $\bar{\alpha} = 1.05 \times 10^{-5}$ m^2/s for the 5 micron drums and $\bar{\alpha} = 1.29 \times 10^{-5}$ m^2/s for the 8 micron drums.

Based on known values of c_p and ρ of molybdenum disulfide at room temperature ($c_p = 373.5$ J/(kg·K) and $\rho = 5060$ kg/m^3) we can estimate $k = a^2 \rho c_p/(5\tau)$ from experimental values of τ. Fig. 6.2**c** shows the cumulative density function (CDF) calculated for each drum. We find a mean of k, $\bar{k} = 19.8$ W/(m· K) with a standard deviation of 9.3 W/(m· K) for the 5 micron drums and for the 8 μm drums we find $\bar{k} = 24.7$ W/(m·K) with standard deviation $\sigma_k = 8.4$ W/(m· K). We thus observe a considerable spread between devices. Moreover, most of the values of k found here are smaller compared to previous observations in literature that used exfoliated MoS_2 devices [132, 133], but are larger than CVD MoS_2 values [134].

6.3.1. COMPARISON TO THE RESONANT PROPERTIES

The transient mechanical characterization allows one to study whether the mechanical properties of the suspended drums are correlated to the thermal properties. This might be expected since the acoustic phonon velocities can be tension dependent, which would result in a correlation between the resonance frequency and the thermal diffusivity. Also, mechanical damping in MoS_2 due to defects could cause increased phonon scattering, which would lead to a lower thermal conductivity for drums with a low mechanical Q.

To study this, the resonance peaks were fitted by a harmonic oscillator model (chapter 2) to extract the resonance frequency and the quality factor. The distribution of all the resonance frequencies is shown in Fig. 6.3**a** and the quality factors are shown in Fig. 6.3**c**. We first investigate whether the thermal diffusivity is affected by strain in the resonator. The fundamental resonance frequency f of a circular drum resonator is given by

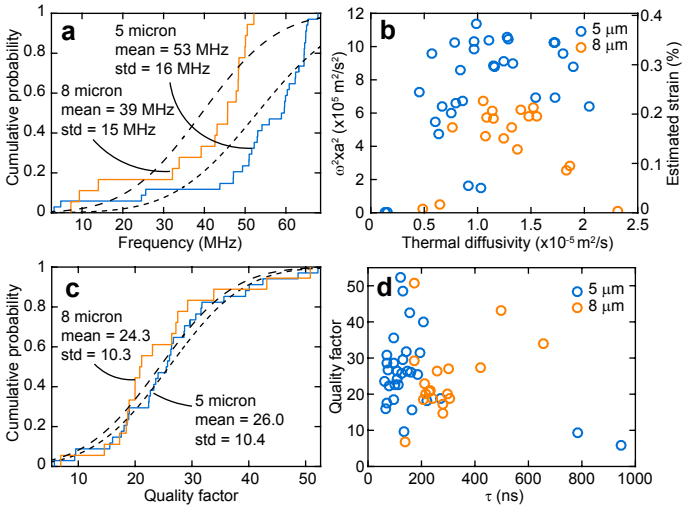

Figure 6.3: Investigation of correlations between the mechanical and thermal properties. **a** CDF of the resonance frequency for both diameters. **b** Scatter plot with the thermal diffusivity on the horizontal axis and frequency times radius squared (which is proportional to tension) on the vertical axis. **c** CDF of the quality factor for both diameters. **d** Scatter plot with the thermal time constant on the horizontal and quality factor of resonance on the vertical axis.

(chapter 2):

$$f = \frac{2.4048}{2\pi a}\sqrt{\frac{n_0}{\rho h}}, \tag{6.3}$$

where $h = 0.615$nm is the thickness of the drum and n_0 the tension in the membrane. From this, we deduce that $f^2a^2 \propto n_0$ if ρh is the same for each drum. Figure 6.3**b** shows a scatter plot of f^2a^2 versus the thermal diffusivity for each drum. The strain was estimated using the expression:

$$\epsilon \approx \frac{n_0}{E_{2D}} = \frac{4\pi^2 f^2 a^2 \rho h}{2.4048^2 E_{2D}}, \tag{6.4}$$

where we assume the membrane has the ideal mass and the 2D Young's modulus was taken as 160 N/m [137, 144]. No meaningful correlation between tension and the thermal diffusivity could be uncovered in Fig. 6.3**b**.

We further investigate whether the mechanical dissipation is related to the heat transport properties of these drums by examining the correlations to the quality factor. Figure 6.3**d** shows a scatter plot of the quality factor of resonance versus the thermal time constant. No significant correlation between the thermal time constant and the quality factor of resonance is found from the experimental data. The quality factor is nearly independent of diameter as shown in Fig. 6.3**c**, we find $\bar{Q} = 26.0$ with standard deviation 10.4 for the 5 μm drums and $\bar{Q} = 24.3$ with standard deviation $\sigma_Q = 10.3$ for the 8 μm drums.

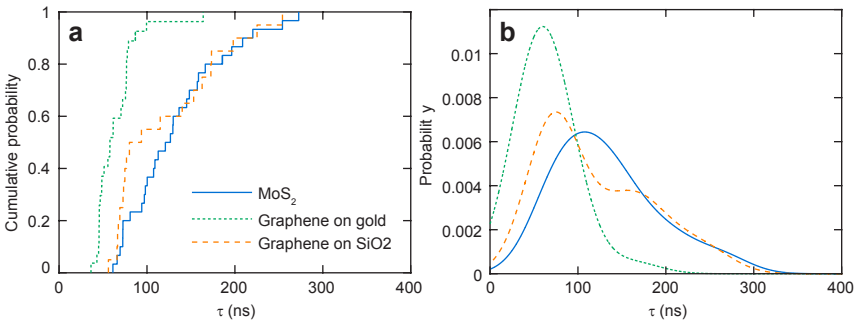

Figure 6.4: **a** Cumulative probabilities from the experimental values of the thermal time constant in this work and for the case of single-layer graphene for drums with a 5-micron diameter from chapter 5. **b** Empirical distribution functions found by fitting a Kernel distribution with a 30 ns bandwidth to the data.

6.3.2. PHONON RELAXATION TIME AND MEAN FREE PATH

The thermal conductivity can be expressed as $k \approx \rho c_p v \lambda$, [79] where v and λ are appropriately averaged phonon group velocity and mean free path, respectively. Substituting this expression in eq. 6.6 gives:

$$\tau = \frac{a^2}{5v\lambda} = \frac{a^2}{5v^2\tau_{ph}}, \tag{6.5}$$

where $\tau_{ph} = \lambda / v$ is the phonon relaxation time. We take the averaged velocity as $v \approx 300$ m/s based on calculations from several theoretical works [127, 145, 146] and use Eq. 6.5 to estimate τ_{ph} and λ. For the 5 micron drums we find an average phonon relaxation time and mean free path of 116 ps and 34.9 nm, respectively. For the 8 micron drums we find 143 ps and 43.2 nm. For both cases we again find device-to-device variations due to the spread in the measured values of τ.

6.4. DISCUSSION

6.4.1. COMPARISON TO SINGLE-LAYER GRAPHENE

In Fig. 6.4 we compare the experimentally obtained values of τ with experimentally obtained values of single-layer graphene (data from previous work in chapter 5) for drums with a 5 μm diameter. From the CDF in Fig. 6.4**a** it can be seen that both materials have a thermal time constant with the same order of magnitude. This is striking because even in the worst case scenario (CVD graphene with a lot of defects, $k \approx 600$ W/(m·K)) graphene should have a thermal diffusivity at least ten times higher than MoS_2. In this previous work on single-layer graphene we attributed the anomalous diameter-dependence of τ to boundary effects that were limiting the heat transport. Since we only measured two diameters in this work, we cannot use diameter dependence to draw conclusions. Nevertheless, the values of τ on MoS_2 are in good agreement with the theory of diffusive heat transport. This can be seen by comparing the measured values of τ to the theoretical predictions from literature as shown in Fig. 6.2**a**. Any effects of a thermal boundary resistance based on the measurements on MoS_2 are too small to be discerned. Molybdenum disulfide has a much lower thermal conductivity than graphene, which means

that the intrinsic thermal resistance is more important than thermal resistance at the boundary of the drum, if such a resistance is present at all in the case of MoS_2.

It is interesting to study the sign of the phase in Fig. 12.2**c**: at low frequencies, the response is out-of-phase with the optical drive. We found that all the drums in this work show an out-of-phase response at low frequencies, in the case of graphene in chapter 5, we also found such a preference [60] where only a handful of graphene drums show an opposite phase. The opto-thermal drive works by modulation of the tension in the membrane [147] and some initial out-of-plane deflection is necessary in order for this to result in out-of-plane motion (chapter 7). Whether this deflection is up or down, determines the phase of the low-frequency response. Both graphene and MoS_2 thus have a preferred initial deflection. However, to determine whether this is up or down requires further characterization of the optical properties of the cavity, that determines the sign of $\mathrm{d}I/\mathrm{d}x$, the derivative of diode intensity I with respect to membrane position x [57] (chapter 4).

6.4.2. RELATION BETWEEN MECHANICAL AND THERMAL PROPERTIES

We could not uncover any meaningful correlation between strain and the thermal diffusivity from the experimental data. The spread in the strain between the devices estimated from the resonance frequency is no more than 0.4%, which should result in a spread in the thermal conductivity of approximately 3% [148]. The measured device-to-device spread is significantly larger and strain-dependence is thus not the cause of the observed variations. It should be considered however that the value of f^2a^2 could actually show spread between devices due to variations in the mass due to contamination. Since contamination might affect the properties of 2D materials, atomic force microscopy measurements were performed to estimate the amount of residues as shown in the Appendix A3. We find a layer of contamination approximately 1 nm thick, indicating that the mass is underestimated and the variations in strain are actually larger than shown in Fig. 6.3**b**. Upon removing the contamination using contact-mode atomic force microscopy (AFM) [149], we find the thermal time constant increases significantly by approximately 20%. This systematic error is considerably lower that the device-to-device spread in the thermal diffusivity observed in this work which suggest that the effect of contamination on the measured values of τ is small.

6.4.3. DEVICE-TO-DEVICE SPREAD

The observed device-to-device variations in τ might be attributed to variations in microscopic (point defects) and macroscopic imperfections between devices, that could alter the phonon relaxation times between devices explaining our result in Fig. 6.2**c**. From calculations from the literature [145] using the Boltzmann transport equation for phonons, we would expect a mean free path of 316.5 nm for naturally occurring MoS_2. The significantly shorter mean free paths (~20 to 60 nm) found here might be related to our use of CVD MoS_2 rather than pristine exfoliated samples. Additional defects can increase the phonon scattering rate, lowering the phonon relaxation time and the mean free path. Also, the contamination on the samples found in the Appendix A3 might be of influence, as was found in the case of graphene [150]. However, we show in the Appendix A3 that removing the contamination did not significantly reduce the device-to-device spread,

which suggests that its effect on τ is small. Most of the drums show a higher value of k than previous observations on CVD-grown MoS_2 [134], which could be related to differences in quality of the sample. The value of the mean free path shows that $\lambda << a$, this supports our notion that heat transport can be described by continuum models in these devices.

6.4.4. SPECIFIC HEAT

Given the arguments above, the significant spread in τ is most likely related to the scattering mechanisms. However, we cannot fully exclude the possibility that the heat capacity of the drums is responsible for the spread in τ. Little is known about potential mechanisms that can affect the specific heat of single-layered two-dimensional materials due to the lack of experimental data. However, the specific heat is most likely not very different from the bulk material since the number of vibrational degrees of freedom is the same. Also, the weak temperature dependence of the value of c_p is expected since the experiments are performed above the Debye temperature, therefore most degrees of freedom in the lattice are thermalized.

What we can conclude is that some of the literature values of k are impossible to have occurred in our measurements, since they would violate the Petit-Dulong limit (c_p = 468.8 J/(kg·K)). The fastest 5-micron diameter drum has τ = 61 ns, which means that there is a limit on the thermal conductivity: $k \leq 48$ W/(m·K). For the fastest 8-micron diameter drum, τ = 138 ns and it is impossible that the thermal conductivity of this drum exceeded 55 W/(m·K). Therefore, the highest reported value of k = 84 W/(m·K), [133] cannot have occurred in the drums used in this study. Also, the reported value of k = 34.5 W/(m·K), [132] would implicate that the Petit-Dulong limit is violated in most of the devices.

The most representative study, since it uses both CVD MoS_2 and conducted the experiment in vacuum, is $k = 13.3 \pm 1.4$ W/(m·K) [134]. Using this value, we can use the experimentally obtained values of τ to estimate the specific heat of MoS_2. For the 5 micron drums, we find $c_p = 278 \pm 118$ J/(kg·K) and for the 8 micron drums we find $c_p = 215 \pm 73$ J/(kg·K). The errors represent the standard deviation due to the large device-to-device spread, nevertheless this analysis suggests that most of the devices have a specific heat that is significantly lower than the bulk value. Future work can combine the transient characterization with existing methods, such as Raman spectroscopy or electrical heaters, to extract the thermal resistance R. In that case, the heat capacity C can be derived and provide more accurate measurements on the specific heat of 2D materials. The transient characterization thus provides a means to perform calorimetry on suspended 2D materials.

6.5. CONCLUSION

We measured the thermal time constants of suspended monolayer molybdenum disulfide drums. In contrast to previous measurements on single-layer graphene, we find that the values of τ are in agreement with the classical Fourier theory of heat transport. From the values of τ we can estimate the thermal conductivity to be between 10 and 40 W/(m·K), which is lower than previous measurements on exfoliated MoS_2 but in agree-

ment with measurements on CVD-grown MoS_2. Significant device-to-device variation in thermal time constants is observed. This variation is not correlated to the resonance frequency or Q-factor of the membranes, which shows that mechanisms that determine the macroscopic damping are probably not responsible for the observed spread. We therefore conclude that the variations in thermal diffusivity are caused by microscopic defects that have a large impact on phonon scattering, but do not affect the resonance frequency and damping of the membrane's lowest eigenmode. The method can be used to estimate the specific heat of single layer MoS_2, with our results suggesting its value might be lower than the bulk value. Future work can combine this technique with existing thermal conductivity measurements to perform calorimetry on suspended 2D materials, enabling one to determine whether the specific heat of 2D materials is equal to its bulk value.

APPENDIX

A1: COMSOL MODEL

Here we show the COMSOL model used to derive the expression for τ used in the main section of this chapter. An analytic expression was derived for the thermal time constant τ in the case of a uniformly heated circular disk [142]:

$$\tau = \frac{a^2 \rho c_p}{\mu^2 k}, \tag{6.6}$$

where a is the drum radius, ρ the density, c_p the specific heat, k the thermal conductivity the material and $\mu = 2.4048$ is the first root of the Bessel function $J_0(x)$. Since the experiment uses a laser spot with a size that is much smaller than the drum diameter to heat the drum, equation 6.6 needs to be modified in order to accurately describe the time constant of the system. Our approach is to choose a fixed value of the specific heat $c_p = 373.5$ J/(kg·K) and vary both a and k to find a new value of μ that will enable us to accurately determine the value of k or the thermal diffusivity α from the experiment.

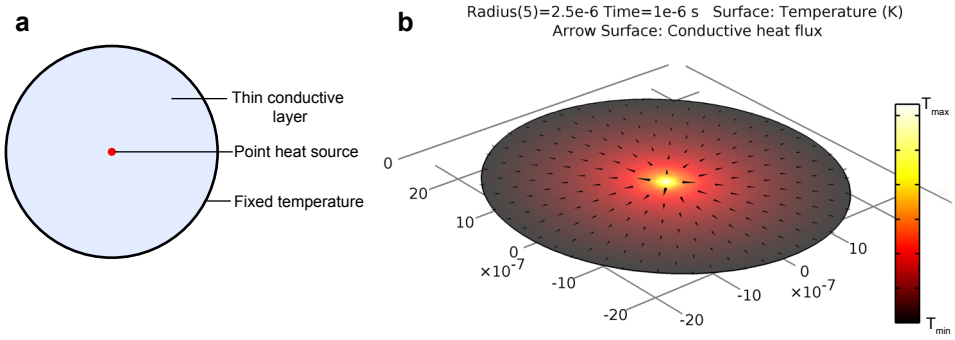

Figure 6.5: **a** Schematic drawing of the simulation. **b** Temperature profile at the end of the simulation for a 5 micron diameter drum.

Figure 6.5 shows the setup of the COMSOL simulation in order to find the thermal time constant τ. A simple circular domain was defined and the heat tranport is simulated using the "heat transport in thin shells" module. A point source in the center was used to simulate the heat flux and the boundaries of the domain were kept at a fixed temperature.

In order to find the time constant τ, a time-dependent simulation was performed that simulates the response to a step function in the heat source. The resulting time dependent temperature increase was calculated by taking the average over the entire domain. This results in the time-dependent traces shown in Fig. 6.6. For each trace, the time constant is found by fitting:

$$T(t) = T_0 + T_{\text{end}} \exp(-t/\tau). \tag{6.7}$$

The diameter-dependence is simulated using a range of values of k, we selected a suitable range by selecting values found in literature. It is found that for the range be-

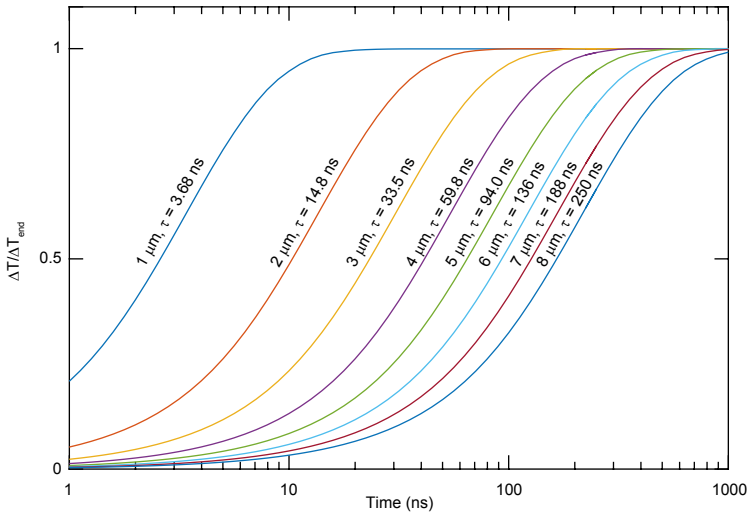

Figure 6.6: Simulated temperature as function of time, from which τ can be derived for different diameters. The temperature is calculated using the average value over the drum surface.

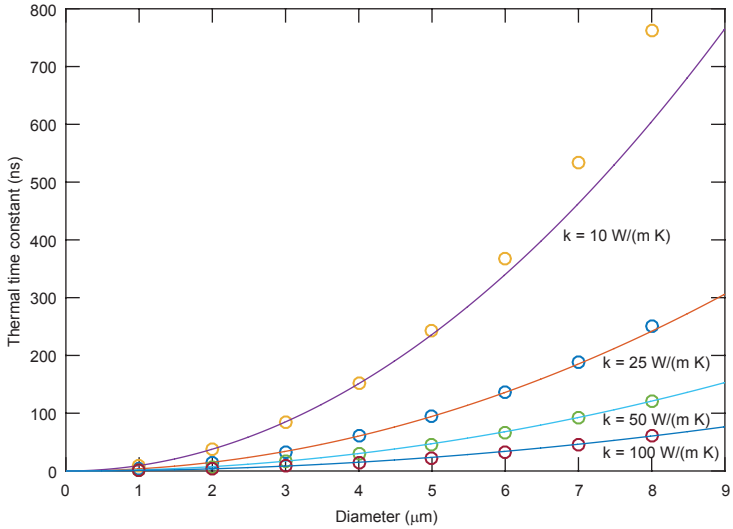

Figure 6.7: Diameter dependence of τ for different diameters and different values of k.

tween $10 < k < 100$ we find values of $\mu^2 \approx 5.0$. This model is shown as solid lines in Fig. 6.7. We find that $\mu^2 = 5.0$ yields good agreement at the higher values of k. Low values of k results in larger deviations at larger diameters, which can also be attributed to the a^2 dependence of τ. From this model, we find that the value of τ with $\mu^2 = 5.0$ should produce the correct value of k or α within 10% error as long as $15 < k < 100$ W/(m·K) and $2a \leq 8$ μm.

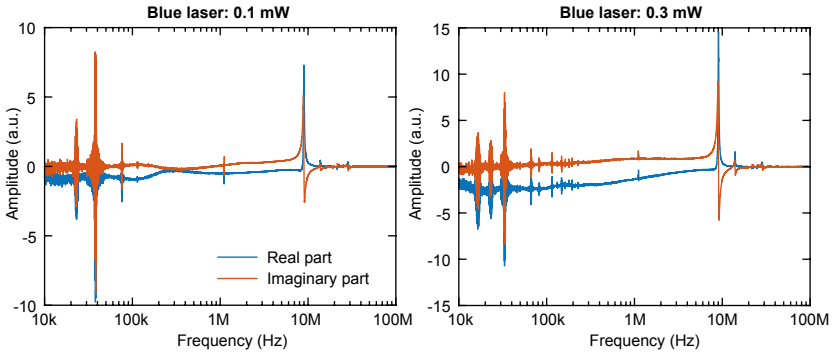

Figure 6.8: Additional measurements on single-layer graphene to identify electrical crosstalk. The left figure shows a measurement with exactly the same blue and red laser powers as the experiments with MoS_2. On the right, the neutral density filter behind the blue laser was changed to change the power to 0.3 mW. The electrical cross-talk feature between 100 kHz and 1 MHz diminishes due to the higher optical gain.

A2: ADDITIONAL DISCUSSION ON CROSSTALK

Here we discuss the identification of the electrical cross-talk in the experiments. In Fig. 6.8 we measure a single layer graphene resonator since these drums do not break at higher laser powers. The left figure shows the frequency response at the same DC laser powers and modulation current as used in the experiments with MoS_2. The electrical crosstalk is more prominently visible since the MoS_2 drums show a much stronger amplitude of the signal compared to graphene. Increasing the laser power by a factor of 3 by changing the neutral density filter after the blue laser, gives the frequency response to the right. This shows that the feature between 100 kHz and 1MHz almost fully disappears, from which we conclude that this feature cannot be attributed to the mechanical motion of the drum. Most likely capacitive coupling of the diode laser and photodetector components to the optical table is the cause of this crosstalk. We also found that this feature changes in frequency and amplitude if the mantles of the RF-cables are directly grounded to the table. Our measurement of the parasitic phase shifts in the system cannot correct for this effect, because it involves a parallel path to the optical path. Increasing the optical power would reduce this effect, but results in failure of the MoS_2 drums. However, the MoS_2 drums show a much larger signal compared to graphene at the same laser powers, meaning that the magnitude of electrical cross-talk is already less in these drums and the effect is easily accounted for by selecting proper frequency windows for fitting.

A3: AFM CHARACTERIZATION OF CONTAMINATION

In order to characterize contamination of the sample which can influence the experimental results, we use mechanical cleaning by contact mode AFM [149]. A 2 by 2 microns area was scanned with a velocity of 8 μm/s, after which the area was inspected by tapping mode AFM as shown in Fig. 6.9**a**. A square of contamination can be seen around the area that was scanned using contact mode AFM. Inside the square, we find a mean roughness $R_a = 0.73$nm and outside the square we find $R_a = 1.76$ nm. The reduction of roughness is

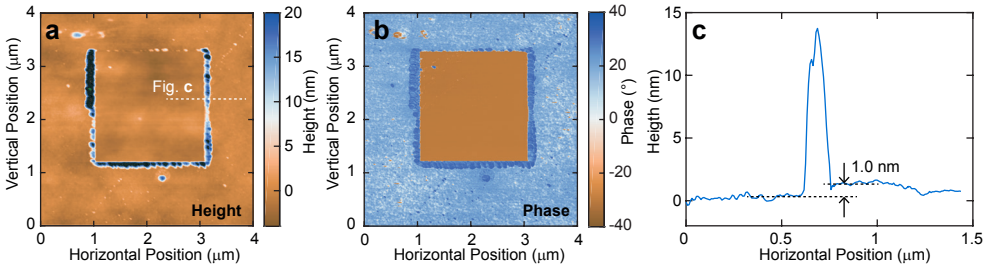

Figure 6.9: Characterization of contamination using mechanical cleaning in an atomic force microscope (AFM). **a** Height scan obtained by tapping mode AFM of the 2 by 2 microns area scanned by contact-mode AFM. The white dashed line indicates the trace taken to estimate the height of the contamination. **b** Phase channel of the tapping mode scan, this shows more clearly than the height channel that the scanned area has reduced roughness, indicating that the scanned area has indeed been cleaned. **c** Height profile to estimate the thickness of the contamination, we find the height difference between the cleaned part and the sample to be approximately 1 nm.

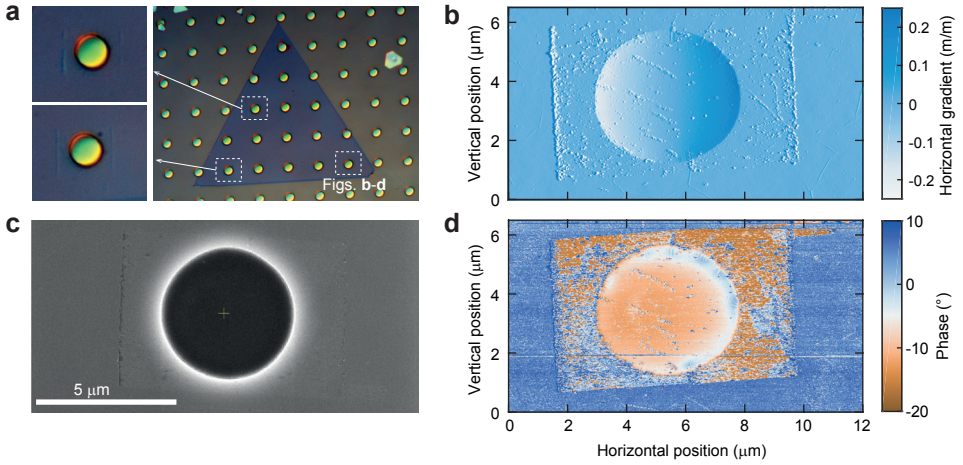

Figure 6.10: Characterization of the drums after mechanical cleaning using contact-mode AFM. **a** Optical image of the flake using differential interference contrast microscopy, showing contamination towards the sides of the scanning area. Image was obtained using the raw camera output and automatic enhancement of the contrast in Adobe Photoshop. **b** Gradient of the height channel in the horizontal direction obtained in tapping-mode AFM on drum 14 after cleaning. **c** Scanning electron microsope image of drum 14, the scanned area appears somewhat brighter and contamination on the borders of the contact mode scanning area is visible. **d** Phase channel of the tapping mode AFM. A significant difference in phase is detected in the area scanned by contact mode.

more visible in the phase channel shown in Fig. 6.9**b**. The reduction of roughness inside the square is an indication that we indeed cleaned the sample. Comparing the heights inside and outside the square in Fig. 6.9**c**, we find that the contaminants form a layer approximately 1 nm thick.

To order to study the effect of the contaminants on the transient heat transport of the drums, we attempted to clean 14 drums on the same single layer MoS_2 flake shown in

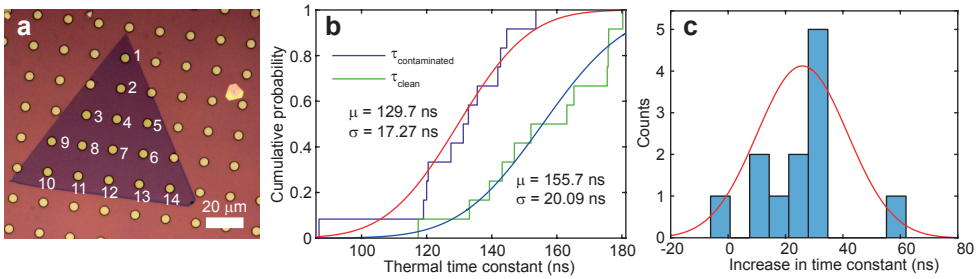

Figure 6.11: Thermal characterization before and after mechanical cleaning of suspended drums. **a** Optical image of the flake with the numbers corresponding to table 6.1. **b** Cumulative probability of the thermal time constant before and after mechanical cleaning. **c** Histogram of the increase in thermal time constant.

Fig. 6.11**a**. On the suspended drums, a soft cantilever was used for contact-mode AFM to prevent breaking of the suspended drums. After scanning, a stiffer cantilever was used to inspect the area with tapping-mode AFM. Figure 6.10**a** shows an optical image of the flake after mechanical cleaning, close to the drums the contamination at the borders of the scanning area is visible, but no significant change in optical contrast is observed. In scanning electron microscopy in Fig. 6.10**c** a slight change in contrast is observed, as the cleaned area is slightly brighter. Tapping mode AFM of the drums reveals that some contamination remains after the scan as shown in Figs. 6.10**b** and **d**. Although the scan settings are the same as the smaller test area in Fig. 6.9, more residue is visible in the phase channel. This could be due to the large height variations, because the drums are deflected downwards by approximately 200 nm due to air pressure in the environment. Nevertheless, a significant portion of the contamination should be removed as evidenced by the pileup of contamination at the sides (Figs. 6.10**a** and **b**), the contrast in the electron microscopy (Fig. 6.10**c**) and the phase channel in Fig. 6.10**d**.

Due to the low permeability of the drums there is no significant air leakage during the AFM scan, allowing us to immediately measure the thermal time constants after cleaning the sample while the cavity remains in vacuum. The thermal time constants before and after cleaning are shown in Table 6.1, the corresponding drum numbers are labeled in Fig. 6.11**a**. Taking the cumulative probability in Fig. 6.11**b**, we find a significant increase of the mean of the time constants by 26 ns on average (Fig. 6.11**c**). The device-to-device spread did not decrease significantly, as the standard deviations are similar. The contamination of the drums thus induces a systematic error of approximately 20% in single layer drums with a 5 micron diameter, this is however relatively small compared to the device-to-device spread observed in this work.

Table 6.1: Thermal time constants of the single layer MoS_2 drums in Fig. 6.11**a** before and after mechanical cleaning using contact mode AFM. (*Drum broken during AFM)

Drum	τ before cleaning (ns)	τ after cleaning (ns)	$\Delta\tau$ (ns)
1	108	-*	
2	120	133	13,2
3	154	152	-1,5
4	145	175	30,9
5	133	165	32,4
6	161	150*	
7	142	176	33,9
8	143	176	33,2
9	87	117	30,5
10	136	163	27,5
11	131	139	8,1
12	127	147	19,5
13	120	143	22,7
14	119	180	61,2

PART III: NONLINEAR DYNAMICS OF GRAPHENE MEMBRANES

7

MULTI-MODE PARAMETRIC RESONANCE IN GRAPHENE MEMBRANES

In the field of nanomechanics, parametric excitations are of interest since they can greatly enhance sensing capabilities and eliminate cross-talk. Above a certain threshold of the parametric pump, the mechanical resonator can be brought into parametric resonance. Here we demonstrate parametric resonance of suspended single-layer graphene membranes by an efficient opto-thermal drive that modulates the intrinsic spring constant. With a large amplitude of the optical drive, a record number of 14 mechanical modes can be brought into parametric resonance by modulating a single parameter: the pretension. A detailed analysis of the parametric resonance allows us to study nonlinear dissipation mechanisms, nonlinear dynamics and loss tangent of graphene resonators. It is found that a van der Pol term is indispensable to describe dissipation in graphene at high amplitudes.

Parts of this chapter have been published in Scientific Reports **8**, 9366 (2018) [60].

THE history of parametric oscillations dates back to the 19th century and the observation of surface waves in the famous singing wineglass experiment of Michael Faraday [151]. A mechanical system can be parametrically excited when its stiffness is modulated at a frequency of $2\omega_0/n$, where ω_0 is the system's resonance frequency and n an integer [152]. Above a certain modulation amplitude, the system becomes unstable and exhibits parametric resonance. The advent of micro and nano engineering brought to life new ideas for exploiting parametric excitation for enhancing force and mass sensitivity [152–157], effective quality factor [158], and signal to noise ratio [153] of tiny resonators. To date, many sensors, including gyroscopes [159–161], mass sensors [156, 157] and even mechanical memories [162–165] employ parametric excitation for improved performance.

Resonators employing two-dimensional materials such as graphene or molybdenum disulfide have attracted considerable interest in the scientific community [12, 64, 68, 69]. They are promising candidates for various sensing applications (chapters 9 to 14) [11, 33, 35, 58, 59, 166] due to their ultra-high surface to mass ratio, combined with their high strength [10]. The quality factor of resonance is relatively low in these resonators [49, 64, 68] compared to other nano-electromechanical systems, limiting their accuracy as a resonant sensing element. It is thus of interest to apply parametric amplification schemes to raise their effective quality factor and improve their performance. Several groups have successfully demonstrated such an amplification scheme by applying an electrostatic spring force to the membrane and modulating its strength [167, 168]. It is well known that above a certain critical force of this parametric pump, the device will become unstable and exhibit parametric resonance [47, 152, 169]. Although such behavior has been previously observed, we demonstrate that parametric resonance holds important information about the nonlinear damping of graphene that has been a subject of strong debate in the community [49–53]. In addition, we show that such resonance opens a new window for investigating new nonlinear dynamic phenomena in graphene membranes that have not been observed before and cannot be explained by classical continuum models.

In this work, it is demonstrated that opto-thermal tension modulated single-layer graphene is an ideal system to study parametric resonance. These resonators were fabricated from chemical vapor deposited graphene as shown in chapter 3. Despite the relatively low Q-factor of the graphene resonances (<1000), it is shown that a record number of 14 modes can be brought into parametric resonance [152, 163]. The origin of the effectivity of graphene for parametric resonance is the large tension modulation that can be achieved by opto-thermal means [58, 68], which is related to the large Young's modulus of graphene. Understanding parametric resonance is of fundamental interest, but also provides an interesting alternative to direct excitation in future applications, that could reduce noise and facilitate large amplitude driving in resonators and oscillators. The parametrically excited nonlinear mechanical response is analyzed and a model is proposed that can simulate both parametric and directly driven responses. This nonlinear Duffing response, caused by the direct drive, has previously been studied to obtain the stiffness properties of graphene devices [63, 170]. In this work, we focus the analysis on dissipation mechanisms in graphene. Period doubling bifurcations are almost fully governed by the linear dissipation terms, while the saddle-node bifurcation of the para-

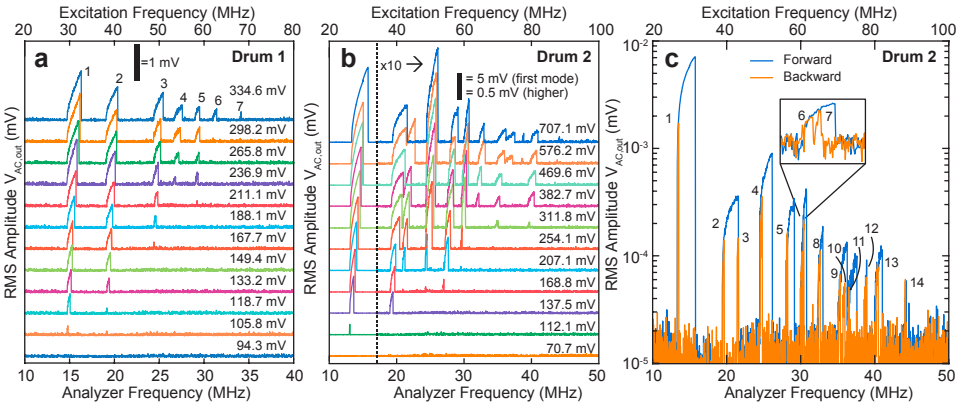

Figure 7.1: Multi-mode response of parametrically driven graphene resonators. **a** Waterfall plot of the multi-mode response at different driving amplitudes. Each mode appears at different driving levels due to variations in quality factor and effective driving force between them. The scale bar indicates the root mean square value (RMS) of $V_{\mathrm{ac,out}}$ and the labels on the right indicate the RMS driving amplitude $V_{\mathrm{ac,in}}$. **b** Waterfall plot for a different drum, showing more mechanical modes and modal interactions. **c** Forward and backward frequency sweep at the highest parametric driving amplitude for the drum in Fig. 7.1**b**, revealing 14 distinct mechanical modes in parametric resonance.

metric resonance is fully governed by nonlinear dissipation terms [47]. From this analysis, we can conclude that nonlinear damping in graphene can be accurately described by a dissipation term of the van der Pol type. Comparing this to the cubic stiffness term allows us to extract the mechanical loss tangent of graphene which is orders of magnitude larger than expected. Tracking the period doubling bifurcations shows that the region of instability is asymmetric. This unexpected deviation from the theoretical response suggests that unconventional dynamic phenomena govern the linewidth of graphene resonators.

7.1. MULTI-MODE NONLINEAR RESONANCE

In Fig. 7.1**a**, the blue laser is driven at $2f$, while detecting the photodiode signal at f. When increasing the blue laser driving voltage $V_{\mathrm{ac,in}}$ a remarkable effect is observed. One-by-one, the parametric resonances of graphene appear, up to 7 different modes. Each mode reaches resonance at a different threshold driving amplitude $V_{\mathrm{ac,in}}$, due to differences in quality factor and the frequency dependence of the parametric driving parameter δ [60]. The experiment is repeated on a different drum in Fig. 7.1**b**. Interestingly, in this case, an overlap between parametric resonances is observed at high driving levels. When the overlap occurs, a direct transition between the high-amplitude solution of two adjacent parametric resonances is observed, e.g. at $V_{\mathrm{ac,in}} = 382.7$ mV (RMS) between the second and third resonance. Interestingly, in some cases also transitions between the high-amplitude and low-amplitude solutions are observed, e.g. at $V_{\mathrm{ac,in}} = 489.6$ mV (RMS) between the same 2 modes. This pseudorandom process is attributed to a strong dependence of the basin of attractions of the parametric high-amplitude and low-amplitude solutions on the initial conditions [171]. Hence, the am-

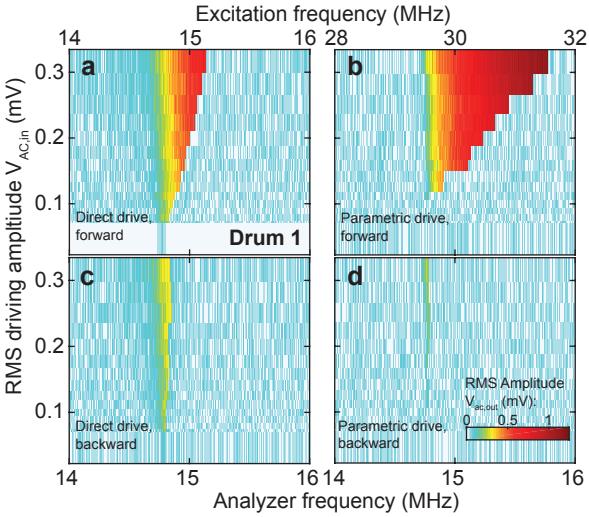

Figure 7.2: Frequency response of the fundamental mode to direct and parametric drive, for forward and backward frequency sweeps. **a**, Direct drive with the frequency swept forwards. **b** Parametric drive with the frequency swept forwards. Below a driving threshold near $V_{ac,in} \approx 0.11$ mV (RMS) no mechanical response is observed. **c**, Direct drive with the frequency swept backward. **d**, Parametric drive with the frequency swept backward.

7

plitude can fall into two stable solutions: either the high amplitude solution of the third mode or the zero amplitude solution of the third mode which is also observed at higher driving amplitudes ($V_{ac,in} = 576.2$ and 707.1 mV (RMS)).

Due to the overlap of parametric resonances in this drum, some resonances are skipped and not all resonances are found by sweeping from low to high frequency. Instead, when sweeping the frequency backward as shown in Fig. 7.1**c**, as many as 14 parametric resonances are observed in this system. To our knowledge, this is the largest number of parametrically excited modes in a single mechanical element, as previously only 7 modes could be excited in cryogenic environments [163].

For a more detailed analysis of the physics, we focus on the frequency response of the fundamental mode to both direct and parametric drives. Figure 7.2 shows direct and parametric resonance of the fundamental mode as a function of driving level, on a different drum than Fig. 7.1. The VNA is configured to detect the directly driven frequency response (Fig. 7.2**a**,**c**). Sweeping the frequency forward (Fig. 7.2**a**) and backward (Fig. 7.2**b**) results in a hysteresis, that grows as the driving level is increased. This is typical for the geometric nonlinearity of the Duffing-type resonator, where the stiffness becomes larger at high amplitudes. In order to detect the parametric resonance, the VNA was configured in a heterodyne scheme at which $V_{ac,out}$ is detected at half of the driving frequency $V_{ac,in}$. Similar to the directly driven case, a hysteresis occurs between the forward (Fig. 7.2**b**) and backward (Fig. 7.2**d**) sweeps in frequency. Below an RMS drive amplitude of 0.11 mV, no response is observed. To show that the parametric resonance shows two stable phases of resonance separated by 180 degrees [162], we performed an additional measurement which is shown in the Appendix A2.

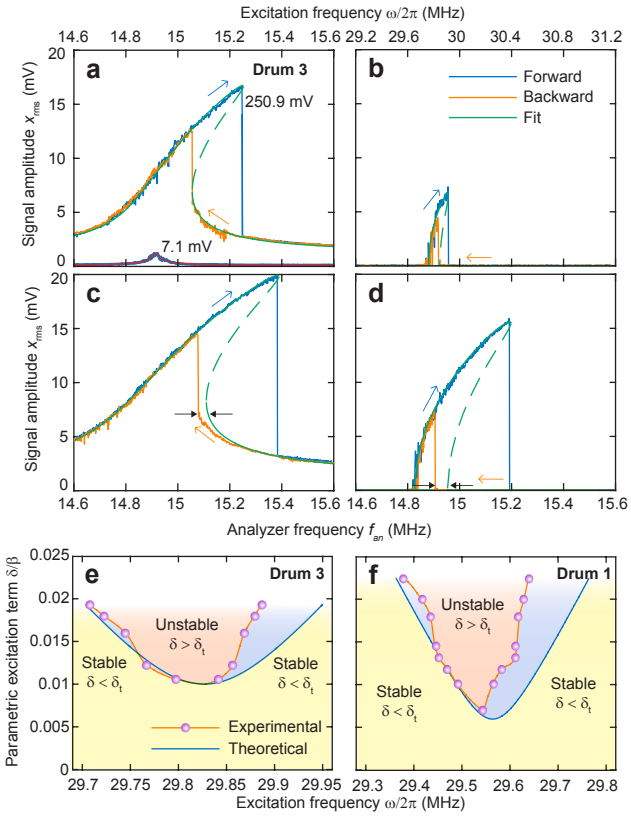

Figure 7.3: Comparison of experimental mechanical responses to theory. **a**, Directly driven response at 7.1 and 250.9 mV RMS driving voltage and the fit obtained from eq. 7.1. **b**, Parametric response and fit at 250.9 mV RMS driving voltage and the fit from eq. 7.1. **c**, Directly driven response at 446.2 mV RMS driving level, the fit from eq. 7.1 shows a disagreement with the backward sweep, highlighted by black arrows. **d**, Parametric response at 446.2 mV (RMS). Black arrows highlight the disagreement between eq. 7.1 and experiment. **e**, Parametric resonance instability map for the fundamental mode of drum 2, compared to the prediction from eq. 7.1. **f**, Parametric resonance instability map for the fundamental mode of drum 1 (Fig. 7.1).

Figure 7.3**a**-**d** shows both directly and parametrically driven responses at different driving levels. In order to eludicate the effect of nonlinearities on the observed mechanical responses, a single degree-of-freedom model is derived that describes the motion of the resonator (see Appendix A4) and this is fitted to the response curves in Fig. 7.3**a**-**d** (see Appendix A1, A5). The model is a combination of the Duffing, van der Pol and Matthieu-Hill equation also used in other works [47, 51, 172, 173]:

$$\ddot{x} + \mu\dot{x} + \nu x^2\dot{x} + (\beta + \delta\cos\omega t)x + \gamma x^3 = F\cos\omega t, \tag{7.1}$$

where x is the displacement (which is approximately proportional to $V_{\mathrm{ac,out}}$), μ is the damping coefficient, ν the nonlinear damping coefficient, β the linear stiffness coefficient, γ the nonlinear stiffness coefficient, $\delta\cos\omega t$ the parametric driving and $F\cos\omega t$ the direct driving term. By setting $\gamma = 0$ and $\nu = 0$ one can fit the response at low drive

level (Fig. 7.3**a**) and obtain an initial value for μ, β and F. Initially fitting at high driving levels was attempted by setting $\nu = 0$, however it is found that such a model cannot account for the observed parametric response: nonlinear damping is indispensable to describe the maximum amplitude. Next, γ, ν and F are used as fitting parameters to describe the nonlinear response (Fig. 7.3**a**-**d**). Numerical values for the fit parameters are provided in the Appendix A1.

Figure 7.3 compares the fitted model and the experimental data for the directly- and parametrically driven fundamental resonance. This shows excellent agreement at lower driving levels (Fig. 7.3**a**). We note that the fitting parameters μ, ν, β and γ are the same in the direct and parametric response within the error of the fitting procedure (see Appendix A1) and that both δ and F are very nearly proportional to driving voltage $V_{\mathrm{AC,in}}$. It is however observed that the region of instability (Figs. 7.3**e**, **f**) is narrower in our experiments than what is expected from eq. 7.1.

7.2. REGION OF INSTABILITY

The asymmetry around ω_0 observed in the region of instability (Fig 7.3) is a surprising result: such an asymmetry should not arise for the equation of motion (eq. 7.1) used in the analysis. Something similar is observed in the directly driven response, where the lower saddle-node bifurcation in the downward frequency sweep is always found at a lower frequency than simulated (Fig. 7.3**c**) at high driving levels. Possibly, this indicates that the forcing terms are nonlinear [174]. However, we find that both forcing terms δ and F extracted from the fits are linear with the applied modulation amplitude and the forward frequency sweeps are well-described by this model (see Appendix A1). The observed deviations (e.g. in Fig. 7.3) can therefore not be explained by forcing nonlinearities.

The asymmetry and apparent decrease in resonance linewidth (Fig. 7.3) thus suggest that a more unconventional dissipation model should be considered, including further terms to describe the amplitude-dependence of the dissipation. Similar deviations from conventional dissipation models have been previously found in multi-layered graphene resonators [53], where it was concluded that the van-der-Pol term $\nu x^2 \dot{x}$ does not describe the nonlinear damping. Here we conclude that the van-der-Pol term is generally in agreement with the experiments, since it describes the saddle-node bifurcation of the parametric resonances well, however additional dissipation terms might be needed to account for the asymmetry and narrowing of the parametric stability region (Fig. 7.3**e**,**f**).

7.3. MECHANICAL LOSS TANGENT

The fit to the nonlinear response of the membrane allows us to extract a number for the Duffing (γ) and van-der-Pol terms (ν) in our resonators. As shown in the Appendix A6, the mechanical loss tangent of graphene $\tan\delta_l$ at the resonance frequency can be determined from the ratio of these terms, $\tan\delta_l = \nu/\gamma$. From the values of the fits we obtain $\tan\delta_l = 0.34$ for drum 2 and $\tan\delta_l = 0.15$ for drum 3. The values of these loss tangents are in the same range as found by Jinkins *et al.*[175]. The obtained values for the loss tangent are relatively high for a crystalline material as graphene, therefore the observed nonlinear damping is not likely due to the intrinsic material properties but to other effects, such as sidewall adhesion [176] or unzipping of wrinkles [177].

7.4. PARAMETRIC AMPLIFICATION

Here we investigate the effects of the parametric drive at low driving levels ($\delta < \delta_t$) by examining the parametric amplification of the directly driven resonance. To measure parametric amplification, it is required to simultaneously drive the system at f and $2f$ (where f is near the resonance frequency f_0). This is realized by splitting the driving circuit connected to the diode laser into two parts. One path provides a small direct drive that excites the primary resonance of the membrane in the linear regime. The second path contains a frequency doubler, amplifier, and phase shifter to enable parametric driving with controllable phase and gain with respect to the direct drive. A harmonic oscillator model is fitted to the response to extract the amplitude and the effective quality factor. The relation between amplitude gain G, parametric drive amplitude δ and phase shift ϕ of the direct drive is given by [153, 158]:

$$G(\delta,\phi) = \left[\frac{\cos^2\phi}{(1+\delta/\delta_t)^2} + \frac{\sin^2\phi}{(1-\delta/\delta_t)^2} \right]^{1/2}. \tag{7.2}$$

First, the amplification effect as function of parametric pumping amplitude in Fig. 7.4**a** was examined by keeping the phase ϕ fixed at ϕ = -45 degrees. Increasing the amplitude of parametric drive increases the amplitude at resonance by a factor of 3-4 (Fig. 7.4**b**) and the effective quality factor of resonance by almost a factor of 3 (Fig. 7.4**c**). Figure 7.4**d** shows that shifting the phase of the parametric drive significantly changes the amplitude of harmonic resonance. Figure 7.4**e**-**f** shows that the gain G and effective Q-factor Q_{eff} depend strongly on the phase of the parametric drive with respect to the direct drive. Fits of the data in Fig. 7.4**b**, **e** show that the drive and phase-dependence of the parametric amplification is in accordance with theory.

7.5. DISCUSSION

Here we discuss the efficiency of the tension modulation for parametric excitation of the graphene membrane. The tension modulation $\Delta n_0(t)$ is given by $\Delta n_0 = \alpha E_{2D} \Delta T/(1-\nu)$, where α is the thermal expansion coefficient, E_{2D} the 2D Young's modulus, ν the Poisson ratio and ΔT the temperature modulation. Using approximate values from literature [10, 178], one finds that $\Delta n_0(t) \approx 0.003 \Delta T$ Nm^{-1}K^{-1}, which means that a temperature modulation of 1 K already results in a tension modulation of the order of the intrinsic pre-tension n_0 (estimated to be between 0.003 N/m and 0.03 N/m [60]) of the graphene membranes studied here. One can define the relative shift of the resonance frequency per unit of temperature as a figure of merit for the efficiency of the opto-thermal parametric drive: $\frac{1}{f_{\text{res}}} \frac{\Delta f_{\text{res}}}{\Delta T} = 0.1$ to 1 K^{-1}. This estimated value for graphene is 500-5000 times larger than in other optically excited oscillators [179]. From the fits in Fig. 7.3 we obtain an value of $\frac{\delta}{\beta} = \frac{\Delta f_{\text{res}}^2}{f_{\text{res}}^2} = 0.0225$ in drum 1 and $\frac{\delta}{\beta} = 0.0193$. Using the approximative values above, we estimate the temperature modulation ΔT lies between 0.13 K and 1.5 K. These moderate temperature modulations illustrate that the parametric driving scheme for graphene membranes is a very efficient method for reaching parametric resonance. It should be noted however, that the model proposed in chapter 5 implies a frequency-dependent α, implying that these temperature modulations could be underestimated.

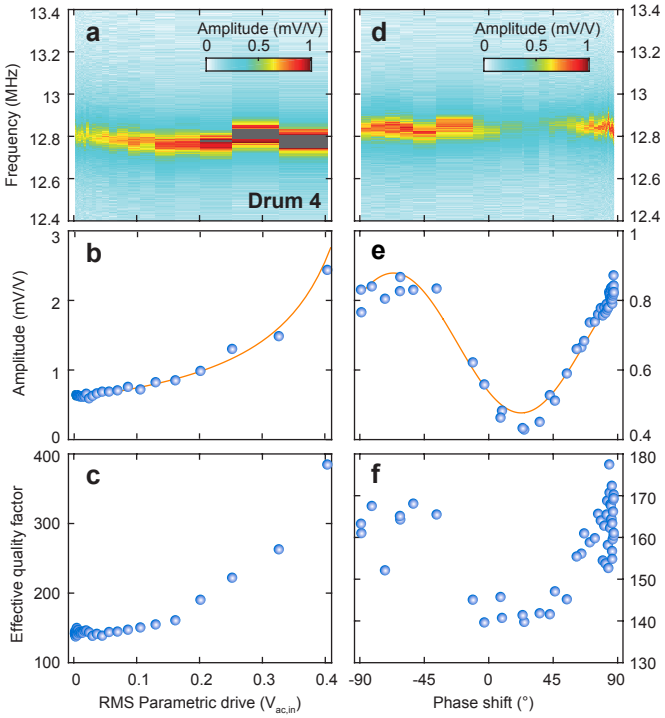

Figure 7.4: Parametric amplification in graphene: direct driven resonance with a sub-threshold ($\delta < \delta_t$) parametric drive. **a**, Transmission function of the direct drive as function of parametric drive. **b**, Amplitude of resonance obtained from a fit to a harmonic oscillator model as function of parametric drive, the red line is a fit to the theoretical behavior predicted by eq. 7.2. **c**, Effective quality factor, obtained from a fit to a harmonic oscillator model, as function of parametric drive. **d**, Transmission funciton as function of phase shift ϕ. **e** Amplitude of resonance as function of phase ϕ, the red line is a fit using eq. 7.2. **f**, Effective quality factor as function of phase ϕ.

Multi-mode parametric oscillators are interesting for applications where accurate frequency tracking of multiple modes is necessary. We list here three potential applications. (1) Radio receivers in the MHz range where multiple radio channels need to be monitored and received simultaneously to maximize data rates, or to allow seamless switching between channels without having to tune the channel [180]. (2) Inertial imaging [181], where accurate tracking of multiple resonances allows one to determine the mass, location and shape of a particle on top of a resonator, which has applications in biotechnology [182]. (3) Parametric oscillators can also be used to build a binary information and computation system [163], where information is stored in the phase of the resonator. Multi-mode resonators have the potential of enabling parallel processing and data storage. The high resonance frequencies and relatively low Q of the graphene membranes can increase computation speed.

A unique feature of the demonstrated graphene system is that all of these modes can be simultaneously parametrically amplified via tension modulation. The use of parametric amplification, therefore, has the advantage that no feedback loops or special fil-

ters or actuation schemes are needed to select the desired resonance mode. Moreover, parametric amplification effectively results in an amplitude dependent gain, which can be used to generate higher output signals than with a constant gain. Moreover, since the driving frequency is double the readout frequency, parametric driving is less sensitive to cross-talk that is often hampering resolving signal detection in directly driven resonators [152].

7.6. CONCLUSIONS

In conclusion, we report on multi-mode parametric resonance and amplification in single layer graphene resonators by an opto-thermal tension modulation technique. It is demonstrated that the tension-dominated restoring force results in parametric excitation of multiple resonance modes in the system when the system is opto-thermally driven. The parametrically and directly driven resonances are compared to a single degree-of-freedom model based on the Duffing, van der Pol and Matthieu equations, with good agreement at low driving levels. This allows simultaneous determination of nonlinear stiffness and damping coefficients and results in a high-frequency determination of graphene's mechanical loss tangent. Graphene resonators are thus an interesting platform to study parametric excitations and their utilization for sensors with improved performance.

APPENDIX

A1: COMPLETE DATASETS FOR THE ANALYSIS OF MECHANICAL NONLINEARITIES

Figure 7.3 in the main text shows the fitting of the nonlinear mechanical response of the resonator (drum 3). In this section the remainder of this analysis is presented and the complete dataset from the fundamental mode of drum 1 is shown (Figs. 7.1**a**, 7.2, 7.3**f**).

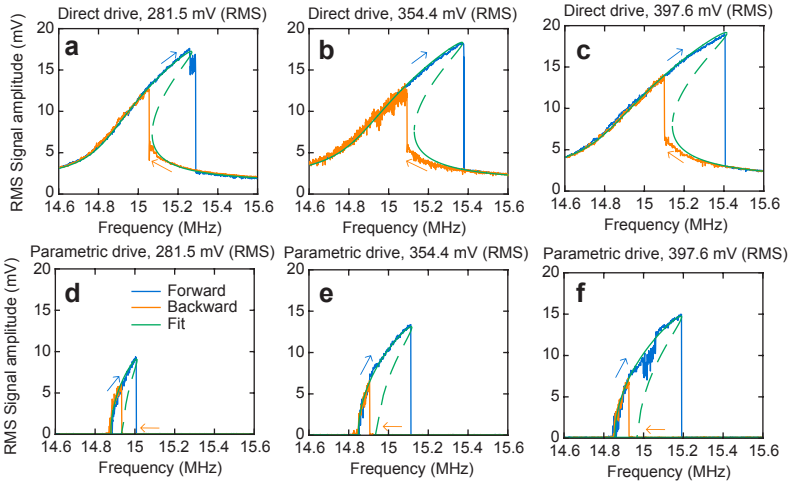

Figure 7.5: Remainder of the dataset presented in Figs. 7.2 and 7.3**a**-**e**.

Table 7.1: Values obtained from the fits on the response from drum 3 in Fig. 7.5 and Figs. 7.3**a**-**e** in the main text

	Direct drive				Parametric drive			
RMS Drive (mV)	μ/β	ν/β	γ/β	$F/\beta \times 10^{-5}$	μ/β	ν/β	γ/β	$\delta/\beta \times 10^{-2}$
250.9	0.0045	70	225	8	0.0045	76	215	1.06
281.5	0.0045	72	220	9.2	0.0045	76	220	1.22
354.4	0.0045	74	230	11.7	0.0045	79	225	1.6
397.6	0.0045	76	230	14.2	0.0046	80	225	1.8
446.2	0.0045	76	230	15.5	0.0046	80	225	1.93

DATASET OF DRUM 1

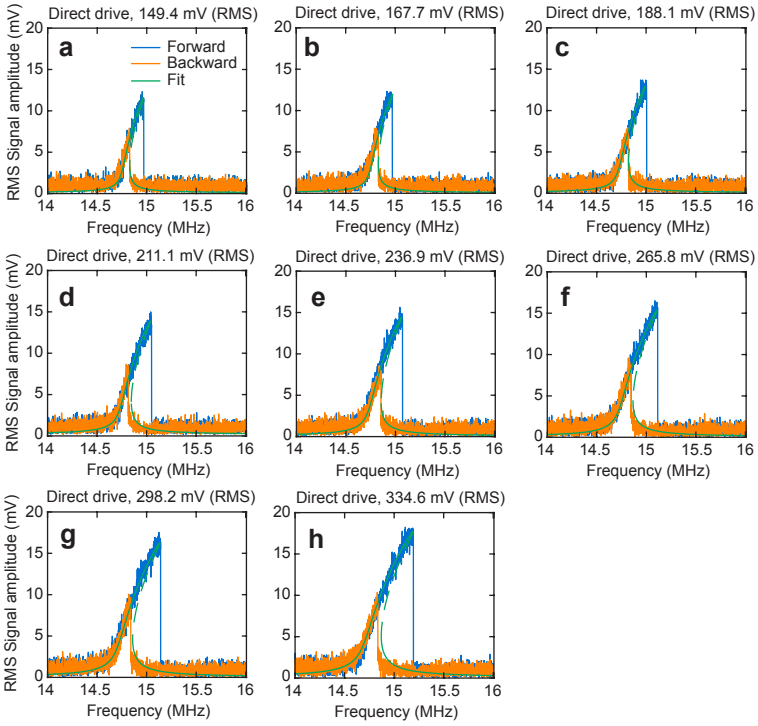

Figure 7.6: Analysis of directly driven response of the fundamental mode of drum 1 (Figs. 7.1**a**, 7.2, 7.3**f**).

Table 7.2: Values obtained from the fits on the response from drum 1 in Figs. 7.6, 7.7 and Figs. 2**a**, 3, 4**f**.

	Direct drive				Parametric drive			
RMS Drive (mV)	μ/β	ν/β	γ/β	$F/\beta \times 10^{-5}$	μ/β	ν/β	γ/β	$\delta/\beta \times 10^{-2}$
149.4	0.0030	36	250	1.42	0.0030	36	250	0.74
167.7	0.0030	37	245	1.6	0.0030	36	220	1.01
188.1	0.0030	37	245	2.0	0.0030	34	225	1.18
211.1	0.0030	37	245	2.5	0.0030	34	225	1.31
236.9	0.0030	37	250	2.8	0.0030	33	225	1.46
265.8	0.0030	36	250	3.3	0.0030	34	225	1.81
298.2	0.0030	35	250	3.9	0.0030	35	225	2.05
334.6	0.0030	35	250	4.5	0.0030	35	225	2.25

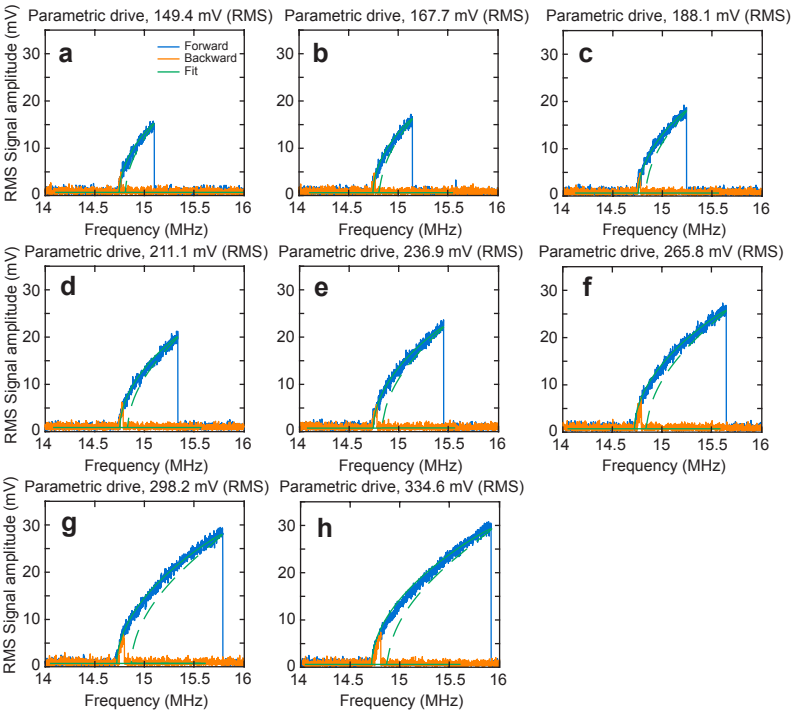

Figure 7.7: Analysis of parametrically driven response of the fundamental mode of drum 1 (Figs. 7.1**a**, 7.2, 7.3**f**). The horizontal axis indicates the frequency at the analyzer port of the VNA, the frequency at the actuation port was doubled.

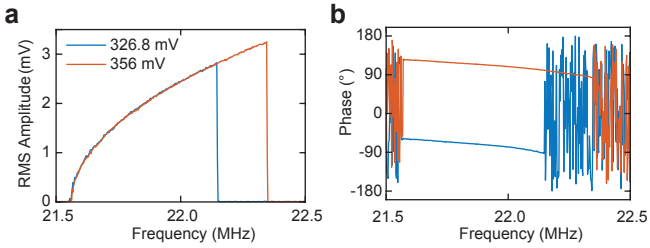

Figure 7.8: Additional experiment of parametric resonance. Parametric excitation was achieved using the frequency doubler (as shown in Fig. 1 in the main text) instead of the frequency conversion on the vector network analyzer. **a** Amplitude of the response at two different driving powers and **b** the phase of these responses. The phase shows two stable phases separated by 180 degrees as expected.

A2: ADDITIONAL EXPERIMENT SHOWING TWO STABLE PHASES

The frequency conversion option on the vector network analyzer loses information on the phase at which the resonator is oscillating. To show that the parametrically excited resonance has two stable phases separated by 180 degrees, the experiment was repeated by using a frequency doubler in the circuit used for the parametric amplification experi-

ment. Using this, the VNA is not required to perform a frequency conversion and phase information is preserved. This results in the mechanical responses shown in Fig. 7.8.

A3: ADDITIONAL DISCUSSION: THE MECHANISM FOR DIRECT AND PARAMETRIC DRIVING

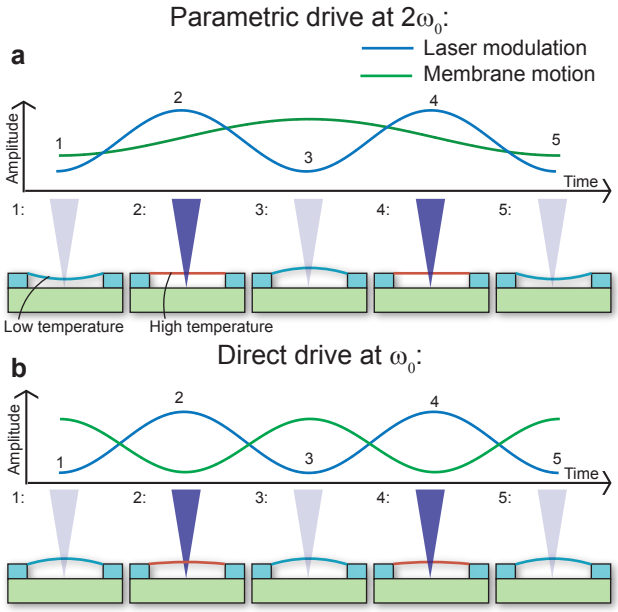

Figure 7.9: Explanation of the actuation mechanisms of the opto-thermal drive. For an illustration of the mechanism, it is assumed the membrane motion follows the force adiabatically (phase delays are omitted). A blue membrane represents low temperature and a red membrane represents high temperature. **a** Parametric excitation, this is due to the pre-tension modulation of the membrane. Each time the tension is maximum the membrane passes through its equilibrium position, leading to a period doubling. This mechanism activates the resonance if the driving frequency is twice the resonance frequency. **b** Direct excitation, which exists due to a small initial deviation from equilibrium. This mechanism does not cause period doubling, but instead, it activates the resonance if the driving frequency is equal to the resonance frequency.

Opto-thermal driving leads to two mechanisms that can excite the resonance in the graphene resonators. Parametric drive (Fig. 7.9**a**) occurs due to the modulation of pre-tension $n_0(t)$ in the membrane via laser heating and thermal expansion since the stiffness term for the out-of-plane deflection field w of the membrane is determined by the pre-tension. Parametric driving will only activate the parametric resonance if the modulation of the blue laser is near twice the mechanical resonance frequency.

As demonstrated in the main text (Figs. 7.2, 7.3), the experiments also show a direct driving component. This can be explained [173] by assuming a small initial membrane displacement w_0 from equilibrium (Fig. 7.9**b**). In graphene resonators rippling, wall adhesion or out-of-plane crumples could lie at the root of such an initial displacement. In chapter 10 we show an experiment that confirms that out-of-plane deviations are the

root cause of direct drive.

In order to analyze the data, we will derive the equations of motion (eq. 7.12) using a Lagrangian approach by including this initial deflection field. In this manner, the equations are reduced to a single-degree-of-freedom (s-dof) model that can be used to fit the data, significantly simplifying the analysis. The derivation of this s-dof model is shown below in section A4.

A4: EQUATIONS OF MOTION

A Lagrangian approach is used to obtain equations of motion of an opto-thermally excited monolayer graphene membrane. In this respect, the potential energy of the thermally actuated circular membrane is obtained as [183]:

$$U = \int_0^{2\pi} \int_0^R \frac{h}{2}\Big(\sigma_{rr}(\epsilon_{rr} - \alpha\Delta T) + \sigma_{\theta\theta}(\epsilon_{\theta\theta} - \alpha\Delta T) + \tau_{r\theta}\gamma_{r\theta}\Big) r\,dr\,d\theta, \tag{7.3}$$

where h is the thickness, R is the radius, α is the thermal expansion coefficient, and ΔT is the temperature change in the membrane. Moreover, σ_{rr} , $\sigma_{\theta\theta}$, $\tau_{r\theta}$, are the Kirchhoff stresses that can be obtained as follows:

$$\begin{aligned}
\sigma_{rr} &= \frac{E}{1-\nu^2}(\epsilon_{rr} + \nu\epsilon_{\theta\theta} - \alpha(1+\nu)\Delta T),\\
\sigma_{\theta\theta} &= \frac{E}{1-\nu^2}(\epsilon_{\theta\theta} + \nu\epsilon_{rr} - \alpha(1+\nu)\Delta T),\\
\tau_{r\theta} &= \frac{E}{2(1+\nu)}\gamma_{r\theta},
\end{aligned} \tag{7.4}$$

in which ϵ_{rr}, $\epsilon_{\theta\theta}$, and $\gamma_{r\theta}$ are the Green strains and are derived as:

$$\begin{aligned}
\epsilon_{rr} &= \frac{\partial u}{\partial r} + \frac{1}{2}\Big(\frac{\partial w}{\partial r}\Big)^2 + \Big(\frac{\partial w}{\partial r}\Big)\Big(\frac{\partial w_0}{\partial r}\Big),\\
\epsilon_{\theta\theta} &= \frac{\partial v}{r\partial\theta} + \frac{u}{r} + \frac{1}{2}\Big(\frac{\partial w}{r\partial\theta}\Big)^2 + \Big(\frac{\partial w}{r\partial\theta}\Big)\Big(\frac{\partial w_0}{r\partial\theta}\Big),\\
\gamma_{r\theta} &= \frac{\partial v}{\partial r} - \frac{v}{r} + \frac{\partial u}{r\partial\theta} + \Big(\frac{\partial w}{\partial r}\Big)\Big(\frac{\partial w}{r\partial\theta}\Big) + \Big(\frac{\partial w}{\partial r}\Big)\Big(\frac{\partial w_0}{r\partial\theta}\Big) + \Big(\frac{\partial w_0}{\partial r}\Big)\Big(\frac{\partial w}{r\partial\theta}\Big),
\end{aligned} \tag{7.5}$$

where u, v and w are the radial, tangential and transverse displacements, respectively. Moreover, w_0 is the deviation of the membrane from flat configuration, E is the Young's modulus and ν is the Poisson's ratio.

The temperature difference ΔT can be obtained by solving the following heat conduction equation:

$$\frac{\partial\Delta T}{\partial\tilde{t}} + \frac{\Delta T}{\tau} = \frac{P_{abs}\cos(\omega\tilde{t})}{C_t}, \tag{7.6}$$

in which P_{abs} is the power absorbed by the membrane, τ is the thermal time constant [60], C_t is the thermal capacitance, and $\tilde{t}$ represents the time variable.

For a membrane with fixed edges u and w shall vanish at $r = R$. Moreover, u should be zero at $r = 0$ for continuity and symmetry. Furthermore, assuming only axisymmetric vibrations ($v = 0$ and $\partial u/\partial\theta = \partial v/\partial\theta = \partial w/\partial\theta = 0$), the solution can be approximated as [63]:

$$w = x(\tilde{t}) J_0\Big(\alpha_0 \frac{r}{R}\Big), \tag{7.7}$$

$$u = u_0 r + r(R-r) \sum_{k=1}^{\bar{N}} q_k(\tilde{t}) r^{k-1}. \tag{7.8}$$

Here it should be noted that for axisymmetric vibrations the shear strain $\gamma_{r\theta}$ would become zero. In equation (7.7), $x(\tilde{t})$ is the generalized coordinate associated with the fundamental mode of vibration. Furthermore, in equation (7.8), $q_k(\tilde{t})$'s are the generalized coordinates associated with the radial motion. Moreover, J_0 is the zeroth order Bessel function of the first kind and $\alpha_0 = 2.40483$. In addition, $\bar{N}$ is the number of necessary terms in the expansion of radial displacement and u_0 is the initial displacement due to pre-tension n_0 that is obtained from the initial stress $\sigma_0 = n_0/h$ as follows :

$$u_0 = \frac{\sigma_0(1-\nu)}{E}. \tag{7.9}$$

The kinetic energy of the membrane neglecting in-plane inertia, is given by:

$$T = \frac{1}{2}\rho h \int_0^{2\pi} \int_0^R \Big(\frac{\partial w}{\partial \tilde{t}}\Big)^2 r\, dr\, d\theta. \tag{7.10}$$

The Lagrange equations of motion are given by:

$$\frac{d}{dt}\Big(\frac{\partial T}{\partial \dot{\mathbf{q}}}\Big) - \frac{\partial T}{\partial \mathbf{q}} + \frac{\partial U}{\partial \mathbf{q}} = 0, \tag{7.11}$$

and $\mathbf{q}$=$[x(\tilde{t}), q_k(\tilde{t})]$, $k = 1, \ldots, \bar{N}$ is the vector containing all the generalized coordinates. Equation (7.11) leads to a system of nonlinear equations comprising of a single differential equation associated with the generalized coordinate $x(\tilde{t})$ and $\bar{N}$ algebraic equations in terms of $q_k(\tilde{t})$. By solving the $\bar{N}$ algebraic equations it is possible to determine $q_k(\tilde{t})$ in terms of $x(\tilde{t})$ [63]. This will reduce the $\bar{N}$+1 set of nonlinear equations to the following Duffing-Matthieu-Hill equation:

$$m\ddot{x} + c_1\dot{x} + c_2 x^2 \dot{x} + [k_1 + F_p \cos(\omega\tilde{t})]x + k_2 x^2 + k_3 x^3 = F_d \cos(\omega\tilde{t}), \tag{7.12}$$

where $(\dot{\bullet})$ represents derivative with respect to time $\tilde{t}$ and m is the mass. c_1 and c_2 are the linear viscous damping coefficient and nonlinear material damping coefficient, respectively [47, 184]. They are added to the equation of motion explicitly to introduce dissipation. k_1 represents the linear stiffness term dominated by the pre-tension n_0 and F_p is the amplitude of parametric drive resulting from temperature variation ΔT. Moreover, k_2 represents the quadratic nonlinear stiffness coefficient due to imperfection w_0 and k_3 denotes the cubic nonlinear stiffness coefficient arising from geometric nonlinearity. Finally, F_d is the amplitude of direct drive term due to the presence of imperfection w_0, and ω is the excitation frequency. Indeed for a flat membrane, $k_2 = F_d = 0$.

A5: NUMERICAL SIMULATIONS

In order to perform the numerical simulations, equation (7.12) is normalized with respect to the mass m of the membrane and the fundamental frequency ($t = \tilde{t}\omega_0$) as follows:

$$\ddot{x} + \mu\dot{x} + \nu x^2\dot{x} + [\beta + \delta\cos(\Omega t)]x + \gamma_2 x^2 + \gamma_3 x^3 = F\cos(\Omega t), \tag{7.13}$$

where $\beta = 1$ due to the normalization. Introducing an effective stiffness nonlinearity γ, whose value is given by $\gamma = \left(\gamma_3 - \frac{10\gamma_2^2}{9}\right)$ [185], equation (7.13) is reduced to:

$$\ddot{x} + \mu\dot{x} + \nu x^2\dot{x} + [\beta + \delta\cos(\Omega t)]x + \gamma x^3 = F\cos(\Omega t), \tag{7.14}$$

where the normalized coefficients are given in table 7.3.

Definition	Normalized parameter
$(\dot{\bullet}) = \frac{d(\bullet)}{dt}$	Scaled time derivative
$\Omega = \frac{\omega}{\omega_0}$	Non-dimensional excitation frequency
$\mu = \frac{c_1}{2m\omega_0}$	Scaled linear damping coefficient
$\nu = \frac{c_2}{m\omega_0}$	Scaled nonlinear damping coefficient
$\beta = \frac{k_1}{m\omega_0^2} = 1$	Scaled linear stiffness coefficient
$\delta = \frac{F_p}{m\omega_0^2}$	Scaled parametric excitation amplitude
$\gamma_2 = \frac{k_2}{m\omega_0^2}$	Scaled nonlinear quadratic stiffness coefficient
$\gamma_3 = \frac{k_3}{m\omega_0^2}$	Scaled nonlinear cubic stiffness coefficient
$\gamma = \gamma_3 - \frac{10\gamma_2^2}{9}$	Scaled effective nonlinear stiffness coefficient
$F = \frac{F_d}{m\omega_0^2}$	Scaled direct excitation amplitude

Table 7.3: Normalized parameter definitions

Here it should be noted that, mass m of the single layer graphene membrane is unknown. Without the exact mass value, optical transduction factors present between the voltage signal measured by the VNA during the experiment and the actual motion of the membrane in physical units cannot be calibrated. Thus, the normalized coefficients

shown in table 7.3 include a linear transduction factor 'κ' for the oscillation amplitude ($x = \kappa V_1$), η for the parametric drive amplitude ($F_p = \eta V_2$) and λ for the direct drive amplitude ($F_d = \lambda V_3$). Where V_1, V_2 and V_3 are voltage signals measured in the experiment.

Finally, the equation (7.14) is simulated using a pseudo-arclength continuation and collocation technique [186] to detect bifurcations and obtain periodic solutions. The simulations are performed as follows:

1. The bifurcation analysis is carried out with the coefficient F as the first continuation parameter and is incremented to the desired value in order to match the experimental direct response.

2. Once the desired value of F is obtained, the parametric drive amplitude δ is used as the second continuation parameter and a value is chosen to replicate the experimental parametric response.

3. After reaching the desired δ value, the analysis is continued with the frequency ratio Ω as the final continuation parameter. This value is spanned around the spectral neighborhood of $\Omega = 1$ and $\Omega = 2$ in order to obtain the direct and parametric response curves.

A6: MECHANICAL LOSS TANGENT OF GRAPHENE

In ref. [63] it is shown that the Duffing term γ is proportional to the Young's modulus E:

$$\gamma = CE, \tag{7.15}$$

where C is a constant. In case of material damping, a complex Young's modulus can be introduced: $E = E' + iE''$ and the nonlinear stifness term γx^3 near the resonance frequency ω_0, for $x = x_0 e^{-i\omega_0 t}$ becomes:

$$CEx^3 = CE'x^3 + CE''\frac{x^2}{\omega_0}\dot{x} = \gamma x^3 + \nu x^2 \dot{x}. \tag{7.16}$$

From this equation it can be seen that the loss tangent $\tan\delta_l = E''/E'$ [187] can be calculated by the ratio ν/γ if the resonator is vibrating near its resonance frequency:

$$\tan\delta_l = \frac{\nu}{\gamma}. \tag{7.17}$$

8

HIGH-FREQUENCY STOCHASTIC SWITCHING OF GRAPHENE DRUM RESONATORS

Stochastic switching between the two bistable states of a strongly driven mechanical resonator enables detection of a weak signal based on probability distributions, in a manner that mimics biological systems. However, even resonators at the microscale require a large amount of fluctuation power to achieve a switching rate in the order of a few Hertz. Here, we employ graphene membrane resonators of atomic thickness to achieve 100 times faster switching rates than current state-of-the-art, while the effective temperature of the fluctuations can be ten times lower. This shows that these membranes are potentially useful to transduce weak signals in the audible frequency domain.

Parts of this chapter consists of an article in preparation [188].

STOCHASTIC switching is the process by which a system transitions randomly between two stable states, mediated by the fluctuations in the environment. This phenomenon has been observed in a variety of physical and biological systems [189–196]. Mechanical resonators that are strongly driven can show stochastic switching between two stable attractors [197–199]. This can potentially improve the transduction of small signals in a manner that mimics nature, by the stochastic resonance phenomenon [200–204]. Despite the high resonance frequencies achieved by scaling down the resonators to the micro- or nanoscale regime, the switching rate is often quite low, in the order of 1 to 10 Hz. Furthermore, high fluctuation power, far above the fluctuations present at room temperature needs to be applied to achieve stochastic switching. Extending this frequency range to the kHz regime, while lowering the fluctuation power, opens the door for new applications in the audible domain. Mechanical resonators consisting of an atomically thin membrane are ideal candidates to raise the switching rate. Their low mass ensures an ultrahigh resonance frequency while at the same time can be easily brought in the nonlinear regime. Graphene is a single layer of carbon atoms with excellent mechanical properties. Several works have demonstrated graphene resonators [12, 69], showing nonlinear behavior [48, 147] and several practical applications such as pressure [11, 33, 51, 59] and gas sensors [35, 58]. Due to the low mass, resonance frequencies are typically found in the 10-100 MHz range, which should allow stochastic switching to occur at higher frequencies. The lower mass and low stiffness by virtue of the membranes thinness allows this to be achieved at lower fluctuation levels.

Here we demonstrate stochastic switching in strongly driven single-layer graphene drum resonators. Using an optical drive and readout, we bring the resonator into the bistable regime. By artificially adding random fluctuations to the drive, the effective temperature of the fluctuations is increased. We observe that the switching rate is increased with an effective temperature dependence that follows Kramer's law. Switching rates as high as 1.2 kHz are observed at effective temperatures of 63×10^3K, which is a two order of magnitude increase in switching rate at an order of magnitude lower effective temperatures than the state-of-the-art reported in the literature. Thus demonstrating the potential of graphene membranes to transduce signals in the audible frequency range.

8.1. PREPARING BISTABLE STATE AND CALIBRATION

In this chapter, we use the single layer graphene samples with a 5-micron diameter and the experimental setup from chapter 3. In order to prepare the resonator in a bistable state, the system is driven in the nonlinear regime as shown in Fig. 8.2**a**. The frequency is swept forward and backward to reveal the hysteretic behavior of the device. The bistable system is now created by choosing the drive frequency to be in the center between the two saddle-node bifurcations. The resonator is artificially heated by adding random fluctuations through the arbitrary waveform generator. In order to relate this to an effective temperature, the Brownian motion of the device is measured as a function of fluctuation power (Fig. 8.2**b**). From a Lorentzian fit, the mean square amplitude of the device is derived which we use to define the effective temperature T_{eff} (chapter 2) [54]:

$$T_{\text{eff}} = \frac{m_{\text{eff}}\omega^2\langle a^2(t)\rangle}{k_B} \tag{8.1}$$

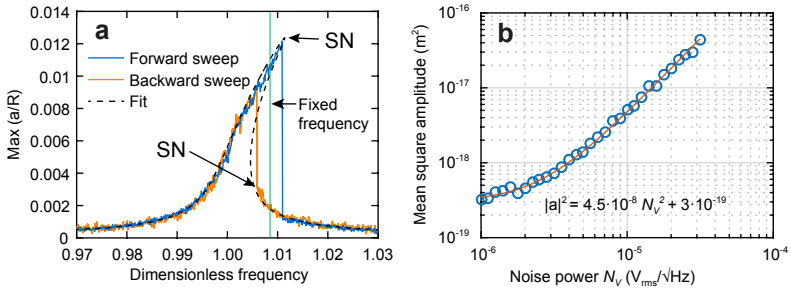

Figure 8.1: **a** Frequency sweeps at high modulation power, showing the Duffing response and the bistable region. During measurements, the frequency is fixed in the center of the bistable region, which is found by finding the jumps in amplitude associated with the saddle-node bifurcation (SN). **b** Mean square amplitude of resonance as a function of applied fluctuation power, this graph is used as calibration to extract the effective temperature.

This effective temperature is a means to express the fluctuation level in an intuitive manner.

Since the amplitude is calibrated the mean square amplitude at low fluctuation powers (where $T_{\text{eff}} \approx T$) can also be used to determine the modal mass m_{eff} of the resonance. From equipartition theorem [54]:

$$m_{\text{eff}} = \frac{k_B T}{\omega^2 \langle a^2(t) \rangle} \tag{8.2}$$

we find $m_{\text{eff}} = 1.85$ fg. With the known modal mass, we can use the frequency response in Fig. 8.1**d** to find the equation of motion. By fitting this frequency response we find the (dimensionless) equation of motion:

$$\ddot{x} + 2\zeta\dot{x} + x + \alpha x^3 = \lambda \cos\omega_F t \tag{8.3}$$

with $\zeta = 0.0006$ the damping coefficient, corresponding to a quality factor of 833, $\alpha = 200$ the cubic stiffness coefficient and $\lambda = 3 \times 10^{-5}$. The natural frequency of the resonance is 13.92 MHz. The equation uses the generalized coordinate $x(t)$ which represents the deflection of the membrane's center and uses scaled variables to introduce only the relevant combinations of the parameters (see Appendix A1).

8.2. RESULTS

During the experiment the system is driven at a fixed driving frequency ω_F centered between the saddle node bifurcations, while the amplitude and phase of the resonator are probed as function of time using the VNA. There are two signal sources driving the system: the fixed driving frequency and the random fluctuations provided by the arbitrary waveform generator. At a fluctuation power of approximately 25×10^3K the stochastic switching events are observed as shown in Fig. 8.2**a**. The amplitude $x(t)$ is split into the in-phase (P) and out-of-phase (Q) part ($x(t) = P(t)\cos\omega_F t + Q(t)\sin\omega_F t$) as shown in Fig. 8.2**b**, which reveals the two stable configurations of the resonator. Increasing the

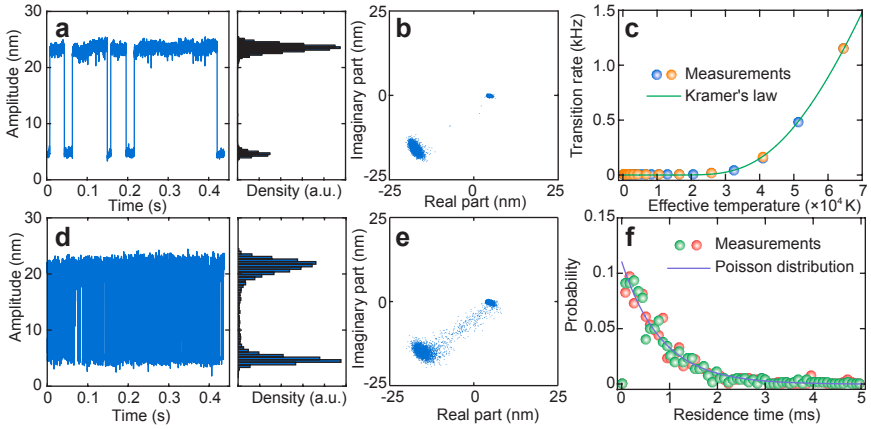

Figure 8.2: Experimental results showing stochastic switching of the nonlinear resonator. **a** Amplitude as function of time for an effective temperature $T_{\text{eff}} = 25 \times 10^3$ K, showing a total of 8 fluctuation-induced transitions. **b** Amplitude in the P-Q space for $T_{\text{eff}} = 25 \times 10^3$ K, each point is one sample of the measurement in Fig. **a**. **c** Transition rate as function of effective temperature, fitted with Kramer's law (eq. 8.4), two sets of consecutive measurements are shown to check for consistency. **d** Amplitude as function of time for an effective temperature $T_{\text{eff}} = 65 \times 10^3$ K, showing a total of 502 transitions. **e** Amplitude in the P-Q space for $T_{\text{eff}} = 65 \times 10^3$ K. **f** Residence time distribution for $T_{\text{eff}} = 65 \times 10^3$, a Poisson distribution (eq. 8.5) is fitted to the data and gives a transition time $\tau_k = 0.83$ ms, corresponding to a transition rate $r_k = 1.2$ kHz.

fluctuation power results in more and more switching events as shown in Fig. 8.2**d** at 65×10^3K. Also broadening the stable attractors somewhat as shown in Fig. 8.2**e**. Figure 8.2**c** shows the experimentally observed switching rate as function of the fluctuation power expressed in T_{eff}. The experiment was repeated twice to check whether effects of slow frequency drift or other instabilities are affecting the experimental result, however both measurements show the same trend. From measurements on other mechanical systems, we expect the switching rate between the stable attractors to follow Kramer's law [189, 195, 204]:

$$r_k = A \exp\left(\frac{-\Delta E}{k_B T_{\text{eff}}}\right) \tag{8.4}$$

where r_k is the transition rate, ΔE is an effective energy barrier, k_B Boltzmann constant and A a parameter used for fitting. Fitting eq. 8.4 to the experimentally observed transition rate in Fig. 8.2**b** shows good agreement with the experimental result. From the fit, we obtain an effective energy barrier of 2.95 aJ.

To further investigate the transition dynamics of the system, we plot the residence time distribution of two separate measurements at 65×10^3K as shown in Fig. 8.2**d**. The residence time distribution should follow a Poisson distribution:

$$N(\tau) = \frac{B}{\tau_k} \exp\left(\frac{-\tau}{\tau_k}\right) = B r_k \exp\left(-\tau r_k\right) \tag{8.5}$$

which is used to fit to the experimental data. From the fit, we find that the transition time $\tau_k = 0.83$ ms, which corresponds to a transition rate of 1.20 kHz. This is close to the experimentally obtained value of 1.15 kHz.

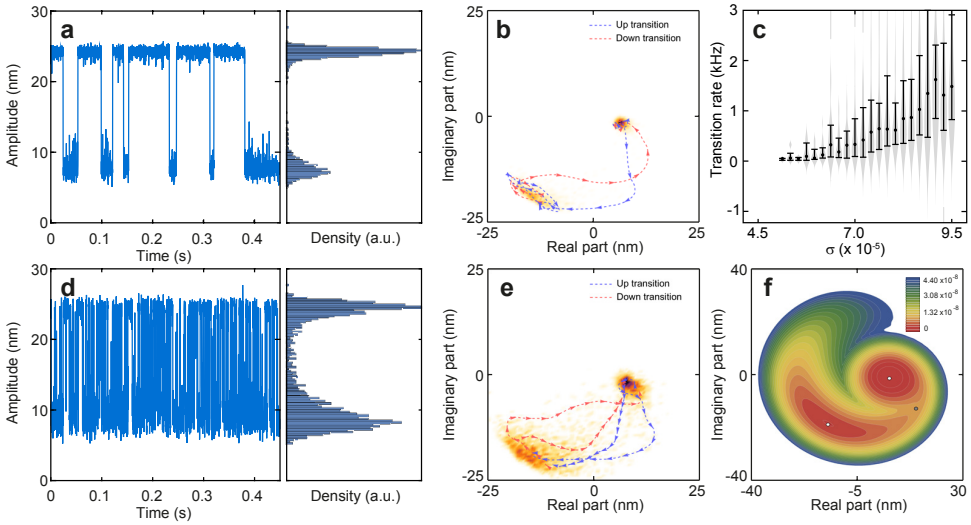

Figure 8.3: Simulations of stochastic switching of the nonlinear resonator in close agreement with the experiments in Fig. 8.2. **a** Time evolution of the stochastic system ($\sigma = 0.000057$, $\Delta t = 15$). Realization of 0.45 s of the system. A Histogram of the distribution of the solution is shown on the right; **b** Density histogram of the solution for the long-term realization of the system. Darker regions refer to states with more probable occurrence. **c** Distribution chart of the switching rate as function of the imposed random fluctuations σ. The upper and lower fences are linked to the 75% and 25% quantile by the vertical whisker lines. **d** Time evolution of the stochastic system ($\sigma = 0.000086$, $\Delta t = 15$). **e** Density histogram of the solution for the long-term realization of the system. **f** Top view of the quasi-potential for excitation frequency $\omega_F = 1.0063$.

8.3. SIMULATIONS

In order to further understand the dynamic behavior of the device, equation (8.3) is used to perform numerical simulations of the system in the presence of fluctuations to compare to the experimental results. We analyze the dynamics of the nonlinear oscillator using the method of averaging [198, 205]. This method describes the change of the vibration amplitude in time from the fast oscillating coordinates to the slow variables (see Appendix A1 for further details). Averaging is appropriate since the quality factor is high and the transition rate is much lower than the resonance frequency.

First, a linear stability analysis is performed for the deterministic system. The eigenvalues of the linearized systems predict two stable equilibria separated by an unstable equilibrium (a saddle). The original model is perturbed by adding a Gaussian white noise process, $dW(t)$, that is a normally distributed random variable with mean zero and variance dt. Its intensity will be referred as σ, which was matched to the experiments by evaluating the mean square amplitude due to the fluctuations $\langle x^2 \rangle$ from the simulations and matching them to the experimentally measured mean square amplitude in Fig. 8.1**b**. The stochastic switching behavior obtained via numerical integration of the stochastic differential equations is shown in Figure 8.3.

We simulate a time evolution of the system as shown in Fig. 8.3**a**, matching the time and effective temperature of the fluctuations of the experiment in Fig. 8.2**a**. From these simulations, it seems that the large amplitude solution is the most probable state for the

low-fluctuation configuration because the system resides more in the basin of attraction of this stable point (histogram in Fig. 8.3**a**). Fig. 8.3**d**, which corresponds to the measurement in Fig. 8.2**d**, shows a massive number of transitions for the resonator with a more equal residence time distribution in the two separate states. The numerical prediction is in qualitative agreement with the switching density illustrated in Figs. 8.2**a** and **d**.

The standard linear stability analysis has only a limited utility since the effect of the fluctuations change the dynamics, along with the probability in a specific steady-state solution. Further insight should be provided by the potential function V, but this cannot be defined for our system in slow variables since it is a non-gradient system. Nevertheless, we can obtain useful information by means of the quasi-potential function calculated by solving the Hamilton-Jacobi equation associated with the equations for P and Q. Details about the quasi-potential and its computation are given in the Appendix A2. In contrast with the linear stability analysis, the quasi-potential gives the qualitative picture of the realizations of the system, i.e. with the quasi-potential surface shape in the proximity of the fixed points of the system, this is reported in Fig. 8.3**f**.

Both Fig. 8.3**a** and **d** highlight wide oscillations around the low-amplitude stable equilibrium, in contrast to a more confined motion around the high-amplitude equilibrium state. Indeed the quasi-potential well associated with the low-amplitude state has a more broad shape allowing for larger cycling before the transition. The density diagrams of the solution for the long-term (0.45 s) realization of the system are reported in Fig. 8.3**b**, **c** and **e**.

At low-fluctuation levels (Fig. 8.3**b**) the cloud spread is limited and the switching paths are concentrated in crossing the saddle. The direction of the trajectories is in full accordance with the rotation of the orbits predicted by the stability analysis. Figure 8.3**e** illustrates a comb of paths used by the system to revert its states. Moreover, it shows a vast distribution spread in the phase-space, mainly due to abundant in-well cycling. Finally, the switching rate as a function of the intensity of the additive Gaussian noise is reported in Fig. 8.3**e**. For the case of $T_{\text{eff}} = 65 \times 10^3$ K, corresponding to $\sigma = 0.000086$, the estimated transition rate is 1.05 kHz, consistent with the experimental findings.

8.4. CONCLUSION

In conclusion, we have shown stochastic switching on the order of kHz in graphene drum resonators. The switching rate is two orders of magnitude higher, while the effective temperature of the fluctuations is one order of magnitude lower than in state of the art MEMS devices. The dynamical behavior and the shape of the cycling paths are qualitatively explained by the shape of the potential wells around the two meta-stable equilibria. Future work can focus on design optimization to achieve even higher switching rates, this could enable detection of very weak audio signals by stochastic resonance.

APPENDIX

A1: EQUATIONS OF MOTION

THE DETERMINISTIC SKELETON

The single degree of freedom system considered to model the drum is:

$$m\ddot{q} + c\dot{q} + k_1 q + k_3 q^3 = f\cos\Omega_F \tau. \tag{8.6}$$

that in dimensionless coordinates is

$$\ddot{x} + 2\zeta\dot{x} + x + \alpha x^3 = \lambda\cos\omega_F t. \tag{8.7}$$

where

$$\begin{aligned} t &= \omega_0 \tau, \\ x &= q/a, \\ 2\zeta &= c/\left(\omega_0 m_{eff}\right), \\ \alpha &= a^2 k_3/\left({\omega_0}^2 m_{eff}\right), \\ \lambda &= f/\left(a{\omega_0}^2 m_{eff}\right), \\ \omega_F &= \Omega_F/\omega_0. \end{aligned} \tag{8.8}$$

Here, the solution is assumed to have the form

$$x = p(t)\cos\omega_F t + q(t)\sin\omega_F t \tag{8.9}$$

in which $p(t)$ and $q(t)$ are slowly varying functions of time. Furthermore, the solution if subject to the condition [205]

$$\dot{p}(t)\cos\omega_F t + \dot{q}(t)\sin\omega_F t = 0. \tag{8.10}$$

Following the method of averaging [198], we substitute eq. (8.9) with its corresponding time derivatives into eq. (8.7). By using eq. (8.10), we obtain

$$\begin{cases} \dot{p} = \dfrac{{\omega_0}^2 - {\omega_F}^2}{2\omega_F} q - \Gamma p + \dfrac{3}{8}\dfrac{\gamma}{\omega_F} q\left(p^2 + q^2\right) \\ \dot{q} = -\dfrac{{\omega_0}^2 - {\omega_F}^2}{2\omega_F} p - \Gamma q - \dfrac{3}{8}\dfrac{\gamma}{\omega_F} p\left(p^2 + q^2\right) + \dfrac{F}{2\omega_F} \end{cases}. \tag{8.11}$$

STOCHASTIC DIFFERENTIAL SYSTEM

The deterministic skeleton of the system shows 3 equilibria: $e_A = \{0.00246073, -0.000508264\}$, $e_B = \{-0.00600831, -0.00778412\}$ and $e_S = \{0.00613994, -0.00527489\}$. A linear stability analysis tells us that e_A and e_B are the stable equilibria, whereas e_S is a saddle point. The real part of the eigenvalues of the Jacobian for the stable equilibrium is the same for both the stable equilibrium points ($-0.00012 \pm 0.00376934i$ for e_A, $-0.00012 \pm 0.0053184i$ for e_B, -0.00461927 and 0.00221927 for e_S) suggesting an equal stability.

The deterministic system of eqs. (8.11) is then perturbed by a Gaussian white noise processes with intensity σ_1 and σ_2 in the equations for $\dot{p}$ and $\dot{q}$, respectively. To emphasize that the dynamic of the system is now a stochastic process, and not anymore a

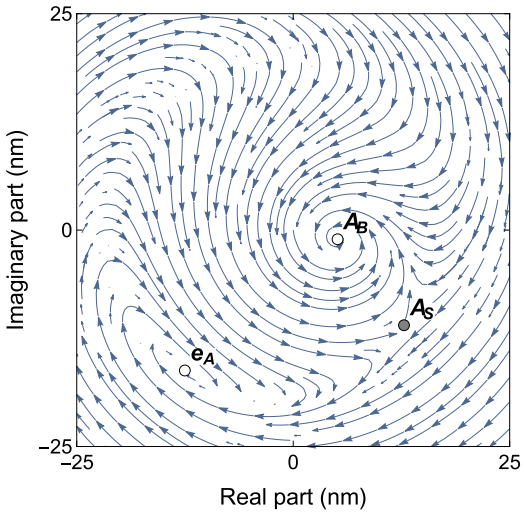

Figure 8.4: Stream plot for the deterministic vector field of the model in eq. (8.11). Unstable and stable equilibrium points are reported with white and gray disks, respectively. and stable equilibria are gray disks. Blue lines and arrows show the direction of trajectories $\omega_F = 1.0063$.

deterministic fuction of time, the notation is switched from $p(t)$ to $P(t)$ and from $q(t)$ to $Q(t)$. The system of stochastic differential equations (SDE) with additive fluctuations is:

$$\begin{cases} dP = \left(\dfrac{{\omega_0}^2 - {\omega_F}^2}{2\omega_F} Q - \Gamma P + \dfrac{3}{8} \dfrac{\gamma}{\omega_F} Q \left(P^2 + Q^2 \right) \right) dt + \sigma_1 dW_1 \\ dQ = \left(-\dfrac{{\omega_0}^2 - {\omega_F}^2}{2\omega_F} P - \Gamma Q - \dfrac{3}{8} \dfrac{\gamma}{\omega_F} P \left(P^2 + Q^2 \right) + \dfrac{F}{2\omega_F} \right) dt + \sigma_2 dW_2 \end{cases} \tag{8.12}$$

in which $W_1(t)$ and $W_2(t)$ are independent Wiener processes, normally distributed random variables with mean zero and variance dt. The change in notation is needed since SDE differ from the deterministic DE. Neither W nor the state variables P and Q are nowhere differentiable. For the integration of Eqs.(8.12), the Itô scheme will be employed [206].

A2: QUASI-POTENTIAL

A generic n-dimensional system of stochastic differential equations considering the effect of additive fluctuations can be written as:

$$d\mathbf{X} = f(\mathbf{X})\, dt + \sigma d\mathbf{W} \tag{8.13}$$

where $\mathbf{X} = (X_1, ..., X_n)^T$ is a vector of state variables, $\mathbf{W} = (W_1, ..., W_n)^T$ is a vector of n independent Wiener processes, f is the deterministic skeleton of the system and, finally, σ is the fluctuation intensity. The state variables in the deterministic system are indicated with lowercase notation, i.e. $\mathbf{x} = (x_1, ..., x_n)^T$. The vector field f, for every $\mathbf{x}$ specify the direction in which the deterministic trajectory moves.

If $n = 1$ eq. (8.13) reduces to:

$$dX = -U'(X)\,dt + \sigma\,dW \tag{8.14}$$

in which U is the *potential function* (or potential). Furthermore, the function is related to specific characteristics of the stochastic process. In the stochastic process (8.14), the probability density function $p(x,t)$ related to the random variable X, describing the probability that $X(t) = x$ obeys a Fokker–Planck equation:

$$\frac{\partial p(x,t)}{\partial t} = \frac{\partial}{\partial x}\left(U'(x)\,p(x,t)\right) + \frac{\sigma^2}{2}\frac{\partial^2 p(x,t)}{\partial x^2}. \tag{8.15}$$

The steady state solution is such that $\dfrac{\partial p(x,t)}{\partial t} = 0$. The steady state probability distribution $p_s(x)$ is readily obtained by:

$$p_s = \frac{1}{\int_0^\infty e^{-2U/\sigma}} e^{-\frac{2U}{\sigma}} \tag{8.16}$$

The steady state solution shows that the probability is maximized (more likely states for the system) in the minima valleys of the potential.

For the case $n = 2$ in eq. (8.13) we still have the Fokker-Plank equation:

$$\frac{\partial p}{\partial t} = -\frac{\partial(f_1 p)}{\partial x_2} - \frac{\partial(f_2 p)}{\partial x_2} + \frac{\sigma^2}{2}\left(\frac{\partial^2 p}{\partial x_1^2} + \frac{\partial^2 p}{\partial x_2^2}\right). \tag{8.17}$$

Conversely to the gradient example, in this case there is no function playing the same role as U. However it is possible to assume the presence of a function $V(\mathbf{x})$, with $\mathbf{x} = (x_1, x_2)$, able to describe the steady state solution of the system:

$$p_s(\mathbf{x}) = k e^{-\frac{2(\mathbf{x})}{\sigma}}. \tag{8.18}$$

If σ is small we can approximate V by a function V_0 that satisfies the Hamilton-Jacobi equation [207]:

$$\nabla V_0 \cdot \nabla V_0 + f \cdot \nabla V_0 = 0 \tag{8.19}$$

in which $f = (f_1, f_2)$. The function V_0 is a useful analog of the potential of gradient systems. It specifies a 2D surface in which all the trajectories move *downhill* in the absence of perturbations. In details, it is the component $-\nabla V_0$ leading to the downhill movement. However, being $f\mathbf{x}$ the deterministic skeleton causing the trajectories to move all around the landscape, we can write the decomposition of f as

$$f = Q(\mathbf{x}) - \nabla V_0 \tag{8.20}$$

in which Q is the so-called the *circulatory* component. Since V_0 is the solution of eq. (8.20), $Q \cdot \nabla V_0 = 0$, thus Q and ∇V_0 are perpendicular. Without additional external forces Q creates the circulation of trajectories around levels of V_0.

The function V_0 is a scalar multiple of the Freidlin-Wentzell quasi-potential, it generalizes the potential function to n-dimensional non-gradient systems. Although the definition of the Freidlin-Wentzell quasi-potential is $\Phi = 2V_0$, in this paper V_0 is used to avoid the inconvenient generated by the Freidlin-Wentzell definition. Indeed, the functions Φ and V_0 measure the same properties, and one can be immediately related to the other.

Part IV: Dynamics of graphene membranes interacting with fluids

9

GRAPHENE SQUEEZE-FILM PRESSURE SENSORS

The operating principle of squeeze-film pressure sensors is based on the pressure dependence of a membrane's resonance frequency, caused by the compression of the surrounding gas which changes the resonator stiffness. To realize such sensors, not only strong and flexible membranes are required, but also minimization of the membrane's mass is essential to maximize responsivity. Here, we demonstrate the use of a few-layer graphene membrane as a squeeze-film pressure sensor. A clear pressure dependence of the membrane's resonant frequency is observed, with a frequency shift of 4 MHz between 8 and 1000 mbar. The sensor shows a reproducible response and no hysteresis. The measured responsivity of the device is 9000 Hz/mbar, which is a factor 45 higher than state-of-the-art MEMS-based squeeze-film pressure sensors while using a factor of 25 smaller membrane area.

Parts of this chapter have been published in Nano Letters **16** (1), 568–571 (2016) [59]

GRAPHENE has the highest surface-to-mass ratio and lowest bending rigidity of all impermeable membranes [11]. These properties make graphene a suitable material for nanomechanical sensors. Currently, pressure sensors are the most widespread membrane-based mechanical sensors and are present in most modern mobile handsets. Commercial microelectromechanical system (MEMS) based pressure sensors feature membranes of several hundreds of nanometers in thickness. Replacing these by thin graphene membranes would allow an increase in responsivity and a size reduction by orders of magnitude. In order to exploit these advantages, several studies [11, 33, 208, 209] have demonstrated the feasibility of sensing pressure changes with a graphene membrane suspended over a reference cavity at pressure p_{ref}. When the ambient pressure (p_{amb}) changes, the pressure difference ($p_{\text{amb}} - p_{\text{ref}}$) causes a deflection of the membrane. This has been directly detected by atomic force microscopy (AFM) and via a tension-induced change in the membrane's resonance frequency [11]. Also the change in piezoresistance [33] has been used to detect the change in pressure. However, the drawback of these pressure-difference based sensing methods is that they require a stable reference pressure p_{ref} over the ~10 years lifetime of the sensor, posing extreme demands on the hermeticity of the reference cavity. Even though graphene sealed cavities were shown to have leak time constants of many hours [11], at this stage, it is unclear whether these can ever be increased to timescales of years. It is therefore of interest to develop pressure sensors that do not rely on the presence of an impermeable reference cavity.

In this work, we demonstrate the feasibility of using graphene as a squeeze-film pressure sensor. The sensor consists of a membrane that covers a gas cavity. The main difference with conventional pressure sensors is the presence of an open venting channel that maintains the average pressure inside the cavity equal to the ambient pressure. Squeeze-film pressure sensors operate by compressing gas in the cavity that is at ambient pressure p_{amb}. When the compression is performed at a high frequency, the gas fails to escape its effective position because of the viscous forces [43]. The added stiffness due to the compression of the gas is a function of pressure. For isothermal compression, this will change the resonance frequency (f_{res}) of the resonator according to:

$$f_{\text{res}}^2 = f_0^2 + \frac{p_{\text{amb}}}{4\pi^2 g_0 \rho h}. \tag{9.1}$$

Here, f_{res} is the membrane's resonance frequency at pressure p_{amb}, f_0 the resonance frequency in vacuum, g_0 the gap size between the membrane and the substrate that lies underneath the membrane and ρh the mass per unit square (see Appendix A2). Note, that the smaller the mass per unit square ρh, the larger the frequency shift. The low mass density of graphene thus makes it a perfect material for this type of sensor.

As is shown in the Appendix A2, at high enough frequencies eq. 9.1 is independent of mode-shape, thickness and boundary conditions of the membrane. The independence of the boundary conditions shows that the venting channel has no influence on the responsivity ($R = \mathrm{d}f_{\text{res}}/\mathrm{d}p_{\text{amb}}$) of the device. Several works have demonstrated MEMS-based squeeze-film pressure sensors with responsivities of up to 200 Hz/mbar [210–213].

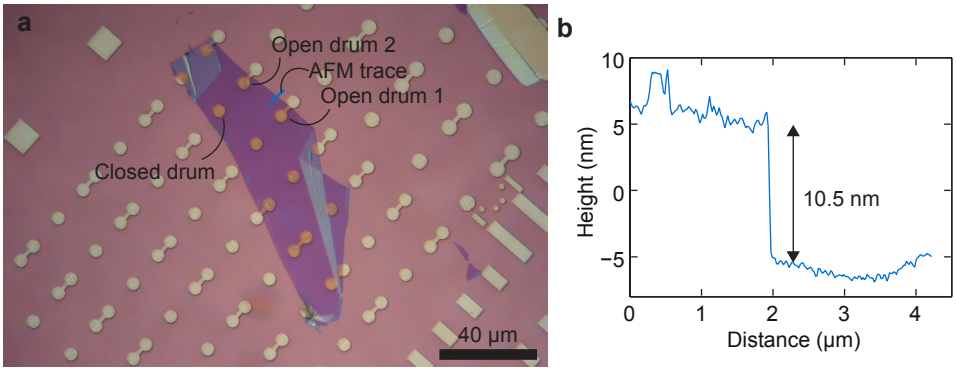

Figure 9.1: **a** Optical image of the graphene flake transferred on dumbbell and circular shaped holes in a SiO_2 substrate. The diameter of the drums is 5 μm and the thickness of the oxide 400 nm. Open and closed drums used in the study are highlighted and the trace used for atomic force microscopy (AFM) to measure the flake thickness is indicated. **b** Height profile from AFM, showing that the membrane is 10.5 ± 0.7 nm thick.

9.1. SAMPLE

We use an exfoliated few-layer graphene (FLG) flake that is suspended over dumbbell shaped holes using a dry stamping method [56, 68, 214] (chapter 3). The dumbbells have a diameter of 5 μm and are etched into a 400 nm SiO_2 layer on a silicon substrate (Fig. 9.1**a**). The thickness of the flake after the transfer is measured to be about 10.5 nm using atomic force microscopy (Fig. 9.1**b**). The stamping method allows accurate placement of the flake such that it covers half of the dumbbell shape, thus creating a graphene-based squeeze-film pressure sensor with a lateral venting channel. To demonstrate the importance of the venting channel for the sensor response, several sealed (closed) drums are created with the same flake.

9.2. RESULTS

The pressure-dependent resonance frequency of the sensor is studied by ramping the pressure upward and downward at a constant rate. During the pressure ramp, the VNA continuously measures frequency spectra from 5-30 MHz at a rate of about 1 sweep every 2 seconds. Figure 9.2 shows these frequency spectra at 4 different pressures. At 8 mbar 4 resonance modes are visible. At higher pressures, the frequency of the fundamental mode increases while its Q-factor decreases. A damped harmonic oscillator model (chapter 2) is fitted (red lines) to the data to extract the resonance frequency and quality factor as a function of pressure. The total frequency shift between 8 mbar and 1000 mbar is 4 MHz.

Figure 9.3**a** shows the frequency spectra taken during a pressure ramp in a contour plot. The frequencies of the first, third and fourth resonance modes increase as a function of pressure in close agreement (black dashed lines) with eq. 9.1. The intensity of the second mode vanishes above ~50 mbar; therefore it is not possible to compare its response to eq. 9.1. For all modes, the intensity decreases rapidly with pressure. The resonance frequency is plotted versus pressure in Fig. 9.3**b** for a measurement at a ramp

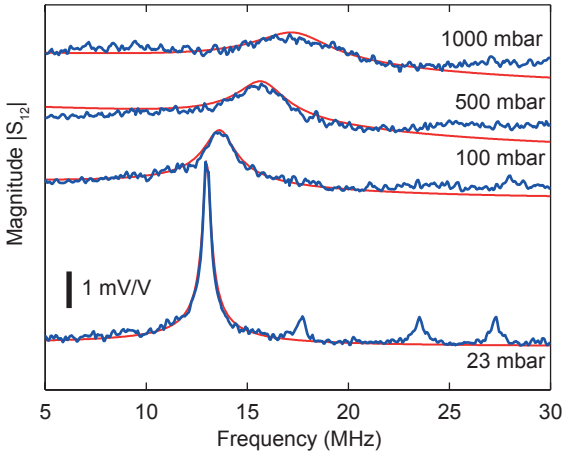

Figure 9.2: Frequency spectra (blue) obtained from the VNA at different pressures. A damped harmonic oscillator model is fitted (red) to the fundamental mode to determine its resonance frequency and Q-factor.

rate of 3.3 mbar/s. This measurement demonstrates the reproducibility of the sensor, showing no hysteresis as the pressure readings during upward and downward sweep are equal within the inaccuracy of the measurement. Equation 9.1 is plotted (dashed black line) in Fig. 9.3**b** using the measured f_0 and no additional fit parameters. The theoretical curve is in close agreement with experimental data up to pressures of 200 mbar. Above 200 mbar, the measured resonance frequency deviates from eq. 9.1. This indicates that the assumptions underlying this equation cannot account anymore for the resonance frequency behavior at these higher pressures and will be investigated further in chapter 10.

The quality factor is determined from the harmonic oscillator fits (Fig. 9.2) and plotted in Fig. 9.3**c**. Three regimes can be distinguished: at pressures lower than 100 mbar, the quality factor drops as a function of pressure, approximately proportional to $1/p_{\mathrm{amb}}$. It is predicted by Bao et. al. [215] that the quality factor scales with $1/p_{\mathrm{amb}}$ in the free molecular flow regime. Between 100 and 500 mbar the quality factor appears to be more or less constant. Above 500 mbar the Q-factor reduces further approximately proportional to $1/p_{\mathrm{amb}}$. More sophisticated modeling is needed to explain the behavior of quality factor as a function of pressure.

9.2.1. MEASUREMENTS WITH DIFFERENT GASES

In this section measurement results are presented with different gases, these measurements will show whether compression in these systems is isothermal or adiabatic. According to Andrews et al. [212] the response of frequency versus pressure for the case of adiabatic compression is given by:

$$\omega^2 = \omega_0^2 + \gamma \frac{p_{\mathrm{amb}}}{g_0 \rho h}, \tag{9.2}$$

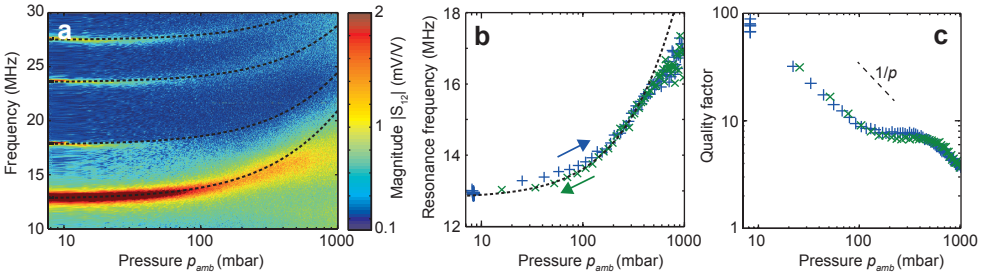

Figure 9.3: Pressure dependent resonances. **a** Contour graph of the VNA frequency spectra versus pressure at a ramp rate of 0.55 mbar/s. Dashed black lines are plotted using eq. 9.1 with g_0 = 400 nm and $\rho h = 23.8 \times 10^{-6}$ kg m^{-2} (31 layers of graphene) using the measured f_0 and no fitting parameters. **b** Resonance frequencies extracted from an up (+) and down (×) pressure sweep at a rate of 3.3 mbar/s, showing the reproducibility of the frequency response. **c** Quality factors from an up (+) and down (×) pressure sweep at a rate of 0.55 mbar/s. To reduce the amount of data, the mean of the pressure and average of the quality factor for 10 data points was taken.

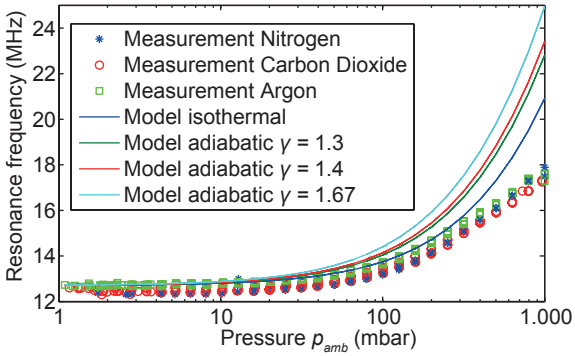

Figure 9.4: Frequency response for nitrogen, argon and carbon dioxide in the chamber. Solid lines are models for isothermal compression (γ = 1) and adiabatic compression for argon (γ = 1.3), nitrogen (γ = 1.4) and carbon dioxide (γ = 1.67).

where γ is the adiabatic index. For monatomic ideal gases such as argon, γ = 1.3, for a diatomic gas such as nitrogen, γ = 1.4 and for a collinear molecule such as carbon dioxide γ = 1.67. For isothermal processes one can use γ = 1 independent on the gas used, which makes eq. 9.2 equal to eq. 9.1. In order to examine whether the compression in graphene-based squeeze-film sensors is adiabatic or isothermal, pressure sweeps were performed on the same open drum as Fig. 9.3 using three gases with different adiabatic indexes (Fig. 9.4). This measurement shows that compression in graphene squeeze-film pressure sensors is isothermal, since no significant change in stiffness is observed with different gases. This suggests that the thermal time constant of the thin film of gas is short compared to the period of oscillation.

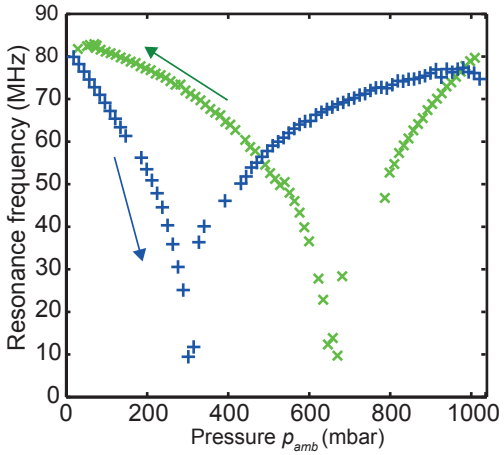

Figure 9.5: Frequency response of a closed drum as a function of pressure.

9.2.2. MEASUREMENTS ON A CLOSED DRUM

To compare the response of the open drums with those of closed drums, measurements were performed on a drum without venting channel on the same flake with an equal diameter (see Fig. 9.1). The pressure was ramped up and down at a rate of 0.55 mbar/s. The frequency response is strikingly different from the ones observed in open drums, with a clear hysteresis caused by gas leakage of the cavity. As shown in Fig. 9.7, the frequency shifts observed are around 85 MHz, much larger than for the squeeze-film effect. It is concluded that these shifts are tension-induced by the pressure difference over the membrane, in agreement with observations by Bunch et. al. [11].

9

9.3. DISCUSSION

From the data in Fig. 9.3**b** it is possible to estimate the responsivity of the device: at low pressures the responsivity is approximately 9000 Hz/mbar while at atmospheric pressure it is 1000 Hz/mbar. The highest reported responsivity in squeeze-film MEMS pressure sensors is 200 Hz/mbar [211]. The responsivity of the graphene-based sensor is thus a factor of ~5-45 larger than that of a MEMS sensor. At the same time the area of the graphene sensor is a factor 25 smaller. It should be noted however that a hermetically sealed cavity exhibits a larger resonance shift, which means that if a hermetically sealed cavity becomes feasible, it should be an attractive concept for a graphene-based pressure sensor.

Based on eq. 9.1, further improvement of the demonstrated squeeze-film pressure sensor concept is possible by reducing the thickness of the membranes. It is estimated that using a single-layer graphene resonator will increase the frequency response by a factor of 5.6. However, the quality factor reduces for thinner membranes. Therefore the trade-off between responsivity and quality factor might result in a larger optimum thickness. A reduction of the gap size g_0 can enable a further increase of the responsivity.

9.4. CONCLUSION

A graphene squeeze-film pressure sensor has been demonstrated that does not need an impermeable reference cavity at a stable reference pressure. Reproducible sensor response is demonstrated and a 4 MHz resonance frequency shift between 8 and 1000 mbar is measured. The resonance frequency closely follows the squeeze-film model up to 200 mbar, but at higher pressures, deviations from the model are observed that require further theoretical study. In comparison with MEMS-based squeeze-film sensors, the responsivity of the sensor is a factor 5-45 larger with factor 25 smaller area. A further increase of the responsivity can be obtained using thinner membranes and reducing the gap size. In comparison to other graphene-based pressure sensing concept, the squeeze-film pressure sensor has the advantage that it does not rely on an impermeable reference cavity at constant pressure. Therefore, it provides a promising route towards size reduction and sensitivity improvements of pressure sensors.

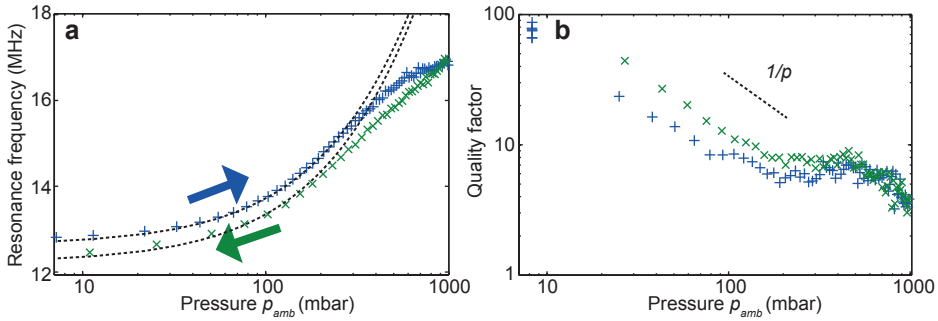

Figure 9.6: **a** Frequency response of a measurement taken with a sweep rate of 0.55 mbar/s; the quality factors from this measurement are shown in fig. 9.3**c**. **b** Quality factors from a measurement taken with a different ramp rate of 3.3 mbar/s, the frequencies are shown in fig. 9.3**b** in the article.

APPENDIX

A1: ADDITIONAL MEASUREMENT RESULTS CORRESPONDING TO FIG. 9.3

Additional graphs are presented corresponding to the measurement data shown in Fig. 9.3. Figure 9.6**a** shows the frequencies corresponding to the quality factors in Fig. 9.3**c**, with the pressure ramping at 0.55 mbar/s. Drift is observed, which we attribute to movements in the measurement setup, which change the position of the laser spot on the membrane in the course of the one-hour measurement. This modifies the way the substrate thermally expands, thereby changing the tension in the membrane. The drift observed in Fig. 9.6**a** is therefore an expected inaccuracy of the measurement. The data fits (dashed lines) are produced using eq. 9.1 with $f_0 = 12.3$ MHz and $f_0 = 12.7$ MHz to correct for the drift.

Figure 9.6**b** shows the quality factors corresponding to Fig. 9.3**b**. The pressure was ramped at a rate of 3.3 mbar/s. The data is in good agreement with Fig. 9.3**c**.

MEASUREMENT ON OPEN DRUM 2

In this section, measurement results are presented on a different open drum on the same flake (see Fig. 9.1). It is found that the response is very similar as is shown in Fig. 9.7. The pressure was changed in logarithmic steps between 3 and 1000 mbar, both upwards and downwards. The total duration of the measurement was 900 seconds. The frequency response is very similar to the other open drum, within the inaccuracy of the measurement. The quality factor shows a slightly different slope than the other open drum.

A2: SQUEEZE-FILM EFFECT IN THE HIGH-FREQUENCY LIMIT

In this section eq. (9.1) from is derived using the equations of motion for a piston and a membrane combined with Boyle's law of an infinitesimal part of the gas film. For the derivation of this equation, it is assumed that the compression frequency is so high that the gas effectively has no time to allow for significant lateral gas flow within 1 period. The validity of this assumption is investigated using the linearized Reynolds equation in the second part of this section. In the entire analysis, only the gas dynamics in the thin gas film underneath the membrane is considered.

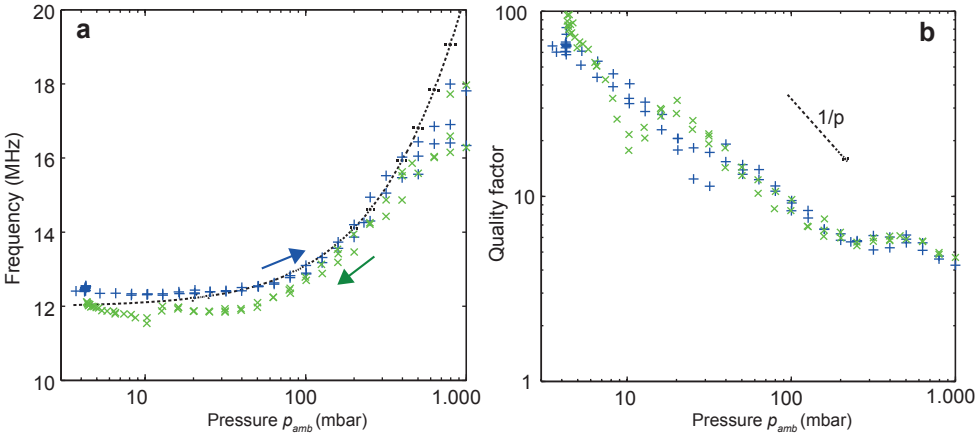

Figure 9.7: Frequency response and quality factor for another open drum on the same flake (see Fig. 9.1**a**).

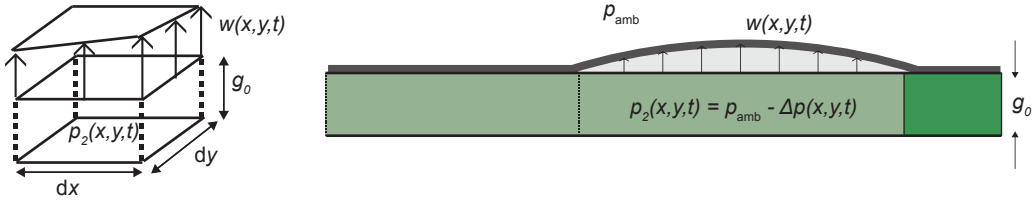

Figure 9.8: Infinitesimal part of the fluid film beneath the resonator and cross section of the sensor.

DERIVATION OF FREQUENCY-PRESSURE RELATION FOR A PISTON

In this section eq. 9.1 is derived, first for a piston followed by the derivation for a membrane. Assuming ideal compression in the squeeze-film, Boyle's law can be applied to an infinitesimal part of the film (Fig. 9.8):

$$p_{\text{amb}} V_1 = p_2 V_2, \tag{9.3}$$

$$p_{\text{amb}} g_0 \mathrm{d}x\mathrm{d}y = p_2 (g_0 + w)\mathrm{d}x\mathrm{d}y, \tag{9.4}$$

$$p_{\text{amb}} g_0 = p_2 (g_0 + w), \tag{9.5}$$

by substituting $p_2 = p_{\text{amb}} - \Delta p$:

$$p_{\text{amb}} w = \Delta p g_0 + \Delta p w. \tag{9.6}$$

Assuming $\Delta p << p_{\text{amb}}$ and $w << g_0$ we obtain the following expression:

$$\Delta p = \frac{p_{\text{amb}}}{g_0} w, \tag{9.7}$$

which gives the pressure field, which is in turn proportional to the deflection field. This result is equivalent to the one that was obtained by Bao and Yang for a squeeze-film

between two rigid plates[43]. The equation of motion for a piston can then be written as[216]:

$$\rho h \frac{\mathrm{d}^2 w}{\mathrm{d}t^2} = -\Delta p = -\frac{p_{\mathrm{amb}}}{g_0} w. \tag{9.8}$$

For which one can directly obtain the resonance frequency:

$$\frac{\mathrm{d}^2 w}{\mathrm{d}t^2} + \frac{p_{\mathrm{amb}}}{g_0 \rho h} w = 0. \tag{9.9}$$

This is the equation for a harmonic oscillator with frequency:

$$\omega^2 = \frac{p_{\mathrm{amb}}}{g_0 \rho h}, \tag{9.10}$$

which gives the pressure response $\Delta\omega = \sqrt{p_{\mathrm{amb}}/g_0 \rho h}$.

DERIVATION OF THE FREQUENCY-PRESSURE RELATION FOR A FLEXIBLE MEMBRANE

In this section we derive the frequency pressure relation for a membrane that has both tension (or compression) n_0 and bending rigidity D. This analysis shows that the response of the frequency is equal to the situation of a piston. The equation of motion is given by [216]:

$$\rho h \frac{\partial^2 w}{\partial t^2} + D\nabla^4 w - n_0 \nabla^2 w = -\frac{p_{\mathrm{amb}}}{g_0} w. \tag{9.11}$$

Equation 9.11 can be solved by separation of variables:

$$w(x, y, t) = W(x, y) T(t), \tag{9.12}$$

$$\frac{\rho h}{D} \frac{1}{T} \frac{\mathrm{d}^2 T}{\mathrm{d}t^2} + \frac{p_{\mathrm{amb}}}{g_0 D} = \frac{n_0}{D} \frac{\nabla^2 W}{W} - \frac{\nabla^4 W}{W} = \lambda^4, \tag{9.13}$$

with λ as the separation variable. From eq. 9.13 one can obtain the time-dependent equations which will be used to calculate the eigenfrequency:

$$\frac{\mathrm{d}^2 T}{\mathrm{d}t^2} + \left(\frac{p_{\mathrm{amb}}}{g_0 \rho h} + \lambda^4 \frac{D}{\rho h} \right) T = 0. \tag{9.14}$$

This equation describes an harmonic oscillator:

$$\frac{\mathrm{d}^2 T}{\mathrm{d}^2 t} + \omega^2 T = 0, \tag{9.15}$$

which means that the resonance frequencies become:

$$\omega^2 = \frac{p_{\mathrm{amb}}}{g_0 \rho h} + \lambda^4 \frac{D}{\rho h}. \tag{9.16}$$

If the frequency in vacuum ($p_{amb} = 0$) is written as ω_0, the resonance frequency as function of pressure can be written as:

$$\omega^2 = \omega_0^2 + \frac{p_{amb}}{g_0 \rho h}. \tag{9.17}$$

The result is consistent with the one obtained by Andrews et al. [210] for a square plate and equal to the pressure response of a piston since $\Delta\omega^2 = p_{amb}/(g_0\rho h)$. Note, that the shape, boundary conditions, thickness and tension do influence ω_0, but not the pressure response. Only the mass of the membrane and gap size influence the pressure response. This is a useful property, since the behavior of the sensor can be predicted by measuring the gap size, flake thickness and frequency at vacuum, which simplifies the analysis of the measurement.

From eq. 9.13 a useful identity can derived that will be used in the next section:

$$\left(\nabla^4 - \frac{n_0}{D}\nabla^2 - \lambda^4\right) W = 0, \tag{9.18}$$

$$\left(\nabla^2 + \alpha^2\right)\left(\nabla^2 - \left(\frac{n_0}{D} + \alpha^2\right)\right) W = 0, \tag{9.19}$$

$$\alpha^2 = -\frac{\nabla^2 W}{W} \text{ and } \frac{n_0}{D} + \alpha^2 = \frac{\nabla^2 W}{W}. \tag{9.20}$$

Note, that as a result of the separation of variables the ratio $\frac{\nabla^2 W}{W}$ becomes a constant that is no longer dependent on position. In eqs. 9.13 and 9.20, the relation between the constants α and λ is:

$$\lambda^2 = \alpha^2 \sqrt{\frac{n_0}{D} + \alpha^2}. \tag{9.21}$$

For circular plates we can write:

$$\alpha = \frac{\gamma_{mn}}{a}, \tag{9.22}$$

where γ_{mn} is the root of the frequency relation [217], which depends on the boundary conditions and mode-shape of the diaphragm. a is the radius of the diaphragm.

A3: FREQUENCY RANGE FOR COMPRESSION IN SQUEEZE-FILM SENSORS

In the derivation of the pressure response of the sensor (eq. 9.17) it is assumed that the gas is compressed at very high frequency. In this section we derive the minimal frequency at which this assumption is valid. For this purpose, the linear Reynolds equation is written as [43]:

$$p_{amb}\nabla^2 p - \frac{12\mu}{g_0^2}\frac{\partial p}{\partial t} = \frac{12\mu p_{amb}}{g_0^3}\frac{\partial g}{\partial t}. \tag{9.23}$$

Use $g = g_0 + w$ and substitute eq. 9.7:

$$\frac{p_{amb}^2}{g_0}\nabla^2 w + \frac{12\mu p_{amb}}{g_0^3}\frac{\partial w}{\partial t} = \frac{12\mu p_{amb}}{g_0^3}\frac{\partial w}{\partial t}. \tag{9.24}$$

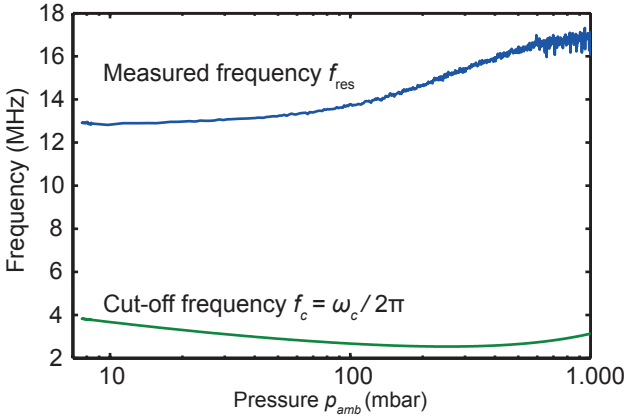

Figure 9.9: Measured resonance frequencies compared to the cut-off frequency (eq. 9.26).

The left and right side become equal when the following condition applies:

$$\frac{p_{\text{amb}}^2}{g_0}\nabla^2 w << \frac{12\mu p_{\text{amb}}}{g_0^3}\frac{\partial w}{\partial t}. \tag{9.25}$$

Since w is assumed to undergo harmonic motion, one can write $w = CW(x,y)\sin\omega t$, where C is the amplitude and $W(x,y)$ the mode-shape. Using $\frac{\nabla^2 W}{W} = -\frac{\gamma_{mn}^2}{a^2}$ from the previous section, we can write for circular diaphragms:

$$\omega >> \omega_c = \frac{p_{\text{amb}} g_0^2 \gamma_{mn}^2}{12\mu a^2}. \tag{9.26}$$

9

The frequency from Fig. 9.6**a** (upwards sweep) is plotted in Fig. 9.9 and compared to eq. 9.26. The measured frequency is much higher than the cut-off frequency, which shows that eq. 9.17 should be valid. Since the mean free path of the gas molecules is of the same order as the dimensions of our device, it is no longer valid to use the bulk viscosity (μ_0). Instead, the model proposed by Veijola [218] is used to approximately correct the viscosity (μ_{eff}) with the formula:

$$\mu_{\text{eff}} = \frac{\mu_0}{1 + 9.638\text{Kn}^{1.159}}, \tag{9.27}$$

where Kn is the Knudsen number defined as the ratio between the mean free path and the gap size. Note, that this model loses its validity at pressures lower than approximately 30 mbar, since the mean free path becomes of the same order as the diameter of the cavity. More sophisticated modeling is necessary to determine a more appropriate effective viscosity for this situation.

10

SQUEEZE-FILM EFFECT ON SINGLE LAYER GRAPHENE RESONATORS: INERTIAL EFFECTS AND GAS ACTUATION

Vibrating graphene membranes present an excellent opportunity for sensing because of their very high surface-to-mass ratio combined with their ultimate strength. Suspending these membranes over a thin film of gas is a promising concept for a pressure sensor using the squeeze-film effect. Development of such sensors requires an understanding of their pressure-dependent stiffness and dissipation, but also requires a feasible actuation mechanism. Here we study the effects of a squeezed film of gas coupled to a single layer graphene resonator. The squeeze-film stiffness effect is found to significantly decrease when the Reynolds number is near 1, resulting in undesired gas dependence of the resonance frequency. We also show that an optical drive can be used to modulate the temperature in the squeeze-film of the gas, resulting in a high-frequency pressure modulation. This provides a high actuation force compared to the force in a vacuum environment and shows that thermal actuation can be very efficient in graphene squeeze-film pressure sensors.

Parts of this chapter consists of an article in preparation [219].

THE hexagonal structure of graphene gives rise to unique electronic properties, which has attracted considerable interest in the scientific community [2]. Moreover, the strong bonds between the carbon atoms make this material one of the strongest materials ever measured [10, 220]. Combined with its ultrahigh surface-to-mass ratio by virtue of its thinness, makes this material very interesting for various sensing applications such as pressure and gas sensors [11, 35, 44, 58, 59]. Graphene pressure sensors using the squeeze-film effect have been proposed, since they promise high responsivity, while at the same time significantly reducing the sensor area [44, 59] (chapter 9). These sensors compress the gas in a shallow cavity underneath the vibrating membrane, raising the stiffness of the system. For pressure sensor operation, it is required that this stiffness effect is independent of the composition of the gas. Since the quality factor of resonance limits the pressure range in which these sensors can operate, it is also of interest to study the pressure and gas dependence of the quality factor. While several studies have shown pressure-dependence of 2D material resonators in air or a few gases [59, 209], there is no systematic study showing the gas dependence of the squeeze-film effect with a diverse range of gases. This needs further investigation as the resonance frequency and dimensions of the device are orders of magnitude different from MEMS squeeze-film pressure sensors [59, 211, 213], which might have a severe impact on the sensor performance.

Here we study the squeeze-film effect on single-layered graphene resonators by measuring the pressure and gas dependence of the resonance frequency and quality factor. We use opto-thermally actuated drum resonators with a diameter of 5 microns suspended over a 300 nm deep cavity with a venting channel to the environment. The fabrication of these devices and the setup to actuate and detect their motion is shown in chapter 3. The squeeze-film effect arises due to the high-frequency motion of the graphene resonator, which compresses the thin layer of gas in the cavity [43, 59, 210–213, 221]. Ideally, the pressure-dependent resonance frequency ω of the membrane is described by:

$$\omega^2 = \omega_0^2 + \frac{p}{g_0 \rho h} \tag{10.1}$$

where ω_0 is the resonance frequency in a vacuum environment, p the pressure, g_0 the distance between the moving membrane and fixed substrate and ρh the membrane's mass per unit square (see chapter 9 for the derivation).

Equation 10.1 predicts a linear dependence on stiffness as a function of pressure, which is gas-independent. We find however in the experiments that the stiffness increase is sublinear. This deviation occurs when the Reynolds number is near 1, which makes inertial forces in the gas flow important and affects the compressibility of the squeeze-film. The quality factor of resonance is very low at high pressures, between 1 and 3, with weak gas dependence and little effect from the inertia forces. Finally, we show that the opto-thermal drive results in a high-frequency temperature and pressure modulation in the squeezed-film of gas, which actuates the membrane. We find that the actuation force at 1000 mbar is three times higher than the force in a vacuum environment. This shows that thermal modulation is an efficient actuation mechanism for graphene squeeze-film pressure sensors.

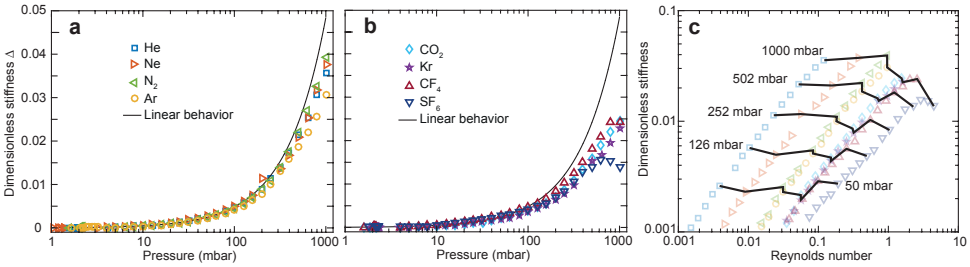

Figure 10.1: Squeeze-film stiffness as function of pressure and gas. **a, b** Dimensionless stiffness Δ as function of gas pressure for eight different gases. The linear behavior line in both figures is obtained by fitting a polynomial to the helium response and plotting only the linear part. **c** Δ as function of Reynolds number. Black are connect the different gases at certain fixed pressures, which ideally should be constant but instead shows a deviation for Re > 1.

10.1. RESULTS

Figures 10.1**a,b** show the dimensionless squeeze-film stiffness Δ as function of pressure for eight different gases. Δ is defined based on eq. 10.1:

$$\Delta = (\omega^2 - \omega_0^2)\frac{\rho h g_0}{P_{\text{ref}}}, \tag{10.2}$$

where P_{ref} is a reference pressure chosen to be 1000 mbar, ρh is assumed to be 7.7×10^{-7} kg/m^2 and g_0 is assumed to be 300 nm. For all gases, the stiffness increases as a function of gas pressure as expected from eq. 10.1. The solid black lines in Figs. 10.1**a,b** are obtained by fitting a second order polynomial to the Δ of helium and plotting only the linear part. Ideally one expects linear behavior from Δ as a function of pressure. It is observed, however, that for all gases in this drum Δ is sublinear. While for all the gases Δ matches closely up to 100 mbar, at higher pressure significant deviations between the gases are observed. Denser gases tend to show larger deviations in Δ as the pressure is increased, suggesting that the density of the gas is the root cause of the effect.

To study this further, Δ is plotted as a function of the Reynolds number Re certain at constant pressures, as shown in Fig. 10.1**c**. The Reynolds number is defined as:

$$\text{Re} = \frac{\omega \rho_g g_0^2}{\mu} \tag{10.3}$$

where ρ_g is the density of the gas and μ the viscosity. The Reynolds number compares the inertial forces to the viscous forces in the squeeze-film gas flow. When Re $\ll 1$, inertial forces are negligible and eq. 10.1 should be valid provided that the resonance frequency is high enough. Plotting the dimensionless stiffness as a function of Reynolds number in Fig. 10.1**c** shows that at low pressures (approximately $p < 100$ mbar) Δ is close to constant within the accuracy of the measurement. This corresponds to a Δ that only depends on pressure, as expected from eq. 10.1. Significant gas dependence of Δ occurs at high pressures approximately when Re > 1. This represents the regime where inertial forces are affecting the squeeze-film effect in this drum since stiffness depends on the gas density.

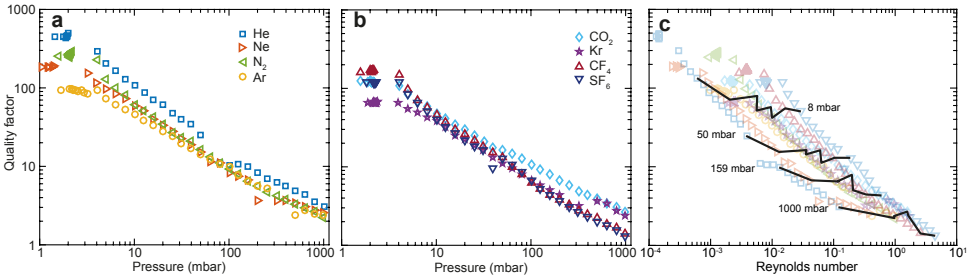

Figure 10.2: Squeeze-film damping as a function of pressure and gas. **a,b** Quality factor of the fundamental resonance as a function of pressure for eight different gases. **c** Quality factor as a function of Reynolds number for 3 fixed pressures.

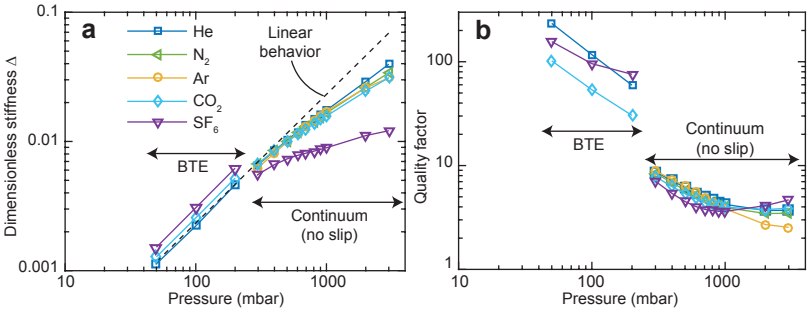

Figure 10.3: Simulations of resonance frequency and quality factor for a representative squeeze-film pressure sensor. **a** Dimensionless frequency shift, showing a clear deviation for sulfur hexafluoride. **b** Quality factor of resonance.

The quality factor as a function of gas pressure is shown in Fig. 10.2**a**,**b**. For all gases, the quality factor decreases as a function of pressure due to the viscous dissipation forces, with a similar slope on a logarithmic scale. Throughout the pressure range studied here, low-density gases tend to show less dissipation than high-density gases. The quality factor changes with less than an order of magnitude as a function of molecular weight of the gases, which means that the impact on the functionality as a squeeze-film pressure sensor is relatively low. The inertial forces do not introduce a clear effect when $\mathrm{Re} > 1$. However, the low values of the quality factor limit the pressure range in which these devices could operate as a pressure sensor.

10.2. SIMULATIONS OF INERTIAL EFFECTS

To understand the effect of the gas flow on the membrane's resonance properties, more sophisticated methods are needed in order to investigate whether eq. 10.1 is valid. Several assumptions lie behind this equation, it is, for example, assumed that the resonance frequency is sufficiently high for compression. Furthermore, inertia effects are ignored and rarefied gas effects are not included. The mean free path of nitrogen is 70 nm at 1000 mbar and the cavity depth is 300 nm, therefore rarefied gas dynamics should play a large

role in this system.

Two approaches were used to check whether eq. 10.1 is valid. First, finite element simulations were performed by solving the compressible unsteady Stokes equation for the gas together with Navier's equation for the solid membrane using the eigenfrequency solver of COMSOL Multiphysics [222, 223]. An axisymmetric slice of the drum is considered in this continuum model (see Appendix A3). No-slip boundaries were implemented, meaning that this model includes inertia effects but no rarefied gas effects.

To obtain more certainty regarding the effects of rarefaction, an additional set of simulations were performed using the frequency-domain Monte Carlo method [224, 225]. This approach solves the Boltzmann Transport Equation (BTE), therefore it should provide more accurate results for low gas pressures. Since the mass of the membranes studied here is not certain due to contamination, we simulate a different device with 31 layers graphene, a gap size of 400 nm and a diameter of 5 micron from chapter 9. The simulations were benchmarked against these results as shown in the Appendix A3.

10.2.1. SIMULATION RESULTS

Figure 10.3 shows the dimensionless frequency shift and the quality factor from simulations of the device in chapter 9. In agreement with the experiments performed here we find that the continuum simulations predict a density dependence of the stiffness (Fig. 10.3**a**). In particular sulfur hexafluoride shows a clear deviation from the other gases. The deviation of all the gases around 200 mbar was also observed experimentally in chapter 9 [59]. But since only helium, nitrogen and carbon dioxide were studied, the gas dependence could not be clearly observed. In the benchmark in Appendix A3 we qualitatively compare the experimental results from chapter 9 to the simulations.

The simulated quality factor as a function of pressure in Fig. 10.3 shows a similar weak gas dependence as a function of molecular weight. At high pressures, however, the simulations suggest that the quality factor could increase as a function of pressure. This behavior has not yet been observed in experiments due to the limited pressure range that could be achieved. The BTE simulations show a significantly larger quality factor since slip flow is included in this model.

10.3. GAS ACTUATION

While performing these measurements we observe an unusual pressure-dependence of the amplitude of the resonator, as shown in Fig. 10.4 for the case of a neon atmosphere. At the red dashed line in Fig. 10.4**a**-**b** it is observed that the magnitude of the response is diminished and the motion changes phase by 180 degrees. From the amplitude A, resonance frequency ω and quality factor Q, we can estimate the actuation force on the resonator: $F \propto A\omega^2/Q$, which is normalized to yield $F = 1$ at the lowest pressure. Fig. 10.4**c**, shows that F shows a minimum around 200 mbar and then increases again as the pressure increases. The force even exceeds three times the force in vacuum at 1000 mbar. This result is unexpected since the force is coming from the thermal actuation of the membrane. Since the conductance is expected to increase as a function of pressure due to heat conduction through the gas, the temperature modulation should be lower at higher pressures. Consequently, it is expected that the force decreases monotonically as

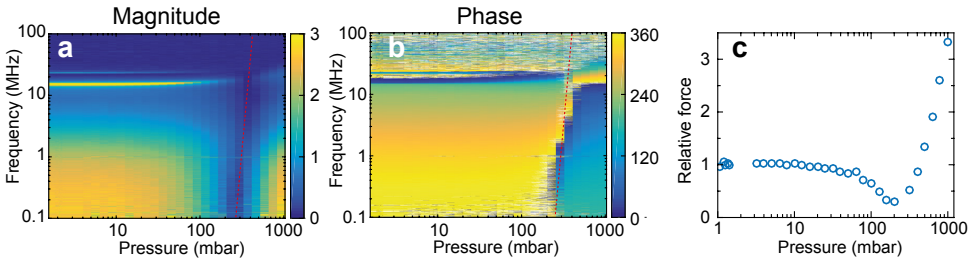

Figure 10.4: Pressure dependence of the mechanical response in a neon environment. **a** Magnitude of the transmitted signal as a function of pressure. The red dashed line marks the zero magnitudes as a guide to the eye. **b** Phase of the transmitted signal as a function of pressure, the red dashed line indicates the phase shift of 180 degrees, which coincides with the zero magnitudes. **c** The actuation force with respect to the force in vacuum extracted from the fundamental resonance.

a function of pressure.

This effect can be explained if we assume that the gas in the squeeze-film is temperature modulated along with the membrane. Due to this temperature modulation, the gas will expand which in turn results in pressure modulation. If the resonance frequency is much higher than the inverse of the pressure relaxation time τ_P of the cavity $\omega \ll 1/\tau_P$, this pressure will actuate the membrane. We will measure τ_p to confirm this condition is met as shown below. There are thus two distinct forces arising from the opto-thermal drive: (1) the thermal expansion force in the membrane and (2) the pressure modulation in the cavity.

The thermal expansion force can only actuate the membrane if we assume that the membrane has some out-of-plane static deflection w_0, which can be induced by the wrinkles or other imperfections in the graphene membrane. If w_0 is positive, the mechanical response is in-phase with the drive at low frequencies, while if w_0 is negative, the mechanical response will be 180 degrees out of phase with the optical drive. This mechanism is confirmed by applying a pressure difference over a membrane without a venting channel as shown in the Appendix A2. In this particular case, the membrane has a positive w_0, which means that an increase in temperature results in a downward net force on the membrane. The gas expansion will, however, result in a net upwards force as the temperature increases. These mechanisms are competing and around 200 mbar both forces exactly cancel out, resulting in zero motion. As the pressure is increased further, the gas expansion force dominates and the mechanical response is out-of-phase compared to vacuum.

Further information on this mechanism can be found by examining the mechanical response below the resonance frequency, to study the frequency-dependence of the actuation force. As the blue laser heats up the membrane periodically we find that the amplitude responds with a typical time delay $\tau \approx 70$ ns, due to the time necessary for the heat to diffuse through the membrane (see chapters 5 and 6) [60]. At frequencies below the resonance frequency, we can approximate this response by:

$$z_\omega = \frac{AP_{\text{ac}}R}{i\omega\tau + 1} = AP_{\text{ac}}R\frac{1 - i\omega\tau}{1 + \omega^2\tau^2}. \tag{10.4}$$

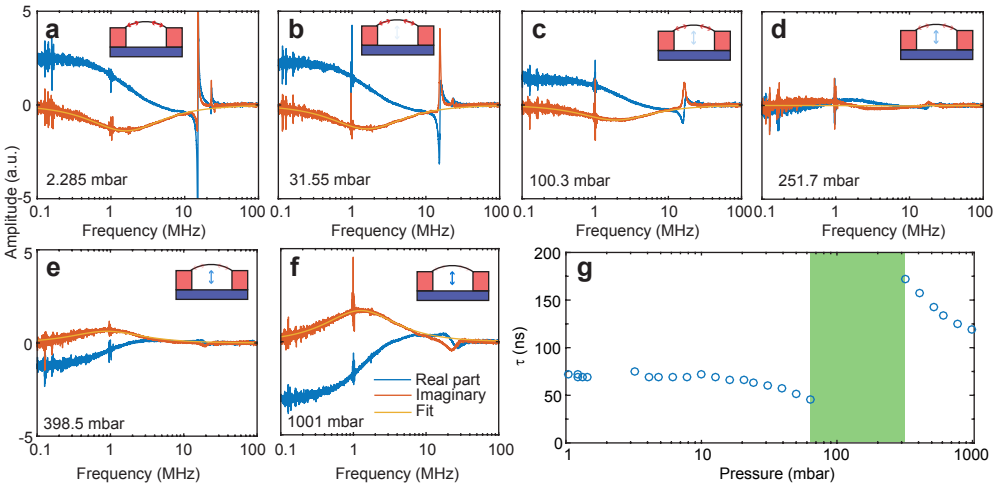

Figure 10.5: Pressure dependence of the mechanical response in neon atmosphere. The insets in each figure indicate whether the thermal expansion force (red arrows) or the gas expansion force (blue arrows) dominates. **a** In-phase (Real) and out-of-phase (Imaginary) component of the amplitude at 2.285 mbar, **b** 31.55 mbar, **c** 100.3 mbar, **d** 251.7 mbar, **e** 398.5 mbar and **f** 1001 mbar. **g** Time constants extracted from the imaginary part of the response as function of pressure. In the green area the frequency-dependence of both actuation forces is present, which means that we could not use eq. 10.4 to fit to the response and extract τ.

In Fig. 10.5**a**-**f** the real and imaginary part of the response are shown for different pressures. We use only the imaginary part to find the time constant as the real part might be affected by optical cross-talk. We observe a decreasing amplitude until the response is almost flat at 257.7 mbar (Fig. 10.5**d**). As the pressure is increased, real and imaginary part change their sign and the amplitude increases as a function of pressure.

Extracting the thermal time constant as a function of pressure in Fig. 10.5**g**, reveals that the time constants in the high- and low-pressure regimes are different. At low pressures, the thermal time constant is decreasing as a function of pressure. This decrease is indicative of the Pirani effect, making conduction of heat in the gap pressure-dependent. The additional conduction path decreases the time necessary to heat up the membrane, thus decreasing τ. The distinct difference in time constant in the high-pressure regime suggests that the underlying mechanism behind the actuation is indeed different from the low-pressure regime because we would expect a monotonic decrease of τ as a function of pressure. Therefore, the time constant in the high-pressure regime is most likely the pressure relaxation time of the cavity τ_p. Note that the two different values of the time constants explain why the minimum in amplitude is not found at a fixed pressure but is both pressure- and frequency-dependent as shown by the red dashed line in Fig. 10.4.

10.4. DISCUSSION

We observe that at high pressures the dimensionless stiffness becomes gas dependent and is correlated to the density of the gas. Figure 10.1**c** shows that this occurs if the

Reynolds number is close to 1. Most of the previously studied devices [59, 211, 213] operate in the regime where Re $\ll 1$, which means that the Navier Stokes equation reduces to the Reynolds equation that neglects the inertial forces of the gas [43]. Neglecting the inertial forces results in eq. 10.1, if the frequency is sufficiently high. The measurements in Fig. 10.5**g** verify that the resonance frequency is sufficiently high since $\omega \gg \frac{1}{\tau_p}$. We thus conclude that inertial forces cannot be neglected and this explains why eq. 10.1 fails to accurately describe the resonance frequency of the system. This is supported by the continuum simulations which show similar effects as observed in the experiments.

The gas dependence of the frequency response has an important consequence on the application of these membranes as pressure sensors. A squeeze film pressure sensor is ideally only sensitive to the pressure according to eq. 10.1. Our results suggest that the gas dependence is reduced if the Reynolds number Re $\ll 1$. To obtain pressure sensor functionality around a pressure of 1000 mbar, the gap size of the sensor should be reduced since Re $\propto g_0^2$ if the pressure dependence of ω is small. Including the pressure dependence of ω and assuming the intrinsic stiffness of the device is small: Re $\propto g_0^{3/2}$.

In the Appendix A1, we show a second drum with a 4-micron diameter. This drum shows significantly higher gas-dependence of the dimensionless stiffness, which can be attributed to the higher vacuum resonance frequency since $\omega_0 \propto a^{-1}$. This yields a higher Reynolds number and explains the larger deviations. Also, we observe that gas-dependent deviations start at a lower Reynolds number around 0.1. This suggests that a different dimensionless number might be more appropriate. For Re $\ll 1$ the squeeze-number σ is often employed [43] (chapter 9):

$$\sigma = \frac{12\mu\omega a^2}{P_a g_0^2}, \tag{10.5}$$

but this cannot be employed in this case since the Reynolds number is too high. Adapting the squeeze-number to include inertial effects in the gas flow could be more insightful to accurately predict deviations from eq. 10.1 and include any size dependence of the drum.

It should be noted that we should expect that $\Delta = 1$ at 1000 mbar, since we used a reference pressure of 1000 mbar and a reference mass ρh of single-layer graphene. However, we measured a significantly lower stiffness effect for all gases. It is thus very likely, that the mass of these membranes is significantly higher, where a mass increase with a factor of 25 would agree with our experimental results. Different works have measured the mass of single-layer graphene and in almost all cases it is significantly higher than its theoretical value [11, 12, 62, 226, 227]. We also find strong indications that the mass of these resonators is significantly higher in the outlook, although 25 times higher seems too much to be explained by the preliminary measurements in chapter 13. High-temperature annealing of the graphene was attempted to solve this problem, but this results in failure of the suspended drums.

The increased mass of the membranes reduces the frequency shift, but reducing the mass ρh will probably not result in the ultra-high frequency shift promised by eq. 10.1. Because of the high resonance frequency that should occur at high pressures, the Reynolds number will be very high. This will result in the lower stiffness and gas dependence observed in this work. Therefore, the optimal design of a graphene squeeze-film

pressure sensor should use multi-layer graphene, to ensure that ω is not too high and that $\mathrm{Re} \ll 1$ in the desired pressure range. In that respect, multi-layer graphene pressure sensors could be closer to an optimal solution such as the wafer scale fabricated sensors in chapter 13 [44]. Also, the tunable gap size of those sensors can be very useful to reduce inertial effects on the gas flow, since the Reynolds number reduces with a smaller gap size.

10.5. CONCLUSION

We measure the effects of a thin layer of gas underneath a single layer graphene resonator. Due to the squeeze-film effect, the stiffness of the resonator increases as a function of pressure. This stiffness increase is linear and gas-independent at low pressures. At high pressure above ~100 mbar, the stiffness becomes sublinear as a function of pressure and gas dependent. Gases with a high molecular mass show a lower stiffness effect at high Reynolds numbers. The quality factor decreases strongly as a function of pressure and shows a weak gas dependence. Gases with a low molecular mass show the highest quality factor. Finally, we show that the squeeze-film effect can be used to actuate the resonator by high-frequency modulation of the pressure in the gas film. Depending on the configuration of the membrane, this force can counteract the thermal actuation of the membrane and result in a stagnated motion at a certain pressure. Future work will focus on characterizing, understanding and reducing the apparent higher mass of the single layer graphene resonator. Also, further optimization of multilayer graphene sensors can be performed to minimize inertial effects in the gas flow.

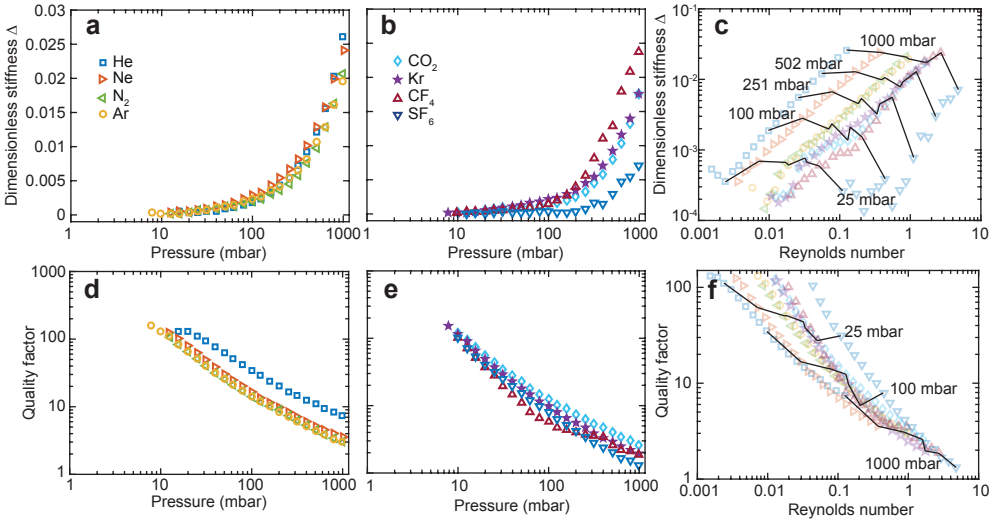

Figure 10.6: Results on a different drum with a diameter of 4 micron. **a**,**b** Pressure-dependent dimensionless stiffness for 8 different gases. **c** Dimensionless stiffness as function of Reynolds number, black lines indicate certain constant pressures. **d**-**e** Quality factor of the fundamental resonance as function of pressure for 8 different gases. **f** Quality factor as function of Reynolds number, solid black lines indicate certain fixed pressures.

APPENDIX

A1: ADDITIONAL MEASUREMENTS

Figure 10.6 shows the pressure and gas dependence of the dimensionless stiffness of a 4 micron diameter drum. We observe in Figs. 10.6**a** and **b** that the dimensionless stiffness is gas dependent and the gases with high molecular mass show low compression. The stiffness of SF_6 is significantly lower even at lower pressures. Plotting the dimensionless stiffness as function of the Reynolds number shows that the transition occurs at lower Reynolds number, as discussed above. The quality factor of resonance in Fig. 10.6**d**-**e** shows similar behavior and values as the 5 micron drum. No significant deviations of the quality factor are found once the Reynolds number is close to 1 (Fig. 10.6**f**).

A2: PHASE-DEPENDENCE OF THE MECHANICAL RESPONSE ON THE INITIAL DEFLECTION

To show that the thermal actuation depends on the up-or-down configuration of the membrane, we perform an experiment on a closed drum. Figure 10.7**a** shows the complex amplitude of the membrane without pressure difference, due to the imperfections in the membrane it is effectively deflected upward. Immediately after pressure is increased to 200 mbar, the complex amplitude has changed sign (Fig. 10.7**b**), which corresponds to a 180 degrees phase shift. Due to leakage, the pressure difference over the drum decreases, which is observed as a gradual decrease in amplitude in Figs. 10.7**c**-**d**. The membrane passes through a flat configuration in Fig. 10.7**e**, where we observe

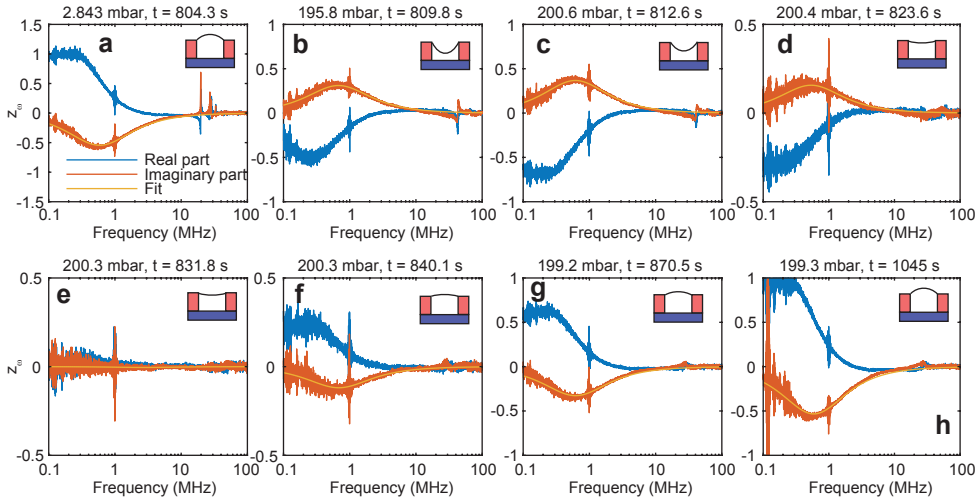

Figure 10.7: Measurement with a pressure difference over a 5-micron diameter closed drum to show that the thermal actuation depends on the configuration of the membrane. The insets show the configuration of the membrane, each subfigure corresponds to a different time.

that the signal almost completely disappears. After a few seconds, in Fig. 10.7**f** the signal reappears with opposite sign. Gradually the amplitude of signal further increases when the pressure difference decreases further (Fig. 10.7**g**). After a long time, the low-frequency response is close to the original amplitude, but the resonance is damped due to the gas that has permeated into the cavity (Fig. 10.7**h**). These measurements confirm the mechanism for direct actuation discussed in chapter 7.

A3: SIMULATIONS

Figure 10.8 shows the simulations of the 31 layer graphene drum from chapter 9, we use this sample as the mass of this membrane is well known. We consider an axisymmetric domain around the center of the membrane (Fig. 10.8**c**) and calculate the resonance frequency and quality factor of the fundamental mode. In the experiments a deviation from eq. 10.1 was observed above 200 mbar. Both the continuum and the BTE model correctly predict this deviation as shown in Fig. 10.8**a**. The quality factor shows reasonable agreement with the experiments (Fig. 10.8**b**).

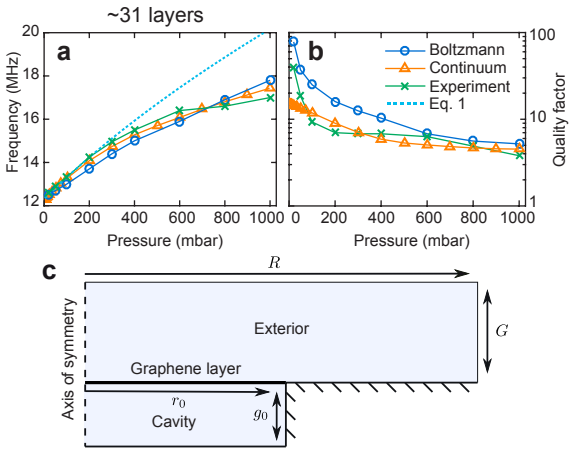

Figure 10.8: Benchmark of the 3 theoretical models and experimental results on multilayer graphene. **a** Resonance frequency as a function of pressure for a ~31 layered device [59] with a 5-micron diameter in a nitrogen environment. **b** Quality factor as a function of pressure for the ~31 layer device. **c** Schematic of the domain used for numerical simulations. For both the Navier-Stokes (NS) and Boltzmann Transport Equation (BTE) simulations the domain was taken to be axisymmetric around the center of the device, with the drum being fully enclosed. For each of the pressures shown in a-d, the bounds on the exterior domain, R, and G, were increased until a consistent frequency and quality factor was achieved. In the case of the BTE simulations, bounds of at least $R = 3r_0$ and $G = 40g_0$ were used.

11

GAS OSMOMETERS

We show that graphene membranes that separate two gases at identical pressure are deflected by osmotic pressure. The osmotic pressure is a consequence of differences in gas permeation rates into a few-layer graphene enclosed cavity. The deflection of the membrane is detected by measuring the tension-induced resonance frequency with an interferometric technique. Using a calibration measurement of the relationship between the resonance frequency and pressure, the time-dependent osmotic pressure on the graphene is extracted. The time-dependent osmotic pressure for different combinations of gases shows large differences that can be accounted for by a model based on the different gas permeation rates. In this way, a graphene-membrane based gas osmometer with a responsivity of ~60 kHz/mbar and nanoscale dimensions is demonstrated.

Parts of this chapter have been published in 2D Materials **4** (1), 011002 (2017) [58].

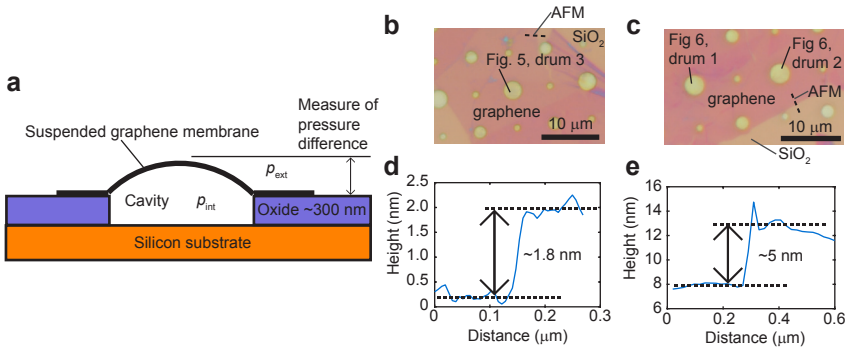

Figure 11.1: **a** Schematics of a graphene-based osmometer. **b** Optical image of the graphene resonators presented in this study in Fig. 11.5. **c** Optical image of the graphene resonators presented in Fig. 11.6. **d** Atomic force microscopy (AFM) trace corresponding to Fig. 11.1**b**, showing that the graphene resonator has a thickness of about 1.8 nm. **e** AFM trace corresponding to Fig. 11.1**c**; these drums have a thickness of approximately 5 nm.

GRAPHENE in its pristine form is impermeable to gases [11]. However, when pristine graphene is suspended over cavities in silicon dioxide, non-zero permeation rates between the cavity and the environment have been measured [11]. The permeation rate was found to depend on the type of gas even in pristine samples [35] and graphene enclosed cavities can, therefore, be selectively-permeable. The leakage between the cavity and its environment can be attributed to slow permeation through the silicon dioxide layer [11, 228] or along the graphene-oxide interface. In addition, selectivity has also been measured in thinly layered graphene membranes [229].

When a selectively-permeable membrane separates different gases, osmotic gas flow causes a pressure difference across the membrane which is defined as the osmotic pressure [230]. The high Young's modulus [10] and low bending rigidity of graphene cause a large pressure-induced frequency shift and deflection, which is beneficial for several types of pressure sensors [33, 59, 231]. In this work, we combine the selective leak rates that graphene-sealed cavities can exhibit with the excellent responsivity that suspended graphene membranes show when subjected to a pressure difference. We use graphene enclosed cavities which are selectively permeable to demonstrate osmotic pressure sensing for several combinations of gases, creating a nanoscale osmometer. Due to osmosis between the cavity and environment, it is observed that a pressure difference builds up over the membrane, even though the pressure on both sides is equal at the start of the experiment. This shows that these systems respond to changes in gas composition in the environment.

11.1. FABRICATION AND CALIBRATION OF OSMOMETERS

Graphene membranes are suspended over cavities etched in thermally grown silicon dioxide. A schematic device cross-section is shown in Fig. 11.1**a**. A few-layer graphene flake with varying thickness is exfoliated from natural graphite. The flake is transferred

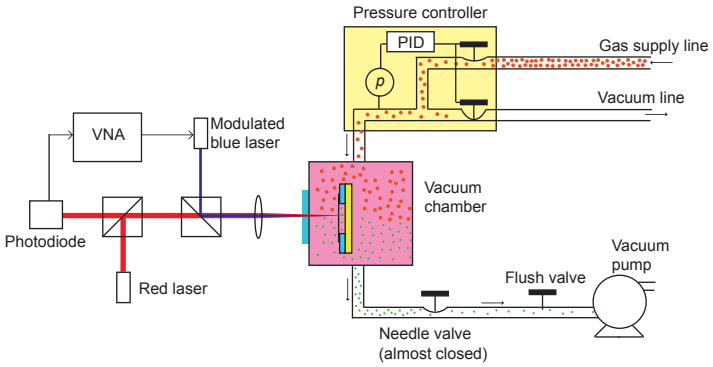

Figure 11.2: Laser interferometer setup (left-hand side of the figure) used to detect the resonance frequency and the vacuum chamber with the most important components for flushing the system at constant pressure (right-hand side of the figure).

by a deterministic dry-transfer method [56] to enclose cavities with a diameter of 3 μm (Fig. 11.1**b**–**e**, see also chapter 3 for the fabrication method). It is found that such a device creates a selectively permeable system, without any further processing necessary.

The pressure difference across the membrane can be determined using the membrane's resonance frequency [11, 35, 59], measured by the interferometric setup shown in Fig. 11.2**a** [67, 68]. A modulated blue laser provides opto-thermal actuation, while a red laser is used for interferometric readout of the deflection. A vector network analyzer (VNA) probes the mechanical frequency response of the membrane (Fig. 11.2**b**). The sample is mounted in a vacuum chamber with optical access and a dual valve pressure controller is used to keep the pressure in the chamber (p_{ext}) constant throughout the experiment. A line to the vacuum pump is connected to the chamber with a flush valve. The gas in the chamber is changed by switching the gas supply line and opening the flush valve. A needle valve restricts the flow to minimize pressure drops between the controller and the chamber. This prevents membrane deflections due to changes in p_{ext}.

Previous methods to extract the pressure difference from the resonance frequency of the membrane rely on the knowledge of the mechanical properties as mass and Young's modulus and the application of equations governing the membrane behavior [11]. These are difficult to obtain experimentally. Instead, we determine the pressure difference over the membrane by a calibration procedure (Fig. 11.3) from which the relation between pressure difference and the resonance frequency is directly determined. The procedure works as follows; first, the membrane is kept in $p_{\text{ext}} = 0$ until the pressure difference is relaxed, which gives the first calibration point (green hexagon in Fig. 11.3**c**). By increasing the pressure in the chamber rapidly, the membrane will deflect downwards and therefore the pressure difference becomes negative. The immediate change in resonance frequency gives a calibration point at negative pressure (Fig. 11.3, point A). Due to the gas leakage, the pressure over the membrane will equilibrate, the frequency is measured at this point to quantify the squeeze-film effect (see Appendix A2). After this, the chamber is rapidly evacuated to $p_{\text{ext}} = 0$. Since the membrane will deflect upwards in that case, a calibration point for positive pressure difference is obtained (Fig. 11.3, point

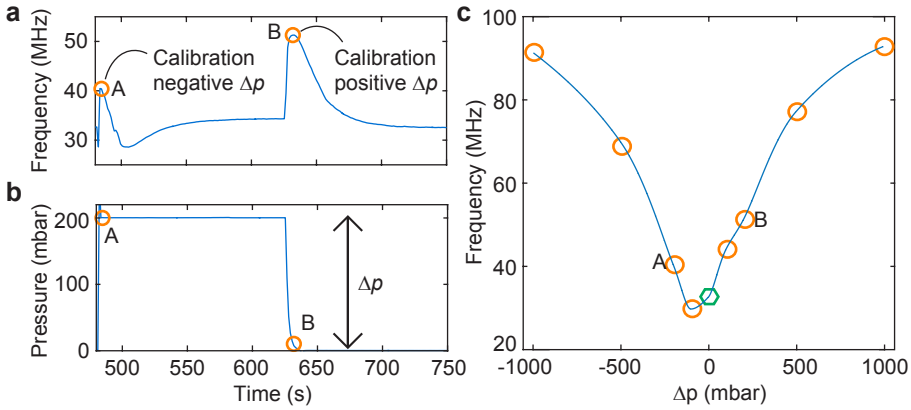

Figure 11.3: Calibration method to extract the relation between pressure difference and frequency. This figure shows the calibration point for −200 mbar (point A) and +200 mbar (point B) for drum 3. **a** Resonance frequency versus time when the external pressure is varied as shown in figure **b**. **c** The calibration curve for drum 3 resulting from the calibration procedure; the hexagon represents the calibration point of the relaxed membrane at a pressure difference of zero and $p_{ext} = 0$.

B). By repeating this procedure for different pressures, the relation between frequency and pressure difference is obtained as shown in Fig. 11.3**c**. Using this relation the time-dependent osmotic pressure can be determined in the experiments, without having to rely on knowledge of the mechanical properties of the graphene membrane itself.

It is important to note that from Fig. 11.3**c**, it is observed that the minimum in frequency does not correspond to a pressure difference of zero, but is shifted towards negative pressure differences and is around -100 mbar in this case. This is not in agreement with the conventional theory which predicts a symmetric response around $\Delta p = 0$. The cause of this effect is unknown, however, we take advantage of this since it allows us to distinguish between positive and negative pressure differences as shown in section 11.3. From the calibration curve, it is further concluded that this graphene-based osmometer has an average responsivity of approximately 60 kHz/mbar over the entire pressure range.

11.2. EXPERIMENTAL PROCEDURE

In the experiment, the gas outside the cavity is changed, while the pressure outside the cavity p_{ext} is kept constant. Deflections of the membrane due to external pressure changes are avoided and changes in the pressure difference $\Delta p = p_{int} - p_{ext}$ across the membrane should be attributed to changes in the internal pressure p_{int}.

Figure 11.4**a** shows the measurement procedure for studying the time dependent osmotic pressure across the membrane. The sample is kept for a long time (at least 1.5 hours) at a constant pressure in gas 1 (red), such that the internal and external pressure equalize $p_{ext} = p_{int}$ (Fig. 11.4**a**1). The external gas 1 is replaced by gas 2 (green molecules) while keeping the pressure p_{ext} constant (Fig. 11.4**a**2,3). This replacement is done rapidly to ensure that gas 1 remains present in the cavity at the same partial pres-

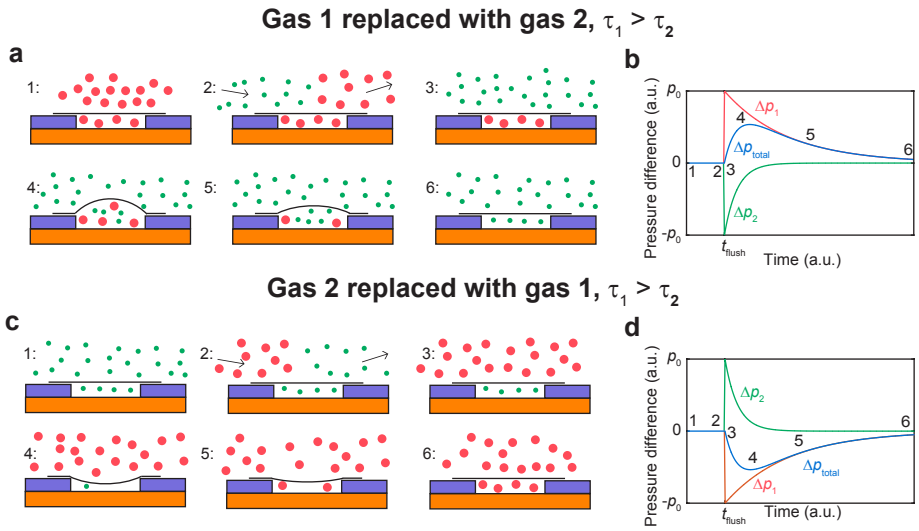

Figure 11.4: **a** Measurement sequence when replacing gas 1 (red) with a large leak time constant τ_1 by gas 2 (green) with a short leak time constant τ_2. **b** Time dependent partial pressures differences Δp_{part} of both gases and the total osmotic pressure Δp as described by eq. (11.1) for the measurement sequences depicted in Fig. 11.4**a**. **c** Measurement sequence when replacing gas 2 with a short leak time constant τ_2 by gas 1 (red) with a long leak time constant τ_1. **d** Partial pressures and total osmotic pressure for the sequence in Fig. 11.4**c**

sure as gas 2 in the vacuum chamber ($p_{1,\text{int}} = p_{2,\text{ext}}$). If the leak rate of gas 2 is higher than that of gas 1, gas 2 has a higher flux into the cavity than gas 1 flows out of it. Since the pressure inside the cavity is the sum of the partial pressures of gas 1 and 2, a positive pressure difference Δp arises that is the osmotic pressure (Fig. 11.4**a**4). Subsequently, gas 1 will leak out of the cavity at a slower rate (Fig. 11.4**a**5) until gas 1 fully disappears and the pressure difference returns to zero $\Delta p \approx 0$ (Fig. 11.4**a**6).

In a subsequent measurement gas 2 can be replaced by gas 1 in a similar manner which leads to the sequence shown in Fig. 11.4**d**. The main difference is that in this case a negative pressure difference Δp arises. Since the gas leakage has an exponential time dependence (see Appendix A5) the pressure difference versus time $\Delta p(t)$ can be expressed by the partial pressure differences (Δp_1 and Δp_2) for each gas as a function of time: $\Delta p_1 = p_0 e^{-t/\tau_1}$ and $\Delta p_2 = -p_0 e^{-t/\tau_2}$. Combining these equations gives for the total pressure difference:

$$\Delta p(t) = \Delta p_1 + \Delta p_2 = p_0(e^{-t/\tau_1} - e^{-t/\tau_2}), \tag{11.1}$$

where p_0 is the constant pressure in the environment, $\tau_{1,2}$ are the leak-time constants inversely proportional to the permeability of gas 1 and gas 2, respectively. The expected time dependence of the osmotic pressure Δp between two gases 1 and 2 with leak rates τ_2 and τ_1 as described by eq. (11.1) is depicted in Fig. 11.4**b**,**c**.

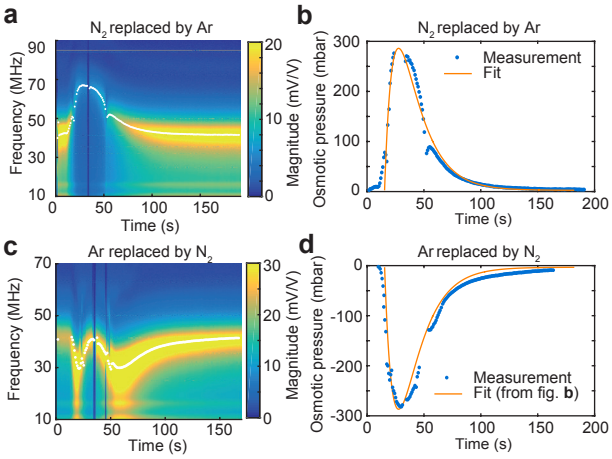

Figure 11.5: Measurement of the osmotic pressure between argon and nitrogen for drum 3 (Fig. 11.1b). a) Intensity plot of the frequency response function when nitrogen is replaced by argon in the chamber. White points show the extracted resonance frequency obtained from the fits. b) Osmotic pressure extracted from the experiment in Fig. 11.5a, fitted by a time-shifted version of eq. (11.1). c) Intensity plot of the reverse experiment, where argon gas was replaced by nitrogen. d) Extracted osmotic pressure from the experiment in Fig. 11.5c. The fit from Fig. 11.5b is plotted with opposite sign.

11.3. RESULTS

Figure 11.5 shows the results of an experiment where nitrogen gas was replaced with argon gas and vice versa, at a constant chamber pressure of $p_{\text{ext}} = 1000$ mbar. The resonance frequency is found by fitting the data to the frequency response function (Fig. 11.2**b**), which in turn yields the time-dependent resonance frequency. To extract the osmotic pressure from the experiment, we use the frequency-pressure difference relation shown in Fig. 11.3**c**.

Figure 11.5**a**,**c** show the intensity plots of the frequency response function as function of time. White points indicate the resonance frequencies determined by the fits. The strong difference between the two curves is a consequence of the shifted calibration curve, which allows us to distinguish between positive and negative osmotic pressure. Therefore, from Fig. 11.5**a** we can conclude that argon was permeating into the cavity faster than nitrogen could escape, creating a positive pressure difference. In Fig. 11.5**c**, the frequency passes through a minimum twice; a clear indication that a negative pressure difference has formed over the membrane. In this case, argon was escaping the cavity faster than nitrogen could enter. From the time-dependent resonance frequency and the calibration curve in Fig. 11.3**c**, the time-dependent osmotic pressure can be extracted as shown in Fig. 11.5**b**,**d**. Equation 11.1 (adapted to include a time shift between the start of the measurement and the gas being replaced) is fitted against the data in Fig. 11.5**b** to extract the leak time-constants of the gases [232]: $\tau_{N_2} = 19$ s and $\tau_{Ar} = 8$ s. The osmotic pressure as a function of time from this fit is plotted in Fig. 11.5**d** in good correspondence to the measurement result of the reversed experiment. This agreement between both experiments demonstrates that the osmotic pressure reverses sign when

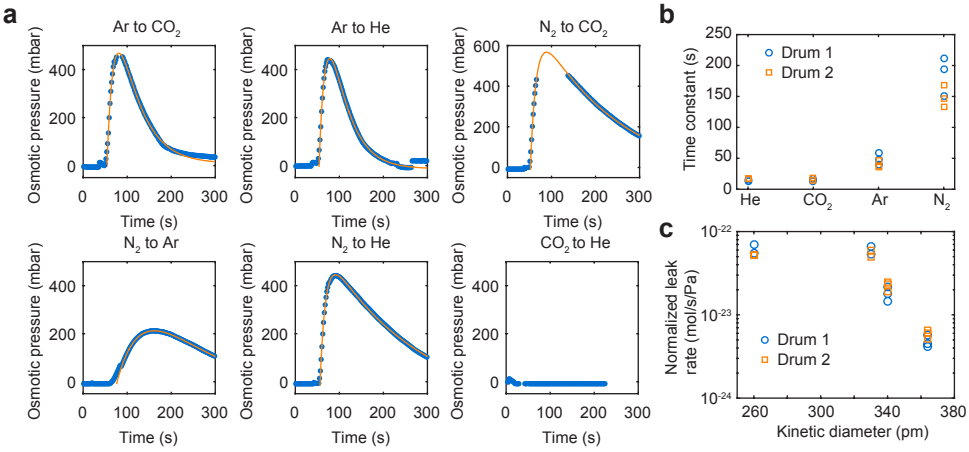

Figure 11.6: a) Measurement sequences as in Fig. 11.4a for 6 different gas combinations on a 5 nm thick drum (Drum 1) measured at 500 mbar. b Leak time constants τ extracted for 4 different gases using the fits in Fig. 11.6a using two different 5 nm thick drums. Drum 2 is measured at 1000 mbar. An optical image of both drums is shown in Fig. 11.1c. c) Normalized leak rates calculated from the leak time constants in Fig. 11.6b.

interchanging the gases in the experiment.

Figure 11.6**a** shows the experimental osmotic pressure versus time for different gas combinations, extracted using the same method as in Fig. 11.5 but on a different drum. Experiments were carried out with helium, argon, carbon dioxide and nitrogen gas. Equation 11.1 is fitted to all the 6 osmotic pressure curves to extract the leak time constants as shown in Fig. 11.6**b**. A factor of 10 difference is observed in the leak time constant of helium compared to that of nitrogen gas. Also, the time constant of nitrogen is higher in these samples than the thinner sample shown in Fig. 11.5. Besides thickness, the presence of crystal defects and wrinkles might be responsible for the observed leak rate differences.

11.4. DISCUSSION

It is important to note that the presented experiments cannot determine the exact leakage path of the gas molecules into the graphene cavity, although the results do allow to exclude some possible causes. If pores are present that are much larger than the molecular size, Graham's law for effusion predicts leakage rates to be proportional to the square root of the molecular mass ($\tau_1/\tau_2 \propto \sqrt{M_1/M_2}$). However, it is observed that carbon dioxide and helium have almost the same leak rate, despite their large difference in molecular mass. On the other hand, carbon dioxide has a larger mass than nitrogen, but a lower leak rate, again inconsistent with Graham's law for effusion. From this, we conclude that in this study the leakage is not dominated by effusion through pores slightly larger than or comparable to the molecular size of the gases. For example, permeation across pores much larger than the gas molecular dimension but smaller than the gas mean free path has been investigated by Celebi et al. [37], who found that Graham's law does hold true in that case.

Looking at the leak rates for the different gases in Fig. 11.6**b**, it is found that they follow the order of the kinetic diameters d of the gases: (d_{He} = 260 pm, d_{CO_2} = 330 pm, d_{Ar} = 340 pm, d_{N_2} = 364 pm). Thus, gases with a kinetic diameter larger than ~330 pm have a lower leak rate than gases with a kinetic diameter smaller than ~330 pm as shown in Fig. 11.6**c**. This kind of selectivity in leak rates is similar to the one observed by Koenig et. al. [35] in pristine graphene, although the leak rates observed here are higher. Other research [229] suggests transport could take place between the layers, also resulting in selective gas transport.

If the gas selectivity of the graphene enclosed cavities can be understood and engineered to a larger degree, for example by creating pores of controlled size [35, 38, 40, 233, 234], multiple semi-permeable membranes can be used for gas analysis. This can be achieved by filling these systems with a known gas and subsequently monitoring their time-dependent osmotic pressure while exposing them to an unknown gas mixture.

In this work, we show results of graphene drums fabricated from natural graphite. These samples showed relatively high lake rates, which allowed repeating the experiment with different gases in a reasonable time span of a few hours. However, in the Appendix A1, we show that we can also measure osmosis between cavities sealed by 31 layers of graphene (sample from chapter 9) and in cavities sealed by single-layer graphene grown by chemical vapor deposition. These samples also show selective leakage without any processing necessary, demonstrating that our method can be widely applied.

11.5. CONCLUSION

We have demonstrated osmotic pressure sensing with graphene enclosed cavities. The osmotic pressure is a consequence of differences in the molecular leakage rate, which reduces with increasing kinetic diameter, resulting in a spontaneous flux of gas against the pressure gradient. Due to the high flexibility and Young's modulus of graphene, the responsivity of the graphene osmometer is as high as 60 kHz/mbar. We show that these systems are thus able to detect changes in gas composition in its environment, even when the pressure in this environment is kept constant.

APPENDIX

A1: MEASUREMENTS OF OSMOTIC PRESSURE WITH SINGLE-LAYER GRAPHENE AND KISH-GRAPHITE

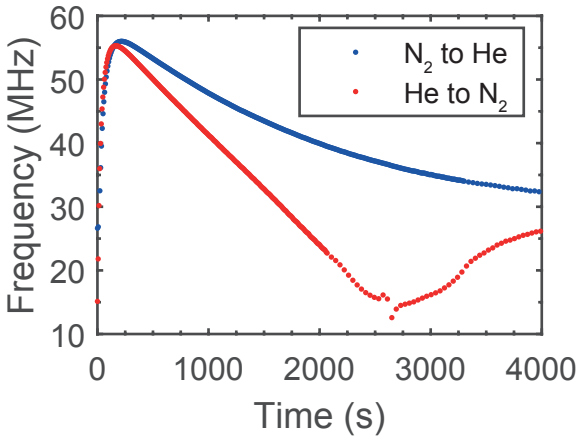

Figure 11.7: Experimental results showing osmosis in a 31-layer KISH graphene sample. Because of the large time-scale of leakage, the experiment was not repeated with all the gases.

The results presented in the main text show three drums resonators fabricated from natural graphite. These could be calibrated easily since their relatively high leak-rate made it possible to perform the calibration and repeat the measurement with different gases in a reasonable timescale. Here we want to point out that the time-dependent osmotic pressure is an effect that could be reproduced in many graphene-sealed cavities. In Fig. 11.7, we show results on a sample that consists of 31 layers of graphene exfoliated from KISH graphite.

In addition, we show results of single-layer graphene membranes (Fig. 11.8), however, these samples are significantly affected by drift. This makes it hard to calibrate and determine the pressure difference during the experiment. In addition, single-layered graphene membranes are more susceptible to the squeeze-film effect. From the data, it is clear that the system shows a selectivity between carbon dioxide and helium. This is already different from the case of natural multi-layer graphene, where no selectivity between these gases is observed.

A2: SQUEEZE FILM EFFECT

Due to the squeeze film effect, it is expected that the resonance frequency is also a function of the pressure p_{int} inside the cavity [59], even at $\Delta p = 0$. To examine this effect, the calibration procedure can be used. When a certain pressure step is applied, we wait long enough for the pressure difference to become close to zero. This gives the calibration curve for the squeeze film effect as shown in Fig. 11.9 for drum 3. These curves show that the frequency shifts cannot fully be attributed to pressure differences Δp that induces tension to the membrane but are also partly caused by the squeeze film effect that

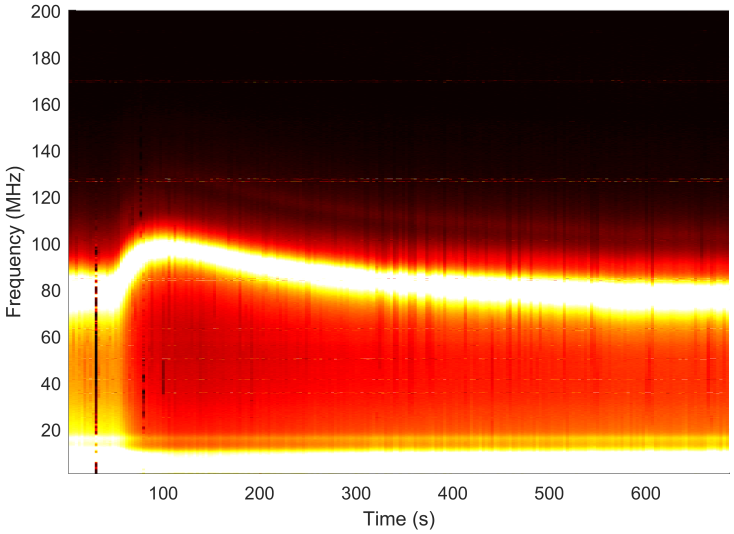

Figure 11.8: Experimental result showing osmosis with carbon dioxide being replaced with helium. The 4 μm diameter cavity is sealed with single-layer graphene grown by chemical vapor deposition.

only depends on p_{int}.

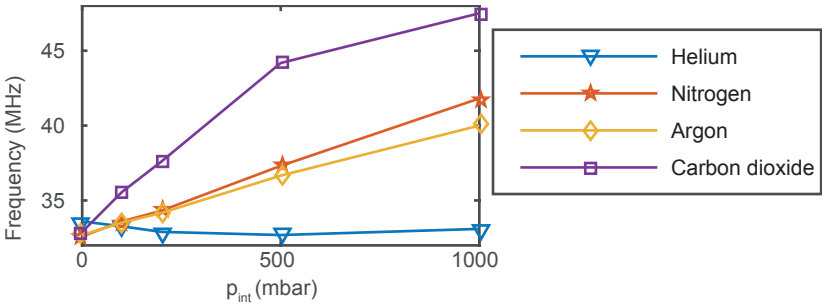

Figure 11.9: Gas and pressure dependence of the frequency at a pressure difference of zero for drum 3.

11

A3: FULL RAW DATASET OF DRUM 3 IN THE MAIN TEXT

Figure 11.10 shows the full dataset of the drum presented in Fig. 4 in the main text. This was measured using the calibration procedure, by taking the frequency when the membrane is fully relaxed ($\Delta p = 0$). This gives the result shown in Fig. 11.9.

A4: FULL RAW DATASETS OF DRUM 1 AND 2 IN THE MAIN TEXT

Figure 11.11 shows the full raw dataset for drum 1 in the main text and Fig. 11.12 for drum 2. For both experiments, the figures on the top right show negative pressurer dif-

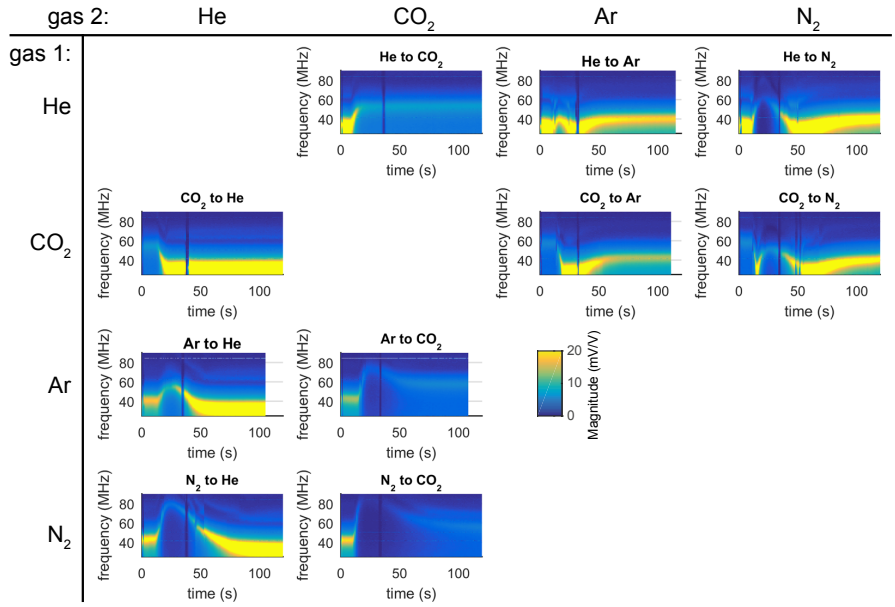

Figure 11.10: Full raw dataset corresponding to the drum in Fig. 11.5 in the main text, measurements between argon and nitrogen are presented in the main text.

ference while the bottom left figures show positive pressure difference. The nomenclature "Gas 1 to Gas 2" means that Gas 1 is initially in the chamber and cavity and the gas in the chamber is replaced by Gas 2.

A5: MATHEMATICAL DERIVATIONS

Dalton's law states that for a mixture of gases the total pressure p_{tot} is equal to the sum of the partial pressures of the individual components:

$$p_{\text{tot}} = p_1 + p_2, \tag{11.2}$$

where p_1 is the partial pressure of gas 1 and p_2 the partial pressure of gas 2. This allows us to calculate the pressure inside the cavity. Leakage between the cavity and the environment can be modelled using the equation:

$$\frac{\mathrm{d}\Delta p_i}{\mathrm{d}t} = -\frac{1}{\tau_i}\Delta p_i, \tag{11.3}$$

where Δp_i the partial pressure difference of gas i over the membrane and τ_i represents the leak time constant of that gas.

If it is assumed that the mixture of gases is ideal, according to eq. 11.2 we can also describe the permeation by the partial pressure differences between the cavity and sur-

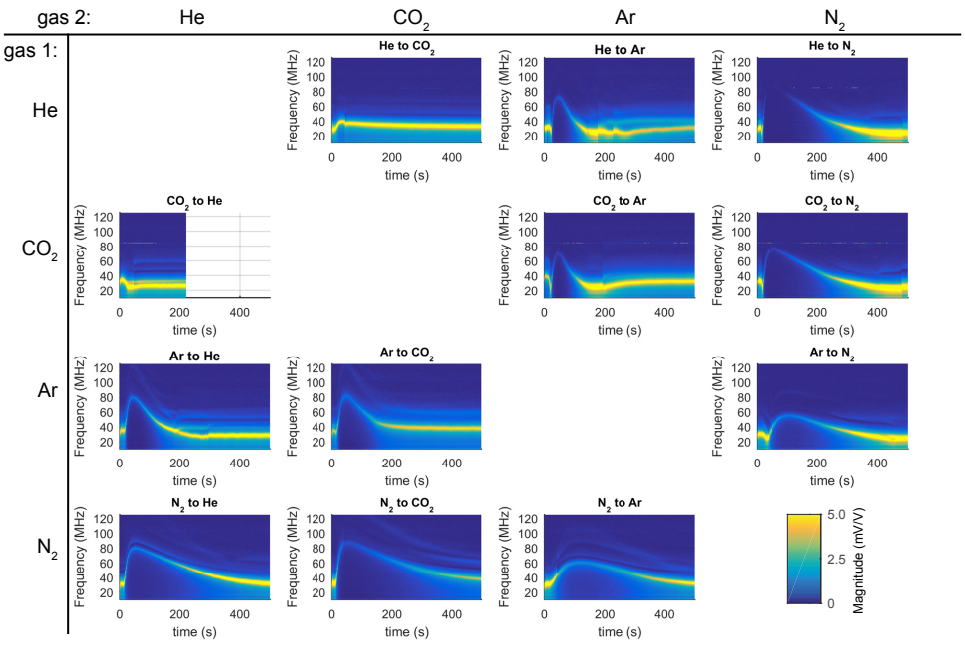

Figure 11.11: Full raw dataset for drum 1 in the main text, measurement was performed at constant 500 mbar chamber pressure.

roundings. Therefore we can write:

$$\frac{\mathrm{d}\Delta p_1}{\mathrm{d}t} = -\frac{1}{\tau_1}\Delta p_1, \tag{11.4}$$

$$\frac{\mathrm{d}\Delta p_2}{\mathrm{d}t} = -\frac{1}{\tau_2}\Delta p_2. \tag{11.5}$$

These equations have the following solutions:

$$\Delta p_1(t) = k_1 \mathrm{e}^{-t/\tau_1} = p_{1,\mathrm{int}} - p_{1,\mathrm{ext}}, \tag{11.6}$$

$$\Delta p_2(t) = k_2 \mathrm{e}^{-t/\tau_2} = p_{2,\mathrm{int}} - p_{2,\mathrm{ext}}. \tag{11.7}$$

Now we assume the initial conditions of the experiment. At $t = 0$ the cavity is filled with pure gas 1 and the outside with pure gas 2 at pressure p_0. Substituting $t = 0$ into both solutions gives that $\Delta p_1(0) = k_1 = p_0$ and $\Delta p_2(0) = k_2 = -p_0$. Adding the partial pressure differences over the membrane according to eq. 11.2 gives the total pressure difference as function of time:

$$\Delta p(t) = p_0 \mathrm{e}^{-t/\tau_1} - p_0 \mathrm{e}^{-t/\tau_2} = p_0(\mathrm{e}^{-t/\tau_1} - \mathrm{e}^{-t/\tau_2}) \tag{11.8}$$

We use eqs. 11.4–11.5 to calculate the normalized leak rate $\frac{1}{\Delta p_i}\frac{\mathrm{d}n_i}{\mathrm{d}t}$. This indicates the number of moles n_i of gas that passes through the membrane every second for a certain

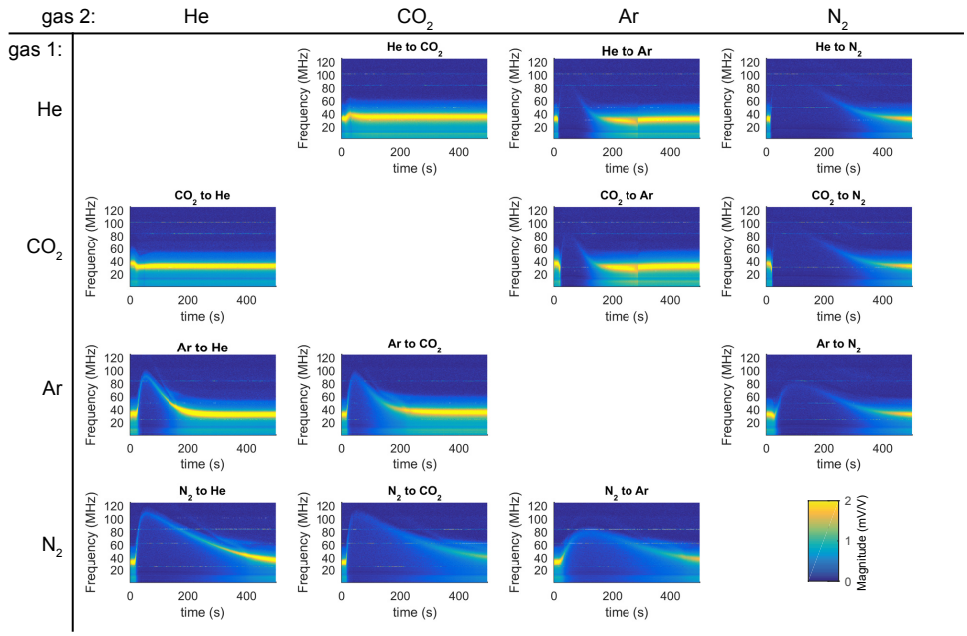

Figure 11.12: Full raw dataset for drum 2 in the main text, measurement was performed at 1000 mbar constant chamber pressure.

partial pressure difference . By assuming that the volume V is constant we obtain the expression:

$$\frac{1}{\Delta p_i}\frac{\mathrm{d}\Delta p_i}{\mathrm{d}t} = -\frac{1}{\tau_i}, \tag{11.9}$$

$$\frac{1}{\Delta p_i}\frac{\partial n_i}{\partial t} = \frac{1}{\tau_i}\frac{V}{RT}, \tag{11.10}$$

where R is the universal gas constant and T the absolute temperature (293.15 K). This is used to calculate the normalized leak rate in Fig. 11.6**c** in the main text.

12

SUSPENDED GRAPHENE DEFLECTED BY OSMOTIC PRESSURE

Semi-permeable graphene membranes are of considerable interest for water purification and energy generation. Here, we demonstrate that a graphene membrane sealing a cavity with a volume of only a few femtoliters can be deflected by osmotic pressure. Using atomic force microscopy in water we can detect the exponentially time-dependent deflection that occurs once the sucrose concentration in the environment is changed. Thus demonstrating that the osmotic pressure of a sucrose concentration gradient can be detected by monitoring the deflection of graphene membranes.

Parts of this chapter consists of an article in preparation [235].

IMPLANTABLE glucose sensors for continuous monitoring of blood sugar levels for diabetes patients is a long-sought goal [236, 237]. One development in this direction is the use of micro-electromechanical systems as osmotic pressure sensors. These combine a piezoresistive pressure sensor with a semi-permeable membrane to detect the osmotic pressure from the surrounding environment, from which the glucose level of the patient can be determined [238]. Such a design has the major advantage that it can operate without the use of enzymes, which are highly sensitive but also susceptible to environmental instabilities such as temperature, humidity, pH-level, ionic detergents, and toxic chemicals [239, 240]. However, the requirement of a separate semi-permeable membrane and pressure sensor makes the implementation of these devices complex and the device itself is relatively large: in the order of millimeters. In addition, obtaining high selectivities of glucose remains challenging in this type of sensor.

Here, we propose an implementation of the osmotic pressure sensor using graphene-sealed femtolitre cavities. Graphene is a single layer of carbon atoms strongly bonded in a hexagonal lattice [2], with superior chemical stability [241]. The ability of graphene to support subnanometer pores while retaining its high mechanical strength [220, 242], makes it a very promising material for a selectively permeable membrane with high throughput. This has attracted considerable attention for macro-scale applications such as water purification [39–41, 233, 234, 243–247] and gas separation [36, 37, 229, 248]. On the microscale, selective permeation has been proposed for gas sensing applications [35]. Osmotic gas pressure sensors based on semi-permeable graphene-sealed cavities have been proposed in chapter 11, that can determine the gas composition in their environment [58]. In this concept, the graphene membrane is used as both the semi-permeable membrane and the pressure sensor element. The realization of such a concept in liquids can result in a compact and cost-effective osmotic pressure sensor. With the ability to tune pores to realize different selectivities, in particular towards ionic solution [38, 233, 249], the applications could reach far beyond glucose monitoring.

By employing atomic force microscopy in a liquid cell, we demonstrate the feasibility of experiments to characterize the deflection of a graphene membrane fully submerged in water. We show that suspended graphene membranes sealing a cavity can be deflected by osmotic pressure, caused by a concentration difference of sucrose in solution between the cavity and its surroundings. The results thus provide a viable route for the development of osmotic pressure sensors to analyze the concentration of solutes in liquids.

12.1. EXPERIMENTAL SETUP

We demonstrate the detection of osmotic pressure using cavities sealed with single-layer graphene grown by chemical vapor deposition. The steps taken for sample preparation are shown in Fig. 12.1. Fabrication starts with a silicon chip with a layer of 300 nm of thermally grown silicon dioxide. Circular cavities were patterned using electron beam lithography and etched in the oxide layer using reactive ion etching. A sheet of single-layer graphene grown by chemical vapor deposition (CVD) was transferred over the chip, protected by a water-soluble polymer. This polymer is dissolved in water, after which the sample is never dried. The sample is stored in deionized water for at least three weeks before the experiment was started, in order to allow the water to permeate into the cav-

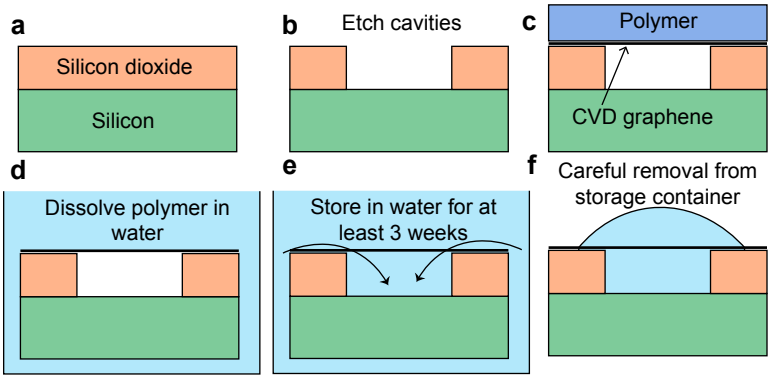

Figure 12.1: Illustration of the steps taken to prepare the sample for the experiment.

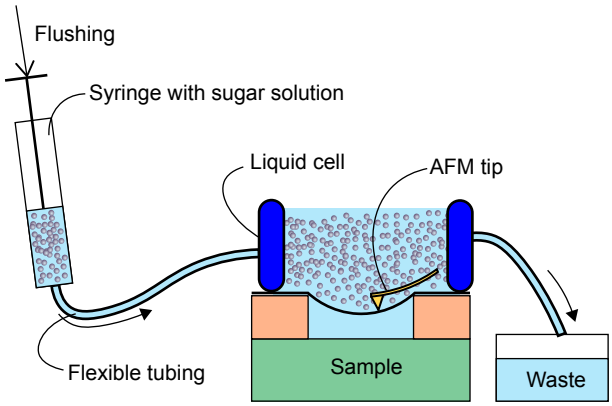

Figure 12.2: Measurement setup to detect the deflection due to osmotic pressure over the graphene membrane.

ities and to let the gas in the cavity permeate out and dissolve in the water. This simple approach indeed resulted in cavities filled with water in two out of the four samples that were fabricated, even when the graphene membrane completely seals the cavity. No effort was made to create pores in the graphene since we found that this fabrication process already resulted in a selectively permeable system.

The deflection of the membranes is measured using atomic force microscopy in a liquid cell shown in Fig. 12.2. The sample is carefully removed from the container before the experiment, making sure that a droplet of water remains on the center part of the chip and the cavities remain fully submerged under water. The sample is moved to an atomic-force microscope with a flexible silicon-rubber liquid cell. The chip forms the bottom of the liquid cell, while the rubber encapsulation of the liquid cell ensures the chip remains fully emerged in water during the experiment. The AFM scans over the surface until a suspended graphene drum is found that fully covers the cavity. The liquid cell is accessible by two flexible tubes, which can be used to flush the cell with a solution.

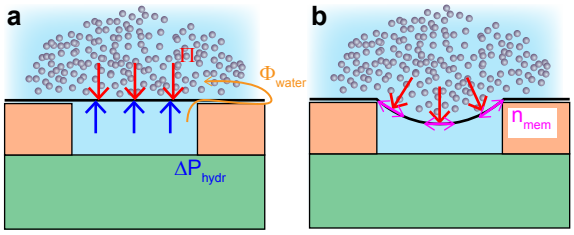

Figure 12.3: Illustration of the forces on the membrane: **a** immediately after increasing the sugar concentration in the environment and **b** in thermodynamic equilibrium.

A syringe with a sucrose solution of a well-known concentration is connected to one of the tubes and the system is carefully flushed with the solution to change the osmotic pressure in the environment. If care is taken during this step, the AFM can remain in contact with the substrate and continue scanning, although there will be some mechanical disturbance visible in the scan. After flushing, the AFM continues to scan the drum in order to measure the deflection due to osmotic pressure.

We expect that the graphene-sealed cavity will be permeable to water due to the very small kinetic diameter (2 angstrom) of water particles, which allows it to permeate through several possible mechanisms. The first possibility is through the small intrinsic defects in the CVD-graphene sheet, second is the wrinkles of the graphene on top of the silicon dioxide and third through the SiO2-graphene interface. Sucrose in a water solution has a kinetic diameter of 9 angstroms [250], causing it to diffuse much slower through these (sub)nanometre-scale defects in the graphene. If the graphene-sealed cavity is fully impermeable to the sucrose-particles and fully permeable for the water particles, the concentration inside the cavity will remain zero and the osmotic pressure is given by van 't Hoff's law [230]:

$$\Pi = k_B T c_s, \tag{12.1}$$

where k_B is Boltzmann constant, T is temperature and c_s the concentration of sucrose in the liquid cell environment.

To explain what happens during the experiment, we consider the system being in the water for a long time. Figure 12.3**a** shows the forces on the membrane immediately after the environment is flushed with a solution. The solutes cause an osmotic pressure on the membrane pushing it downwards. However, the water in the cavity is incompressible, causing it to build a compressive hydraulic pressure in the cavity exactly equal to the osmotic pressure. The fluid in the environment has no hydraulic pressure, thus there is a difference in pressure ΔP_{hydr} between the water inside the cavity and outside the cavity. This hydraulic pressure difference drives the flux of water Φ_{water} from the cavity through the possible pathways between the cavity and the environment. This reduces the volume of the cavity, causing the membrane to deflect downwards thereby tensioning the membrane. The tension in the membrane n_{mem} causes a force upwards that exactly compensates for the loss of hydraulic pressure in the cavity. The system finally reaches thermodynamic equilibrium when the hydraulic pressure difference is exactly zero and the upwards force due to the tension in the membrane exactly compensates for the total force induced by the osmotic pressure difference (Fig. 12.3**b**). Note that throughout

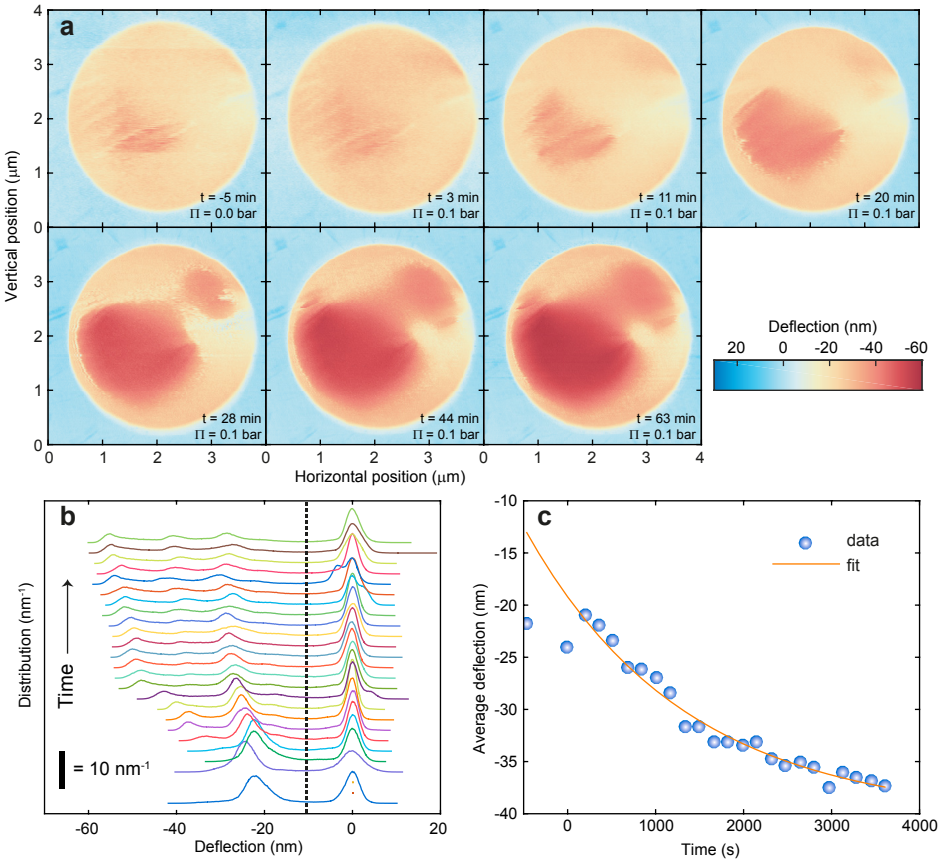

Figure 12.4: Time-dependent deflection of a 3.4-micron diameter graphene drum subjected to 10 kPa of osmotic pressure. **a** Height scans of the drum at different times, flushing with a sucrose solution with $\Pi = 0.1$ bar starts at $t = -2$ min and ends at $t = 0$ min. **b** Deflection distribution for all the scans in the experiment, only the part of the distribution with deflection less than 10 nm is used to calculate the average drum deflection. **c** Average deflection of the membrane as a function of time. A model with an exponential time constant (eq. 12.2) is fitted to the experimental data.

this entire process the system was out of thermodynamic equilibrium, but remained in mechanical equilibrium.

12.2. RESULTS

Figure 12.4**a** shows the height profile of a 3.4-micron diameter drum during the experiment. At $t = -5$ minutes the chip has been in DI-water for three weeks. Flushing with a sucrose solution ($\Pi = 0.1$ bar) starts at $t = -2$ min and ends at $t = 0$ min, during the flushing the AFM tip remains in contact with the substrate, but a significant amount a mechanical disturbance is present and these scans are therefore omitted. The first scan after the flush ends at $t = 3$ mins, the difference between this scan and the scan at $t = -5$

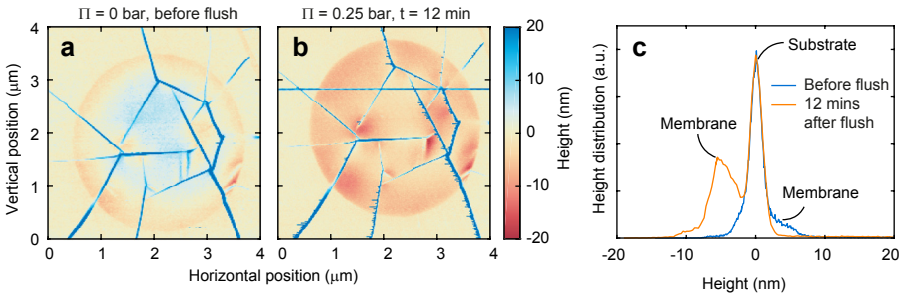

Figure 12.5: Experimental result on a different drum. **a** Height scan of the drum before flushing (the colorbar is the same as **b**). **b** Height scan 12 minutes after flushing the liquid cell with a sugar solution (Π = 0.25 bar)). **c** Height distribution before and after flushing.

min is small. Over time the membrane steadily deflects downwards as expected for osmotic pressure. It can be seen that the deflection is not uniform, suggesting that the tension distribution in this membrane is not uniform, similar to what was found in other works [67].

The height maps were used to calculate the average deflection of the drum over time as shown in Figure 12.4**b**,**c**. All height maps were corrected for tilt using the substrate next to the drum, whose height was set to zero. A histogram of the deflection distribution (Fig. 12.4**b**) reveals a peak near 0 nm that can be attributed to the silicon oxide surface. Even in the initial scan without osmotic pressure difference, the membrane is already deflected downwards, mainly due to ~19 nm of sidewall adhesion at the edge of the drum. The average deflection of the membrane is therefore calculated by integrating the histogram using only the deflections below -10 nm since these deflections can be attributed to the suspended graphene drum. The non-uniformity of the drum deflection is prominently visible in the histogram: as the hydrostatic pressure over the drum increases, multiple peaks start to appear in the deflection distribution.

Figure 12.4**c** shows the calculated average deflection of the drum as function of time. In agreement with Figs. 12.4**a**-**b** the average deflection shows the membrane is gradually moving down over time, indicating that water permeates out of the cavity due to the osmotic pressure as expected. Since the water permeation is a diffusive process, an exponential time-dependency of the average deflection is expected. The average deflection δ as function of time t is therefore fitted with an exponential function:

$$\delta = \delta_{\text{end}} + A e^{-t/\tau}, \tag{12.2}$$

where δ_{end} is the equilibrium position of the membrane under osmotic pressure, A the difference between initial and end position, and τ the leak time constant. The fit is in reasonable agreement with the experiment and we find $\delta_{\text{end}} = -40$ nm, $A = 21$ nm and $\tau = 1.8 \times 10^3$ s.

12.2.1. RESULTS ON A DIFFERENT DRUM

Figure 12.5 shows the experimental results on a second 3.4-micron drum. This drum shows clear wrinkles over the surface of the drum, which remain after flushing. The

membrane is slightly deflected upwards in Fig. 12.5**a** and shows the expected downwards movement after flushing (Fig. 12.5**b**), which can also be deduced from the height distribution in Fig. 12.5**c**. Time-dependent deflection was not studied in this drum, because the AFM lost contact with the substrate during the flushing. Figure 12.5**b** shows the first scan after re-approaching the surface. No significant change in deflection was detected after this scan, indicating that this drum permeates significantly faster than the drum in Fig. 12.4 and already reached equilibrium, perhaps due to additional permeation channels induced by the wrinkles. The average deflection is not calculated in this drum since the drum is initially deflected upwards and due to the wrinkles. This made it impossible to define a threshold and separate the substrate from the drum in the height distribution (Fig. 12.5**c**).

12.2.2. COMPARISON TO THEORY

It is interesting to compare the measured deflections to the expected deflection based on membrane theory. For the drum in Fig. 12.4 the total change in average deflection δ_{avg} due to the osmotic pressure difference is $\delta_{\text{avg}} = A = 21$ nm. To see whether this is reasonable, we compare this result to well to the expected deflection from theory. The relation between the pressure difference over the membrane Π and the *center* deflection δ_0 is [11, 143]:

$$\Pi = \frac{4n_0\delta_0}{a^2} + \frac{8Eh\delta_0^3}{3a^4(1-\nu)}, \tag{12.3}$$

where E is the Youngs modulus, h is the thickness, n_0 the pretension, a the radius and ν the Poisson ratio. Ignoring the pretension, we can write for the *average* deflection of the membrane ($\delta_0 = 3\delta_{\text{average}}$):

$$\delta_{\text{average}} = \left(\frac{\Pi a^4(1-\nu)}{72Eh}\right)^{1/3}, \tag{12.4}$$

now taking the membrane radius $a = 1.7$ μm, $Eh = 340$ N/m and $\nu = 0.165$ we expect $\delta_{\text{average}} = 14.2$ nm. We measure a larger average deflection of 21 nm, thus the membrane is more compliant than expected from theory. Assuming $Eh = 100$ N/m yields the correct average deflection difference of 21 nm. A lower Youngs modulus has been observed in other works [48, 251, 252]. It should however be considered that our deflection shape deviates a lot from the ideal spherical blister, which is likely to impact our result as well.

For the drum in Fig. 12.5 we expect from eq. 12.4 an average deflection of $\delta_{\text{average}} = 19$ nm assuming $Eh = 340$ N/m. While we cannot exactly calculate the average deflection in Figure 12.5**c**, we can estimate that this corresponds more to the maximum deflection of the membrane and the average deflection should be significantly less than 19 nm. Thus, in contrast to the drum in Fig. 12.4, the drum in Fig. 12.5 is less compliant than expected from theory. This may be attributed to the wrinkles that are prominently present in this membrane, which acts as scaffolds to increase the stiffness.

12.3. DISCUSSION

We have demonstrated the mechanical characterization of suspended graphene membranes fully submerged in water. While the deflection of the membrane due to osmotic

pressure could be readily detected, it proved challenging to repeat the experiment with different concentrations. The main limitation is the formation of bubbles when syringes containing the solution are exchanged. If these bubbles reach the substrate with the suspended graphene structures, the water meniscus causes the AFM tip to lose contact with the substrate and causes rupture of graphene drums. In order to fully test the potential of these systems as osmotic pressure sensors, the setup needs to be improved to prevent bubble formation. Alternatively, the membranes itself could be made more robust by employing few-layer graphene membranes instead of single-layer graphene. The latter could also be important to improve sensor reliability in commercial applications. Future work can address these issues and the concentration-dependence of the deflection can be studied.

The drawback of current osmotic pressure sensors is the limited selectivity of the device to the solutes in the surrounding. Therefore, current MEMS implementations of the osmotic pressure sensors employ enzymes to improve selectivity, but this makes the sensor highly sensitive to environmental factors such as temperature, pH-level, and toxic chemicals. Graphene presents an exciting opportunity as several works have shown that selectivity between ionic solutes can be achieved by tuning the pore sizes in the membrane [38, 233, 249]. By employing several drums in parallel with different pores, one could achieve better glucose selectivity by using one membrane with larger holes to measure the ionic contribution to the osmotic pressure. Introducing pores will certainly improve the response time of the device, which is currently in the order of hours or tens of minutes, but should be in the order of seconds for commercial applications. Efforts to achieve a more homogeneous tension-distribution in the membrane will help to achieve a more uniform response from device-to-device.

While liquid-cell AFM has proven to be a suitable method for the readout of the membrane's deflection, commercial sensor applications require on-chip electrical readout of the deflection. Readout of the resonance frequency, which was highly sensitive in gas osmometers [58], is not an option in liquids due to the large dissipation forces. Static capacitive readout of single graphene drums has recently been demonstrated in graphene pressure sensors [45] and could work in this system if the cavity remains free of ionic solutes.

12.4. CONCLUSION

We demonstrate that graphene membranes that seal a cavity are deflected by osmotic pressure induced by a sucrose solution. This deflection is characterized by atomic force microscopy in water, providing the first mechanical characterization of graphene in a liquid environment. When the concentration of sucrose in the surroundings is changed, the membrane deflects downwards with an exponential time-dependency due to the osmotic pressure difference. Future directions can focus on improvements in the measurement setup to reduce bubble formation, tuning the selectivity of permeation by fabricating nanopores, achieving a more uniform tension distribution in the membrane and on-chip electronic readout strategies of the sensor.

Part V: Outlook and valorization

13

OUTLOOK

This chapter gives a brief overview of continued projects and research that builds on the work in this thesis. First, we discuss the efforts to characterize the mass of graphene. After this, the progress on the wafer-scale integration of squeeze-film pressure sensors is shown, followed by the Pirani pressure sensor and the effusion-based gas sensor. The last section of this chapter shows continued work on the nonlinear dynamics by showing the initial results on quasiperiodic attractors in nonlinear graphene resonators.

13.1. CHARACTERIZING THE MASS OF GRAPHENE RESONATORS

In chapter 10 we find that the frequency shift due to the squeeze-film effect is much lower than expected, for which the most simple explanation is that the mass of the resonator is much higher than expected. Previous works have estimated the mass by applying a large out-of-plane load to the membrane and tracking its resonance frequency [11, 12, 62, 226, 227], in almost all cases it was found that the mass of the membrane is significantly higher than the theoretical mass of graphene ($\rho h = 7.7 \times 10^{-7}\text{kg/m}^2$). The experimental result on the squeeze-film pressure sensors in chapter 10 shows the need to characterize the mass of the single-layer graphene resonators for sensor applications.

13.1.1. LARGE DEFLECTION METHOD

Most works apply a large out-of-plane force to the graphene membrane and use the following theory to compare the experimental results to the frequency shift, for a circular membrane:

$$\omega_0 = \frac{\gamma_0}{a}\sqrt{\frac{n_0 + n(\delta_0)}{\rho h}}, \tag{13.1}$$

where $n(\delta_0)$ is the additional tension due to the out-of-plane deflection δ_0 and n_0 the pre-tension. From the experimental frequency shift one can then derive the mass if one can apply a model for $n(\delta_0)$. For the first mode of a circular membrane subject to gas pressure Δp and assuming the deflection shape has a constant curvature:

$$\omega_0 = \frac{2.4048}{a}\sqrt{\frac{n_0}{\rho h} + \frac{2Eh\delta_0^2}{3a^2(1-\nu)\rho h}} \tag{13.2}$$

Where δ_0 is the new static position due to the pressure, E is the Young's modulus and ν the Poisson ratio. δ_0 can be related to Δp using:

$$\Delta p = \frac{4n_0\delta_0}{a^2} + \frac{8Eh\delta_0^3}{3a^4(1-\nu)}. \tag{13.3}$$

While simply adding the tension seems reasonable at first in eq. (13.1), we have to consider that the system is nonlinear. The derivation above essentially linearized the problem around $\delta_0 = 0$. However to find the resonance frequency, one should linearize around the new static equilibrium position of the membrane. Doing this while assuming constant curvature results in [254]:

$$\omega_0 = \frac{2.4048}{a}\sqrt{\frac{n_0}{\rho h} + \frac{2Eh\delta_0^2}{a^2(1-\nu)\rho h}}. \tag{13.4}$$

Note, that incorrectly taking into account the nonlinearities in the system results in a underestimation of the mass by a factor of 3. Similar underestimations have been made by using an electrostatic gate. Further drawbacks of this method is that the force and elastic properties of the membrane have to be well-known, which means additional characterization is necessary. We thus prefer to develop a different method to find the mass of the resonators to solve these problems.

Parts of section 13.1 consists of an article in preparation [253].

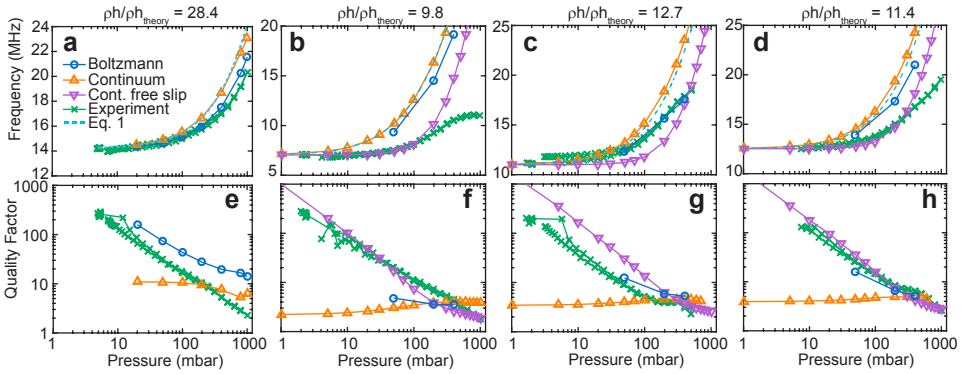

Figure 13.1: Comparison of the squeeze-film effect of resonators with a known mass to several theoretical models. 4 different single-layer graphene resonators are shown all with a diameter of 5 microns in a helium environment.

13.1.2. THERMOMECHANICAL METHOD

Due to the venting channel in the squeeze-film pressure sensors, no gas pressure difference can be applied and no electrostatic gate is present, this means that we cannot use the large out-of-plane deflection method. However, the calibration technique proposed in chapter 4 allows us to measure the mass of these resonators. By first measuring the transduction coefficient of the system to convert the voltage of the signal to meters, we can perform a second measurement to measure the Brownian motion of the system. Using equipartition theorem we can relate the measured mean-square amplitude $\langle \delta^2(t) \rangle$ to the effective mass of the system [54] (chapter 2):

$$m_{\text{eff}} = \frac{k_B T}{\omega^2 \langle \delta^2(t) \rangle}, \tag{13.5}$$

where m_{eff} is the modal mass of the resonator, k_B the Boltzmann constant and T the temperature. Once the m_{eff} is known, it can be converted to the actual mass of the resonator using $m = \frac{m_{\text{eff}}}{0.2695}$ from which the mass-per-unit square is known using the known area of the resonator.

To test the thermomechanical method we also measure the squeeze-film effect to see if there are correlations between the frequency shift and the measured mass. Figure 13.1 shows the experimental resonance frequency and quality factor as a function of pressure for 4 different drums. We compare these results to numerical simulations that use the measured mass as an input. It is striking that for the drums in Figs. 13.1**a** and **c** the Boltzmann transport equation (BTE) is close, even predicting the lower frequency shift at high pressures due to inertia in the gas flow in Fig. 13.1**c**. In the other cases however (Figs. 13.1**b**, **d**) the BTE predicts a higher frequency, but the continuum model with free-slip boundary condition matches up at low pressures. However, there is no physical reason why this model should apply to this system and we expect BTE to be more accurate.

Thus in some cases, we can match the mass measured by thermomechanical calibration to the measured frequency shift due to the squeeze-film effect, but not in all

cases. Considering that the thermomechanical method assumes a mode-shape, but the squeeze-film effect is in principle independent of the mode shape, this is most likely the cause of the deviation. While we did not characterize any mode shapes in this work, the drums used in chapter 12 (made from identical graphene with an identical transfer method used for the drums here) reveal deflection shapes that suggest that the fundamental mode shape can deviate significantly. The method should be refined by verifying the relation $m = \frac{m_{\text{eff}}}{0.2695}$ by measurement of the mode-shape of the drum, for example by using the technique of Davidovikj *et al.* [67].

13.2. CHARACTERIZING THE MASS OF GRAPHENE USING QUARTZ CRYSTAL MICROBALANCES

Fabrication of graphene devices on wafer scale often requires a transfer of sheets of single-layer graphene grown by chemical vapor deposition, usually requiring a support polymer. It is inevitable that this introduces some transfer contamination on top of the graphene, significantly impacting the device's electronic or dynamical properties. A standardized test to determine the amount of contamination on top of graphene is therefore of high interest to the community. However, with current popular characterization techniques such as Raman spectroscopy, optical microscopy, and atomic force microscopy it is difficult to quantify the amount of contamination on top of graphene.

To solve this problem we employ quartz crystal microbalances to directly determine the mass of graphene. The quartz crystal microbalance consists of a piezoelectric quartz crystal that can be brought into resonance by applying an oscillating voltage. This is a widely popular tool in thin film deposition and biochemical applications. By transferring the graphene on top of such crystals, the measurement is no longer sensitive to the mechanical properties of the graphene and thus facilitates a direct measurement of the mass.

Figure 13.2 shows the experimental protocol and setup to detect the mass of graphene. We use oxygen plasma to etch away the graphene since the quartz and gold electrodes of the QCM are not affected by this plasma. Continuous monitoring of the resonance frequency allows one to determine the mass that is being removed and extract the etch rate.

13.2.1. RESULTS

Figure 13.3**a** shows the frequency shift measured on a clean crystal, which only underwent the procedure to clean the crystal before the transfer. Nevertheless, we observe that a mass approximately equal to a monolayer of graphene was removed from the crystal. Figure 13.3**b** shows the frequency shift during etching of the dummy sample. The dummy sample was exposed to the transfer procedure but no actual graphene was transferred. The crystal was not fully etched at the end of the experiment, but an additional 4 equivalent monolayers of graphene mass has been removed in a second experiment.

Figure 13.3**c** shows the frequency shift during etching of a crystal covered with single layer graphene. A mass that is equivalent to almost 8 monolayers of graphene is re-

Parts of section 13.2 consists of an article in preparation [255] and have been published in the Master thesis of Mick Hsu [256].

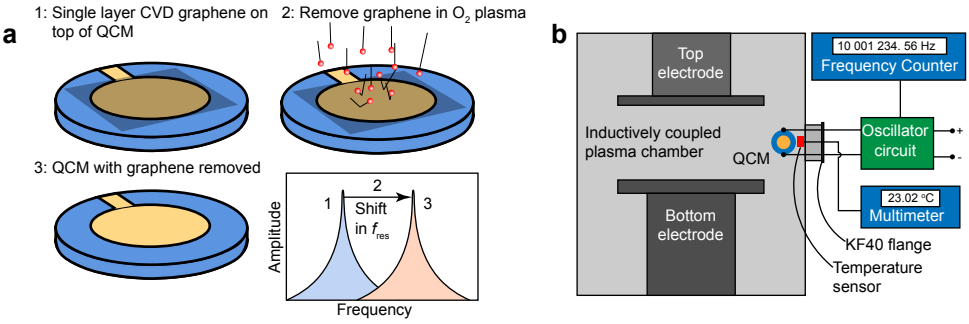

Figure 13.2: **a** Experimental procedure to measure the mass of graphene using the quartz crystal microbalance (QCM). The measurement starts with a QCM with a sheet of CVD graphene covering one of the electrodes. The oxygen plasma etches away the graphene and any contaminants until the etching stops. Continuous monitoring of the resonance frequency of the crystal allows one to determine the mass that has been removed by the plasma. **b** Experimental setup to read-out the QCM frequency and chamber temperature while the crystal is exposed to oxygen plasma.

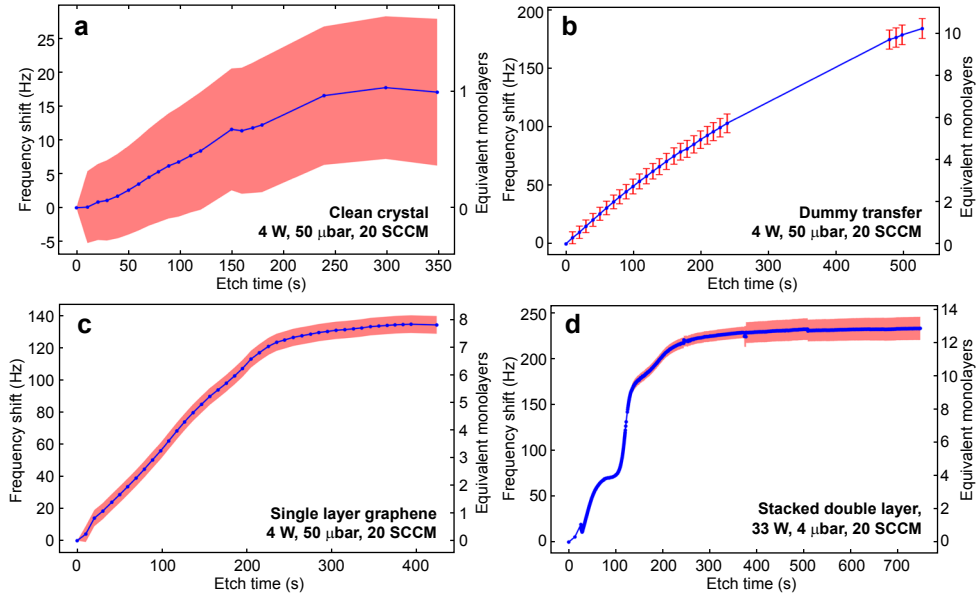

Figure 13.3: Measured frequency shift as a function of etching time for 4 different quartz crystal microbalances. **a** Uncoated quartz crystal that was only exposed to the cleaning procedure. **b** Dummy sample which was exposed to the transfer-polymer but no actual graphene was transferred. **c** Crystal containing a sheet of single-layer graphene on one of the electrodes, graphene was not fully etched but significantly damaged as confirmed by Raman. **d** Crystal with two single-layer graphene sheets stacked on top of each other to form double-layer graphene.

moved, suggesting that significant contamination is present on the sample. The etch rate is similar to the one found on the dummy sample, which could indicate that the transfer-polymer is indeed the cause of the contamination. During subsequent Raman spec-

troscopy measurements we found that the graphene was not completely removed but considerably damaged. This shows that the etching of graphene is significantly slower than the contaminants.

Figure 13.3**d** shows the results of a crystal covered with double-layer graphene, created by stacking two single-layer graphene sheets on top of each other using the same transfer method. For this measurement, higher plasma powers were used with lower pressures to ensure the graphene is fully etched. A striking observation is that the etching slows down twice during the experiments. This could be due to the slower etching of the graphene layer. First, the sample etches fast due to the polymer, then slows down as it etches the graphene layer, speeds up again to etch away the contaminants between the layers, slows down on the second layer and finally etches away the remaining residue slowly until the crystal is fully clean. Further measurements are necessary to confirm this mechanism, stacking more layers of graphene could be very useful to confirm this effect. These results are described in more detail in the MSc thesis of Mick Hsu [256].

13.3. WAFER SCALE FABRICATION OF SQUEEZE-FILM PRESSURE SENSORS

Mechanical exfoliation of the transfer of large sheet of CVD single layer graphene provides us with a means to fabricate prototypes of graphene resonators, well suited for scientific research. However, these fabrication techniques are not suitable for industrial application due to their limited yield of devices. To solve this problem, the transferless process was developed by Sten Vollebregt et al. [44] which allows for large scale production of graphene resonators in a process with is compatible with existing CMOS technologies.

The fabrication process of these resonators is shown in Fig. 13.4. Transferless production of suspended graphene resonators starts with a silicon wafer with a layer of 90 nm thermally grown silicon dioxide. Molybdenum is sputtered on the wafer and subsequently dry-etched to the shape of the graphene resonator (Fig. 13.4**a**). This molybdenum acts as the catalyst during the growth of graphene by chemical vapour deposition (Fig. 13.4**b**). After graphene growth, electrical contacts consisting of 5 nm chromium and 100 nm gold are patterned, which act as electrical contacts and clamps to keep the graphene suspended (Fig. 13.4**c**). Finally, the molybdenum is etched using a peroxide solution and subsequently dried using critical point drying to prevent the collapse of the graphene membrane (Fig. 13.4**d**).

13.3.1. MECHANICAL CHARACTERIZATION

The mechanical characterization revealed a problem with the current design of the squeeze-film pressure sensor. The pressure-dependent resonance frequency reported in [44] reveals a frequency shift that corresponds to a ρh of 100 nm of gold, from which it is concluded that the suspended part of the gold is moving. To find whether any mode can be attributed to the suspended graphene, we investigate the mechanical response of the

Parts of section 13.3 have been published in the proceedings of the 19th International Conference on Solid-State Sensors, Actuators and Microsystems (IEEE-TRANSDUCERS), 770-773 (2017) [44] and the MSc thesis of Manvika Singh [257].

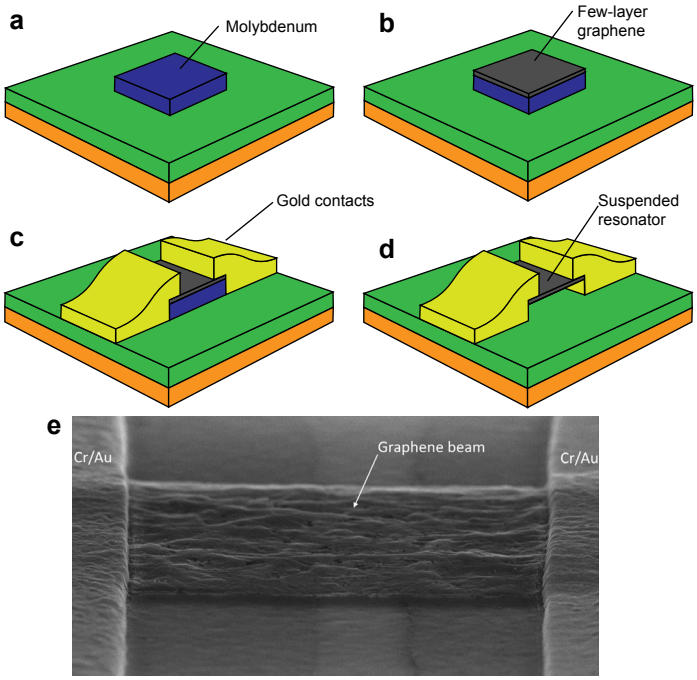

Figure 13.4: Transferless process to produce graphene resonators on wafer-scale. **a** Molybdenum is deposited and patterned in the shape of the graphene resonator. **b** Multilayer graphene is grown on the molybdenum catalyst by chemical vapor deposition. **c** Gold contacts are patterned on top of the chip using lift-off. **d** The molybdenum is etched and subsequently dried using critical point drying to create a suspended resonator. **e** Scanning electron microscope image of a suspended graphene resonator.

modes at high driving power. We find at high frequencies near 130 MHz one mode that shows strong nonlinear behavior (Fig. 13.5**a**), while the other modes show only little nonlinearity (Fig. 13.5**b**).

Since the graphene is much thinner than the gold clamps, we conclude that this nonlinear response can be attributed to the motion of graphene. However, its resonance frequency is so high that the squeeze-film response is too low for any pressure sensing applications. To solve this problem, in future work it should be attempted to reduce the movement of the clamps and uncouple this motion from the motion of the graphene resonator. This can be achieved by increasing the thickness of the clamps, as doubling the thickness would increase the stiffness by a factor of 8. Furthermore, a lower density material such as aluminium can be employed to raise the resonance frequency of the clamps. If the resonance frequency of the clamps is sufficiently high, it can uncouple the graphene resonator and reveal its low-frequency modes. In that case, the system could perform very well as a squeeze-film pressure sensor, as the multi-layer graphene combined with a low gap-size should ensure the Reynolds number of the gas flow much smaller than one as discussed in chapter 10. The fabrication and mechanical characterization of these sensors are shown in more detail in the MSc thesis of Manvika Singh

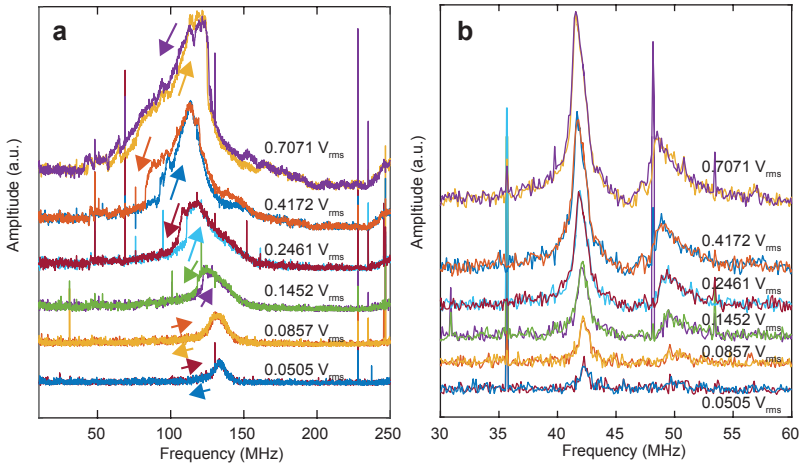

Figure 13.5: Resonant behavior of the graphene resonator with moving gold clamps. **a** Resonance at high frequencies showing nonlinear behavior. **b** A low-frequency resonance showing only weak nonlinearities at the same driving level.

[257].

13.4. PIRANI PRESSURE SENSORS

Pirani pressure sensors operate by exploiting the pressure-dependent thermal conductance of gas in a nanogap [260]. The pressure is usually deduced from the temperature-dependent electrical resistance of a suspended bridge which is heated by an electrical current. Pirani pressure sensors are an attractive concept because they require no hermetic cavity, moving parts or accurate detection of the deflection. Reducing the size and power consumption of Pirani sensors requires a material with a high surface to mass ratio and which has a temperature dependent resistance, for which graphene is a good candidate. Figure 13.6**a** shows an scanning electron microscope image of a suspended graphene bridge. The graphene was fabricated by the transferless process in (Fig. 13.4), but the graphene was made to collapse on the silicon dioxide substrate by under-etching before depositing the gold clamps. The cavity was later under-etched in silicon dioxide (600 nm) using wet etching to ensure the graphene is suspended.

The relative change in electrical resistance as a function of gas pressure for suspended and non-suspended devices is shown in Fig. 13.6**b**. A clear pressure dependence of the suspended devices is visible, while the non-suspended devices show no pressure dependence. Thus demonstrating that the heat is indeed conducted through the nanogap and demonstrating the Pirani effect. Since the pressure-dependence of the thermal conductance through the nanogap depends on the mean free path of the gas, we expect a gas-dependence of the electrical resistance. Figure 13.7 shows the change

Parts of section 13.4 have been accepted for publication in the proceedings of the 13th International Conference on Nano/Micro Engineered and Molecular Systems (IEEE-NEMS) [258], the MSc thesis of Joost Romijn [46] and an article in preparation [259].

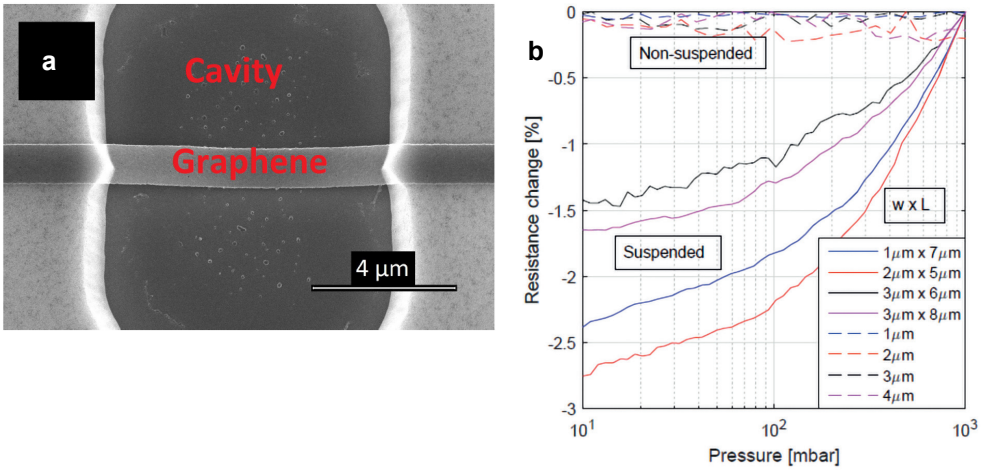

Figure 13.6: **a** Scanning electron microscope image of a Pirani pressure sensor consisting of a graphene bridge suspended over a cavity etched in silicon dioxide. **b** Resistance change as a function of pressure for bridges that are suspended and non-suspended bridges that are supported by the silicon dioxide.

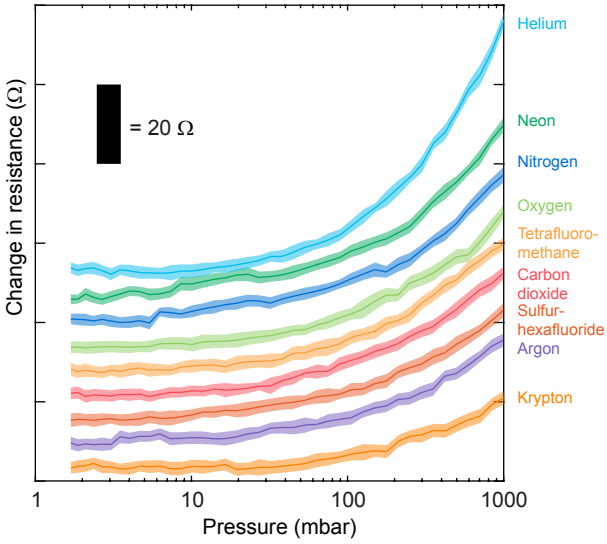

Figure 13.7: Change of the electrical resistance of the graphene Pirani pressure sensor as a function of pressure for different gases.

in electrical resistance for different gases. Indeed the response is found to be gas dependent, which could be applied in future gas sensing concepts. Considerable efforts have been made by Joost Romijn [261] to fabricate and integrate these sensors in a CMOS-compatible process.

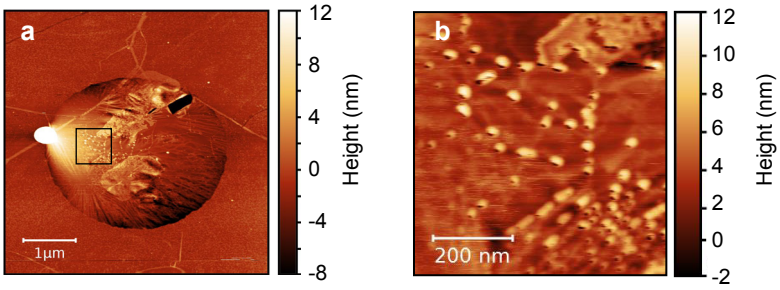

Figure 13.8: Atomic force microscopy of a porous single-layer graphene drum.

13.5. EFFUSION GAS SENSORS

The concept behind the frequency-dependent actuation force (chapters 2, 5, 6 and 10) can be extended to extract both the pressure-dependent thermal time constant and leak time constant of a graphene resonator. If both these time constants can be measured simultaneously, it could be an interesting concept to measure gas composition and pressure. To test this idea, we use the graphene drums in Fig. 13.8, which were bombarded with Xe^{23+} ions at the SME beamline of GANIL (Caen, France) [263]. These introduce large defects and small pores, making the graphene drums permeable. Since the size of the defects is in the order of the mean free path of the gas, we expect that Graham's law for permeation holds:

$$\tau_1/\tau_2 \propto \sqrt{M_1/M_2}, \tag{13.6}$$

where τ_i is the leak time constant of gas i and M_i is the molar mass. For a graphene drum with both a leak time and a thermal time the complex amplitude can be described by:

$$z_\omega = \frac{\alpha R\mathscr{P}_{AC}}{i\omega\tau_{th}+1} + \frac{(1-\beta\gamma)R\mathscr{P}_{AC}}{i\omega\tau_{gas}+1} + \frac{\alpha\beta\gamma R\mathscr{P}_{AC}\tau_{gas} * i\omega}{-\omega^2\tau_{th}\tau_{gas}+i\omega\tau_{th}+i\omega\tau_{gas}+1}, \tag{13.7}$$

of which the imaginary part can be used to fit to the measured mechanical response as shown in Fig. 13.9**a**. The frequency at the extrema of this response roughly correspond to the leak time constant and the thermal time constant. From a seperate measurement in vacuum it can be determined that the time constant between 1 and 10 MHz is the thermal time constant while the one between 0.1 and 1 MHz is the leak time constant. The leak time constant depends strongly on the type of gas used as shown in Fig. 13.9**a**. If we plot these leak times versus the square root of the mass in Fig. 13.9**b**, we find that at low pressures there is excellent agreement with Graham's law. Deviations from Graham's law occur at high pressures because most of the mean free path of most of the gases becomes shorter than the gap size of the large defect in Fig. 13.8, making viscous effects more important.

Parts of section 13.5 have been published in the MSc thesis of Irek Rosłoń [262].

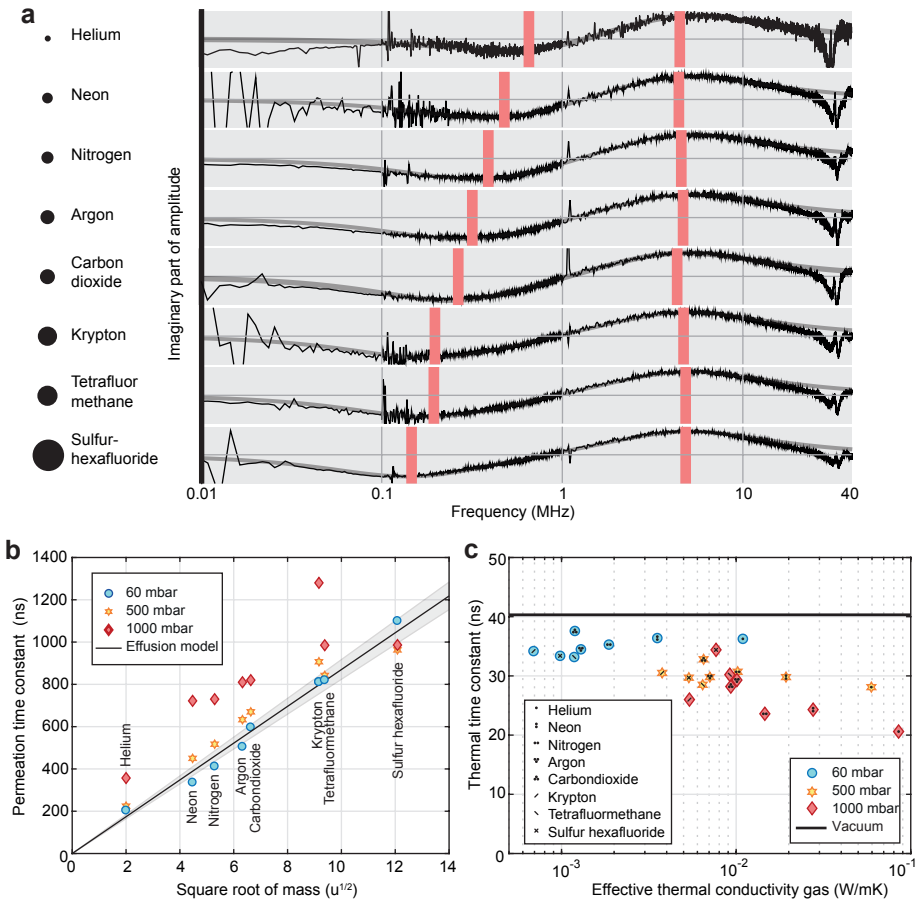

Figure 13.9: Mechanical delay times in a nanoporous graphene drums. **a** Imaginary part of the mechanical response as function of frequency for different gases. **b** Permeation time constant versus the square root of the molar mass of the gas. **c** Thermal time constant versus the effective thermal conductivity of the gas.

We also observe pressure-dependence of the thermal time constant, which can be related to the effective thermal conductivity k_{eff} of the gas. For this one can use a phenomenological model from literature [264]:

$$\frac{k_{\text{eff}}}{k} = \frac{1}{1 + \frac{CT}{pg_0}}, \tag{13.8}$$

where k is the thermal conductivity of the gas, $C = 7.6 \times 10^{-5}$, p the gas pressure and g_0 the gap size between membrane and substrate. Figure 13.9**c** shows that the thermal time constant τ_{th} and the effective thermal conductivity are indeed correlated, however the change in τ_{th} is relatively small. Combined with the deviations in the measured thermal time constant makes it difficult to show a strong correlation between these quantities. More details on these experiments and mathematical derivations can be found in the

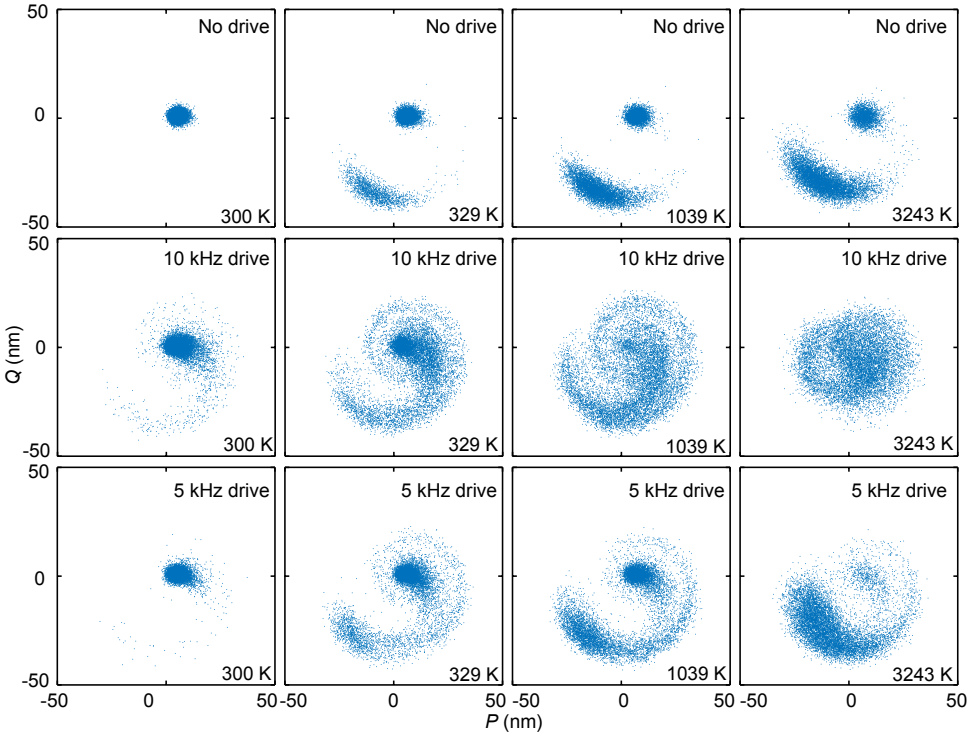

Figure 13.10: Experimental time-traces represented in the in-phase (P) and out-of-phase component (Q). A phase-shift of 240 degrees is added to the experimental data in order to correct for the additional phase shifts in the electronic and optical components. Distinct features appear around the low-amplitude attractor and the high-amplitude attractor is displaced in P-Q-space at high noise levels.

MSc thesis of Irek Rosłoń [262].

13.6. STOCHASTIC EFFECTS IN NONLINEAR GRAPHENE RESONATORS DRIVEN BY TWO INCOMMENSURATE FREQUENCIES

The directly driven Duffing resonator has two stable attractors, which can be described as points in the P-Q space as shown in chapter 8. However, this assumes the system is driven by a single frequency near the resonance frequency. If two incommensurable frequencies are applied to the system, the complexity of the dynamic behavior increases dramatically. One example of this is stochastic resonance when Kramer's rate (chapter 8) matches with the frequency (much lower than the resonance frequency) of a small signal that drives the system, it achieves an optimum switching rate that can be used to amplify signals [189, 195, 204]. When we study graphene membranes and slowly modulate them, however, we find that the complexity of the dynamics increases dramatically

Parts of section 13.6 have been published in the proceedings of the EUROMECH Colloquium 603: Dynamics of Micro and Nanosystems [265] and consists of an article in preparation [266].

and we cannot regard the system as having two stable attractors.

To study the effects of slow modulation, we repeat the experiment in chapter 8 and only add a slow drive to the system. Figure 13.10 shows the P-Q space at 4 different noise levels in the case of no modulation, 10 kHz modulation and the 5 kHz modulation. When no modulation is applied, the system resends most of its time in either one of the stable attractors since the switching rate is low. The position of the high-amplitude attractor is found to be somewhat dependent on the noise level applied to the system. Also, the spread around both attractors is increased, due to the stronger fluctuation amplitude.

When slow modulation is applied to the system, several effects are observed in Fig. 13.10. An intriguing spiraling pattern is observed with a feature encircling the low amplitude attractor. Compared to the case without modulation, spread around the low amplitude attractor has significantly increased. The high amplitude attractor is displaced more than in the case without modulation. To understand the meaning of these signatures, the transition dynamics of the system is studied in more detail.

Figure 13.11**a** shows the first 2 ms of a time trace of the magnitude of the amplitude at $T_{\text{eff}} = 329\text{K}$. Transitions from the low to high amplitude and vice versa are observed. Besides this, cycles are visible where the system departs from the low amplitude attractor, reaches a higher amplitude in between the two attractors and immediately transitions back to the low amplitude attractor. By taking the up-and-downwards rising slope of both the transitions and the cycles, we can visualize the paths in P-Q space. Figure 13.11**b** shows the transitions from the low to high amplitude and vice versa. A clear difference between the escape paths from the low amplitude attractor and the high amplitude attractor is found. From this analysis, it becomes clear that the feature encircling the low amplitude attractor in Fig. 13.10 is the escape path from the high to low amplitude attractor. No signatures of such oscillations could be uncovered for transitions to the high amplitude attractor, if they exist they are obscured by fluctuations.

Simulating the system without noise using the method of averaging shows that the observed behavior is most likely due to the slow drive modulating the resonance frequency rather than directly driving the system. In chapter 7 we have shown that the blue laser is very efficient to modulate the resonance frequency due to the thermal expansion which modulates the tension. The simulations show that we can no longer describe the system by having two stable attractors. Increasing the low-frequency drive in Fig. 13.11**d** shows that the two attractors described as points in the P-Q space become a quasi-periodic attractor. This quasi-periodic motion is due to the incommensurable frequencies driving the system. A direct overlap between the experiments and the simulations in Fig. 13.11**e** finds reasonable agreement with the model and the experiments. These simulations suggest that further experiments should be performed on the system without raising the noise level, but rather increasing the amplitude of the slow drive to more accurately measure the behavior of the quasi-periodic attractor.

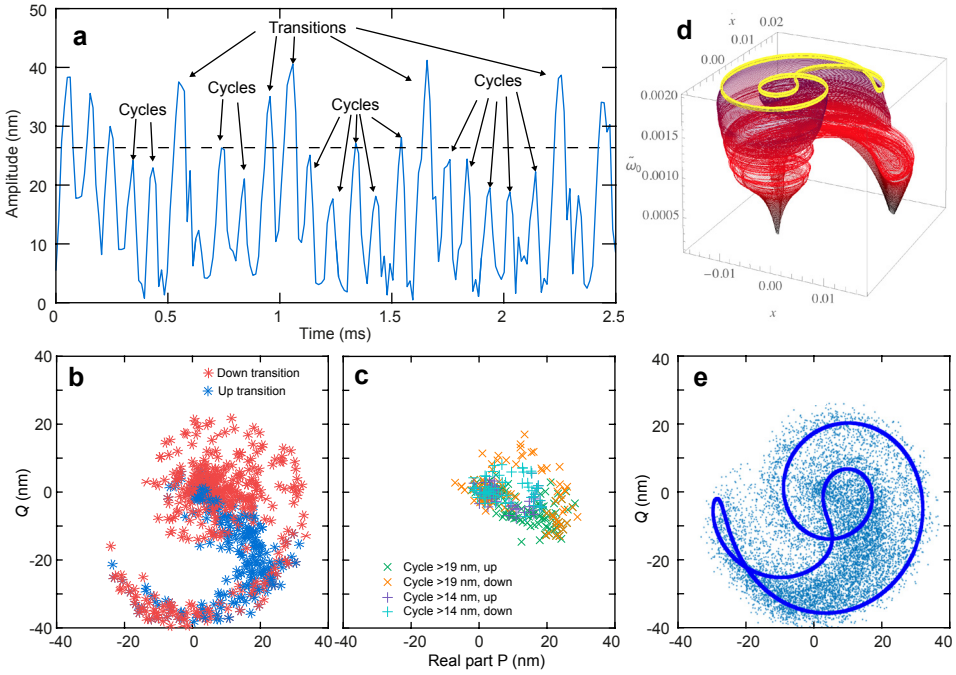

Figure 13.11: Switching behavior of a nonlinear graphene resonator under a slow (10 kHz) modulation. **a** The first 2 ms of the time trace at noise level $T_{\text{eff}} = 329$ K with a 10 kHz modulation, indicating a few examples of cycles and transitions that were manually selected to examine their paths in P-Q space. These were separated into the rising and falling slope to see the differences in the path. **b** Transitions from the low to high amplitude attractor (Up transitions) and from the high to low amplitude attractor plotted in P-Q-space. **c** Cycles of the resonator departing from the low amplitude attractor and immediately transitioning back. Cycles were divided into groups to construct this graph, cycles reaching a maximum amplitude between 19 and ~30 nm and cycles reaching an amplitude between 14 and 19 nm. **d** Evolution of the quasiperiodic motion with respect to the amplitude of the laser power modulation ω_{slow}. The cycling encountered in the experiment is highlighted in yellow. **e** Experimental time-trace represented in the in-phase (P) and out-of-phase component (Q). A phase-shift is added to the experimental data in order to correct for the additional phase shifts in the electronic and optical components. The quasiperiodic attractor is overlapped to the clouds of points.

14

VALORIZATION: TOWARDS PRACTICAL IMPLEMENTATIONS

This chapter discusses how the results in this thesis can be used in practical applications. We discuss the standardized characterization of the mass of graphene using quartz crystal microbalances. This is followed by a section on the graphene pressure sensors, discussing the squeeze-film pressure sensor and the Pirani pressure sensor. We further discuss how the studies on selectively permeable graphene systems could be converted into viable sensor concepts and their applications. Finally, we discuss how the studies of heat transport and the boundary effects in graphene membrane could be an opportunity for infrared sensors and phononic waveguides.

14.1. STANDARDIZED CHARACTERIZATION OF THE MASS OF GRAPHENE

CONTROL of the mass of graphene membranes is crucial to their application as a resonant sensor. During the course of this thesis, extensive characterization has been performed on the single layer graphene used in this study. Significant contamination was revealed on top of the graphene using the quartz crystal microbalance (QCM) technique, which could not be uncovered using popular characterization techniques, such as Raman, optical, scanning electron and atomic force microscopy.

In the current standard for 2D materials (ISO/TS 80004-13:2017), the characterization techniques would likely not perform very well in uncovering transfer residue and other surface contamination. The Quartz Crystal Microbalance technique can be implemented in the graphene standard, as this technique is not only able to qualitatively show the presence of contamination but is also able to quantify it in a very accurate manner. Especially the presence of transfer residue, which is on top of the 2D material, can be accurately shown using the QCM.

14.2. GRAPHENE PRESSURE SENSORS

This thesis focused on pressure sensors that do not require a hermetically sealed cavity to operate. Such sensors still achieve very high responsivity by exploiting the very high surface-to-mass ratio of 2D materials. Hermetic sealing at timescales in the order of decades has to date not been demonstrated. Even if this hermetic sealing could be achieved, it would likely involve expensive and complicated processes, which will add to the costs of the sensor. Furthermore, the sensor would show a nonlinear response, which means that many calibration points are necessary depending on the pressure range of the sensor. Calibration presents a significant portion of the cost of a sensor, and the number of calibration points should be as low as possible.

14.2.1. SQUEEZE-FILM PRESSURE SENSORS

Squeeze-film pressure sensors are in principle relatively straightforward to implement since they only require that the membrane is suspended close to the substrate. The size of the venting channel in principle does not affect its operation. Also, the lower range of the pressure that can be measured is only limited by the accuracy of the frequency measurement, meaning that in principle the sensor can operate in high vacuum environments as well. If the mass and gap size can be well-controlled, only the resonance frequency in vacuum has to be calibrated in order to account for the pre-tension. If not, the sensor requires 2 calibration points, assuming the sensor operates in the low Reynolds number regime. Fabrication is quite simple as it only requires two lithography steps if the transferless method of production is used (chapter 13) [44]. Furthermore, this fabrication could be implemented in the BiCMOS-process including the readout circuitry as shown for the Pirani pressure sensor (chapter 13) [261]. These advantages make this sensor concept very cost-effective once the challenges regarding the design are solved.

This thesis has shown several effects that affect the sensor's response which can serve as a guide to design a squeeze-film pressure sensor with optimal performance. The most

straightforward effect is that graphene resonator can show a significantly higher mass than expected due to contamination. However, we have also shown that the inertial forces in the gas flow become important at high resonance frequencies. This is an important design consideration for these membranes, and it is more reasonable to use a heavier multi-layer graphene membrane than a single-layer of graphene to reduce the resonance frequency at high pressures. Furthermore, the gap size should be made as small as possible, which will also help to achieve low inertial forces and better gas compression. To operate as a sensor in atmospheric conditions, the quality factor of the resonance should be raised in order to allow the sensor to operate in an oscillator circuit. This remains one of the bigger challenges in the design of a squeeze-film pressure sensor for industrial applications.

14.2.2. PIRANI PRESSURE SENSORS

The Pirani pressure sensors shown in this work might not be as responsive as the squeeze-film pressure sensor, but the ease of their readout through the electrical resistance is a big advantage. This allowed us to show for the first time that graphene sensors can be integrated into the BiCMOS fabrication process [261], which is a big step forward in the implementation of graphene sensors in the industry. It also makes graphene Pirani pressure sensors very interesting candidates to be implemented in any silicon-based sensor or electronic circuit that requires the vacuum in their package to be monitored. A drawback of the Pirani sensors is that a lot of calibration points are necessary due to the non-linearity of the Pirani effect.

During our study of the single-layer squeeze-film effect (chapter 10, Fig. 10.5) and the effusion gas sensors (chapter 13, Fig. 13.9), it was found that the relative change of the thermal time constant is significantly higher than the relative change in the electrical resistance measured in the Pirani sensors. This shows that the thermomechanical low-frequency response of a squeeze-film pressure sensor can be used as a Pirani pressure sensor. The low heat capacity of single-layer graphene contributes to the large change in thermal time constant. Thus we can propose a new type of thermomechanical Pirani pressure sensor based on this work, that measures the thermal time constant from the mechanical motion instead of the electrical resistance.

14.3. GRAPHENE SENSORS BASED ON SELECTIVE PERMEABILITY

In this thesis, several sensor concepts are proposed that work on selective permeability. Sensors based on selective permeability have the major advantage that they do not rely on chemical reactions, reducing their sensitivity to environmental disturbances such as temperature, PH-level or humidity. Graphene is especially powerful for this type of sensor, since (sub)nanometer pores can be induced in the material, while the membrane is still able to sustain large pressure loads. Furthermore, the large deflections that graphene can sustain allow it to be used as a pressure transducer as well. This means that graphene enables significant simplification of the fabrication process since the graphene acts as both the selectively permeable membrane and the pressure sensing element. In this section, we discuss how the physical effects related to selective permeability can be

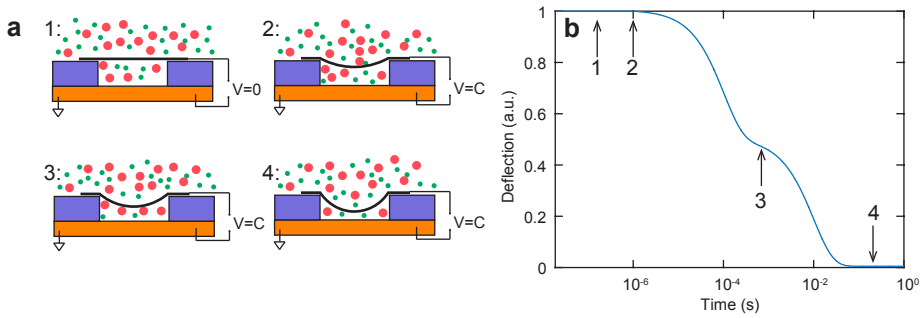

Figure 14.1: Practical implementation of the gas osmometer. **a** Operating principle, 1: The cavity and the surroundings contain a mixture of gases, the composition inside and outside the cavity is the same. 2: An electrostatic gate applies a step voltage, pulling the membrane down and reducing the volume. This compresses the gas in the cavity, making the partial pressures of both gases higher than the environment. 3: The gas with small leak time will escape the cavity until the partial pressure is equilibrated. 4: The gas with the slower time constant permeates out until its partial pressure is equal, equilibrium is reached once both gases have the same partial pressures as in the environment. **b** Expected deflection as function of time for this device. For illustration, the step is applied at $t = 1 \times 10^{-6}$ s and the leak times of the gases are 1×10^{-4} and 1×10^{-6}s.

applied in a practical sensing concept.

14.3.1. GAS OSMOMETERS

The gas osmometers in chapter 11 operate by bringing the system out of thermodynamic equilibrium and observing the relaxation process towards equilibrium. This was achieved by keeping the system in a well-known environment, such that the partial pressure inside the cavity is well known. By flushing the chamber with a different gas at constant pressures, the composition of the gas in the environment is changed and the system is out of equilibrium. The relaxation towards equilibrium results in a time-dependent osmotic pressure due to the different leak time constants that can be detected. The gas can be identified based on its leak time constant.

The experimental procedure in chapter 11 is not suitable for a practical application since the well-known environment requires a supply of reference gas to be present near the sensor. This removes all the advantages of scaling down the sensor to such a small size and requires a complicated control system to be built around the sensor. To solve this problem, a different strategy is proposed to bring the system out of equilibrium and monitor its relaxation towards equilibrium as shown in Fig. 14.1. The system is kept in the environment of which the composition needs to be determined long enough to make sure the gas composition in the cavity is equal to the environment. An electrostatic gate can be used to pull on the graphene membrane, reducing the volume of the cavity and compressing the gas. Now the partial pressure of both gases is higher than the environment, the system is therefore out of thermodynamic equilibrium. Gas will escape from the cavity with its characteristic leak time constant, resulting in a time-dependent deflection that is characteristic for the composition of the gas (Fig. 14.1**b**). This concept does not require a well-known reference gas and can continuously operate this cycle in order to determine the composition of the gas in the environment.

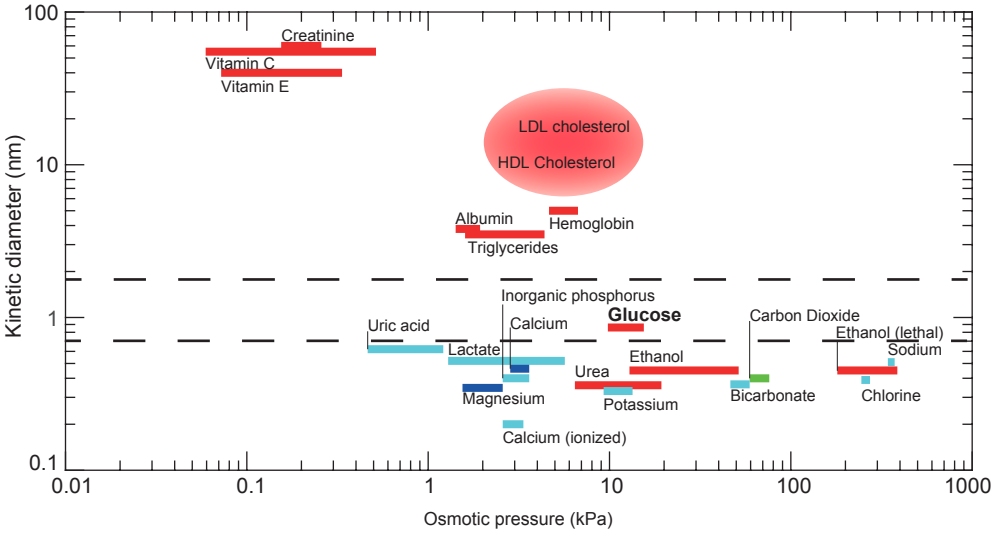

Figure 14.2: Reference values for osmotically active substances in human blood, with osmotic pressure on the horizontal axis versus the (estimated) kinetic diameter of the substance in water.

14.3.2. EFFUSION GAS SENSOR

The effusion gas sensor, shown in section 13.5, provides an alternative to the gas osmometer. Effusion is simply a consequence of the larger pores size and the larger size makes it simpler to fabricate in a reproducible manner using existing lithography based technology. The main advantage of this concept, however, is its ability to detect very fast leak time constants by examing the frequency-dependence of the actuation force. Since the readout is performed in a homodyne detection scheme while the membrane operates at high frequencies, reducing the noise level is easier than the quasi-static readout of the position in the gas-osmometer.

14.3.3. LIQUID OSMOMETERS

The graphene osmometers operating in liquids are mainly interesting for biomedical applications. One particular application is the detection of glucose concentration in blood for diabetes patients as discussed in chapter 12. Current sensors use enzymes to measure the blood sugar levels, but these are highly sensitive to environmental instabilities such as temperature, humidity, pH-level, ionic detergents, and toxic chemicals [239, 240]. If these factors lead to a false blood sugar reading, it poses a serious threat to the patients' health. It is therefore of interest to develop glucose sensors that do not require enzymes to operate.

Many works have reported on fabricating pores with controllable pore size in graphene and other 2D materials and have shown that this leads to tunable selectivities of permeation [35, 38, 233, 249, 267, 268]. With the controllable pore size of 2D materials is might be possible to sense the osmotic pressure from glucose in blood without the use of enzymes. Figure 14.2 shows the osmotic pressure (reference values) from different species

in blood with the kinetic diameter of the species on the vertical axis. The kinetic diameter gives a rough idea of the sieving capability of a pore, but it should be noted that this can very significantly. From Fig. 14.2, selective detection of the glucose concentration is possible if two osmotic pressure sensors are employed. The first osmometer has pored such that it is completely impermeable to species larger than ~2 nm, but completely permeable to species smaller than ~2 nm. The second osmometer would ideally be completely impermeable to species larger than ~0.7 nm but completely permeable to species with a smaller size. If such a system can be realized it would be possible to derive the glucose concentration from the difference in osmotic pressure between both devices.

14.4. APPLICATIONS FOR HEAT TRANSPORT IN GRAPHENE

One explanation for the long thermal time constants measured in single layer graphene is a large thermal resistance at the edge of suspended graphene. Further measurements are required to verify whether this model is correct. However, if heat transport in graphene is indeed limited by the boundaries, it would provide an interesting opportunity for the application of suspended graphene membranes as bolometers. Since they have a large thermal resistance at the edge, but a very low heat capacity, it would show a fast and high response. This could be useful to construct cheaper and faster infrared camera's.

The geometric phonon mismatch model in chapter 5 suggests that flexural phonons will almost always show total internal reflection when incident on a 90-degree kinked boundary. Combined with the low scattering rate of flexural phonons this might make suspended graphene interesting as a flexural phonon waveguide. Recently phonon waveguides to create all phononic NEMS circuits have been proposed [269]. The very low angle at which total internal reflection occurs should allow graphene flexural phonon waveguides to make very sharp bends, which helps to reduce the area footprint of the waveguide. Furthermore, the implementation of such a waveguide is quite straightforward, since only a channel (with sharp sidewalls) needs to be etched in the substrate. Transfer of graphene will immediately induce the sidewall adhesion on the edge of the channel, resulting in the kink that gives these waveguides their favorable boundary conditions.

15

CONCLUSIONS

The central theme around this thesis is around the mechanical motion of graphene membranes and how this motion interacts with its environment. In this chapter, we summarize the conclusions of this work and its implications. We present these in separate sections for each interaction that a moving graphene membrane can show.

15.1. THE INTERACTION BETWEEN MOTION AND LIGHT

First, we study the interaction between light and motion in chapter 4. In a Fabry-Perot interferometer, the transduction of the motion is nonlinear. This gives rise to harmonics in the signal that can be exploited to calibrate the amplitude, only requiring a good understanding of the optical properties of the membrane and the wavelength of the light. This can be done analytically for thin membranes, while more advanced optical models and numerical techniques can be applied to calibrate multi-layer and strongly absorbing materials.

The method is quite powerful, as it enables us to measure the mass of individual graphene resonators by combining the nonlinear transduction method with the thermomechanical method in chapter 13. This also lies at the foundation of chapter 8, where we extract the full equation of motion experimentally, enabling us to make sophisticated models of graphene membranes showing nonlinear behavior. This technique allows researchers to find every mechanical property of a suspended drum relevant for its dynamical behavior in a fully contactless manner.

The interaction between graphene and light is largely based on optical absorption. This implies that the lasers are heating the graphene membrane, which brings us to the next interaction.

15.2. THE INTERACTION BETWEEN MOTION AND HEAT

Graphene and other 2D materials interact with heat on many levels and plays a central role in the experiments performed in chapters 5 to 8 and 10. The lumped element model with a single characteristic time constant proposed chapter 5 was the cornerstone to the data analysis in chapters 5 and 6 and to a lesser extend in chapter 10.

Chapter 5 presents measurements of the thermal time constants of graphene, which we find to be two orders of magnitude higher than predicted by theory. The diameter dependence of the thermal time constant suggests that the edge of the suspended graphene drum plays a large role in transient heat transport. More sophisticated models suggest that the measured time constant can be attributed to the low scattering rate between different acoustic phonon modes, causing the flexural phonons to heat up much slower than the in-plane phonons due to boundary effects. Chapter 6 presents the same transient thermal characterization on a different material: single-layer MoS_2. This material shows a much lower thermal conductivity and shows thermal time constants within the range expected from the theory. These measurements allow us to estimate the specific heat of a 2D material for the first time, found to be 255 ± 104 J/(kg·K) for single-layer MoS_2.

15.3. NONLINEAR DYNAMICS

The temperature modulation of the membrane induced by the laser causes a modulation of the tension in the single layer graphene membrane. This is a very efficient mechanism to induce parametric resonance as shown in chapter 7, where we achieved a record number of 14 modes that can be brought into parametric resonance. A detailed analysis of the parametric resonance allows us to study nonlinear dissipation mechanisms, nonlinear dynamics and loss tangent of graphene resonators. This holds important clues to

how the energy in these resonators is dissipated to the environment.

Due to the finite temperature of the membrane, fluctuations are present in the environment that affect its motion. When the membrane is driven into the nonlinear regime, these fluctuations can cause the motion to switch between the two stable attractors. This stochastic switching effect is studied in chapter 8 and shows that it occurs with much higher frequencies and at much lower temperatures than state-of-the-art MEMS resonators. This can potentially be applied to transduce signals in the audible regime in a manner that mimics nature.

15.4. THE INTERACTION BETWEEN MOVING GRAPHENE AND FLUIDS

With the interaction between heat and the mechanics of graphene membranes well understood, the thesis continues by studying the mechanics in a fluidic environment. In chapter 9 we demonstrate the use of a few-layer graphene membrane as a squeeze-film pressure sensor. Due to the squeeze-film effect, the resonance frequency shifts as a function of gas pressure, resulting in a responsivity that is a factor 45 higher than state-of-the-art MEMS while using 25 times smaller membrane area. The study of these sensors is continued on single-layer devices in chapter 10, with an extensive investigation into the gas dependence on stiffness and dissipation in these sensors. At high Reynolds numbers, the squeeze-film stiffness reduces due to inertial effects in the gas flow. We also show that thermal modulation of the squeeze-film can be used as an efficient actuation mechanism to excite the resonator's motion at high gas pressures, connecting the squeeze-film effect to the work in chapter 5. In chapter 13, we also show that pressure-dependent heat transport can be used to build graphene Pirani pressure sensors.

For squeeze-film pressure sensors it is crucial to understand the mass of the suspended graphene, which led to the development of several methods shown in the outlook chapter 13. For reliable mass measurements, no knowledge of the mechanical properties of the membrane should be required, this makes the quartz crystal microbalance approach the most promising.

The following chapter 11 continues the study of gas-graphene interactions by investigating the effects related to selective gas permeation. Due to selective permeation, a large osmotic pressure difference can form over the membrane if the composition of gases in the environment is changed. The characteristic leak times associated with this process can be used in future applications to determine the composition of gases in the environment. A possible implementation for such a sensor is proposed in the valorization chapter 14. Leak times at very short timescales can be detected using the methods for transient heat transport in chapters 5 and 6, this is shown in chapter 10 where the leak time of a squeeze-film pressure sensor is detected or the effusion gas sensor proposed in chapter 13.

The selective permeation properties in gases extend to liquids, which is studied in chapter 12. By using atomic force microscopy in a liquid cell, we show that graphene membranes exposed to a concentration gradient of sucrose in water are deflected by osmotic pressure. This is an interesting concept for biomedical sensors since it does not require enzymes to operate, while the unit costs are potentially low since the graphene

is both the semi-permeable membrane and the pressure sensor (chapter 14).

REFERENCES

REFERENCES

[1] K. S. Novoselov, A. K. Geim, S. V. Morozov, D. Jiang, Y. Zhang, S. V. Dubonos, I. V. Grigorieva, and A. A. Firsov, *Electric field effect in atomically thin carbon films,* Science **306**, 666 (2004).

[2] A. K. Geim and K. S. Novoselov, *The rise of graphene,* Nature Materials **6**, 183 (2007).

[3] K. S. Novoselov, A. K. Geim, S. Morozov, D. Jiang, M. Katsnelson, I. Grigorieva, S. Dubonos, Firsov, and AA, *Two-dimensional gas of massless Dirac fermions in graphene,* Nature **438**, 197 (2005).

[4] K. Novoselov, D. Jiang, F. Schedin, T. Booth, V. Khotkevich, S. Morozov, and A. Geim, *Two-dimensional atomic crystals,* Proceedings of the National Academy of Sciences **102**, 10451 (2005).

[5] Y. Zhang, Y.-W. Tan, H. L. Stormer, and P. Kim, *Experimental observation of the quantum Hall effect and Berry's phase in graphene,* Nature **438**, 201 (2005).

[6] R. R. Nair, P. Blake, A. N. Grigorenko, K. S. Novoselov, T. J. Booth, T. Stauber, N. M. Peres, and A. K. Geim, *Fine structure constant defines visual transparency of graphene,* Science **320**, 1308 (2008).

[7] S. Bae, H. Kim, Y. Lee, X. Xu, J.-S. Park, Y. Zheng, J. Balakrishnan, T. Lei, H. Ri Kim, Y. I. Song, Y.-J. Kim, K. S. Kim, B. Özyilmaz, J.-H. Ahn, B. H. Hong, and S. Iijima, *Roll-to-roll production of 30-inch graphene films for transparent electrodes,* Nature Nanotechnology **5**, 574 (2010).

[8] T. Mahmoudi, Y. Wang, and Y.-B. Hahn, *Graphene and its derivatives for solar cells application,* Nano Energy **47**, 51 (2018).

[9] J. C. Meyer, A. K. Geim, M. I. Katsnelson, K. S. Novoselov, T. J. Booth, and S. Roth, *The structure of suspended graphene sheets,* Nature **446**, 60 (2007).

[10] C. Lee, X. Wei, J. W. Kysar, and J. Hone, *Measurement of the elastic properties and intrinsic strength of monolayer graphene,* Science **321**, 385 (2008).

[11] J. S. Bunch, S. S. Verbridge, J. S. Alden, A. M. Van Der Zande, J. M. Parpia, H. G. Craighead, and P. L. McEuen, *Impermeable atomic membranes from graphene sheets,* Nano Letters **8**, 2458 (2008).

[12] C. Chen, S. Rosenblatt, K. I. Bolotin, W. Kalb, P. Kim, I. Kymissis, H. L. Stormer, T. F. Heinz, and J. Hone, *Performance of monolayer graphene nanomechanical resonators with electrical readout,* Nature Nanotechnology **4**, 861 (2009).

[13] F. Ricciardella, S. Vollebregt, T. Polichetti, M. Miscuglio, B. Alfano, M. L. Miglietta, E. Massera, G. Di Francia, and P. M. Sarro, *Effects of graphene defects on gas sensing properties towards NO_2 detection,* Nanoscale **9**, 6085 (2017).

[14] F. Schedin, A. Geim, S. Morozov, E. Hill, P. Blake, M. Katsnelson, and K. Novoselov, *Detection of individual gas molecules adsorbed on graphene,* Nature Materials **6**, 652 (2007).

[15] S. Rumyantsev, G. Liu, M. S. Shur, R. A. Potyrailo, and A. A. Balandin, *Selective gas sensing with a single pristine graphene transistor,* Nano Letters **12**, 2294 (2012).

[16] A. A. Balandin, S. Ghosh, W. Bao, I. Calizo, D. Teweldebrhan, F. Miao, and C. N. Lau, *Superior thermal conductivity of single-layer graphene,* Nano Letters **8**, 902 (2008).

[17] S. Ghosh, I. Calizo, D. Teweldebrhan, E. Pokatilov, D. Nika, A. Balandin, W. Bao, F. Miao, and C. N. Lau, *Extremely high thermal conductivity of graphene: Prospects for thermal management applications in nanoelectronic circuits,* Applied Physics Letters **92**, 151911 (2008).

[18] W. Cai, A. L. Moore, Y. Zhu, X. Li, S. Chen, L. Shi, and R. S. Ruoff, *Thermal transport in suspended and supported monolayer graphene grown by chemical vapor deposition,* Nano Letters **10**, 1645 (2010).

[19] S. Chen, A. L. Moore, W. Cai, J. W. Suk, J. An, C. Mishra, C. Amos, C. W. Magnuson, J. Kang, L. Shi, and R. S. Ruoff, *Raman measurements of thermal transport in suspended monolayer graphene of variable sizes in vacuum and gaseous environments,* ACS Nano **5**, 321 (2010).

[20] D. L. Nika and A. A. Balandin, *Two-dimensional phonon transport in graphene,* Journal of Physics: Condensed Matter **24**, 233203 (2012).

[21] A. A. Balandin, *Thermal properties of graphene and nanostructured carbon materials,* Nature Materials **10**, 569 (2011).

[22] C. Faugeras, B. Faugeras, M. Orlita, M. Potemski, R. R. Nair, and A. Geim, *Thermal conductivity of graphene in Corbino membrane geometry,* ACS Nano **4**, 1889 (2010).

[23] X. Xu, L. F. Pereira, Y. Wang, J. Wu, K. Zhang, X. Zhao, S. Bae, C. T. Bui, R. Xie, J. T. Thong, B. H. Hong, K. P. Loh, and D. Donadio, *Length-dependent thermal conductivity in suspended single-layer graphene,* Nature Communications **5**, 3689 (2014).

[24] J.-U. Lee, D. Yoon, H. Kim, S. W. Lee, and H. Cheong, *Thermal conductivity of suspended pristine graphene measured by Raman spectroscopy,* Physical Review B **83**, 081419 (2011).

[25] V. E. Dorgan, A. Behnam, H. J. Conley, K. I. Bolotin, and E. Pop, *High-field electrical and thermal transport in suspended graphene,* Nano Letters **13**, 4581 (2013).

[26] S. Chen, Q. Wu, C. Mishra, J. Kang, H. Zhang, K. Cho, W. Cai, A. A. Balandin, and R. S. Ruoff, *Thermal conductivity of isotopically modified graphene,* Nature Materials **11**, 203 (2012).

[27] H. Li, H. Ying, X. Chen, D. L. Nika, A. I. Cocemasov, W. Cai, A. A. Balandin, and S. Chen, *Thermal conductivity of twisted bilayer graphene,* Nanoscale **6**, 13402 (2014).

[28] D. L. Nika and A. A. Balandin, *Thermal transport in graphene, few-layer graphene and graphene nanoribbons,* in *Thermal Transport in Low Dimensions* (Springer, 2016) pp. 339–363.

[29] S. Chen, Q. Li, Q. Zhang, Y. Qu, H. Ji, R. S. Ruoff, and W. Cai, *Thermal conductivity measurements of suspended graphene with and without wrinkles by micro-Raman mapping,* Nanotechnology **23**, 365701 (2012).

[30] H. Wang, S. Hu, K. Takahashi, X. Zhang, H. Takamatsu, and J. Chen, *Experimental study of thermal rectification in suspended monolayer graphene,* Nature Communications **8**, 15843 (2017).

[31] L. Lindsay, D. Broido, and N. Mingo, *Flexural phonons and thermal transport in graphene,* Physical Review B **82**, 115427 (2010).

[32] Y. Manzanares-Negro, P. Ares, M. Jaafar, G. López-Polín, and C. Gómez-Herrero, *Improved graphene blisters by ultra-high pressure sealing,* arXiv preprint arXiv:1809.03786 (2018).

[33] A. Smith, F. Niklaus, A. Paussa, S. Vaziri, A. C. Fischer, M. Sterner, F. Forsberg, A. Delin, D. Esseni, P. Palestri, M. Ostling, and M. Lemme, *Electromechanical piezoresistive sensing in suspended graphene membranes,* Nano Letters **13**, 3237 (2013).

[34] A. D. Smith, S. Vaziri, F. Niklaus, A. C. Fischer, M. Sterner, A. Delin, M. Östling, and M. C. Lemme, *Pressure sensors based on suspended graphene membranes,* Solid-State Electronics **88**, 89 (2013).

[35] S. P. Koenig, L. Wang, J. Pellegrino, and J. S. Bunch, *Selective molecular sieving through porous graphene,* Nature Nanotechnology **7**, 728 (2012).

[36] D.-e. Jiang, V. R. Cooper, and S. Dai, *Porous graphene as the ultimate membrane for gas separation,* Nano Letters **9**, 4019 (2009).

[37] K. Celebi, J. Buchheim, R. M. Wyss, A. Droudian, P. Gasser, I. Shorubalko, J.-I. Kye, C. Lee, and H. G. Park, *Ultimate permeation across atomically thin porous graphene,* Science **344**, 289 (2014).

[38] S. C. O'Hern, M. S. Boutilier, J.-C. Idrobo, Y. Song, J. Kong, T. Laoui, M. Atieh, and R. Karnik, *Selective ionic transport through tunable subnanometer pores in single-layer graphene membranes,* Nano Letters **14**, 1234 (2014).

[39] S. C. O'Hern, C. A. Stewart, M. S. Boutilier, J.-C. Idrobo, S. Bhaviripudi, S. K. Das, J. Kong, T. Laoui, M. Atieh, and R. Karnik, *Selective molecular transport through intrinsic defects in a single layer of CVD graphene,* ACS Nano **6**, 10130 (2012).

[40] S. C. O'Hern, D. Jang, S. Bose, J.-C. Idrobo, Y. Song, T. Laoui, J. Kong, and R. Karnik, *Nanofiltration across defect-sealed nanoporous monolayer graphene,* Nano Letters **15**, 3254 (2015).

[41] D. Cohen-Tanugi and J. C. Grossman, *Water desalination across nanoporous graphene,* Nano Letters **12**, 3602 (2012).

[42] S. Huang, M. Dakhchoune, W. Luo, E. Oveisi, G. He, M. Rezaei, J. Zhao, D. T. Alexander, A. Züttel, M. S. Strano, and K. V. Agrawal, *Single-layer graphene membranes by crack-free transfer for gas mixture separation,* Nature Communications **9**, 2632 (2018).

[43] M. Bao and H. Yang, *Squeeze film air damping in MEMS,* Sensors and Actuators A: Physical **136**, 3 (2007).

[44] S. Vollebregt, R. J. Dolleman, H. S. J. van der Zant, P. G. Steeneken, and P. M. Sarro, *Suspended graphene beams with tunable gap for squeeze-film pressure sensing,* in *Transducers 2017, The 19th International Conference on Solid-State Sensors, Actuators and Microsystems* (IEEE, 2017) pp. 770–773.

[45] D. Davidovikj, P. H. Scheepers, H. S. J. van der Zant, and P. G. Steeneken, *Static capacitive pressure sensing using a single graphene drum*, ACS Applied Materials & Interfaces **9**, 43205 (2017).

[46] J. Romijn, *Design and Integration of Graphene Sensors with Read-Out Electronics: A Graphene-Based Pirani Pressure Sensor Integrated with the BICMOS Process*, Master's thesis, Delft University of Technology (2018).

[47] R. Lifshitz and M. C. Cross, *Nonlinear dynamics of nanomechanical and micromechanical resonators,* in *Reviews of Nonlinear Dynamics and Complexity* (Wiley-Blackwell, 2009) Chap. 1, pp. 1–52.

[48] D. Davidovikj, F. Alijani, S. J. Cartamil-Bueno, H. S. J. van der Zant, M. Amabili, and P. G. Steeneken, *Nonlinear dynamic characterization of two-dimensional materials,* Nature Communications **8**, 1253 (2017).

[49] R. A. Barton, B. Ilic, A. M. Van Der Zande, W. S. Whitney, P. L. McEuen, J. M. Parpia, and H. G. Craighead, *High, size-dependent quality factor in an array of graphene mechanical resonators,* Nano Letters **11**, 1232 (2011).

[50] A. Croy, D. Midtvedt, A. Isacsson, and J. M. Kinaret, *Nonlinear damping in graphene resonators,* Physical Review B **86**, 235435 (2012).

[51] A. Eichler, J. Moser, J. Chaste, M. Zdrojek, I. Wilson-Rae, and A. Bachtold, *Nonlinear damping in mechanical resonators made from carbon nanotubes and graphene,* Nature Nanotechnology **6**, 339 (2011).

[52] J. Güttinger, A. Noury, P. Weber, A. M. Eriksson, C. Lagoin, J. Moser, C. Eichler, A. Wallraff, A. Isacsson, and A. Bachtold, *Energy-dependent path of dissipation in nanomechanical resonators,* Nature Nanotechnology **12**, 631 (2017).

[53] V. Singh, O. Shevchuk, Y. M. Blanter, and G. A. Steele, *Negative nonlinear damping of a multilayer graphene mechanical resonator,* Physical Review B **93**, 245407 (2016).

[54] B. Hauer, C. Doolin, K. Beach, and J. Davis, *A general procedure for thermomechanical calibration of nano/micro-mechanical resonators,* Annals of Physics **339**, 181 (2013).

[55] P. Blake, E. W. Hill, A. Castro Neto, K. S. Novoselov, D. Jiang, R. Yang, T. J. Booth, and A. Geim, *Making graphene visible,* Applied Physics Letters **91**, 063124 (2007).

[56] A. Castellanos-Gomez, M. Buscema, R. Molenaar, V. Singh, L. Janssen, H. S. van der Zant, and G. A. Steele, *Deterministic transfer of two-dimensional materials by all-dry viscoelastic stamping,* 2D Materials **1**, 011002 (2014).

[57] R. J. Dolleman, D. Davidovikj, H. S. J. van der Zant, and P. G. Steeneken, *Amplitude calibration of 2D mechanical resonators by nonlinear optical transduction,* Applied Physics Letters **111**, 253104 (2017).

[58] R. J. Dolleman, S. J. Cartamil-Bueno, H. S. J. van der Zant, and P. G. Steeneken, *Graphene gas osmometers,* 2D Materials **4**, 011002 (2017).

[59] R. J. Dolleman, D. Davidovikj, S. J. Cartamil-Bueno, H. S. van der Zant, and P. G. Steeneken, *Graphene squeeze-film pressure sensors,* Nano Letters **16**, 568 (2016).

[60] R. J. Dolleman, S. Houri, D. Davidovikj, S. J. Cartamil-Bueno, Y. M. Blanter, H. S. van der Zant, and P. G. Steeneken, *Optomechanics for thermal characterization of suspended graphene,* Physical Review B **96**, 165421 (2017).

[61] R. J. Dolleman, D. Lloyd, M. Lee, J. S. Bunch, H. S. van der Zant, and P. G. Steeneken, *Transient thermal characterization of suspended monolayer MoS_2*, arXiv preprint arXiv:1806.10769 (2018).

[62] R. A. Barton, I. R. Storch, V. P. Adiga, R. Sakakibara, B. R. Cipriany, B. Ilic, S. P. Wang, P. Ong, P. L. McEuen, J. M. Parpia, and H. G. Craighead, *Photothermal self-oscillation and laser cooling of graphene optomechanical systems,* Nano Letters **12**, 4681 (2012).

[63] D. Davidovikj, F. Alijani, S. J. Cartamil-Bueno, H. S. J. van der Zant, M. Amabili, and P. G. Steeneken, *Nonlinear dynamic characterization of two-dimensional materials,* Nature Communications **8**, 1253 (2017).

[64] A. M. v. d. Zande, R. A. Barton, J. S. Alden, C. S. Ruiz-Vargas, W. S. Whitney, P. H. Pham, J. Park, J. M. Parpia, H. G. Craighead, and P. L. McEuen, *Large-scale arrays of single-layer graphene resonators,* Nano Letters **10**, 4869 (2010).

[65] C. Chen, V. V. Deshpande, M. Koshino, S. Lee, A. Gondarenko, A. H. MacDonald, P. Kim, and J. Hone, *Modulation of mechanical resonance by chemical potential oscillation in graphene,* Nature Physics **12**, 240 (2016).

[66] V. Singh, B. Irfan, G. Subramanian, H. S. Solanki, S. Sengupta, S. Dubey, A. Kumar, S. Ramakrishnan, and M. M. Deshmukh, *Coupling between quantum Hall state and electromechanics in suspended graphene resonator,* Applied Physics Letters **100**, 233103 (2012).

[67] D. Davidovikj, J. J. Slim, S. J. Cartamil-Bueno, H. S. J. van der Zant, P. G. Steeneken, and W. J. Venstra, *Visualizing the motion of graphene nanodrums,* Nano Letters **16**, 2768 (2016).

[68] A. Castellanos-Gomez, R. van Leeuwen, M. Buscema, H. S. J. van der Zant, G. A. Steele, and W. J. Venstra, *Single-layer MoS_2 mechanical resonators,* Advanced Materials **25**, 6719 (2013).

[69] J. S. Bunch, A. M. van der Zande, S. S. Verbridge, I. W. Frank, D. M. Tanenbaum, J. M. Parpia, H. G. Craighead, and P. L. McEuen, *Electromechanical resonators from graphene sheets,* Science **315**, 490 (2007).

[70] J. Lee, Z. Wang, K. He, J. Shan, and P. X.-L. Feng, *High frequency MoS_2 nanomechanical resonators,* ACS Nano **7**, 6086 (2013).

[71] S. Roddaro, P. Pingue, V. Piazza, V. Pellegrini, and F. Beltram, *The optical visibility of graphene: interference colors of ultrathin graphite on SiO_2*, Nano Letters **7**, 2707 (2007).

[72] I. Jung, M. Pelton, R. Piner, D. A. Dikin, S. Stankovich, S. Watcharotone, M. Hausner, and R. S. Ruoff, *Simple approach for high-contrast optical imaging and characterization of graphene-based sheets,* Nano Letters **7**, 3569 (2007).

[73] C. Casiraghi, A. Hartschuh, E. Lidorikis, H. Qian, H. Harutyunyan, T. Gokus, K. Novoselov, and A. Ferrari, *Rayleigh imaging of graphene and graphene layers,* Nano Letters **7**, 2711 (2007).

[74] D. Abergel, A. Russell, and V. I. Fal'ko, *Visibility of graphene flakes on a dielectric substrate,* Applied Physics Letters **91**, 063125 (2007).

[75] S. J. Cartamil-Bueno, P. G. Steeneken, A. Centeno, A. Zurutuza, H. S. J. van der Zant, and S. Houri, *Colorimetry technique for scalable characterization of suspended graphene,* Nano Letters **16**, 6792 (2016).

[76] S. J. Cartamil-Bueno, A. Centeno, A. Zurutuza, P. G. Steeneken, H. S. J. van der Zant, and S. Houri, *Very large scale characterization of graphene mechanical devices using a colorimetry technique,* Nanoscale **9**, 7559 (2017).

[77] R. De Alba, T. S. Abhilash, R. H. Rand, H. G. Craighead, and J. M. Parpia, *Low-power photothermal self-oscillation of bimetallic nanowires,* Nano Letters **17**, 3995 (2017).

[78] R. J. Dolleman, G. Verbiest, Y. M. Blanter, H. S. J. van der Zant, and P. G. Steeneken, *Transient mechanical response of opto-thermally excited suspended graphene membranes,* (2018), in preparation.

[79] E. Pop, V. Varshney, and A. K. Roy, *Thermal properties of graphene: Fundamentals and applications,* MRS Bulletin **37**, 1273 (2012).

[80] X. Xu, J. Chen, and B. Li, *Phonon thermal conduction in novel 2D materials,* Journal of Physics: Condensed Matter **28**, 483001 (2016).

[81] I. Calizo, A. Balandin, W. Bao, F. Miao, and C. Lau, *Temperature dependence of the Raman spectra of graphene and graphene multilayers,* Nano Letters **7**, 2645 (2007).

[82] S. Ghosh, W. Bao, D. L. Nika, S. Subrina, E. P. Pokatilov, C. N. Lau, and A. A. Balandin, *Dimensional crossover of thermal transport in few-layer graphene,* Nature Materials **9**, 555 (2010).

[83] C. Schwarz, *Optomechanical, vibrational and thermal properties of suspended graphene membranes*, Ph.D. thesis, Institut Néel (2016).

[84] H. Cabrera, D. Mendoza, J. Benítez, C. B. Flores, S. Alvarado, and E. Marín, *Thermal diffusivity of few-layers graphene measured by an all-optical method,* Journal of Physics D: Applied Physics **48**, 465501 (2015).

[85] K. Yoon, G. Hwang, J. Chung, H. goo Kim, O. Kwon, K. D. Kihm, and J. S. Lee, *Measuring the thermal conductivity of residue-free suspended graphene bridge using null point scanning thermal microscopy,* Carbon **76**, 77 (2014).

[86] J. H. Seol, I. Jo, A. L. Moore, L. Lindsay, Z. H. Aitken, M. T. Pettes, X. Li, Z. Yao, R. Huang, D. Broido, N. Mingo, R. Rouff, and L. Shi, *Two-dimensional phonon transport in supported graphene,* Science **328**, 213 (2010).

[87] C. Metzger, I. Favero, A. Ortlieb, and K. Karrai, *Optical self cooling of a deformable Fabry-Perot cavity in the classical limit,* Physical Review B **78**, 035309 (2008).

[88] H. Wang, J. H. Strait, P. A. George, S. Shivaraman, V. B. Shields, M. Chandrashekhar, J. Hwang, F. Rana, M. G. Spencer, C. S. Ruiz-Vargas, and J. Park, *Ultrafast relaxation dynamics of hot optical phonons in graphene,* Applied Physics Letters **96**, 081917 (2010).

[89] G. L. Pollack, *Kapitza resistance,* Reviews of Modern Physics **41**, 48 (1969).

[90] R. J. Stevens, L. V. Zhigilei, and P. M. Norris, *Effects of temperature and disorder on thermal boundary conductance at solid–solid interfaces: Nonequilibrium molecular dynamics simulations,* International Journal of Heat and Mass Transfer **50**, 3977 (2007).

[91] E. T. Swartz and R. O. Pohl, *Thermal boundary resistance,* Reviews of modern physics **61**, 605 (1989).

[92] R. Peterson and A. Anderson, *The Kapitza thermal boundary resistance,* Journal of Low Temperature Physics **11**, 639 (1973).

[93] R. M. Costescu, M. A. Wall, and D. G. Cahill, *Thermal conductance of epitaxial interfaces,* Physical Review B **67**, 054302 (2003).

[94] H.-K. Lyeo and D. G. Cahill, *Thermal conductance of interfaces between highly dissimilar materials,* Physical Review B **73**, 144301 (2006).

[95] Q.-X. Pei, Y.-W. Zhang, Z.-D. Sha, and V. B. Shenoy, *Carbon isotope doping induced interfacial thermal resistance and thermal rectification in graphene,* Applied Physics Letters **100**, 101901 (2012).

[96] W. Xu, G. Zhang, and B. Li, *Interfacial thermal resistance and thermal rectification between suspended and encased single layer graphene,* Journal of Applied Physics **116**, 134303 (2014).

[97] A. Isacsson, A. W. Cummings, L. Colombo, L. Colombo, J. M. Kinaret, and S. Roche, *Scaling properties of polycrystalline graphene: a review,* 2D Materials **4**, 012002 (2016).

[98] Y.-C. Wen, C.-L. Hsieh, K.-H. Lin, H.-P. Chen, S.-C. Chin, C.-L. Hsiao, Y.-T. Lin, C.-S. Chang, Y.-C. Chang, L.-W. Tu, and C.-K. Sun, *Specular scattering probability of acoustic phonons in atomically flat interfaces,* Physical Review Letters **103**, 264301 (2009).

[99] A. A. Evans and A. J. Levine, *Reflection and refraction of flexural waves at geometric boundaries,* Physical Review Letters **111**, 038101 (2013).

[100] M. T. Pettes, I. Jo, Z. Yao, and L. Shi, *Influence of polymeric residue on the thermal conductivity of suspended bilayer graphene,* Nano Letters **11**, 1195 (2011).

[101] A. Y. Serov, Z.-Y. Ong, and E. Pop, *Effect of grain boundaries on thermal transport in graphene,* Applied Physics Letters **102**, 033104 (2013).

[102] J. Atalaya, A. Isacsson, and J. M. Kinaret, *Continuum elastic modeling of graphene resonators,* Nano Letters **8**, 4196 (2008).

[103] X.-J. Ge, K.-L. Yao, and J.-T. Lü, *Comparative study of phonon spectrum and thermal expansion of graphene, silicene, germanene, and blue phosphorene,* Physical Review B **94**, 165433 (2016).

[104] S. Lee, D. Broido, K. Esfarjani, and G. Chen, *Hydrodynamic phonon transport in suspended graphene,* Nature Communications **6**, 6290 (2015).

[105] A. Cepellotti, G. Fugallo, L. Paulatto, M. Lazzeri, F. Mauri, and N. Marzari, *Phonon hydrodynamics in two-dimensional materials,* Nature Communications **6**, 6400 (2015).

[106] G. Fugallo, A. Cepellotti, L. Paulatto, M. Lazzeri, N. Marzari, and F. Mauri, *Thermal conductivity of graphene and graphite: collective excitations and mean free paths,* Nano Letters **14**, 6109 (2014).

[107] J. M. Dawlaty, S. Shivaraman, M. Chandrashekhar, F. Rana, and M. G. Spencer, *Measurement of ultrafast carrier dynamics in epitaxial graphene,* Applied Physics Letters **92**, 042116 (2008).

[108] D. Singh, J. Y. Murthy, and T. S. Fisher, *Spectral phonon conduction and dominant scattering pathways in graphene,* Journal of Applied Physics **110**, 094312 (2011).

[109] A. K. Vallabhaneni, D. Singh, H. Bao, J. Murthy, and X. Ruan, *Reliability of Raman measurements of thermal conductivity of single-layer graphene due to selective electron-phonon coupling: A first-principles study,* Physical Review B **93**, 125432 (2016).

[110] Z. Chen, W. Jang, W. Bao, C. Lau, and C. Dames, *Thermal contact resistance between graphene and silicon dioxide,* Applied Physics Letters **95**, 161910 (2009).

[111] K. F. Mak, C. H. Lui, and T. F. Heinz, *Measurement of the thermal conductance of the graphene/SiO_2 interface,* Applied Physics Letters **97**, 221904 (2010).

[112] M. Freitag, M. Steiner, Y. Martin, V. Perebeinos, Z. Chen, J. C. Tsang, and P. Avouris, *Energy dissipation in graphene field-effect transistors,* Nano Letters **9**, 1883 (2009).

[113] K. E. Gray, *Nonequilibrium Superconductivity, Phonons, and Kapitza Boundaries* (Plenum Press, 1981).

[114] J. Hone, *Phonons and thermal properties of carbon nanotubes,* in *Carbon Nanotubes* (Springer, 2001) pp. 273–286.

[115] I. Lifshitz, *Thermal properties of chain and layered structures at low temperatures,* Zh. Eksp. Teor. Fiz **22**, 475 (1952).

[116] H. Kolsky, *Stress waves in solids*, Vol. 1098 (Dover Publications, 1963).

[117] K. F. Mak, C. Lee, J. Hone, J. Shan, and T. F. Heinz, *Atomically thin MoS_2: A new direct-gap semiconductor,* Phys. Rev. Lett. **105**, 136805 (2010).

[118] A. Splendiani, L. Sun, Y. Zhang, T. Li, J. Kim, C.-Y. Chim, G. Galli, and F. Wang, *Emerging photoluminescence in monolayer MoS_2,* Nano Letters **10**, 1271 (2010).

[119] G. Eda, H. Yamaguchi, D. Voiry, T. Fujita, M. Chen, and M. Chhowalla, *Photoluminescence from chemically exfoliated MoS_2,* Nano Letters **11**, 5111 (2011).

[120] S. Bertolazzi, J. Brivio, and A. Kis, *Stretching and breaking of ultrathin MoS_2,* ACS Nano **5**, 9703 (2011).

[121] B. Radisavljevic, A. Radenovic, J. Brivio, V. Giacometti, and A. Kis, *Single-layer MoS_2 transistors,* Nature Nanotechnology **6**, 147 (2011).

[122] Z. Yin, H. Li, H. Li, L. Jiang, Y. Shi, Y. Sun, G. Lu, Q. Zhang, X. Chen, and H. Zhang, *Single-layer MoS_2 phototransistors,* ACS Nano **6**, 74 (2011).

[123] M. Buscema, J. O. Island, D. J. Groenendijk, S. I. Blanter, G. A. Steele, H. S. van der Zant, and A. Castellanos-Gomez, *Photocurrent generation with two-dimensional van der waals semiconductors,* Chemical Society Reviews **44**, 3691 (2015).

[124] M. Buscema, G. A. Steele, H. S. van der Zant, and A. Castellanos-Gomez, *The effect of the substrate on the Raman and photoluminescence emission of single-layer MoS_2,* Nano Research **7**, 561 (2014).

[125] M. Buscema, M. Barkelid, V. Zwiller, H. S. van der Zant, G. A. Steele, and A. Castellanos-Gomez, *Large and tunable photothermoelectric effect in single-layer MoS_2*, Nano Letters **13**, 358 (2013).

[126] X. Liu, G. Zhang, Q.-X. Pei, and Y.-W. Zhang, *Phonon thermal conductivity of monolayer MoS_2 sheet and nanoribbons*, Applied Physics Letters **103**, 133113 (2013).

[127] Y. Cai, J. Lan, G. Zhang, and Y.-W. Zhang, *Lattice vibrational modes and phonon thermal conductivity of monolayer MoS_2*, Physical Review B **89**, 035438 (2014).

[128] X. Wei, Y. Wang, Y. Shen, G. Xie, H. Xiao, J. Zhong, and G. Zhang, *Phonon thermal conductivity of monolayer MoS_2: A comparison with single layer graphene*, Applied Physics Letters **105**, 103902 (2014).

[129] W. Li, J. Carrete, and N. Mingo, *Thermal conductivity and phonon linewidths of monolayer MoS_2 from first principles*, Applied Physics Letters **103**, 253103 (2013).

[130] J.-W. Jiang, H. S. Park, and T. Rabczuk, *Molecular dynamics simulations of single-layer molybdenum disulphide (MoS_2): Stillinger-Weber parametrization, mechanical properties, and thermal conductivity*, Journal of Applied Physics **114**, 064307 (2013).

[131] N. A. Lanzillo, A. Glen Birdwell, M. Amani, F. J. Crowne, P. B. Shah, S. Najmaei, Z. Liu, P. M. Ajayan, J. Lou, M. Dubey, S. Nayak, and T. O'Regan, *Temperature-dependent phonon shifts in monolayer MoS_2*, Applied Physics Letters **103**, 093102 (2013).

[132] R. Yan, J. R. Simpson, S. Bertolazzi, J. Brivio, M. Watson, X. Wu, A. Kis, T. Luo, A. R. Hight Walker, and H. G. Xing, *Thermal conductivity of monolayer molybdenum disulfide obtained from temperature-dependent Raman spectroscopy*, ACS Nano **8**, 986 (2014).

[133] X. Zhang, D. Sun, Y. Li, G.-H. Lee, X. Cui, D. Chenet, Y. You, T. F. Heinz, and J. C. Hone, *Measurement of lateral and interfacial thermal conductivity of single-and bilayer MoS_2 and $MoSe_2$ using refined optothermal Raman technique*, ACS Applied Materials & Interfaces **7**, 25923 (2015).

[134] J. J. Bae, H. Y. Jeong, G. H. Han, J. Kim, H. Kim, M. S. Kim, B. H. Moon, S. C. Lim, and Y. H. Lee, *Thickness-dependent in-plane thermal conductivity of suspended MoS_2 grown by chemical vapor deposition*, Nanoscale **9**, 2541 (2017).

[135] B. R. Matis, B. H. Houston, and J. W. Baldwin, *Energy dissipation pathways in few-layer MoS_2 nanoelectromechanical systems*, Scientific Reports **7**, 5656 (2017).

[136] J. W. Suk, A. Kitt, C. W. Magnuson, Y. Hao, S. Ahmed, J. An, A. K. Swan, B. B. Goldberg, and R. S. Ruoff, *Transfer of CVD-grown monolayer graphene onto arbitrary substrates*, ACS Nano **5**, 6916 (2011).

[137] D. Lloyd, X. Liu, N. Boddeti, L. Cantley, R. Long, M. L. Dunn, and J. S. Bunch, *Adhesion, stiffness, and instability in atomically thin MoS_2 bubbles*, Nano Letters **17**, 5329 (2017).

[138] D. Lloyd, X. Liu, J. W. Christopher, L. Cantley, A. Wadehra, B. L. Kim, B. B. Goldberg, A. K. Swan, and J. S. Bunch, *Band gap engineering with ultralarge biaxial strains in suspended monolayer MoS_2*, Nano Letters **16**, 5836 (2016).

[139] D. Sercombe, S. Schwarz, O. Del Pozo-Zamudio, F. Liu, B. Robinson, E. Chekhovich, I. Tartakovskii, O. Kolosov, and A. Tartakovskii, *Optical investigation of the natural electron doping in thin MoS_2 films deposited on dielectric substrates,* Scientific Reports **3**, 3489 (2013).

[140] N. Scheuschner, O. Ochedowski, A.-M. Kaulitz, R. Gillen, M. Schleberger, and J. Maultzsch, *Photoluminescence of freestanding single-and few-layer MoS_2,* Physical Review B **89**, 125406 (2014).

[141] H. Li, Q. Zhang, C. C. R. Yap, B. K. Tay, T. H. T. Edwin, A. Olivier, and D. Baillargeat, *From bulk to monolayer MoS_2: evolution of Raman scattering,* Advanced Functional Materials **22**, 1385 (2012).

[142] K. L. Aubin, *Radio frequency nano/microelectromechanical resonators: Thermal and nonlinear dynamics studies.* (2004).

[143] J. S. Bunch, *Mechanical and electrical properties of graphene sheets* (Cornell University Ithaca, NY, 2008).

[144] K. Liu, Q. Yan, M. Chen, W. Fan, Y. Sun, J. Suh, D. Fu, S. Lee, J. Zhou, S. Tongay, *et al.*, *Elastic properties of chemical-vapor-deposited monolayer MoS_2, WS_2, and their bilayer heterostructures,* Nano Letters **14**, 5097 (2014).

[145] B. Peng, H. Zhang, H. Shao, Y. Xu, X. Zhang, and H. Zhu, *Towards intrinsic phonon transport in single-layer MoS_2,* Annalen der Physik **528**, 504, https://onlinelibrary.wiley.com/doi/pdf/10.1002/andp.201500354 .

[146] Y. Gan and H. Zhao, *Chirality and vacancy effect on phonon dispersion of MoS_2 with strain,* Physics Letters A **380**, 745 (2016).

[147] R. J. Dolleman, S. Houri, A. Chandrashekar, F. Alijani, H. S. van der Zant, and P. G. Steeneken, *Opto-thermally excited multimode parametric resonance in graphene membranes,* Scientific Reports **8**, 9366 (2018).

[148] L. Zhu, T. Zhang, Z. Sun, J. Li, G. Chen, and S. A. Yang, *Thermal conductivity of biaxial-strained MoS_2: sensitive strain dependence and size-dependent reduction rate,* Nanotechnology **26**, 465707 (2015).

[149] A. Goossens, V. Calado, A. Barreiro, K. Watanabe, T. Taniguchi, and L. Vandersypen, *Mechanical cleaning of graphene,* Applied Physics Letters **100**, 073110 (2012).

[150] I. Jo, M. T. Pettes, L. Lindsay, E. Ou, A. Weathers, A. L. Moore, Z. Yao, and L. Shi, *Reexamination of basal plane thermal conductivity of suspended graphene samples measured by electro-thermal micro-bridge methods,* AIP Advances **5**, 053206 (2015).

[151] M. Faraday, *On a peculiar class of acoustical figures; and on certain forms assumed by a group of particles upon vibrating elastic surfaces,* Philisophical Transactions of the Royal Society (London) **121**, 299 (1831).

[152] K. L. Turner, S. A. Miller, P. G. Hartwell, N. C. MacDonald, S. H. Strogatz, and S. G. Adams, *Five parametric resonances in a microelectromechanical system,* Nature **396**, 149 (1998).

[153] D. Rugar and P. Grütter, *Mechanical parametric amplification and thermomechanical noise squeezing,* Physical Review Letters **67**, 699 (1991).

[154] R. Karabalin, X. Feng, and M. Roukes, *Parametric nanomechanical amplification at very high frequency,* Nano Letters **9**, 3116 (2009).

[155] R. Karabalin, R. Lifshitz, M. Cross, M. Matheny, S. Masmanidis, and M. Roukes, *Signal amplification by sensitive control of bifurcation topology,* Physical Review Letters **106**, 094102 (2011).

[156] W. Zhang and K. L. Turner, *Application of parametric resonance amplification in a single-crystal silicon micro-oscillator based mass sensor,* Sensors and Actuators A: Physical **122**, 23 (2005).

[157] W. Zhang, R. Baskaran, and K. L. Turner, *Effect of cubic nonlinearity on auto-parametrically amplified resonant MEMS mass sensor,* Sensors and Actuators A: Physical **102**, 139 (2002).

[158] I. Mahboob and H. Yamaguchi, *Piezoelectrically pumped parametric amplification and Q enhancement in an electromechanical oscillator,* Applied Physics Letters **92**, 173109 (2008).

[159] L. A. Oropeza-Ramos and K. L. Turner, *Parametric resonance amplification in a MEMGyroscope,* in *Sensors, 2005 IEEE* (IEEE, 2005) pp. 4–pp.

[160] Z. Hu, B. Gallacher, J. Burdess, C. Fell, and K. Townsend, *A parametrically amplified MEMS rate gyroscope,* Sensors and Actuators A: Physical **167**, 249 (2011).

[161] K. Harish, B. Gallacher, J. Burdess, and J. Neasham, *Experimental investigation of parametric and externally forced motion in resonant MEMS sensors,* Journal of Micromechanics and Microengineering **19**, 015021 (2008).

[162] I. Mahboob and H. Yamaguchi, *Bit storage and bit flip operations in an electromechanical oscillator,* Nature Nanotechnology **3**, 275 (2008).

[163] I. Mahboob, M. Mounaix, K. Nishiguchi, A. Fujiwara, and H. Yamaguchi, *A multimode electromechanical parametric resonator array,* Scientific Reports **4** (2014), 10.1038/srep04448.

[164] M. Roukes, *Mechanical compution, redux?* in *Electron Devices Meeting, 2004. IEDM Technical Digest. IEEE International* (IEEE, 2004) pp. 539–542.

[165] M. Freeman and W. Hiebert, *NEMS: Taking another swing at computing,* Nature Nanotechnology **3**, 251 (2008).

[166] A. Sakhaee-Pour, M. Ahmadian, and A. Vafai, *Applications of single-layered graphene sheets as mass sensors and atomistic dust detectors,* Solid State Communications **145**, 168 (2008).

[167] P. Prasad, N. Arora, and A. Naik, *Parametric amplification in MoS_2 drum resonator,* Nanoscale **9**, 18299 (2017).

[168] J. P. Mathew, R. N. Patel, A. Borah, R. Vijay, and M. M. Deshmukh, *Dynamical strong coupling and parametric amplification of mechanical modes of graphene drums,* Nature Nanotechnology **11**, 747 (2016).

[169] A. Eichler, J. Chaste, J. Moser, and A. Bachtold, *Parametric amplification and self-oscillation in a nanotube mechanical resonator,* Nano Letters **11**, 2699 (2011).

[170] B. Sajadi, F. Alijani, D. Davidovikj, J. Goosen, P. G. Steeneken, and F. van Keulen, *Experimental characterization of graphene by electrostatic resonance frequency tuning,* Journal of Applied Physics **122**, 234302 (2017).

[171] N. E. Sanchez and A. H. Nayfeh, *Prediction of bifurcations in a parametrically excited duffing oscillator,* International Journal of Non-Linear Mechanics **25**, 163 (1990).

[172] S. Houri, S. J. Cartamil-Bueno, M. Poot, P. G. Steeneken, H. S. J. van der Zant, and W. J. Venstra, *Direct and parametric synchronization of a graphene self-oscillator,* Applied Physics Letters **110**, 073103 (2017).

[173] K. Aubin, M. Zalalutdinov, T. Alan, R. B. Reichenbach, R. Rand, A. Zehnder, J. Parpia, and H. Craighead, *Limit cycle oscillations in CW laser-driven NEMS,* Journal of Microelectromechanical Systems **13**, 1018 (2004).

[174] J. F. Rhoads, S. W. Shaw, K. L. Turner, J. Moehlis, B. E. DeMartini, and W. Zhang, *Generalized parametric resonance in electrostatically actuated microelectromechanical oscillators,* Journal of Sound and Vibration **296**, 797 (2006).

[175] K. Jinkins, J. Camacho, L. Farina, and Y. Wu, *Examination of humidity effects on measured thickness and interfacial phenomena of exfoliated graphene on silicon dioxide via amplitude modulation atomic force microscopy,* Applied Physics Letters **107**, 243107 (2015).

[176] J. S. Bunch and M. L. Dunn, *Adhesion mechanics of graphene membranes,* Solid State Communications **152**, 1359 (2012).

[177] C. S. Ruiz-Vargas, H. L. Zhuang, P. Y. Huang, A. M. van der Zande, S. Garg, P. L. McEuen, D. A. Muller, R. G. Hennig, and J. Park, *Softened elastic response and unzipping in chemical vapor deposition graphene membranes,* Nano Letters **11**, 2259 (2011).

[178] D. Yoon, Y.-W. Son, and H. Cheong, *Negative thermal expansion coefficient of graphene measured by Raman spectroscopy,* Nano Letters **11**, 3227 (2011).

[179] M. Zalalutdinov, A. Olkhovets, A. Zehnder, B. Ilic, D. Czaplewski, H. G. Craighead, and J. M. Parpia, *Optically pumped parametric amplification for micromechanical oscillators,* Applied Physics Letters **78**, 3142 (2001).

[180] R. R. Mansour, F. Huang, S. Fouladi, W. D. Yan, and M. Nasr, *High-Q tunable filters: Challenges and potential,* IEEE Microwave Magazine **15**, 70 (2014).

[181] M. S. Hanay, S. I. Kelber, C. D. O'Connell, P. Mulvaney, J. E. Sader, and M. L. Roukes, *Inertial imaging with nanomechanical systems,* Nature Nanotechnology **10**, 339 (2015).

[182] N. Cermak, S. Olcum, F. F. Delgado, S. C. Wasserman, K. R. Payer, M. A. Murakami, S. M. Knudsen, R. J. Kimmerling, M. M. Stevens, Y. Kikuchi, A. Sansikci, M. Ogawa, V. Agache, D. M. Weinstock, and S. R. Manalis, *High-throughput measurement of single-cell growth rates using serial microfluidic mass sensor arrays,* Nature Biotechnology **34**, 1052 (2016).

[183] M. Amabili, *Nonlinear Vibrations and Stability of Shells and Plates* (Cambridge University Press, 2008).

[184] S. Zaitsev, O. Shtempluck, E. Buks, and O. Gottlieb, *Nonlinear damping in a micromechanical oscillator,* Nonlinear Dynamics **67**, 859 (2012).

[185] A. H. Nayfeh and D. T. Mook, *Non-linear oscillations* (Wiley, 1995).

[186] E. J. Doedel, A. R. Champneys, T. F. Fairgrieve, Y. A. Kuznetsov, B. Sandstede, and X. Wang, *Auto 97: Continuation and bifurcation software for ordinary differential equations,* (1998).

[187] R. S. Lakes, *Viscoelastic Materials*, Vol. 1 (Cambridge University Press, New York, USA, 2009).

[188] R. J. Dolleman, P. Belardinelli, S. Houri, H. S. J. van der Zant, F. Alijani, and P. G. Steeneken, *High-frequency stochastic switching of graphene drum resonators,* (2018), in preparation.

[189] L. Gammaitoni, P. Hänggi, P. Jung, and F. Marchesoni, *Stochastic resonance,* Reviews of Modern Physics **70**, 223 (1998).

[190] L. Lapidus, D. Enzer, and G. Gabrielse, *Stochastic phase switching of a parametrically driven electron in a Penning trap,* Physical Review Letters **83**, 899 (1999).

[191] J. Hales, A. Zhukov, R. Roy, and M. Dykman, *Dynamics of activated escape and its observation in a semiconductor laser,* Physical Review Letters **85**, 78 (2000).

[192] O. Tretiakov and K. Matveev, *Stochastic current switching in bistable resonant tunneling systems,* Physical Review B **71**, 165326 (2005).

[193] A. Hibbs, A. Singsaas, E. Jacobs, A. Bulsara, J. Bekkedahl, and F. Moss, *Stochastic resonance in a superconducting loop with a Josephson junction,* Journal of Applied Physics **77**, 2582 (1995).

[194] D. Wilkowski, J. Ringot, D. Hennequin, and J. C. Garreau, *Instabilities in a magneto-optical trap: noise-induced dynamics in an atomic system,* Physical Review Letters **85**, 1839 (2000).

[195] F. Ricci, R. A. Rica, M. Spasenović, J. Gieseler, L. Rondin, L. Novotny, and R. Quidant, *Optically levitated nanoparticle as a model system for stochastic bistable dynamics,* Nature Communications **8**, 15141 (2017).

[196] L. Rondin, J. Gieseler, F. Ricci, R. Quidant, C. Dellago, and L. Novotny, *Direct measurement of Kramers turnover with a levitated nanoparticle,* Nature Nanotechnology **12**, 1130 (2017).

[197] C. Stambaugh and H. B. Chan, *Noise-activated switching in a driven nonlinear micromechanical oscillator,* Physical Review B **73**, 172302 (2006).

[198] M. Dykman, C. Maloney, V. Smelyanskiy, and M. Silverstein, *Fluctuational phase-flip transitions in parametrically driven oscillators,* Physical Review E **57**, 5202 (1998).

[199] H. Chan, M. I. Dykman, and C. Stambaugh, *Paths of fluctuation induced switching,* Physical Review Letters **100**, 130602 (2008).

[200] R. L. Badzey and P. Mohanty, *Coherent signal amplification in bistable nanomechanical oscillators by stochastic resonance,* Nature **437**, 995 (2005).

[201] J. Aldridge and A. Cleland, *Noise-enabled precision measurements of a Duffing nanomechanical resonator,* Physical Review Letters **94**, 156403 (2005).

[202] H. Chan and C. Stambaugh, *Fluctuation-enhanced frequency mixing in a nonlinear micromechanical oscillator,* Physical Review B **73**, 224301 (2006).

[203] T. Ono, Y. Yoshida, Y.-G. Jiang, and M. Esashi, *Noise-enhanced sensing of light and magnetic force based on a nonlinear silicon microresonator,* Applied Physics Express **1**, 123001 (2008).

[204] W. J. Venstra, H. J. Westra, and H. S. Van Der Zant, *Stochastic switching of cantilever motion,* Nature Communications **4**, 2624 (2013).

[205] N. Kryloff, N. Bogoliubov, and S. Lefschetz, *Introduction to Non-linear Mechanics*, Annals of mathematics studies (Princeton University Press, 1947).

[206] B. Oksendal, *Stochastic Differential Equations: An Introduction with Applications*, Universitext (Springer Berlin Heidelberg, 2013).

[207] M. Freidlin and A. Wentzell, *Random Perturbations of Dynamical Systems*, Grundlehren der mathematischen Wissenschaften No. v. 260 (Springer, 1998).

[208] J. Lee and P. X.-L. Feng, *Atomically-thin MoS_2 resonators for pressure sensing,* in *Frequency Control Symposium (FCS), 2014 IEEE International* (IEEE, 2014) pp. 1–4.

[209] J. Lee, Z. Wang, K. He, J. Shan, and P. X.-L. Feng, *Air damping of atomically thin MoS_2 nanomechanical resonators,* Applied Physics Letters **105**, 023104 (2014).

[210] M. Andrews, G. Turner, P. Harris, and I. Harris, *A resonant pressure sensor based on a squeezed film of gas,* Sensors and Actuators A: Physical **36**, 219 (1993).

[211] D. Southworth, H. Craighead, and J. Parpia, *Pressure dependent resonant frequency of micromechanical drumhead resonators,* Applied Physics Letters **94**, 213506 (2009).

[212] M. Andrews, I. Harris, and G. Turner, *A comparison of squeeze-film theory with measurements on a microstructure,* Sensors and Actuators A: Physical **36**, 79 (1993).

[213] L. Kumar, K. Reimann, M. J. Goossens, W. F. Besling, R. J. Dolleman, R. H. Pijnenburg, C. van der Avoort, L. P. Sarro, and P. G. Steeneken, *MEMS oscillating squeeze-film pressure sensor with optoelectronic feedback,* Journal of Micromechanics and Microengineering **25**, 045011 (2015).

[214] A. Castellanos-Gomez, M. Wojtaszek, N. Tombros, N. Agraït, B. J. van Wees, and G. Rubio-Bollinger, *Atomically thin mica flakes and their application as ultrathin insulating substrates for graphene,* Small **7**, 2491 (2011).

[215] M. Bao, H. Yang, H. Yin, and Y. Sun, *Energy transfer model for squeeze-film air damping in low vacuum,* Journal of Micromechanics and Microengineering **12**, 341 (2002).

[216] S. S. Rao, *Vibration of continuous systems* (John Wiley & Sons, 2007).

[217] T. Wah, *Vibration of circular plates,* the Journal of the Acoustical Society of America **34**, 275 (1962).

[218] T. Veijola, H. Kuisma, J. Lahdenperä, and T. Ryhänen, *Equivalent-circuit model of the squeezed gas film in a silicon accelerometer,* Sensors and Actuators A: Physical **48**, 239 (1995).

[219] R. J. Dolleman, D. Chakraborty, D. R. Ladiges, J. E. Sader, H. S. J. van der Zant, and P. G. Steeneken, *Gas actuation and inertial effects on single-layer graphene squeeze-film pressure sensors,* (2018), in preparation.

[220] L. Wang, C. M. Williams, M. S. Boutilier, P. R. Kidambi, and R. Karnik, *Single-layer graphene membranes withstand ultrahigh applied pressure,* Nano Letters **17**, 3081 (2017).

[221] P. Steeneken, T. G. Rijks, J. Van Beek, M. Ulenaers, J. De Coster, and R. Puers, *Dynamics and squeeze film gas damping of a capacitive RF MEMS switch,* Journal of Micromechanics and Microengineering **15**, 176 (2004).

[222] D. Chakraborty, E. van Leeuwen, M. Pelton, and J. E. Sader, *Vibration of nanoparticles in viscous fluids,* The Journal of Physical Chemistry C **117**, 8536 (2013).

[223] D. Chakraborty and J. E. Sader, *Constitutive models for linear compressible viscoelastic flows of simple liquids at nanometer length scales,* Physics of Fluids **27**, 052002 (2015).

[224] D. R. Ladiges and J. E. Sader, *Frequency-domain Monte Carlo method for linear oscillatory gas flows,* Journal of Computational Physics **284**, 351 (2015).

[225] D. R. Ladiges and J. E. Sader, *Frequency-domain deviational Monte Carlo method for linear oscillatory gas flows,* Physics of Fluids **27**, 102002 (2015).

[226] V. Singh, S. Sengupta, H. S. Solanki, R. Dhall, A. Allain, S. Dhara, P. Pant, and M. M. Deshmukh, *Probing thermal expansion of graphene and modal dispersion at low-temperature using graphene nanoelectromechanical systems resonators,* Nanotechnology **21**, 165204 (2010).

[227] X. Song, M. Oksanen, M. A. Sillanpää, H. Craighead, J. Parpia, and P. J. Hakonen, *Stamp transferred suspended graphene mechanical resonators for radio frequency electrical readout,* Nano Letters **12**, 198 (2011).

[228] S. P. Koenig, N. G. Boddeti, M. L. Dunn, and J. S. Bunch, *Ultrastrong adhesion of graphene membranes,* Nature Nanotechnology **6**, 543 (2011).

[229] H. W. Kim, H. W. Yoon, S.-M. Yoon, B. M. Yoo, B. K. Ahn, Y. H. Cho, H. J. Shin, H. Yang, U. Paik, S. Kwon, J.-Y. Choi, and H. B. Park, *Selective gas transport through few-layered graphene and graphene oxide membranes,* Science **342**, 91 (2013).

[230] E. M. Kramer and D. R. Myers, *Five popular misconceptions about osmosis,* American Journal of Physics **80**, 694 (2012).

[231] S.-E. Zhu, M. K. Ghatkesar, C. Zhang, and G. Janssen, *Graphene based piezoresistive pressure sensor,* Applied Physics Letters **102**, 161904 (2013).

[232] P. Sundqvist, *Exponential curve-fitting, without start-guess,* Retrieved 14 March 2016.

[233] R. C. Rollings, A. T. Kuan, and J. A. Golovchenko, *Ion selectivity of graphene nanopores,* Nature Communications **7**, 11408 (2016).

[234] S. P. Surwade, S. N. Smirnov, I. V. Vlassiouk, R. R. Unocic, G. M. Veith, S. Dai, and S. M. Mahurin, *Water desalination using nanoporous single-layer graphene,* Nature Nanotechnology **10**, 459 (2015).

[235] R. J. Dolleman, A. Katan, H. S. J. van der Zant, and P. G. Steeneken, *Suspended graphene deflected by osmotic pressure,* (2018), in preparation.

[236] N. Oliver, C. Toumazou, A. Cass, and D. Johnston, *Glucose sensors: a review of current and emerging technology,* Diabetic Medicine **26**, 197 (2009).

[237] H.-C. Wang and A.-R. Lee, *Recent developments in blood glucose sensors,* Journal of food and drug analysis **23**, 191 (2015).

[238] N. Ch and R. P. Paily, *Design of an osmotic pressure sensor for sensing an osmotically active substance,* Journal of Micromechanics and Microengineering **25**, 045019 (2015).

[239] R. Wilson and A. Turner, *Glucose oxidase: an ideal enzyme,* Biosensors and Bioelectronics **7**, 165 (1992).

[240] H.-C. Wang, H. Zhou, B. Chen, P. M. Mendes, J. S. Fossey, T. D. James, and Y.-T. Long, *A bis-boronic acid modified electrode for the sensitive and selective determination of glucose concentrations,* Analyst **138**, 7146 (2013).

[241] A. Eftekhari and H. Garcia, *The necessity of structural irregularities for the chemical applications of graphene,* Materials Today Chemistry **4**, 1 (2017).

[242] A. Zandiatashbar, G.-H. Lee, S. J. An, S. Lee, N. Mathew, M. Terrones, T. Hayashi, C. R. Picu, J. Hone, and N. Koratkar, *Effect of defects on the intrinsic strength and stiffness of graphene,* Nature Communications **5**, 3186 (2014).

[243] T. Humplik, J. Lee, S. O'hern, B. Fellman, M. Baig, S. Hassan, M. Atieh, F. Rahman, T. Laoui, R. Karnik, and E. Wang, *Nanostructured materials for water desalination,* Nanotechnology **22**, 292001 (2011).

[244] D. Cohen-Tanugi and J. C. Grossman, *Nanoporous graphene as a reverse osmosis membrane: recent insights from theory and simulation,* Desalination **366**, 59 (2015).

[245] M. E. Suk and N. Aluru, *Ion transport in sub-5-nm graphene nanopores,* The Journal of Chemical Physics **140**, 084707 (2014).

[246] D. Cohen-Tanugi and J. C. Grossman, *Water permeability of nanoporous graphene at realistic pressures for reverse osmosis desalination,* The Journal of Chemical Physics **141**, 074704 (2014).

[247] M. E. Suk and N. Aluru, *Water transport through ultrathin graphene,* The Journal of Physical Chemistry Letters **1**, 1590 (2010).

[248] M. S. Boutilier, C. Sun, S. C. O'Hern, H. Au, N. G. Hadjiconstantinou, and R. Karnik, *Implications of permeation through intrinsic defects in graphene on the design of defect-tolerant membranes for gas separation,* ACS Nano **8**, 841 (2014).

[249] K. Sint, B. Wang, and P. Král, *Selective ion passage through functionalized graphene nanopores,* Journal of the American Chemical Society **130**, 16448 (2008).

[250] H. C. Price, J. Mattsson, and B. J. Murray, *Sucrose diffusion in aqueous solution,* Physical Chemistry Chemical Physics **18**, 19207 (2016).

[251] A. Castellanos-Gomez, V. Singh, H. S. van der Zant, and G. A. Steele, *Mechanics of freely-suspended ultrathin layered materials,* Annalen der Physik **527**, 27 (2015).

[252] I. R. Storch, R. De Alba, V. P. Adiga, T. S. Abhilash, R. A. Barton, H. G. Craighead, J. M. Parpia, and P. L. McEuen, *Young's modulus and thermal expansion of tensioned graphene membranes,* Phys. Rev. B **98**, 085408 (2018).

[253] R. J. Dolleman, D. Chakraborty, D. R. Ladiges, D. Davidovikj, S. Vollebregt, H. S. J. van der Zant, J. E. Sader, and P. G. Steeneken, *Inertial characterization of graphene resonators,* (2018), in preparation.

[254] R. J. Dolleman, *Graphene Based Pressure Sensors: Resonant Pressure Transduction using Atomically Thin Materials,* Master's thesis, Delft University of Technology (2014).

[255] R. J. Dolleman, M. Hsu, H. S. J. van der Zant, M. K. Ghatkesar, and P. G. Steeneken, *Quantatative transfer residue characterization of graphene using quartz crystal microbalances,* (2018), in preparation.

[256] M. Hsu, *Investigating the mass of single-layer graphene using a quartz crystal microbalance*, Master's thesis, Delft University of Technology (2018).

[257] M. Singh, *Suspended Graphene Membranes For Electrostatically Actuated Resonators*, Master's thesis, Delft University of Technology (2017).

[258] J. Romijn, S. Vollebregt, R. J. Dolleman, M. Singh, H. S. J. van der Zant, P. G. Steeneken, and P. M. Sarro, *A miniaturized low power pirani pressure sensor based on suspended graphene,* in *NEMS 2018, 13th International Conference on Nano/Micro Engineered and Molecular Systems (IEEE-NEMS)* (IEEE, 2018) accepted for publication.

[259] J. Romijn, S. Vollebregt, R. J. Dolleman, M. Singh, H. S. J. van der Zant, P. G. Steeneken, and P. M. Sarro, *Graphene Pirani pressure sensors,* (2018), in preparation.

[260] K. Khosraviani and A. M. Leung, *The nanogap Pirani—a pressure sensor with superior linearity in an atmospheric pressure range,* Journal of Micromechanics and Microengineering **19**, 045007 (2009).

[261] J. Romijn, *Design and Integration of Graphene Sensors with Read-Out Electronics: A Graphene-Based Pirani Pressure Sensor Integrated with the BICMOS Process*, Master's thesis, Delft University of Technology (2018).

[262] I. Rosłoń, *Graphene gas sensor*, Master's thesis, Delft University of Technology (2018).

[263] L. Madauß, J. Schumacher, M. Ghosh, O. Ochedowski, J. Meyer, H. Lebius, B. Ban-d'Etat, M. E. Toimil-Molares, C. Trautmann, and R. Lammertink, *Fabrication of nanoporous graphene/polymer composite membranes,* Nanoscale **9**, 10487 (2017).

[264] G. Reichenauer, U. Heinemann, and H.-P. Ebert, *Relationship between pore size and the gas pressure dependence of the gaseous thermal conductivity,* Colloids and Surfaces A: Physicochemical and Engineering Aspects **300**, 204 (2007).

[265] P. Belardinelli, R. J. Dolleman, P. G. Steeneken, and F. Alijani, *On the quasiperiodic motion in nonlinear graphene resonators,* in *EUROMECH Colloquium 603: Dynamics of Micro and Nanosystems* (2018).

[266] R. J. Dolleman, P. Belardinelli, S. Houri, H. S. J. van der Zant, P. G. Steeneken, and F. Alijani, *Stochastic effects in nonlinear graphene resonators driven by two incommensurate frequencies,* (2018), in preparation.

[267] G. Danda, P. M. Das, and M. Drndić, *Laser-induced fabrication of nanoporous monolayer WS_2 membranes,* 2D Materials **5**, 035011 (2018).

[268] J. P. Thiruraman, K. Fujisawa, G. Danda, P. M. Das, T. Zhang, A. Bolotsky, N. Perea-López, A. Nicolaï, P. Senet, M. Terrones, *et al.*, *Angstrom-size defect creation and ionic transport through pores in single-layer MoS_2*, Nano Letters **18**, 1651 (2018).

[269] D. Hatanaka, I. Mahboob, K. Onomitsu, and H. Yamaguchi, *Phonon waveguides for electromechanical circuits,* Nature Nanotechnology **9**, 520 (2014).

Curriculum Vitæ

Robin Joey Dolleman

13-06-1991 Born in Gouda, The Netherlands.

Education

2003 – 2009 Preuniversity Secondary Education (Voortgezet Wetenschappelijk Onderwijs)
Minkema College, Woerden, The Netherlands

2009 – 2012 Bachelor of Science in Mechanical Engineering
Delft University of Technology, Delft, The Netherlands
Thesis: The Influence of Diffusion on Graphene Growth
Supervisor: Prof. dr. G. C. A. M. Janssen

2012 – 2014 Master of Science in Mechanical Engineering
Delft University of Technology, Delft, The Netherlands
Thesis: Graphene Based Pressure Sensors
Supervisor: Prof. dr. G. C. A. M. Janssen

2014 – 2018 PhD in Applied Physics
Delft University of Technology, Delft, The Netherlands
Thesis: Dynamics of interacting graphene membranes
Promotor: Prof. dr. P. G. Steenenken
Promotor: Prof. dr. ir. H. S. J. van der Zant

2017 & 2018 Visiting Researcher (total 3 months) in Applied Mathematics
The University of Melbourne, Melbourne, Australia
Host: Prof. dr. J. E. Sader

Awards

2018 Graphene Flagship Mobility Grant

List of Publications

Journal Publications

16. **Robin J. Dolleman**, Pierpaolo Belardinelli, Samer Houri, Herre S. J. van der Zant, Peter G. Steeneken and Farbod Alijani , *Stochastic effects in nonlinear graphene resonators driven by two incommensurate frequencies*, manuscript in preparation

15. Joost Romijn, Sten Vollebregt, **Robin J. Dolleman**, Manvika Singh, Herre S. J. van der Zant, Peter G. Steeneken and Pasqualina M. Sarro, *Graphene Pirani pressure sensors*, manuscript in preparation

14. **Robin J. Dolleman**, Mick Hsu, Herre S. J. van der Zant, Murali K. Ghatkesar and Peter G. Steeneken, *Quantatative transfer residue characterization of graphene using quartz crystal microbalances*, manuscript in preparation

13. **Robin J. Dolleman**, Debadi Chakraborty, Daniel R. Ladiges, Dejan Davidovikj, Sten Vollebregt, Herre S. J. van der Zant, John E. Sader and Peter G. Steeneken, *Inertial characterization of graphene resonators*, manuscript in preparation

12. **Robin J. Dolleman**, Allard Katan, Herre S. J. van der Zant and Peter G. Steeneken, *Characterizing graphene membranes deflected by osmotic pressure using liquid-cell atomic force microscopy*, manuscript in preparation

11. **Robin J. Dolleman**, Debadi Chakraborty, Daniel R. Ladiges, John E. Sader, Herre S.J. van der Zant and Peter G. Steeneken, *Gas actuation and inertial effects on single-layer graphene squeeze-film pressure sensors*, manuscript in preparation

10. **Robin J. Dolleman**, Pierpaolo Belardinelli, Samer Houri, Herre S. J. van der Zant, Farbod Alijani and Peter G. Steeneken, *High-frequency stochastic switching of graphene drum resonators*, manuscript in preparation

9. **Robin J. Dolleman**, Gerard Verbiest, Yaroslav M. Blanter, Herre S. J. van der Zant and Peter G. Steeneken, *Transient mechanical response of opto-thermally excited suspended graphene membranes*, manuscript in preparation

8. André F. Sartori, Pierpaolo Belardinelli, **Robin J. Dolleman**, Peter G. Steeneken, Murali K. Ghatkesar, Josephus G. Buijnsters, *Fabrication of high Q-factor diamond disc resonators by inkjet printing*, manuscript under peer review

7. **Robin J. Dolleman**, David Lloyd, Martin Lee, J. Scott Bunch, Herre S. J. van der Zant, Peter G. Steeneken, *Transient thermal characterization of suspended monolayer MoS_2*, manuscript under peer review

6. **Robin J. Dolleman**, Samer Houri, Abhilash Chandrashekar, Farbod Alijani, Herre S. J. van der Zant, Peter G. Steeneken, *Opto-thermally excited multimode parametric resonance in graphene membranes*, Scientific Reports **8**, 9388 (2018)

5. **Robin J. Dolleman**, Dejan Davidovikj, Herre S.J. van der Zant, Peter G. Steeneken, *Amplitude calibration of 2D mechanical resonators by nonlinear optical transduction*, Applied Physics Letters **111** (25), 253104 (2017)

4. **Robin J. Dolleman**, Samer Houri, Dejan Davidovikj, Santiago J. Cartamil-Bueno, Yaroslav M. Blanter, Herre S.J. van der Zant, Peter G. Steeneken, *Optomechanics for thermal characterization of suspended graphene*, Physical Review B **96** (16), 165421 (2017)

3. **Robin J. Dolleman**, Santiago J. Cartamil-Bueno, Herre S.J. van der Zant, Peter G. Steeneken, *Graphene gas osmometers*, 2D Materials **4** (1), 011002 (2017)

2. **Robin J. Dolleman**, Dejan Davidovikj, Santiago J. Cartamil-Bueno, Herre S.J. van der Zant, Peter G. Steeneken, *Graphene squeeze-film pressure sensors*, Nano Letters **16** (1), 568-571 (2016)

1. Lalit Kumar, Klaus Reimann, Martijn J. Goossens, Willem F.A. Besling, **Robin J. Dolleman**, Remco H.W. Pijnenburg, Cas van der Avoort, Lina P.M. Sarro, Peter G. Steeneken,*MEMS oscillating squeeze-film pressure sensor with optoelectronic feedback*, Journal of Micromechanics and Microengineering **25** (4), 045011 (2015)

CONFERENCE PROCEEDINGS

6. Pierpaolo Belardinelli, **Robin J. Dolleman**, Peter G. Steeneken and Farbod Alijani, *On the quasiperiodic motion in nonlinear graphene resonators*, EUROMECH Colloquium 603: Dynamics of Micro and Nanosystems, *in submission (accepted)*, (2018)

5. Joost Romijn, Sten Vollebregt, **Robin J. Dolleman**, Manvika Singh, Herre S.J. van der Zant, Peter G. Steeneken, Pasqualina M. Sarro, *A miniaturized low power Pirani pressure sensor based on suspended graphene*, 13th International Conference on Nano/Micro Engineered and Molecular Systems (IEEE-NEMS), *in submission (accepted)*, (2018)

4. Sten Vollebregt, **Robin J. Dolleman**, Herre S. J. van der Zant, Peter G. Steeneken, Pasqualina M. Sarro, *Suspended graphene beams with tunable gap for squeeze-film pressure sensing*, 19th International Conference on Solid-State Sensors, Actuators and Microsystems (IEEE-TRANSDUCERS), 770-773 (2017)

3. **Robin J. Dolleman**, Farbod Alijani, Herre S.J. van der Zant, Peter G. Steeneken, *Non-linear dynamics of opto-thermally excited atomically thin graphene resonators*, 9th European Nonlinear Dynamics Conference (2017)

2. **Robin J. Dolleman**, Dejan Davidovikj, Santiago J. Cartamil-Bueno, Debadi Chakraborty, John E. Sader, Herre S.J. van der Zant, Peter G. Steeneken, *Pressure sensors from single-layer graphene*, 13th International Workshop on Nanomechanical Sensing (NMC) (2016)

1. **Robin J. Dolleman**, Peter G. Steeneken, Herre S.J. van der Zant, *Nanomechanical pressure sensors using suspended graphene membranes*, 12th International Workshop on Nanomechanical Sensing (NMC) (2015)

ACKNOWLEDGEMENTS

If you have read this entire dissertation, you might think that this book is the result of me sitting in a lab 24/7 and spending no time on anything else. I can tell you that I am extremely passionate about the subject I am working on. But if you ask me, the thickness of this book reflects more the fantastic help, support and collaborations that I got from other people. So this very important chapter is dedicated to all those people, to express my gratitude for making all this possible. Some of my collegues have raised the bar for this chapter quite high, my style is to keep things a bit more brief (ironically), but please do not mistake this as any less graditute towards anyone.

Peter, if there is anyone I should thank for making this possible, it is you. Looking back on how I started on this project, as a naive master student from mechanical engineering with no experience in experimental physics whatsoever, you gave me the opportunity to do this PhD. I did not expect much when starting this PhD, but now I have found a path that I want to follow for the rest of my career. Thank you for believing in me and giving me the opportunity to develop myself as a physicist.

Next, I want to thank my second promotor. Herre, you might no longer be the head of the department, but I will always remember you as the glorious leader of MED. Whenever I was enthusiastic about a new result, I could always walk into you office and show what I have found. Thanks for nourishing that enthusiasm when appropriate, and also thanks for tuning it down slightly where appropriate.

John, thank you for welcoming me in your department twice. I will never forget the moment after my first international presentation at a conference, where you - basically a god in my eyes - walked up to me and we started our collaboration. It really helped me understand the value of passionate mathematicians in the world of science. Thank you very much for being part of my doctoral committee as well, and I hope we can continue to collaborate future endeavors.

I also want to thank the rest of the great people at the University of Melbourne who contributed greatly to my research. Daniel, Debadi, thank you for all the hard work you put into simulating the devices. It took a lot of time and effort, but I think we finally obtained some good understanding of what is happening in my pressure sensors and I am really proud of what we achieved. Alexander, thank you for jumping so enthusiastically on the calibration method, I hope it makes a great addition to your thesis.

Next in line is a true lifesaver. Sten, without you this thesis would not have a single mention of the word CMOS or integration. You truly developed a beautiful production process that makes me write down proposition 7 with full confidence. Thank you for collaborating so passionately and extensively, and all the fruitful discussions we had.

Samer, If there is one reason there are two chapters in nonlinear dynamics in this thesis, it is you. Your passion was really contagious and you have taught me so much on the experimental parts as well. Your support and all the discussions were crucial to

the success of my PhD. But of course, I would not dare to say anything bad about you because you possess an embarrassing photo of me falling asleep during a conference.

Talking about nonlinear dynamics, I should definitely not forget to mention Farbod. You developed all these nonlinear dynamics that we measured into a useful tool for physicist. Thank you for all the great collaborations and continued support as I was exploring the field of nonlinear dynamics. I also want to thank Pierpaolo for all the simulations and great collaborations, they really bring the nonlinear dynamics I was studying to a new level.

I want to thank Yaroslav for his extensive and indispensable help to develop the models for boundary heat transport in graphene. Also for making the time for fruitful discussions on my experimental results.

Allard, the official AFM-God, thank you for your help in getting the liquid osmometer experiments running. It was such a difficult setup and I could not have done it without your help. I am glad that we were able to get some good results.

I also express my deep gratitude to the people working at Applied Nanolayers, who supplied the high quality samples for my research. Michele, Dominique, Paul, thank you for all your help and thinking along with my research. Richard, thank you for the fruitful discussions and feedback during the user committee meetings and of many thanks for being part in my doctoral committee.

I want to thank Scott Bunch and David Lloyd for the fantastic collaboration on the MoS_2 characterization. Obtaining such a high-quality sample is not easy and I thank you for all the hard work you put in for me.

I extend my gratitude to my committee members that I haven't already mentioned. First of all, I thank for reading this dissertation which is perhaps a bit larger than the average, nevertheless I hope you enjoyed it. Marika, thank you for providing samples for our measurements and fruitful discussions at the Graphene Flagship meetings as well. Gary, especially in the beginning of my PhD we had a lot of discussions and your critical attitude during the werkbesprekingen always kept me sharp. Lina, the collaboration with your department was really a lifesaver for my project, we would never have come this close to CMOS integration without it. I also want to thank Guido, who did not supervise me during my PhD, but as supervisor during my BSc and MSc projects is definitely responsible for putting me on this course. My passion for 2D materials really started there.

During several conferences and schools I met several professors who took the time to discuss my experimental results. In particular I want to thank Steven Shaw, Mark Dykman and Barry Gallacher for having these discussions.

Next up are Walter and Koen, the honorable paranifms. In the Dutch PhD ceremony, the candidate is accompanied by two paranimfs, like best men at a wedding. It was absolutely clear that this was going to be you, my longest lasting and unconditional friends since childhood. The three of us is certainly the best representation of Oudewater since 1572 [1]. Thank you guys for being there for me throughout my life, and thank you for being there to support me during the ceremony.

Next in line is the Steenekenlab. I had the pleasure of joining this lab in its early stages and it was great to see it develop in one of the major players in the field. This would not

[1] Eerste Vrije Statenvergadering in Dordrecht

have been possible by the foundations laid by Warner and Ronald, thank you for all the help at the start of my PhD. Dejan, it was an absolute pleasure to work with you. In such a serious environment, it was great to have someone with the same (sometimes disgusting) sense of humor as me. You were always ready with guidance and support, even with the things outside my research, as a true beacon of wisdom. Academia will truly miss you, but I hope you truly enjoy your new job. Santiago, you were my first introduction to experimental physics, when you helped me do my first experiments during my masters. It was your passion for research that led me to this path. Stay ambitious and I am sure the first graphene product I buy will have been conceived by you.

Makars and Martin, I can see that both of you bring a lot of scientific passion and skill to the lab. Keep up the fantastic job that you are doing.

During this PhD I had the pleasure of (co-)supervising many students during their final projects. Daan, Jeffrey, Abhilash, Manvika, Joost, Mick, Irek, Justin, I hope you learned a lot during your final projects. I know that many of you are doing (or got offered) a PhD, so I think that's a good sign. I am sure you will all end up well. Abhilash, Manvika, Joost, Mick, and Irek, your research ended up in this dissertation and I thank you especially for your contributions.

Alkisti, exploring New Zealand together was one of the most memorable events during my PhD. It was truly great to have you as a travel buddy with me in the exhaustive (but successful) quest to see a kiwi. You have such a positive attitude and energy, which makes me truly look up to you. I wish you all the best with your new job and I will surely come to visit you in Eindhoven.

Another memorable conference was the one in Trieste and it was great to meet all the people who attended. But what made the conference truly special where perhaps the people who were not even in the same conference as me, but were in the same cute Italian hotel next to the venue. Especially George and Sarah, I will never forget the great time we had exploring Ljubljana together. And Sarah, thank you very much for proofreading my dissertation as well, I totally owe you a beer. There were many more people who I met during this great conference, too many to mention, but thank you for making these two weeks in Trieste unforgettable.

I have already thanked all the great collaborators I had in Melbourne. But I should of course not forget to mention all the great people I met when I stayed there, and made my times down-under unforgettable. First the people at Grad House. Bonnie, thanks for making me laugh so hard that I nearly chocked on several occasions. Daisy, thank you for the beautiful work of art, I still keep it as one of my most prized possessions. And of course Giulio, Adrián, Joanna, David, and all the others, it was truly a great time because of you and I truly miss you all.

In Melbourne, I also had the pleasure of joining one of the best offices in academic history: the one-and-only legendary G95. Ben, Joseph, Nem, Nick, Patrick, Tiffany and Zac, I won't write down your last names, but thank you for the beers, great discussions and good vibes. Finally, I also want to thank James and Mette, finding your little company was one of the best things, because it made my stay in Melbourne truly special.

I want to thank all the great people from the department formerly known as MED. I found it an extremely stimulating environment to work in and I want to thank all the PI's, post-docs, PhD's, Master and Bachelor students and the technicians for making it such

a great time. There are so many people that I have discussed with or helped me in little or big ways, that I might possibly forget a few.

Lets start with the great technicians in this department, Mascha, Tino, Ronald, and the rest, who have all helped me build experimental setups and vacuum chambers. Thank you for the fantastic support and help during my PhD.

Of course there are many great PI's in this departments that I haven't mentioned yet. In particular I had many fruitful discussions with Andrea, Simon and Sander, thank you for being so accessible in these last four years and thinking along.

Next up are the officemates that I had the pleasure to work with for a long time. Vera and Holger, thank you for all the scientific and non-scientific interactions over the past four years.

Of course there are so many people I have interacted with over the past for years in this great department. I've had unforgettable times on events such as the pirate boat to Terschelling and the christmas dinners. It was great to work with so many people working on completely different subjects and I really appreciate all the scientific discussions as well. I was all the people at this department that made it so great, and honorable mentions go to Dirk, Mafalda, Yildiz, Inge, Luncinda, Nicola, Giordano, Emre, Dmytro, Richard, João, Igor, Andreas, Maarten, Claus, Matvey, Jérémie, Willeke, Floris, Anna, Ranko, Daniel, Christian, Martijn, Nikos, Mario, Felix, Ines, Joeri, Sabina, Pascal, Davide, Riccardo, Rocco, Jushua, Julien, Anastasia, Alexandra, Ignacio, Max, Andres, Sal and Allesandro. Thank you all for making this time awesome.

There are also many people outside of this department that I had the pleasure to work with, or go to conferences with. Stephanie, thank you also for you help with the transfer techniques at the beginning of my PhD. I also want to thank Banafsheh for the many discussions we had on the buckling.

Ik wil ook al mijn vrienden uit Oudewater en omstreken bedanken, die er voor mij waren tijdens mijn PhD. Joanna, bedankt dat jij de fotograaf wilt zijn, ik weet zeker dat de foto's mooi gaan worden. Jouw studio gaat fantastisch en ik denk dat jij trots kan zijn op jezelf dat je zoiets vanaf de grond op kan bouwen. Laurens, dankzij jou kan ik toch ook van wijn genieten, en dat maakt mij toch iets meer het beschaafde mens dat ik moet zijn na het behalen van deze titel. Bedankt voor alle gezelligheid en gekkigheid de afgelopen 4 jaar. Richa, bedankt voor alle gezelligheid in Rotterdam en Breda, ik weet zeker dat jij goed terecht gaat komen. Verder wil ik ook Marja en Henri bedanken voor jullie gastvrijheid en gezelligheid. En natuurlijk Jasper en Tirza, ik zal zeker nog vaak aan komen schuiven bij Lumière. En er zijn nog veel meer mensen in het mooie Oudewater, Rowan, Jussi, Jantine, Virginia, iedereen bij Lumière, Marcel en de rest, teveel om op te noemen eigenlijk.

Als laatste wil ik mijn familie bedanken. Mijn opa, oma's, ooms, tantes, neven en nichten die mij komen steunen. Ook Sandra, Evi, Niels, Jeroen en Jan en Bart. Ik wil vooral mijn vader en moeder bedanken voor hun warme steun de laatste vier jaren. En natuurlijk mijn broer en zus, voor alle mooie momenten de afgelopen paar jaar en hun onvoorwaardelijke steun. Als laatste wil ik Morris bedanken, omdat ik al ruim 15 jaar iedere dag op een vrolijke begroeting kan rekenen.